Development of highly efficient solid oxide electrolyzer cell systems

Duhn, Jakob Dragsbæk; Jensen, Anker Degn; Wedel, Stig; Wix, Christian

Publication date:
2017

Document Version
Publisher's PDF, also known as Version of record

Citation (APA):
Duhn, J. D., Jensen, A. D., Wedel, S., & Wix, C. (2017). Development of highly efficient solid oxide electrolyzer cell systems. Kgs. Lyngby: Technical University of Denmark (DTU).

PhD Thesis
Doctor of Philosophy

DTU Chemical Engineering
Department of Chemical and Biochemical Engineering

Development of highly efficient solid oxide electrolyzer cell systems

Public version

Jakob Dragsbæk Duhn

Kongens Lyngby 2017

Bibliographic data

PhD Thesis by Jakob Dragsbæk Duhn

Titel: *Development of highly efficient solid oxide electrolyzer cell systems*
Dansk titel: *Udvikling af effektive fast oxid elektrolyse celle systemer*

Main supervisor: Professor Anker Degn Jensen, DTU Chemical Engineering

Co-supervisor: Associate Professor Stig Wedel, DTU Chemical Engineering
Company supervisor: Technology Development Director Christian Wix, Haldor Topsoe A/S

DTU Chemical Engineering
Department of Chemical and Biochemical Engineering
Technical University of Denmark

Søltofts Plads 229
2800 Kgs. Lyngby, Denmark
Phone +45 4525 2800
kt@kt.dtu.dk
www.kt.dtu.dk

Preface

This thesis was prepared at the department of Chemical and Biochemical Engineering at the Technical University of Denmark (DTU) in partial fulfillment of the requirements for the PhD degree at DTU.

The work was partly conducted at the department of Chemical and Biochemical Engineering at DTU and at Haldor Topsoe A/S with financial support from the Innovation Fund Denmark. All parties involved are greatly acknowledged for financial support and for providing facilities. Haldor Topsoe A/S are also acknowledged for providing both cell material and stacks.

This is the public version of the thesis. In the public version of the thesis, Chapter 6 is limited to the material already published in the article "Modelling of Gas Diffusion in Ni/YSZ Electrodes in CO_2 and co-electrolysis*" and parts of the overall discussion is omitted. In both the confidential and public version of the thesis, the actual structure of Haldor Topsoe A/S's cells are blurred.

I am grateful to my supervisors Anker Degn Jensen (DTU), Stig Wedel (DTU) and Christian Wix (Haldor Topsoe A/S) for their guidance, discussions, and proof-reading. A special thanks to Claus Flemming Friis Pedersen (former Haldor Topsoe A/S) for initializing the project and supervision of the first part of the PhD.

I would like to thank my colleagues at Haldor Topsoe A/S and DTU who has assisted and provided help. Especially the "eCOs" and "SOEC" group at Haldor Topsoe A/S has provided invaluable help with the acquisition of cell and stacks, analysis and many fruitful discussions.

Finally, I would like to thank friends and family for support, encouragement, and understanding. Especially to my girlfriend, our son and (currently) unborn second child. I promise: No more thesis writing in the evening.

Kongens Lyngby, June 9, 2017

Jakob Dragsbæk Duhn

---

*DOI: 10.1002/fuce.201700068

Summary

Title: “Development of highly efficient solid oxide electrolyzer cell systems”

Solid oxide electrolyzer cells (SOEC) are electrochemical devices capable of converting H_2O or CO_2 to H_2 and CO, respectively. In this thesis, the possibility of production of CO with SOECs are investigated, since it is currently of commercial interest, but could also play a major role in the future energy system.

The overall objective of the thesis was to investigate the limits for the allowed CO concentration during electrolysis of CO_2 in SOECs and how the limit could be increased. A high CO concentration is desired because it lowers the strain on the separation unit and amount of recycle, when SOECs are used in systems like Haldor Topsoe A/S’s “eCOs”. In this way, the overall efficiency of SOEC systems are increased. The CO concentration was limited by carbon formation via the Boudouard reaction, a non-uniform flow in the fuel channels over the fuel electrode, and the diffusion in the fuel electrode. The thesis has focused on obtaining knowledge on the limiting causes, through both experimental work and modeling.

The formation of carbon leads to delamination of the cell layers and ultimately destroys the cells. It was found that the carbon formation was hindered, when the Boudouard reaction was thermodynamically unfavored. From thermo-gravimetry analyzer experiments, the thermodynamics for the equilibrium for the Boudouard reaction was obtained for Ni-YSZ material used in SOECs.

It is important that the flow distribution in the cell is as uniform as possible, since non-uniformities will lead to regions with flow rate and therefore high CO concentration. The flow distribution in the fuel channels over the fuel electrode was investigated with computational fluid dynamics (CFD) modeling. The flow was optimized by changing the cell inlet geometry and an increase in the flow uniformity was observed. The impact on the allowed average (exit) CO concentration was quite high (from 22 to 32 %).

The effective diffusion in the fuel electrode was investigated with a Wicke-Kallenbach set up. Combined with measurements of the thickness, porosity and pore size, the tortuosity of the material was calculated. This made it possible to implement the diffusion limitation in an in-house 3d stack model and evaluate the impact of diffusion limitations (only included in the confidential version of the thesis). The local CO concentration is limited by the thermodynamics for the Boudouard reaction. The diffusion cause an increase in the CO concentration at the reaction sites, compared to the channel, and diffusion therefore limits the allowed CO concentration in the fuel channel. The diffusion was found to be low, resulting in large concentration gradients between the channel and reaction sites. This mean that the allowed CO concentration in the fuel channel is very limited by diffusion.

Dansk resumé

Dansk titel: “Udvikling af effektive fast oxid elektrolyse celle systemer”

Fast oxid elektrolyse celle (SOEC) systemer er elektrokemiske apparater som kan konvertere H_2O og CO_2 til henholdsvis H_2 og CO. I denne afhandling bliver produktionen af CO via SOEC undersøgt. Produktionen af CO er interessant fra et kommercielt perspektiv, men har også muligheder for at indgå i et fremtidig energisystem.

Det overordnede formål med afhandlingen var at undersøge den maksimale CO koncentration som SOEC systemerne kunne køres ved. Derefter var målet at mindske usikkerheden af de begrænsende faktorer og undersøge hvorledes de begrænsende faktorer kunne mindskes via optimering. De primære begrænsninger for CO koncentrationen blev fundet til at være kuldannelse via Boudouard reaktionen, dårlig flow fordeling i elektrolyse cellerne og diffusionsbegrænsninger i brændselselektroden. De tre begrænsende faktorer blev undersøgt med teoretisk modellering og eksperimentielt arbejde.

Kuldannelse i SOEC leder til delaminering af de enkelte lag i elektrolyse cellerne og medfører ultimativt at cellerne går i stykker. Kuldannelsen blev fundet til at foregå via Boudoaurd reaktionen og værende begrænset af ligevægten for Boudouard reaktionen. Ligevægtsdata blev fundet i litteraturen og sammenholdt med målinger på Ni-YSZ materiale (brugt i elektrolyse cellerne).

Det er vigtig at flow fordelingen i en elektrolyse celle er uniform, eftersom et ikke-uniform flow medfører områder med lavt flow og derfor høj CO koncentration. Høj CO koncentration medfører at ligevægten for Boudouard reaktionen forskydes mod kul. Flowet blev modelleret med computational fluid dynamics (CFD). Forskellige driftsparametres betydning for flowet blev undersøgt og flowet blev optimeret, ved at omdesigne cellens geometriske struktur. Dette medførte en øgning af den mulige CO koncentration fra 22 % til 32 %.

Den effektive diffusion blev målt via et Wicke-Kallenbach setup og de karakterisktiske diffusionsparameter blev udledt derfra. Herefter blev diffusionen i brændselselektroden modelleret og resultaterne implementeret i en intern 3d stack model (kun inkluderet i den fortrolige udgave af afhandlingen). Dette gjorde det muligt at beregne forskellen i CO koncentrationen mellem gas kanalen og reaktionslaget. Beregningerne viste at CO koncentrationen er meget højere i reaktionslaget, sammenlignet med kanalen. Siden den maksimale lokale CO koncentrationen er afgørende for ligevægten af Boudouard reaktionen, medfører diffusionsbegrænsningerne at den tilladelige CO koncentrationen i kanalen må begrænses.

List of publications

During the PhD, the following articles has been published in peer-reviewed articles:

Duhn, J. D., Jensen, A. D., Wedel, S., & Wix, C. (2016). Optimization of a new flow design for solid oxide cells using computational fluid dynamics modelling. *Journal of Power Sources*, 336, 261-271. DOI: 10.1016/j.jpowsour.2016.10.060

Duhn, J. D., Jensen, A. D., Wedel, S., & Wix, C. (in press) (2017). Modelling of Gas Diffusion in Ni/YSZ Electrodes in CO_2 and co-electrolysis *Fuel Cells.* DOI: 10.1002/fuce.201700068

The following has been published as patents:

Friis Pedersen, C. F., Bech, L., Duhn, J. D., & Jakobsson, N. B. (2015). IPC No. H01M 8/ 12 A N. Enhancing SOEC system lifetime by controlling inlet gas composition (Patent No. EP2933357.)

The following has been published at conferences:

Duhn, J. D., Jensen, A. D., Wedel, S., & Wix, C. (2016). Modelling of gas diffusion limitations in Ni/YSZ electrode material in CO2 and co-electrolysis. In *Proceedings of the 12th European SOFC & SOE Forum [B0810] European Fuel Cell Forum.*

The following has been published in non peer-reviewed articles:

Duhn, J. D., Jensen, A. D., Wedel, S., & Friis Pedersen, C. F. (2015). Fastoxid elektrolyseceller: Store muligheder for integration med fremtidens energisamfund. *Dansk Kemi*, 96(10), 16-18.

Contents

Nomenclature

Abbreviations

1d	One-dimensional
2d	Two-dimensional
3d	Three-dimensional
AFC	Alkaline fuel cell
AP	Sample point
BFM	Binary friction model
CPIM	Cylindrical pore interpolation model
CW	Cooling water
DGM	Dusty gas model
E	Electrode
E+ES	Electrode + Electrode support
ES	Electrode support
f.s.	Full scale
FSG	Fuller-Schettler-Giddings
GDC	Graham diffusion cell
HRTEM	High-resolution transmission electron microscopy
LE	Heater
LSCF	Lanthanum strontium cobaltite ferrite
LSM	Lanthanum strontium manganese
MFC	Mass flow controller
MIEC	Mixed ionic–electronic conductor

OCV	Oven circuit voltage
PEM	Proton exchange membrane fuel cell
PLC	Programmable logic controller
sccm	Standard cubic centimeter per minute
SEM	Scanning electron microscope
SEM	Scanning electron microscopy
SOC	Solid oxide cell
SOEC	Solid oxide electrolyzer cell
SOFC	Solid oxide fuel cell
SRU	Single repeating unit
Syngas	Synthetic gas. A mixture of CO, CO_2, H_2 and H_2O
TGA	Thermo-gravimetric analyzer
TPB	Triple phase boundaries
WGS	Water-gas shift reaction
WK	Wicke-Kallenbach
YSZ	Yttria stabilized zirconia

Greek letters

α	Constant, defined as $\alpha = 1 - M_i/M_j$	
α_{KC}	Constant used in the Kozeny-Carman equation Eq. (5.71), p. 75	
α_{sym}	Symmetrical factor	
β	Ratio of gas species at reaction interface	
$\boldsymbol{\tau}_s$	Viscous stress tensor	Pa
$\Delta W_n/W_{r,n}$	Relative change in mass	%
δ	Thickness of the film layer	m
ϵ	Porosity	
η_{act}	Activation overpotential	V
η_{conc}	Concentration overpotential loss	V

η_{diff}	Effective diffusion parameter, defined as $\eta_{diff} = \epsilon/\tau^2$	
η_{ohmic}	Ohmic overpotential	V
γ	Conversion	%
κ	Permeability	$\mathrm{m^2}$
μ	Viscosity	$\mathrm{Pa\,s}$
$\mu^\star$	Contribution from structural defects compared to graphite	$\mathrm{kJ\,mol^{-1}}$
μ_n	Mean value	
Ω_D	Dimensionless collision intergral in the Lennard-Jones (12-6) potential model	
Φ	Potential	V
ρ	Density	$\mathrm{kg\,m^{-3}}$
ρ_{app}	Apparent density	$\mathrm{kg\,m^{-3}}$
σ	Standard deviation	
σ_i	Average collision diameter of species i	Å
τ	Tortuosity	
τ^2	Tortuosity factor	
θ^0	Input parameters	
ς	Conductivity	$\mathrm{S\,m^{-1}}$
ζ	Position in stack	

Roman letters

$\bar{d}_{Ni}$	Average Ni particle diameter	nm or Å
$\bar{r}_{pore}$	Average pore radius	Å
$\bar{u}$	Average velocity	$\mathrm{m\,s^{-1}}$
$\boldsymbol{I}$	Unity tensor	
ΔG	Gibbs free energy	$\mathrm{kJ\,mol^{-1}}$
ΔG_c	Difference in Gibbs free energy for the formation whisker and graphite carbon via the Boudouard reaction	$\mathrm{kJ\,mol^{-1}}$
ΔH	Enthalpy	$\mathrm{kJ\,mol^{-1}}$

ΔP	Pressure difference	mbar
ΔS	Entropy	$\mathrm{J\,mol^{-1}\,K^{-1}}$
$\dot{F}_{air}$	Gas flow to the air side. Typically CO_2, N_2 or air.	$\mathrm{NL\,min^{-1}\,cell^{-1}}$
$\dot{N}_i^d$	Mass diffusion flux	$\mathrm{kg\,m^{-2}\,s^{-1}}$
$\dot{Q}_s$	Heat source/sink	$\mathrm{W\,m^{-3}}$
$(\sum v)_i$	Molar diffusion volume	$\mathrm{m^3}$
$\mathcal{F}$	Faradays constant	$\mathrm{C\,mol^{-1}}$
$\vec{i}_t$	Total current density	$\mathrm{A\,m^{-2}}$
$\vec{N}_i^d$	Diffusion flux	$\mathrm{mol\,m^{-2}\,s^{-1}}$
$\vec{N}_i^{vics}$	Viscous flux	$\mathrm{mol\,m^{-2}\,s^{-1}}$
a_c	Affinity for carbon formation	-
A_{cell}	Active cell area	$\mathrm{m^2}$
c	Fitting parameter	
C_1	Diffusion term	
C_2	Diffusion term	
C_i	Concentration of species i	$\mathrm{mol\,m^{-3}}$
C_i^{bulk}	Concentration of species i at the bulk gas phase	$\mathrm{mol\,m^{-3}}$
C_i^{surf}	Concentration of species i at the surface	$\mathrm{mol\,m^{-3}}$
C_p	Heat capacity	$\mathrm{kJ\,kg^{-1}}$
C_t	Total gas concentration constant	$\mathrm{mol\,m^{-3}}$
D	Diffusion coefficient	$\mathrm{m^2\,s^{-1}}$
d	Fitting parameter	
d_c	Thickness of cell	µm
d_e	Thickness of electrolyte	µm
d_{anode}	Thickness of anode	µm
$D_{i,j}$	Binary diffusion coefficient between species i and j	$\mathrm{m^2\,s^{-1}}$
$d_{i,t}$	Diameter of inner tube	inch

D_{ij}^{eff}	Effective binary diffusion coefficient between species i and j	$\mathrm{m^2\,s^{-1}}$
$D_{K,i}$	Knudsen diffusion coefficient	$\mathrm{m^2\,s^{-1}}$
$D_{K,i}^{eff}$	Effective Knudsen diffusion coefficient	$\mathrm{m^2\,s^{-1}}$
d_{Ni}	Ni particle diameter	nm or Å
d_{par}	Particle diameter	m
d_{sample}	Diameter of sample	mm
d_{tube}	Diameter of tube	m
E	Equilibrium potential	V
e_i	Characteristic Lennard-Jones energy constant	
E_{act}	Activation energy	$\mathrm{kJ\,mol^{-1}}$
F	Volumetric flow at standard conditions (273.15 K, 1 bar)	$\mathrm{m^3\,h^{-1}}$
F_u	Flow uniformity index	-
$f_{N^d}(\theta^0)$	Minimization function with respect to N^d evaluated at θ^0	
$f_{X_{CO}}(\theta^0)$	Minimization function with respect to the outlet mole fraction of CO, $X_{CO,out}$, evaluated at θ^0	
FU	Fuel utilization	%
h_{max}	Maximum height	m
H_{norm}	Height used to normalized $R_{s,i}$	m
H_{sample}	Height of sample	µm
K	Equlibrium constant	$\mathrm{atm^{-1}}$
k	Conductivity	$\mathrm{W\,m^{-1}\,K^{-1}}$
K_1	Equilibrium constant	$\mathrm{atm^{-}1}$
k_B	Boltzmann constant	$\mathrm{J\,K^{-1}}$
k_{mt}	Mass transfer coefficient	$\mathrm{m\,s^{-1}}$
k_{rmax}	Constant	kJ Å $\mathrm{mol^{-1}}$
L	Length	m
L_0	Shortest length	m

L_{eff}	Effective length	m
$L_{h,laminar}$	Entry length for laminar flow	m
m	Fitting parameter	
M_i	Molar mass of species i	$\mathrm{kg\,mol^{-1}}$
n_e	The number of electrons in the reaction	
n_{cell}	Number of cells per stack	
P	Pressure	Pa
P_{atm}	Atmospheric pressure	Pa
Pe	Peclet number	
Q	Reaction quotient	$\mathrm{atm^{-1}}$
Q_j	Joule heating	W
Q_l	Heat loss to surroundings	W
Q_{in}	Heat into the cell/stack	W
Q_{out}	Heat out of the cell/stack	W
Q_r	Reaction heat	W
R	Gas constant	$\mathrm{J\,mol^{-1}\,K^{-1}}$
r	Reaction rate	$\mathrm{mol\,m^{-3}\,s^{-1}}$
$R_{s,i}$	Source/sink of the species i	$\mathrm{mol\,m^{-3}\,s^{-1}}$
R_{sample}	Radius of sample	mm
r_{sample}	Radius of sample	mm
Re	Reynolds number	
s_m	Relative sensitivity of a variation of one σ of parameter m	
S_{pore}	Pore area	$\mathrm{m^2}$
Sh	Sherwood number	
T	Temperature	°C or K
t	Time	sec, min or h

$T_{B,c}$	Experimental equilibrium temperature for the Boudouard reaction, obtained during cooling	K
$T_{B,h}$	Experimental equilibrium temperature for the Boudouard reaction, obtained during heating	K
U	Potential	V
U	Voltage	V
u	Velocity	$\mathrm{m\,s^{-1}}$
u_{max}	Maximal flow velocity	$\mathrm{m\,s^{-1}}$
$v'(r_{pore})$	Pore volume distribution function	$\mathrm{mL\,kg^{-1}}$
v_i	Stochiometric coefficient	
V_{pore}	Pore volume	$\mathrm{m^3}$
w_i	Mass fraction	
w_{pitch}	Halfwidth of the pitch	mm
w_{rib}	Halfwidth of the rib	mm
X	Mole fraction	-
x	Axis coordinate	
x_L	Diffusion length	m
$X_{i,gas}$	Mole fraction of species i in test gas	
$X_{i,mea}$	Measured mole fraction of species i	
y	Axis coordinate	
z	Axis coordinate	

List of figures

List of tables

CHAPTER 1

Introduction

Solid oxide cells (SOC) are considered a very promising technology for the conversion between chemical and electrical energy, and vice-versa. Commonly, the SOCs have been used to convert chemical energy (CH_4 or H_2) to electrical energy. However, except at some minor areas, the breakthrough of the technology has not yet occurred in large commercial scale. The reason for the lack of large commercialization is due to a high cost and low durability [1, 2]. The technology can also be used for the production of H_2 or CO, by electrolysis of H_2O and CO_2. Haldor Topsoe A/S has been involved with solid oxide cells, for chemical to electrical energy conversion, for a long period (previous in the subsidiary company Topsoe Fuel Cell). The company has now changed its focus to the production of CO and H_2, closed the subsidiary company and moved the technology to its main company. With the change of focus from conversion of energy to the production of CO and H_2, the issues affecting the commercialization are now different. This PhD study has been derived out at the different departments responsible for the research and development of the technology at Haldor Topsoe A/S and has tried to enhance the knowledge on issues related to production of CO with SOCs. Beside assisting in the commercialization of Haldor Topsoe A/S's technology, the knowledge obtained in the PhD can also be extended to simultaneous production of CO and H_2 with SOCs. This is interesting from a society point-of-view, since this technology is predicted to be a key technology for future sustainable energy scenarios [3].

The purpose of this chapter is to introduce the reader to the technology of SOCs, particular solid oxide electrolyzer cells (used for production of CO and H_2), its applications and limitations. The focus is particular on the production of CO through electrolysis of CO_2. Based on the limitations, the objective of the thesis is defined and presented. The chapter starts with a brief description of fuel cells in general and solid oxide cells in more detail. The description includes the physical structure and applications of the solid oxide electrolyzer cells. Afterwards, the limitations with respect to CO production is discussed. In the last section, the objective of the thesis is defined and the structure of the thesis is presented.

1.1 Fuel cells

The basic for fuel cells are ascribed to the demonstration of voltage generation, by combining hydrogen and oxygen in the presence of platinum, in 1839 by Grove [4].

However, the development was limited until the 1960's, where the research increased, especially with focus on space, submarine and military applications [5]. Beginning in the mid-1980s, the government agencies in the US, Canada, and Japan, started to increase their funding for fuel cells [6], likely because of the large increase in oil-prices doing the 1970's. Also the production of H_2 from H_2O, instead of fossil fuels, was investigated [7, 8], since it was envisioned that H_2 would be needed as a secondary energy carrier. Today, many companies and universities are developing fuel cell technologies.

Three main types of fuel cells are being investigated: Proton exchange membrane fuel cells (PEM), Alkaline fuel cells (AFC) and Solid oxide fuel cells (SOFC). In addition, several other types are being investigated, such as Phosphoric acid fuel cells and Molten carbonate fuel cells. PEMs use a proton exchange membrane to transport protons across a non-electric conducting membrane, an AFC use a aqueous alkaline solution (e.g. KOH) to transport OH^--ions between the two electrodes, and an SOFC use a solid ceramic oxide to transport O^{2-}-ions between the electrodes. This thesis is about solid oxide fuel cells used in reverse, i.e. as electrolyzer cells.

1.1.1 SOFC and SOEC

SOFCs are electrochemical devices capable of converting chemical energy (released from oxidizing hydrogen, synthesis gas, and many other fuels to H_2O and CO_2) to electrical energy. Traditionally, chemical energy is e.g. converted in power plants where the chemical energy is first converted to heat to generate steam for the steam turbines, and secondly the shaft power from the turbine is used to drive a generator, which converts the kinetic energy to electrical energy. Each conversion step is associated with a loss. For a power plant, the efficiency of chemical energy to electricity is therefore 20-60 % (lower heating value) [9]. For SOFC, the electrical efficiency is about 50 % . However, since the operating temperature of a SOFC is very high (600-800 °C), the exhaust gasses can be used to run a gas turbine, by which the efficiency can reach levels of > 70 % [9, 10].

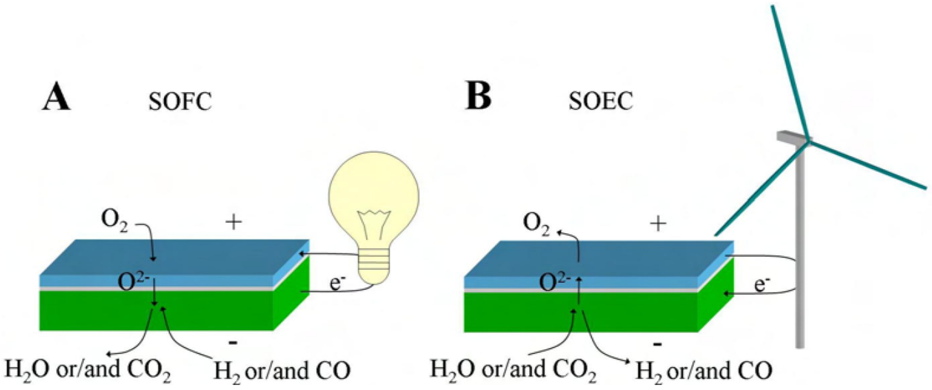

Figure 1.1: Schematic illustration of working principle in SOFC (A) and SOEC (B). Taken from [11]

SOFCs can also be run in reverse mode, i.e. electrical energy is converted into chemical energy, by converting H_2O and CO_2 to H_2 and CO. In addition, O_2 is also produced in a separate stream. When operated in reverse mode, the technology is called “solid oxide electrolyzer cells” (SOEC). Since, SOFCs and SOFCs are highly related, several aspects from SOFC can be transferred to SOEC. This is especially useful, since SOECs has received significant less attention, compared to SOFC. A sketch of the working concept of SOFC and SOEC are shown in Fig. 1.1. In the following, the term “solid oxide cell” (SOC) will be used as a common denominator for both SOFC and SOEC.

SOFCs have been widely studied experimentally in the last decades [12, 13], with respect to design and materials [14–17], and through modeling [18–22]. For the modeling of SOFCs, several review articles are available [23–31].

For SOECs, the number of articles are considerable lower than that of SOFC (Fig. 1.2). Few review articles on the experimental, design, and material aspects of SOECs have been published [32–35].

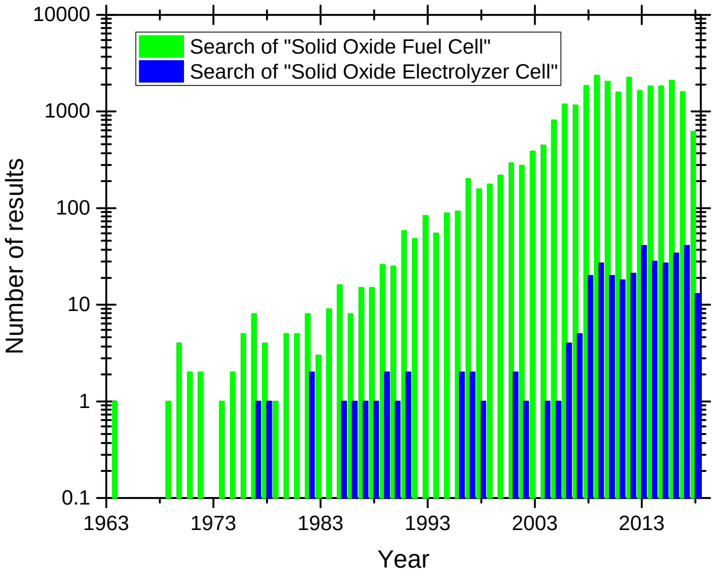

Figure 1.2: Search for “solid oxide fuel cell” and “solid oxide electrolyzer cell” in the bibliographic database Scopus.

1.2 Physical structure and materials

The physical structure of SOCs consists primarily of three layers and two fuel channels (illustrated in Fig. 1.3). In SOFC, fuel (typically H_2 or CH_4) is entering the channel above the anode. In SOEC, an oxidized species (typically CO_2 and H_2O) is entering the same channel, although the electrode is now a cathode (since the cell is operated in reverse mode and the direction of the current is therefore changed). During SOFC, air is entering in the channel below the cell. During SOEC, the gas is commonly air or N_2, since the purpose of the flow is to perform heat transport and dilute the produced O_2 in the electrode above the channel. During production of CO, the flow can also consist of CO_2. This ensures that small leakages between the two sides of the cell only pollutes the CO/CO_2 mixture with CO_2.

To avoid confusion in the thesis about what is the “anode” and “cathode”, the term “fuel-electrode” is used for anode in SOFC and cathode in SOEC. The term “air-electrode” is used for the cathode in SOFC and anode in SOEC. Furthermore, “fuel channel” is used for the channel above the fuel electrode and “air channel” for the channel below the air electrode.

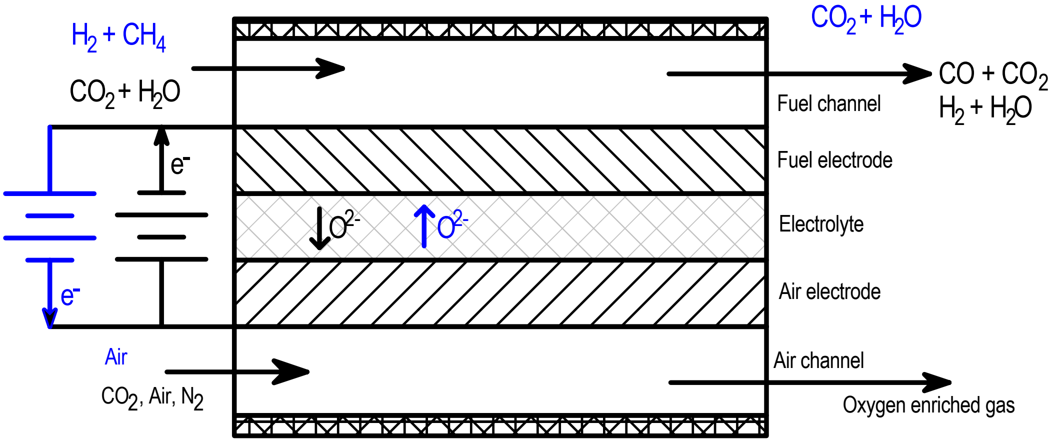

Figure 1.3: Schematic illustration of layers in SOCs. The gas species and direction of the current in blue applies for SOFC and the gas species and current direction in black, applies for SOEC.

From the fuel channel, the gas species are transported to the fuel electrode and diffuse, through the electrode, to the reaction sites located near the fuel electrode and electrolyte interface. At the reaction site, the following reactions takes place in SOFC:

$$H_2 + O^{2-} \rightleftarrows H_2O + 2\,e^- \tag{1.1}$$

$$CO + O^{2-} \rightleftarrows CO_2 + 2\,e^- \tag{1.2}$$

And in SOEC:

$$H_2O + 2\,e^- \rightleftarrows H_2 + O^{2-} \tag{1.3}$$

$$CO_2 + 2\,e^- \rightleftarrows CO + O^{2-} \tag{1.4}$$

The reaction sites are called “triple phase boundaries” (TPB), because the reaction requires three phases. The gas phase supply and remove the gas species, an electric conduction phase conducts the electrons from (in SOFC) and to (in SOEC) the reaction site, and an oxygen ionic conductor transfer the oxygen ions to (in SOFC) and from the reaction site (in SOEC). Fig. 1.4 shows a close up of the interface between the fuel electrode and electrolyte. Without one of the three phases, the electrochemical reactions cannot take place. In the whole fuel electrode, the water-gas shift reaction ($CO + H_2O \rightleftharpoons CO_2 + H_2$) and methanation reaction ($CO + 3\,H_2 \rightleftharpoons CH_4 + H_2O$) might also occur. The directions of the these two reactions will depend on the gas composition and temperature.

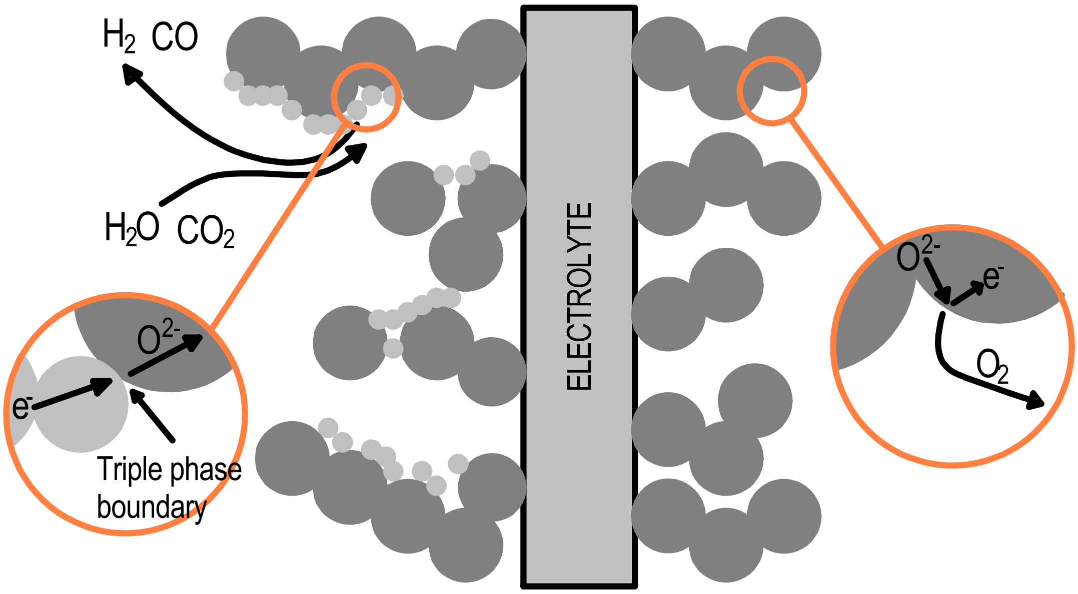

Figure 1.4: Illustration of triple phase boundaries (TPB). To the left of the electrolyte (in the fuel electrode), H_2O and CO_2 diffuse to the TPBs and are reduced to H_2 and CO (SOEC mode). At the TPBs, the electrons for the reactions are supplied via the Ni network and the oxygen ions are transported away through the YSZ (see text). At the right of the electrolyte, the oxygen ions are transported to the surface of the air electrode and reacts to molecular oxygen. The electrons are transported away in the air electrode. Only two phases are required at the air electrode, because the used electrode material (LSCF - see text) is a mixed ionic–electronic conductor, capable of conducting both oxygen ions and electrons.

In the electrolyte, the oxygen ions are transported between the fuel electrode and the air electrode. The electrolyte must be highly electrically insulating (to avoid a short circuit of the cell) and gas tight. At the air electrode, oxygen ions are formed in SOFCs, and oxygen molecule are formed in SOECs:

$$\frac{1}{2}\,O_2 + 2\,e^- \rightleftharpoons O^{2-} \tag{1.5}$$

As in the fuel electrode, the reaction in the air electrode also take place at triple phase boundaries, since transport of gas species, oxygen ions, and electrons must be available at the reaction sites. However, if a mixed ionic–electronic conductor (MIEC - capable of conducting both oxygen ions and electrons), only the solid phase and gas phase is needed. MIEC is not used for the fuel electrode, since the electrical conductivity and electro-catalytic properties of Ni (which is commonly used in fuel electrodes) are very good compared to MIECs.

The materials for the cells used at Haldor Topsoe A/S (and in this thesis) is now described. The fuel electrode is a cermet of Ni and yttria stabilized zirconia (YSZ). Ni is an electrical conductor, transferring the electrons and YSZ, is an ionic conductor, transferring the oxygen ions. The electrolyte is pure YSZ and the air electrode consist of lanthanum strontium cobaltite ferrite (LSCF), which is a MIEC. Between the air electrode and the electrolyte, a thin gadolinia doped ceria layer is placed to avoid the unwanted reaction of strontium, from the air electrode, with the zirconium in YSZ. This reaction forms strontium zirconate ($SrZrO_3$) which is a poor ion conductor and thus increases the resistance of oxygen ion transfer from the electrolyte to the air electrode. Other companies and research institution use and experiments with other materials. However, Ni-YSZ is used by major players, like Sunfire GmbH and Bloom Energy, because of the low cost of Ni, good electro-catalytic properties and thermal expansion compatibility with the YSZ electrolyte [36]. When the cell is heated from room temperature to the operating temperature (600-800 °C), a compatible thermal expansion of the materials is necessary to avoid large thermal stresses.

The thickness of the layers are in the range of 10-15 µm, except for the fuel electrode, which contains a ≈300 µm support layer in addition to the 10-15 µm thick active fuel electrode. The purpose of the support layer is to provide mechanical strength. Haldor Topsoe A/S uses a planar design, but tubular and circular designs are also investigated by others [6, 16, 37] .

In a system, several cells are placed on top of each other in a stack, see Fig. 1.5. To separate the cells from each other, a metal component, called an interconnect, is placed between the cells. The purpose of the interconnect is to distribute the flow in the channels and transfer electrons from the fuel electrode below the interconnect, to the air electrode above the interconnect. Special metals and coatings are used for the interconnect, since it has to withstand the high operating temperature present in SOCs. Furthermore, the metals are chosen so that they form a thin electronically conductive layer, that protect the steel from oxidization. Typically ferrite steels like Crofer 22 APU [38], which contains >20 % chromium and forms a protective chromium-manganese oxide layer, are used to achieve this.

1.3 Applications

SOECs can be coupled with different systems and used for a range of purposes. The role of the SOEC unit can roughly be separated into three categories:

1. Production of H_2

2. Production of CO
3. Production of syngas

1. The production of pure H_2 can be interesting in a future hydrogen society, where H_2 is used as energy carrier. In this scenario, SOECs can be used to convert (renewable) electrical energy into H_2. A hydrogen society would require that the current vehicle fleet is changed and a new infrastructure is built. A hydrogen society is thus not just around the corner. Furthermore, the volumetric energy density of H_2 is roughly one-fourth of gasoline [39], so the range of a hydrogen vehicle is an important issue to solve. In Denmark, Energinet.dk (responsible for the electricity and gas transmission system in Denmark) is currently investigating if the natural-gas infrastructure can be operated stable and safely with varying concentrations (up to 15 %) of hydrogen. If the investigation shows that a significant amount of hydrogen can be added to the natural-gas grid, this could clear the way for hydrogen production for energy storage/consumption purposes.

The production of H_2 can also be used for on-site production for users with a low demand of H_2, e.g. laboratories and small production sites. For larger demands, H_2 produced from conventional steam reforming of e.g. natural gas would be more economical, despite a slightly lower efficiency (Efficiencies of 80-90 %, based on the higher heating value, can be obtained for steam reforming reactors [40] and >94 % for the SOEC [41, 42]) .

If the H_2 production is coupled with catalytic reactors, the H_2 can be used to upgrade biogas. Biogas typically contains around 40 vol% CO_2, depending on the waste source [3]. The CO_2 needs to be removed, before the biogas can be added to the natural-gas grid. Commonly, this is done by removing the CO_2 with e.g. water or amine scrubbing [43]. The produced H_2 from SOECs can be used to react the CO_2 to CH_4 in a methanation

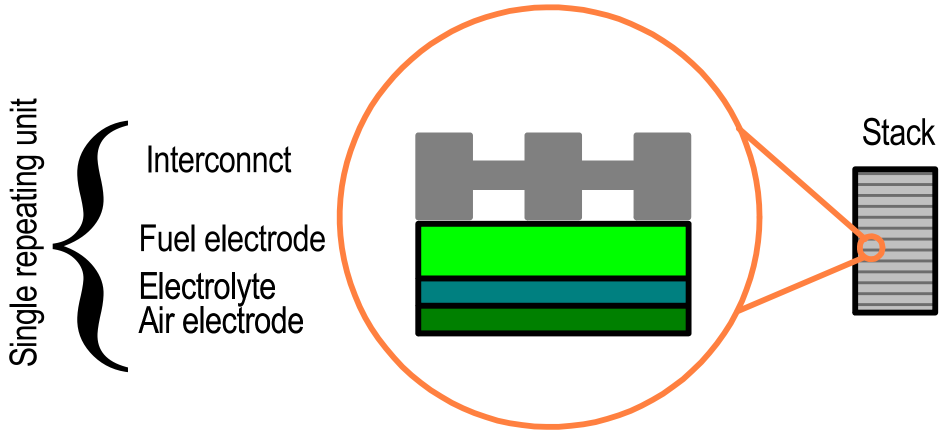

Figure 1.5: Cells and interconnects are stacked on top of each other to form a stack. The combination of a cell and an interconnect is called a “Single repeating unit”, since it is repeated from the bottom to the top of the stack.

reactor [3, 44]. Since the SOEC and methanation reactor can be powered by renewable electrical energy (e.g. from excess production from wind energy), the upgraded biogas can be viewed as a renewable technology. The SOEC and methanation reactor is a good match, since the excess heat energy, generated from the methanation reactor, can be used to generate the steam needed in the SOEC.

2. The production of pure CO from SOECs can be used at small on-site plants (1-200 Nm^3h^{-1}) as demonstrated by Haldor Topsoe A/S in the "eCOs" technology, Fig. 1.6 [45, 46]. Here the SOEC is used to produced a mixture of CO_2 and CO. The gas mixture is then compressed and the CO_2 is separated (by a pressure swing adsorption unit) and recycled (with a low amount of CO). With the SOEC and purification steps, it is possible to obtain 99.999 % pure CO with CO_2 being the main impurity (avoiding H_2O, H_2, CH_4 and O_2). The eCOs technology is commercially available and one plant has been built and another is in the construction phase [47]. In the eCOs technology, the conversion of CO_2 to CO in the SOEC is an important factor, since a higher conversion significantly lowers the requirement of purification and recycling. Furthermore, the life-time of the cells is important for the cost of the produced CO. A longer life-time means that the eCOs system can be operated in longer periods without shutdown and replacement of the stacks.

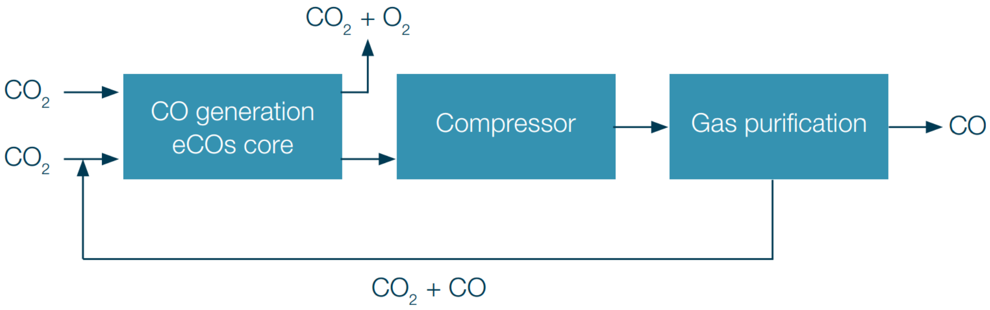

Figure 1.6: Schematic illustration of the eCOs system. Taken from [48].

The electrolysis of CO_2 is also used in the MOXIE project [49], where the intent purpose is to convert the CO_2 from the CO_2-rich atmosphere of Mars to CO and O_2 (see Fig. 1.7). The main purpose is to investigate if SOECs can be used to produce O_2, which would be necessary for human exploration of Mars. CO and O_2 can also be used as a propellant.

3. The production of syngas, through simultaneous electrolysis of H_2O and CO_2 (called co-electrolysis) is interesting, because the syngas can be used to form CH_4 via a methanation reactor or synthetic liquid fuels, such as methanol and others, through the Fischer-Tropsch process [51]. If the recovery of CO_2 from the atmosphere becomes technologically and economically feasible (which it is not at the moment [52]), this allows for a closed loop where CO_2 is emitted from e.g. vehicles, but captured and converted to fuels in the SOEC syngas system. If the CO_2 capture and conversion is solely powered by

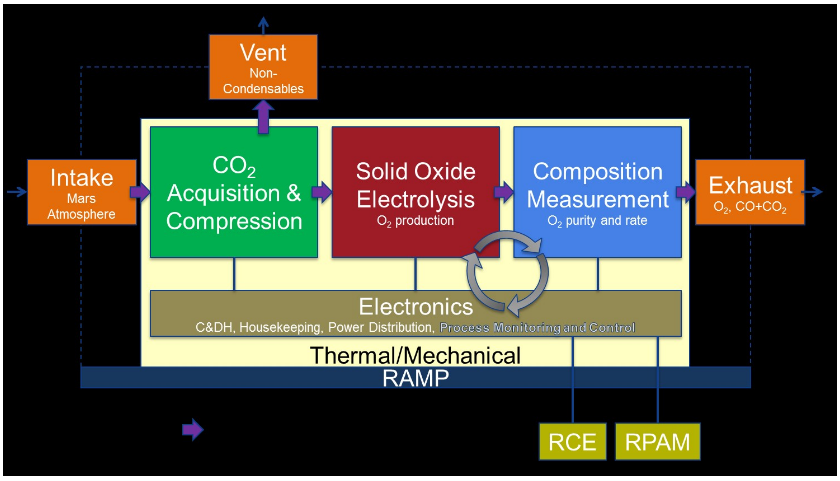

Figure 1.7: Schematic illustration of the MOXIE system showing the SOEC (red), the separation and compression of CO_2 from the Mars atmosphere (green) and the gas measurement and exhaust (blue). The process is connected with the Mars Rover electronics (olive). Abbreviations: Rover Computer Element (RCE), Rover Avionics Mounting Panel (RAMP), Rover Power and Analog Module (RPAM). Taken from [50]

renewable energy sources, the net release of CO_2 would be zero, and thus not contributing to the global greenhouse warming.

1.4 Efficient production of CO through SOEC technology

The electrolysis of CO_2 has received increasing interest in the last years [53, 54], but the main focus remains on the electrolysis of H_2O [33, 55–57] and co-electrolysis [58–64]. To the best of the author's knowledge the only companies working with the electrolysis of CO_2 are Ceramatec, Inc. (working with NASA's MOXIE Mars project describe above) and Haldor Topsoe A/S (working with the commercial eCOs project). An outline of the eCOs system was given in Fig. 1.6, and a more detailed picture is given in Fig. 1.8.

An important parameter in the efficiency for the production of purified CO is the outlet concentration of CO from the SOEC stack. With a low outlet concentration of CO, the amount of recycle increases. From an efficiency point of view, this is unwanted because the recycle requires energy, since the recycle gas is first cooled, compressed and then reheated, before entering the system again (see Fig. 1.8). Furthermore, 1) a low CO concentration requires more of the separation process to reach the required high purity of CO, and 2) a low CO concentration requires that more SOEC stacks/cells are used to achieve a given production rate of CO. Neither a more capable separation process nor a larger number of SOEC stacks/cells are cheap. Therefore it is highly desirable to have

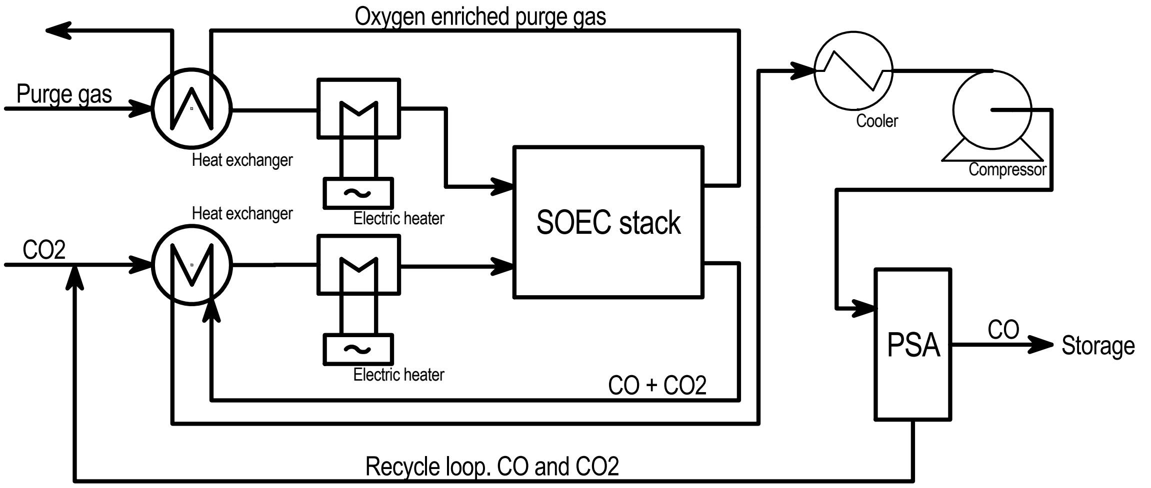

Figure 1.8: Schematic illustration of Haldor Topsoe A/S's eCOs system. Two gas streams are entering the system, a CO_2 stream and a purge gas (CO_2 or alternative air or N_2). The streams are heated to 600-800 °C and enters the SOEC stack. After the stack, the CO_2 stream is now partly converted to CO, cooled and compressed. A separation unit, e.g. a pressure swing adsorper (PSA), separates pure CO (99.5 to 99.999 %) and recycles the CO_2 and a lower amount of CO. The separation in the PSA is driven by different adsorption constants for CO and CO_2. From the stack the purge gas, enriched with O_2, is cooled and exits the system.

the CO outlet concentration as high as possible.

However, a high CO concentration can significantly decrease the life-time of the SOEC cells. As described later in detail (Chapter 3), a high CO concentration can leads to formation of solid carbon via the Boudouard reaction:

$$2\,\mathrm{CO} \rightleftarrows \mathrm{CO} + \mathrm{C(s)} \tag{1.6}$$

The carbon formation decreases the efficiency of the SOEC and, more important, leads to catastrophic failures. The carbon formation can be suppressed by operating the SOEC at a higher temperature. However, with increasing temperature, the rate of corrosion of the metallic interconnect increases [65]. Previously, when SOFCs where operated at around 1000 °C, a ceramic interconnect was used. The ceramic interconnect was difficult to manufacture and has now been replaced with metallic interconnects, produced to be stable at temperature of up to around 800 °C [66]. Furthermore, delamination processes between the electrolyte and air electrode are also accelerated, by the increase of inter-diffusion of metals across the electrolyte/air electrode interface, at higher temperatures [67].

The boundary of the carbon forming reaction in terms of CO in CO_2 mole fraction, as function of the temperature, is given in Fig. 1.9. If the SOEC is operated above the curve, carbon formation is to be expected (described in details later, Chapter 3). However, due to uncertainties in the flow distribution within the cell and diffusion limitations in the fuel electrode, which both can cause high local regions with CO concentrations significantly higher than the average outlet concentration, the SOEC cannot be operated close to the thermodynamic boundary. Furthermore, the normal temperature region of SOCs (600-800 °C) are also shown. Since the exact extent of the flow and diffusion limitations are unknown, a safety margin between the cell temperature, T_c, and Boudouard equilibrium temperature, T_B is used. This is illustrated in Fig. 1.9, where the margin is the length of the line between T_B and T_c. The safety margin is currently being estimated, so it must be sufficiently large to include both the flow and diffusion limitations. Thus, if the uncertainty of the flow and diffusion limitations can be decreased, the safety margin can also be increased. This would allow for a lower operating temperature (which decreases the require energy and slow certain temperature controlled degradation mechanism [69]) or an increase in CO mole fraction (which would be highly desired, as explained above) .

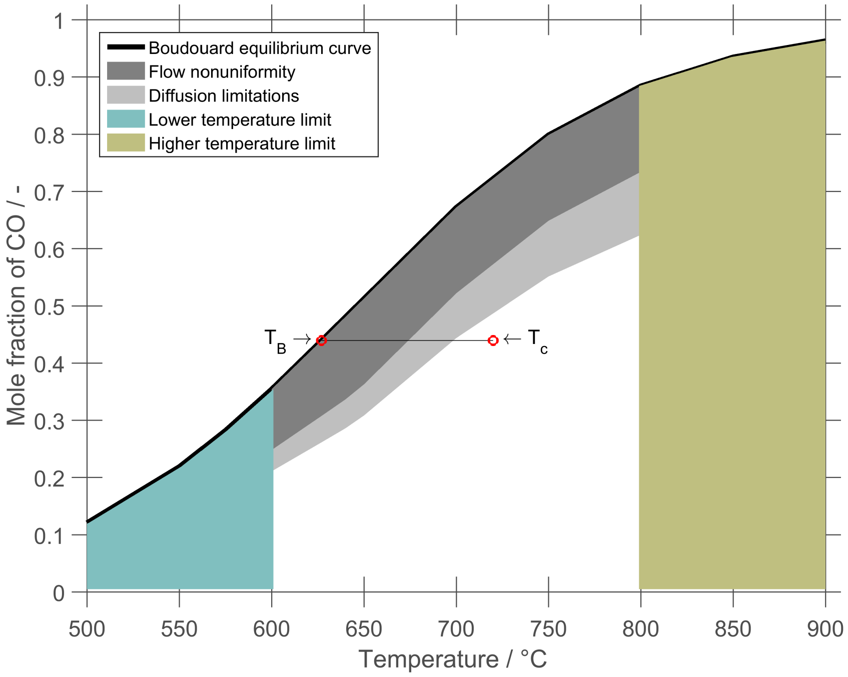

Figure 1.9: Operation space of SOECs, showing the allowed maximum outlet CO mole fraction (in CO_2) as function of the temperature. The operating space (white) is limited in temperature to the temperature interval 600-800 °C due to the used materials. In terms of the mole fraction of CO in CO_2, the operation space is limited by the carbon forming Boudouard reaction Eq. (1.6). The flow nonuniformities and diffusion limitations in the fuel electrode, limits the operation space further. A similar figure has been used in [68].

1.5 Objective and overview of the thesis

As illustrated in Fig. 1.9, the CO mole fraction in SOECs for CO production is limited by carbon formation via the Boudouard reaction, Eq. (1.6). Flow and diffusion limitations leads to higher local CO concentrations, than the average concentration, and thereby limits the outlet CO concentration. However, a high CO outlet mole fraction is desirable, since this will both increase the efficiency of the system and lower the cost of the separation unit and stacks/cells (since a lower number is needed to reach the same production capacity).

In this thesis, the allowed outlet CO concentration is sought improved by investigating the uncertainty of the carbon formation via the Boudouard reaction, the flow nonuniformities and the diffusion limitations . The thesis is related to the eCOs technology and is therefore focused on electrolysis of CO_2. Occasionally, where the concepts and findings from electrolysis of CO_2 can be transferred, the thesis will also relate the results to co-electrolysis of H_2O and CO_2.

Outline of the thesis

Chapter 1 Introduction chapter highlighting the background and presenting the purpose of the PhD thesis.

Chapter 2 Background concepts and terms are introduced.

Chapter 3 The carbon formation from the Boudouard reaction is investigated. The carbon boundary is experimentally investigated with thermo-gravimetry analyzers and thermodynamic values for the carbon formation boundary is derived.

Chapter 4 The flow distribution in the SOECs are investigated. The flow is optimized by changes in the operation conditions and with changes in the geometry of internal parts of the SOEC.

Chapter 5 Parameters for the effective diffusion is obtained by experimental work using a Wicke-Kallenbach setup.

Chapter 6 The parameters for effective diffusion is used to model the diffusion limitations within the fuel electrode.

Chapter 7 The possibility of operation at carbon forming conditions with subsequently carbon removal with water is investigated.

Chapter 8-9 The results of the thesis are summarized and discussed. A final conclusion and suggestions for further work are given.

CHAPTER 2
Background concepts

This chapter will describe the background for some of the terms used in the thesis and give a brief overview of the cell voltage, U, open circuit voltage (OCV), and energy balance of SOECs. An internal 3d stack model (developed by Haldor Topsoe A/S) is also briefly described. The model is used to calculate the gas composition and temperature within a stack, given different operation conditions. Due to confidentiality, the model is not described in more details.

2.1 Cell voltage

The cell voltage, U, of an SOEC is controlled by the gas composition, temperature, and current density and given by Eq. (2.1):

$$U = E + \eta_{conc,a} + \eta_{conc,c} + \eta_{act,a} + \eta_{act,c} + \eta_{ohmic} \tag{2.1}$$

where E is the equilibrium potential, η_{conc} is the concentration overpotential of the anode and cathode, respectively, η_{act} is the activation overpotential of the anode and cathode, respectively, and η_{ohmic} is the ohmic overpotential.

The equilibrium potential for electrolysis of CO_2 is given by Eq. (2.2) [70]:

$$E_{CO} = 1.46713 - 0.0004527T + \frac{RT}{2\mathcal{F}} \ln\left[\frac{P_{CO}P_{O_2}^{0.5}}{P_{\mathrm{CO_2}}}\right] \tag{2.2}$$

where R is the gas constant, T is the temperature, $\mathcal{F}$ is Faradays constant and P_i is the partial pressure of species i

The concentration overpotential accounts for the difference in concentration between the channel and the reaction sites [70]:

$$\eta_{conc,a} = \frac{-RT}{2\mathcal{F}} \ln\left[\left(\frac{P_{O_2}^{TPB}}{P_{O_2}^{ch}}\right)^{0.5}\right] \tag{2.3}$$

$$\eta_{conc,c} = \frac{-RT}{2\mathcal{F}} \ln\left[\frac{P_{CO}^{TPB}P_{CO_2}^{ch}}{P_{CO}^{ch}P_{CO_2}^{TPB}}\right] \tag{2.4}$$

where the superscript “TPB” denotes the partial pressure of species i at the triple phase boundaries and the superscript “ch” denotes that the partial pressure of species i in the channel. With a low diffusion, the concentration at the TPB will increase and thus, η_{conc} will increase.

The activation overpotential, η_{act}, is a measurement of the activity of the electrodes and represent the overpotential required for the electrochemical reaction. It can be calculated implicit with the Butler-Volmer equation [71]:

$$\vec{i} = \vec{i}_{0,a} \left[\exp\left(\frac{\alpha_{sym} n_e \mathcal{F} \eta_{act,a}}{RT} \right) - \exp\left(-\frac{(1-\alpha_{sym}) n_e \mathcal{F} \eta_{act,a}}{RT} \right) \right] \tag{2.5}$$

$$\vec{i} = \vec{i}_{0,c} \left[\exp\left(\frac{\alpha_{sym} n_e \mathcal{F} \eta_{act,c}}{RT} \right) - \exp\left(-\frac{(1-\alpha_{sym}) n_e \mathcal{F} \eta_{act,c}}{RT} \right) \right] \tag{2.6}$$

where $\vec{i}_0$ is the exchange current density, α_{sym} is the symmetrical factor and n_e is the number of electrons in the reaction. Both $\vec{i}_0$ and α_{sym} are fitted to experimental data. [70, 71]. When the current density is increased,, the activation overpotential also increases.

The ohmic overpotential can be calculated with Ohms law from the conductivity, ξ, of the electrodes and electrolyte: $\eta_{ohmic} = \vec{i} A_{cell} \xi$, where A_{cell} is the active area of the cell. The conductivity increases with temperature and is typically fitted to an exponential function with the form [71, 72]: $\xi = C_1 \exp\left(-\frac{C_2}{T}\right)$. When the current density is increased, or the conductivity is decreased (i.e. a decrease in T), the ohmic overpotential will increase.

From the equations describing the voltage of a SOEC, it can be seen that the voltage increase when the current density is increased (η_{act} and η_{ohmic} increase directly, while η_{conc} increase indirectly, due to the increase in concentration gradients with the increase in current density), and decrease when the temperature is increase.

2.2 Open-circuit voltage

When the current density is zero, the overpotentials η_{act} and η_{ohmic} are also zero. Furthermore, η_{conc} will also be zero, since there is no difference in the gas composition in the channel and at the reaction sites. The voltage of the cell will therefore be described by the equilibrium potential E. The voltage when a zero current density is applied is called open-circuit voltage (OCV). In this thesis, the OCV with H_2 and H_2O is used to measure if gas is leaking between the electrodes. With H_2 and H_2O, the equilibrium potential is given as [70]:

$$E_{H_2} = 1.253 - 0.00024516T + \frac{RT}{2\mathcal{F}} \ln\left[\frac{P_{H_2} P_{O_2}^{0.5}}{P_{H_2O}} \right] \tag{2.7}$$

If gas is leaking between the electrodes, the partial pressures of H_2, H_2O and O_2 will change, since H_2 will be combusted ($H_2 + \frac{1}{2} O_2 \longrightarrow H_2O$), because the temperature is above the auto-ignition temperature of H_2.

2.3 Energy balance of SOEC

In an overall energy balance of SOEC, the following terms should be taking into account: 1) transport of energy to the stack by inlet bulk flow, 2) transport of energy from the stack due to outlet bulk flow, 3) heat loss to the surroundings, 4) reaction heat and 5) joule heating.

The overall energy balance for steady state operation is therefore:

$$Q_{in} - Q_{out} - Q_l + Q_r + Q_j = 0 \tag{2.8}$$

where Q_{in} and Q_{out} is the energy transported to and from the stack, Q_l is the heat loss to the surroundings, Q_r is the reaction heat and Q_j is the Joule heat. The heat loss is ignored in the following, since the stack are placed in furnaces in this study. If the stack is not placed in the furnace but insulated, the heat loss should be measured. The measurement can be conducted by flushing the stack with a gas with a known heat capacity and inlet temperature, while measuring the outlet temperature.

The energy transported in and out of the stack is respectively given by:

$$Q_{in} = \sum_i (F_{c,in}\rho_{in}C_pT_{c,in}) + \sum_i (\dot{v}_{a,in}\rho_{in}C_pT_{a,in}) \tag{2.9}$$

$$Q_{out} = \sum_i (F_{c,out}\rho_{in}C_pT_{c,out}) + \sum_i (F_{a,out}\rho_{in}C_pT_{a,out}) \tag{2.10}$$

Where F is the volumetric flow on the cathode and anode side at standard conditions (273.15 K, 1 bar) , C_p is the heat capacity, ρ is the density and T is the temperature of the gas.

The reaction heat is calculated as:

$$Q_r = \frac{\Delta H_r \vec{i} A_{cell} n_{cell}}{n_e \mathcal{F}} \tag{2.11}$$

where ΔH_r is the reaction enthalpy and n_{cell} is the number of cells in a stack.

The Joule heating is calculated as:

$$Q_j = U\vec{i}A_{cell}n_{cell} \tag{2.12}$$

where U is the voltage calculated from Eq. (2.1). Since the voltage increase with current density, Q_J scales approximately with $\vec{i}^2$.

The dominating terms in the energy balance is the reaction heat and the Joule heating. The reaction energy is negative (the reaction is endothermic), while the Joule heating is positive. Since Q_r scales with $\vec{i}$ and Q_J with approx. $\vec{i}^2$, Q_r will be higher than Q_J at lower current densities, whereas Q_J will be higher than Q_r at higher current densities. This corresponds to the gas being cooled when it flows through the stack at low current densities (Q_{out} will be lower than Q_{in}) and heated at higher current densities. When Q_r and Q_J are identical, the stack is operation "thermo-neutral" - i.e. the gas is not cooled in the stack and Q_{out} and Q_{in} are identical.

2.4 Fuel utilization

The term fuel utilization, FU is orignally used in SOFC to describe the fraction of utilization of fuel - e.g. $FU = 50\%$ means that half the fuel is converted. In this thesis, the fuel utilization is used to describe the amount of CO_2 and H_2O converted to CO and H_2. Typically, only the conversion of CO_2 is relevant. When CO_2, with low H_2 concentrations (so Ni oxidation is avoided, see Section 7.1 on page 81), is added to the cell fuel utilization is equal to the conversion and can also be used to calculate the CO/CO_2 ratio:

$$FU = \frac{\frac{\vec{i}}{n_e \mathcal{F}} A_{cell}}{F_{\mathrm{CO_2}} \frac{P}{RT}} \tag{2.13}$$

$$X_{CO} = FU X_{\mathrm{CO_2},in} \tag{2.14}$$

$$X_{\mathrm{CO_2}} = (1 - FU) X_{\mathrm{CO_2},in} \tag{2.15}$$

$$\frac{X_{CO}}{X_{\mathrm{CO_2}}} = \frac{FU}{1 - FU} \tag{2.16}$$

where $X_{\mathrm{CO_2},in}$ can be calculated from the known inlet flows, e.g. when CO_2 and H_2 is supplied to the cell:

$$X_{\mathrm{CO_2},in} = \frac{F_{\mathrm{CO_2}}}{F_{\mathrm{CO_2}} + F_{\mathrm{H_2}}} \tag{2.17}$$

2.5 Topsoe stack model

Haldor Topsoe A/S (and formerly Topsoe Fuel Cell) has developed a 3d stack model in COMSOL capable of simulating a complete stack. The details of the model are confidential, but it is in many ways comparable with other models published in the literature [73–75], since the physics are the same. Due to the confidentiality, the model will only be described on a general level. The 3d model includes the cells, casing and manifold and the following physics are solved:

1. Transport of mass
2. Transport of species
3. Transport of heat

4. Transport of current

1. Both the fuel flow (CO_2 or H_2O) and the purge flow to the air side (CO_2, air or N_2) are modeled with the following equations in the manifold:

$$\nabla(\rho u) = 0 \tag{2.18}$$

$$\rho(u \cdot \nabla)u = \nabla \cdot (-P\boldsymbol{I} + \boldsymbol{\tau_s}) \tag{2.19}$$

Here ρ is the density, $\vec{u}$ is the velocity vector, P is the pressure, $\boldsymbol{I}$ is the unity tensor, and $\boldsymbol{\tau_s}$ is the viscous stress tensor, defined as $\boldsymbol{\tau_s} = \mu(\nabla\vec{u} + (\nabla\vec{u})^T) - 2/3\mu(\nabla \cdot \vec{u})I$ (μ is the viscosity and ^{T} means that the tensor is transposed. In the cells, a homogenized flow field is used (based on rigorous modeling of the flow pattern in the cell channels, see [76]). In brief, the cell structure is taken as one big channel and Eq. (2.19) is replaced with:

$$\rho(u \cdot \nabla)u = \nabla \cdot (-P\boldsymbol{I} + \boldsymbol{\tau_s}) - \frac{\mu}{\kappa(\zeta)}\vec{u} \tag{2.20}$$

where $\kappa(\zeta)$ is an artificial permeability at position ζ, fitted so that the flow in the big channel mimics the flow in the real channels. Since the scale of the cell channels are small (mm) with many walls, a mesh resolving the actual structure would create a system with billions of degrees of freedom. With the homogenization, the number of degrees of freedom is reduced to tens of thousands, which drastically reduce the memory requirement and calculation time. For more details, see [76].

2. The transport of species is modeled with the convection–diffusion equation:

$$\nabla \cdot (D_{i,j}\nabla c_i) - \nabla \cdot (\vec{u}c_i) = -R_{s,i} \tag{2.21}$$

where $D_{i,j}$ is the binary diffusion coefficient, c is the concentration and $R_{s,i}$ is the source/sink of the species i. Only the diffusion in the flow region, and not in the electrode, is taken into account. This is added later in the confidential version of the thesis.

$R_{s,i}$ is given by the local current density:

$$R_{s,i} = v_i \frac{\vec{i}}{n_e\mathcal{F}} \cdot \frac{1}{H_{norm}} \tag{2.22}$$

where v_i is the stochiometric coefficient of the electrochemical reduction of H_2O and CO_2 (Eq. (1.3) and Eq. (1.4) on page 4). The expression is normalized with a an appropriate height, H_{norm}, so that $R_{s,i}$ has the unit $\mathrm{mol\,m^{-3}\,s^{-1}}$.

3. The transport of heat is modeled with the steady-state heat conduction equation:

$$\nabla \cdot (-k\nabla T) = \dot{Q}_s \tag{2.23}$$

where k is the conductivity, T is the temperature and $\dot{Q}_s$ is the heat sources/sinks.

The heat sources/sinks includes:

- Heat of reaction
- Energy loss to surroundings
- Joule heating

4. The transport of current is calculated with Ohm's law:

$$\nabla(\varsigma \cdot \nabla\Phi) = 0 \tag{2.24}$$

where ς is the conductivity and Φ is the potential . The conductivity has been experimentally fitted to several in-house tests.

The output of the 3d stack model is the flow velocity, gas composition, temperature, and current density in every calculated point in the stack. With the model it is possible to investigate the relationship between e.g. the flow pattern and gas composition or calculate the equilibrium temperature for the Boudouard reaction (see Chapter 3) and compare it with the actual temperature.

CHAPTER 3

Carbon formation

In this chapter, the theory for the carbon formation with respect to SOECs are summarized. First the carbon forming reactions and types are described, and then the limitations due to kinetic and thermodynamic are described. Afterwards, an experimental investigation of the thermodynamics for the carbon forming reaction are presented. In the last section, the results of the chapter is summarized.

3.1 Carbon forming reactions and carbon types

The formation of carbon has been experimentally observed during electrolysis and can cause delamination of the cell between the fuel electrode and the electrolyte [77]. Delamination of the cell is highly unwanted, since it increases the resistance of the cell, and may lead to cracks, since the support layer of the fuel electrode acts as mechanical support for the whole cell. During thermocycling (cooling to room temperature and heating to operating temperature) the cell might also be severely affected, since the mechanical strength of the support layer is not fully connected to the electrolyte and air electrode.

Ni containing catalysts are used in different industrial processes such as steam reforming and high temperature methanation, where carbon formation is a risk. The carbon formation on Ni catalysts has therefore been thoroughly studied [78–83].

Carbonaceous gas species might form solid carbon through the Boudouard reaction (Eq. (3.1)) and methane decomposition (Eq. (3.2)) [80, 84]. The carbon can be in the form of graphite [85], pyrolytic carbon, carbides [86, 87], and whisker carbon (also called filamentous carbon) [81, 88]. At the high temperatures used in SOECs, whisker carbon and graphite will be formed [89, 90], see Fig. 3.1. Both whisker carbon, C(s,wc), and graphite carbon, C(s,gr), can be formed via the Boudouard reaction and methane decomposition.

$$\text{Boudouard reaction} \qquad 2\,\mathrm{CO} \rightleftharpoons \mathrm{CO_2} + \mathrm{C(s)} \tag{3.1}$$

$$\text{Methane decomposition} \qquad \mathrm{CH_4} \rightleftharpoons 2\,\mathrm{H_2} + \mathrm{C(s)} \tag{3.2}$$

When both carbon and hydrogen species are present, the water-gas shift reaction and methanation reaction will also take place:

$$\text{Water-gas shift reaction} \qquad CO + H_2O \rightleftharpoons CO_2 + H_2 \tag{3.3}$$

$$\text{Methanation reaction} \qquad CO + 3\,H_2 \rightleftharpoons CH_4 + H_2O \tag{3.4}$$

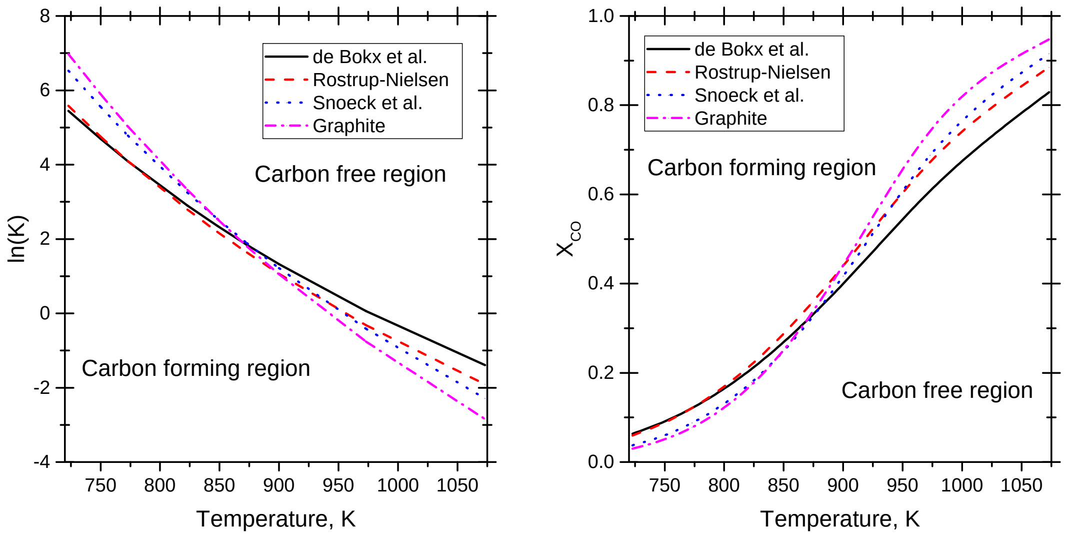

(a) ln(K) vs T for the Boudouard reaction **(b)** X_{CO} vs T for the Boudouard reaction

Figure 3.1: Equilibrium for whisker carbon (three set of literature values shown) and graphite via the Boudouard reaction. a) ln(K) vs 1000/T. b) X_{CO} vs T for the Boudouard reaction. At the temperatures used in SOEC (600–800 °C, 873–1073 K, the equilibrium constant for whisker carbon is higher than graphite, and whisker carbon will therefore form before graphite.

3.1.1 Graphite

Graphite is the most stable form of carbon under standard conditions and is therefore used as the standard form to define heat of formation. It consists of a layered planar structure where carbon atoms are bound to each other with three covalent bonds in a honeycomb lattice structure. The layers are only held together with van der Waals forces [91]. Fig. 3.2 shows the layered planar structure of graphite. Graphite reduce the active area and blocks the pores, whereas whisker carbon are very strong and can lead to catastrophic destruction of the cell [3].

3.1.2 Whisker carbon

Whisker carbon typically grows with a Ni particle at the top. As the whisker grows, the Ni particle is transported away from its original place on the support structure. Whisker

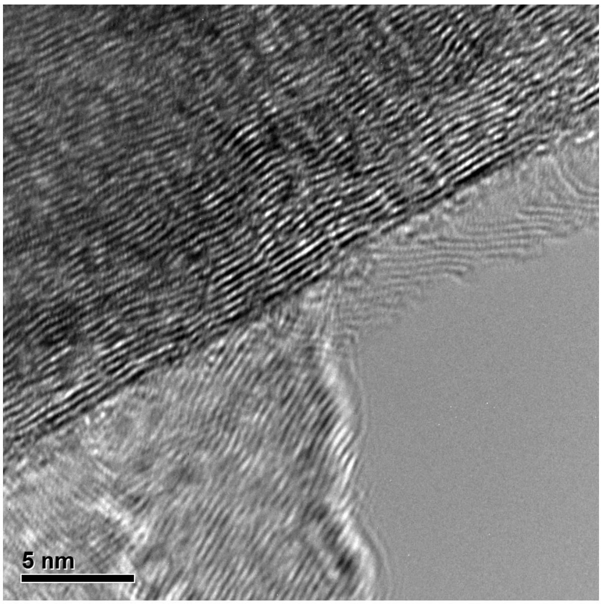

Figure 3.2: TEM image of graphite. Image obtained from sample 1 (see Section 3.3.2) with a TEM CM200

carbon has a high mechanical strength and is capable of completely disintegrating catalyst support structure, making all attempts of regeneration impossible [81, 88].

Whisker carbon has been widely studied in the last four decades, since it is formed in temperature ranges relevant for important catalytical processes, such as methanation and steam-reforming, as mentioned above.

The growth of whisker carbons has previously (since the 1970's) been described as involving dissolution of C in Ni, formation of nickel carbides, and diffusion of C through the Ni particle, followed by nucleation of the carbon fiber on the surface of the Ni particle, when the Ni particle was supersaturated with C [92]. In 2004 Sehested et al. [93] used in situ high-resolution transmission electron microscopy (HRTEM) to study the formation of whisker carbon from methane. Their observations showed that whisker carbon developed through a reaction-induced reshaping of the Ni nanocrystal. The specific formation and restructuring of mono-atomic step edges of the Ni surface was found to assist the nucleation and growth of graphene layers. The graphene layers separates the Ni from the support material. Fig. 3.3 shows how the Ni nanocrystal is first elongated (step a-g) and then contracted (step h).

Tao et al. [94] has also observed that whisker carbon can grow with a Zirconia particle, instead of a Ni particle, during co-electrolysis with high current densities ($2.25\,\mathrm{A\,cm^{-2}}$). The proposed mechanism is illustrated in Fig. 3.4. The formation of carbon can also take place via an electrochemical reaction where adsorped CO on the Ni particle are reduced to solid carbon [89]:

$$\mathrm{CO} + 2\,\mathrm{e}^- \rightleftharpoons \mathrm{C(s)} + \mathrm{O}^{2-} \tag{3.5}$$

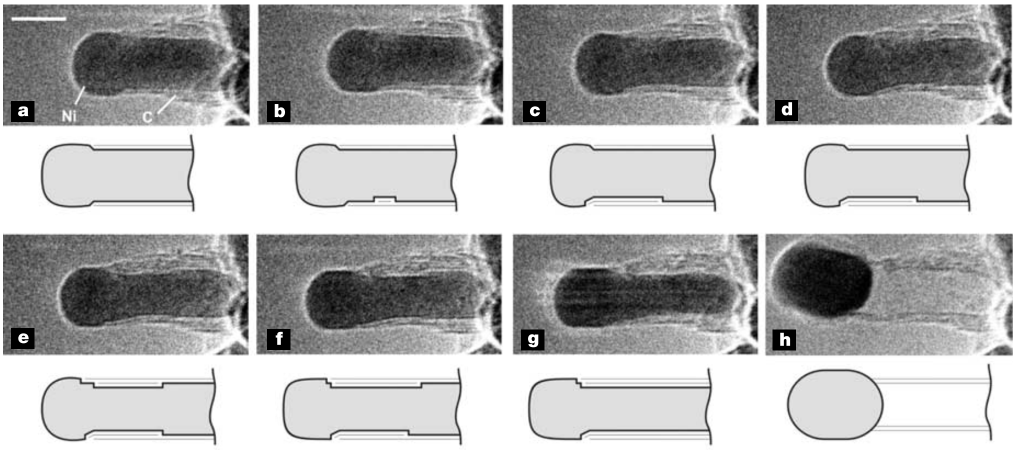

Figure 3.3: Image sequence of a growing carbon nanofibre. Images a–h illustrate the elongation/contraction process. Drawings are included to guide the eye in locating the positions of mono-atomic Ni step edges at the C–Ni interface. The images are acquired in situ with CH_4:H_2 = 1:1 at a total pressure of 2.1 mbar with the sample heated to 536 °C. All images are obtained with a rate of 2 frames s^{-1}. Scale bar, 5 nm. Image taken from [93].

Only the formation of carbon on Ni is included in this thesis. However, future studies of the whisker carbon formation with Zirconia and the electrochemical formation of carbon should be conducted (e.g. if it only occurs at high current densities, or also at more modest current densities).

3.2 Thermodynamic or kinetic limited?

The formation of carbon on Ni catalysts has been studied and found to occur when the equilibrium is exceeded (see Fig. 3.7 of page 29). It is therefore necessary to operate at conditions where the reaction is not thermodynamic favored. The principle of equilibrated gas has been used to assess the risk of carbon formation [95, 96] and states that: *"Carbon formation is to be expected on a nickel catalyst if the gas shows affinity for carbon after the establishment of the methane reforming and the shift equilibria"* [95].

The affinity for carbon formation is calculated from the thermodynamics. The relationship between Gibbs free energy, ΔG, and the equilibrium constant, K, are given by:

$$\Delta G = -RT \ln K \tag{3.6}$$

Where R is the gas constant and T is the temperature.

Gibbs free energy can be expressed by the enthalpy, ΔH, and entropy, ΔS:

$$\Delta G = \Delta H - T\Delta S \tag{3.7}$$

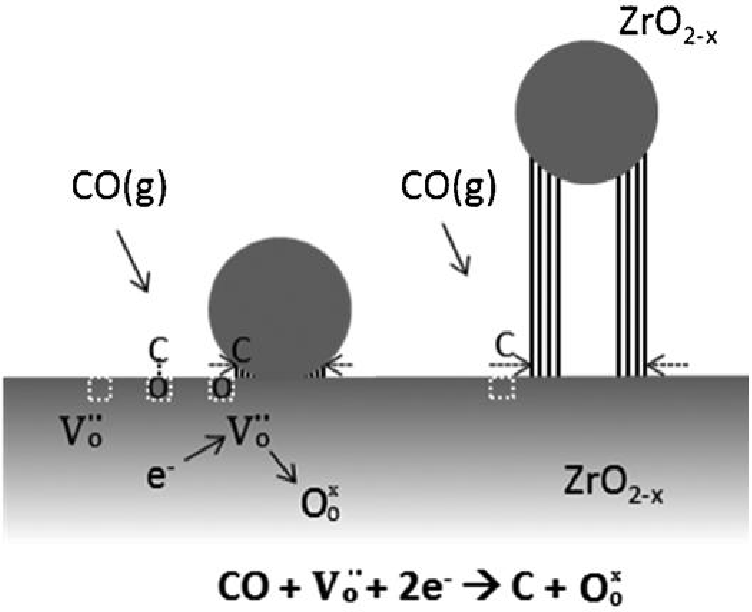

Figure 3.4: Growth of carbon nanotubes on zirconia nanoparticles by an electrocatalytic process. $V_O^{\circ\circ}$ are oxygen vacancies, O_o^x are occupied sites of O in zirconia. Taken from [94].

Combining and rearranging yields:

$$\ln K = \frac{\Delta H - T\Delta S}{-RT} \tag{3.8}$$

The equilibrium constant can also be calculated from the mole fractions, when the system is at equilibrium:

$$K = \frac{X_{CO_2,eq}}{X_{CO,eq}^2 P} \tag{3.9}$$

Where X is the mole fraction of CO and CO_2, respectively, and P is the pressure (for the thermodynamics, P is expressed in atm). The reaction quotient, Q, is calculated from the actual mole fractions:

$$Q = \frac{X_{CO_2}}{X_{CO}^2 P} \tag{3.10}$$

The affinity for carbon, a_c is calculated from the equilibrium constant and the reaction quotient: $a_c = K/Q$. When K and Q have the same value, the system is at equilibrium. This corresponds to $a_c = 1$. There will be affinity for carbon formation, $a_c > 1$, when the CO/CO_2 ratio, or the pressure, is increased.

3.2.1 Influence of Ni particle size

The equilibrium constant for whisker carbon has been found to increase with the size of the Ni particles, d_{Ni}, making it more difficult to form carbon if the particles are small. Rostrup-Nielsen [79] use the following equation to express the difference between ΔG_r for whisker carbon and graphite carbon, and the radius of the largest Ni particle, $d_{Ni,max}$:

$$\Delta G_c = \frac{2k_{rmax}}{d_{Ni,max}} + \mu^\star \tag{3.11}$$

where k_{rmax} is a constant describing the difference of ΔG for the two carbon types with respect to the maximum Ni particle size and $\mu^\star$ is the contribution from structural defects compared to graphite [79]. k_{rmax} and $\mu^\star$ depends on the temperature. At 600 °C, the values can be fitted to $k_{rmax} = 712\,\mathrm{kJ\,Å\,mol^{-1}}$ and $\mu^\star = 6.853\,\mathrm{kJ\,mol^{-1}}$[79, 97].

The average Ni particle size in SOFC (which is similar to SOEC) is typically in the range of 300 nm to 2500 nm [98–102]. During operation, the sintering of Ni increase the average particle size. E.g. a change from an average particle size of 2040 ± 840 nm to 2570 ± 1190 nm during 4000 h of exposure to 4 % H_2 and 3 % H_2O in Ar at 1000 °C has been observed [102]. Hauch et al. [101] reports particle size distributions for three cells (where the Ni particle sizes were intentionally different) with average particle sizes of 1348 nm, 1225 nm and 832 nm, respectively. The maximum Ni particle diameter for all three cells was approximately three times the average diameter.

The Ni particle size used in SOCs are quite large, compared to the sizes encountered by the experiments by Rostrup-Nielsen (12.5 to 250 nm). With the large particles used in SOC, the effect of the particle size is negligible. Fig. 3.5 shows ΔG_c as function of the Ni particle diameter. If the smallest reported average Ni diameter of 300 nm [100] has a maximal Ni diameter of approx. three times the average diameter, the deviation between the ΔG_c value and $\mu^\star$ is 1 %. For larger particles, the deviation will be even lower. It should be noted that the calculations above is outside the range of the fitted function in [79]. Furthermore the slope used to calculate k_{rmax} and $\mu^\star$ from [79] has a relative error of 10-15 %. However, beside the extrapolation and uncertainty for the estimation of ΔG_c, the particles in SOCs are so large that deviations, between the thermodynamics for graphite and whisker carbon, can be seen as independent with respect to the particle size.

3.2.2 Other ways to limit the carbon formation

The formation of carbon can be suppressed by changing the Ni with e.g Ni alloys with noble metals (roughly the second and third row transition metals in groups 8-11) or base metals (Co, Cu or Fe), replacement of Ni with nonmetal electronic conductors or increase the alkalinity [103]. Sulfur, which is known to limit the carbon formation [104], can also be added to the gas stream. All of these methods either impact the performance or economy of SOECs, and are therefore not used. It is therefore still a research area

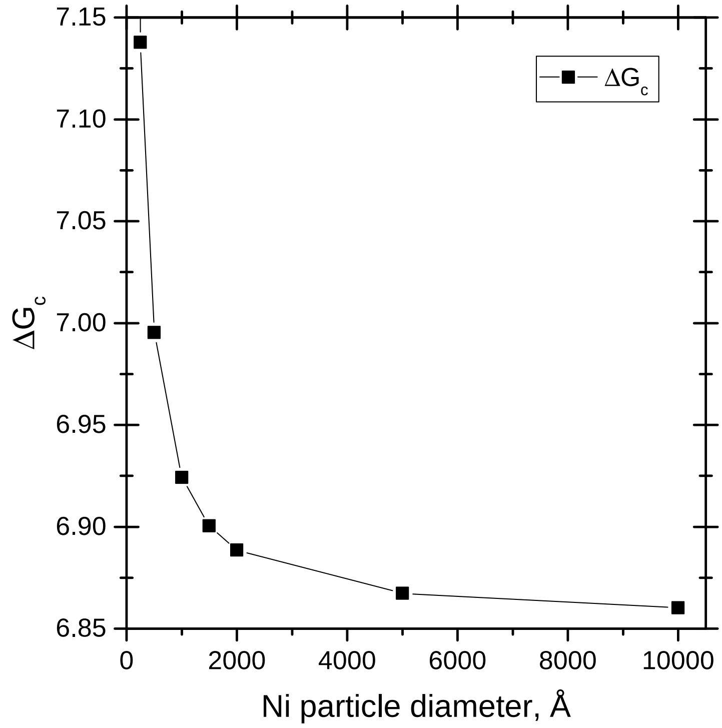

Figure 3.5: ΔG_c as function of Ni particle size. Calculated from Eq. (3.11)

to find a cheap and reliable strategy to suppress carbon formation. The suppression of carbon formation via material change or adding of e.g. sulfur containing compounds to the feed gas, are outside the scope of this thesis.

3.3 Experimental investigation of the Boudouard equilibrium

When looking at the thermodynamics for carbon formation it is important to distinguish between graphite and whisker carbon, since they are not the same [79, 80]. Plotting the equilibrium constant for the graphite and whisker carbon, it can be seen that when going down in temperature, whisker carbon is the first formed type of carbon. If the temperature is decreased a bit more, it will also be thermodynamically possible to form graphite, see Fig. 3.1.

The thermodynamics for graphite is well known and can be found in various databases and textbooks (e.g. [105–107]). Different thermodynamics for whisker carbon has been reported in the literature [79–81], see Table 3.1. The deviation between the thermodynamics for graphite and whisker carbon is ascribed to the extra energy required by the higher surface energy, the elastic energy, and defect structure of the whiskers carbon [78]. Whisker carbon grow with a Ni-particle in front, so the thermodynamics depends on the size of the Ni-particle [79]. Since Ni-YSZ material displays a range of Ni-particle sizes, Lee et al. [31] note that the selection of an appropriate Ni-particle size is not straight forward. However, the particle size of SOC's are so large that the influence of Ni particle size can be ignored (see Section 3.2.1).

In the literature, equilibrium data are available from 723-973 K, 750-900 K, and 773-848 K [79–81]. Extrapolation of the data to 923-1023 K (relevant operation temperature for SOECs) shows a deviation of ln(K) of 0.7 (Fig. 3.1a). This corresponds to mole fraction differences of X_{CO} of 10 percentage point in CO_2 (Fig. 3.1). This uncertainty is a significant limitation for the operating window for CO production (see Fig. 1.9 on page 11), and it is therefore of importance to investigate the thermodynamics of carbon formation on SOEC electrode material with the proper Ni particle size.

Table 3.1: Thermodynamic values for the formation of whisker and graphite carbon with the Boudouard reaction. The enthalpy and entropy are taken as temperature independent. The average Ni particle diameter, $\bar{d}_{Ni}$ and the source of the thermodynamics are also given. The values are given with the number of significant figures given in the source.

Carbon type	ΔH, $\mathrm{kJ\,mol^{-1}}$	ΔS, $\mathrm{kJ\,mol^{-1}\,K^{-1}}$	$\bar{d}_{Ni}$, nm	Source
Wc	-138	-144.6	79.8	Rostrup-Nielsen [79]
Wc	-126	-129	5.4	Bokx et al. [81]
Wc	-162.483	-170.44	15-20*	Snoeck et al. [80]
Gc	-180.965	-192.3	5.4	Snoeck et al. [80]

*: Only the diameter of the whisker carbon is given. Wc=Whisker carbon. Gc = Graphite carbon.

3.3.1 Method

Two different thermo-gravimetric analyzers (TGA) were used to measure the equilibrium of the Boudouard reaction (Fig. 3.6). The two units where essentially similar except that TGA-1 was equipped with a MK2-G5 weigh head from CI Precision (precision 0.1 µg) and only constructed for a low partial pressure of CO, whereas TGA-2 was equipped with a ICANN D-101 micro balance (precision 10 µg) and suitable for high CO levels. The CO/CO_2 gas mixture in TGA-1 was therefore diluted with N_2. Both TGA setups were limited to a maximum temperature of 700 °C (973 K). The Ni-YSZ sample was placed in a basket/sample holder hung in the electro-microbalance. The sample holder was placed in a glass reactor surrounded by an electrically heated furnace. A thermocouple was placed below the sample holder and used to control the temperature during the experiment. The test gas and purge gas (N_2) were mixed prior to entering the reactor and passed through a bed of inert material, so that an even gas flow was obtained. For

TGA-1 all gasses were taken from a common distribution system shared with other setups. For TGA-2 all test gasses (H_2, CO and CO_2) were taken from cylinders and N_2 was taken from a common distribution system shared with other setups. The purity of the gasses were >99.9 % for H_2, >99.997 % for CO, >99.995 % for CO_2 and >99.95 % for N_2. The samples consisted of Ni-YSZ used in Haldor Topsoe A/S's commercial 2.5G cells, which consist of a Ni-3YSZ support layer (ca. 0.3 mm) and a Ni-8YSZ fuel electrode (ca. 10 µm) [108, 109]. As shown in Section 3.2.1, the size of the Ni used in SOCs are so large, that the potential difference in particle size distribution of the two Ni-YSZ cermets, does not influence the results.

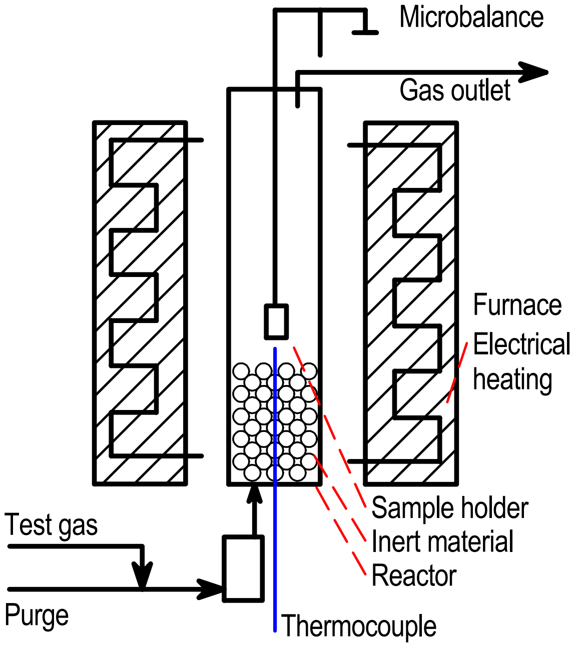

Figure 3.6: Schematic illustration of the thermo-gravimetric setup used to measure the equilibrium of the Boudouard reaction. The test gas is mixed with a purge gas and enters a buffer/mixing tank of approximately 0.1 L before entering the reactor. In the reactor, the bottom is fixed with inert material, so that any pulsations from the mass-flow controllers/gas supply are minimize. The sample is placed in the sample holder, which is connected to the micro balance. The reactor is placed in a electrical heated furnace.

A sample of 100-200 mg was placed in the sample holder and the sample was heated to 700 °C with a 29 % H_2 in N_2 gas composition at a rate of 5 $°C\,min^{-1}$. The sample was held at 700 °C for 2 h to ensure complete reduction. The completion of the reduction was verified by the weight, which decreased during the reduction (as O was removed from the sample) and stabilized when the reduction was complete. After the reduction step, the gas flow was changed according to Table 3.2. The temperature was then lowered with 10 $°C\,min^{-1}$ to 30 °C higher than the expected carbon formation equilibrium temperature, based on the thermodynamics by Rostrup-Nielsen [79], and then lowered with a ramp of

1 °C min^{-1} to 30 °C below the expected equilibrium temperature. The temperature was then raised by 1 °C min^{-1} to 30 °C above the expected equilibrium temperature.

During cooling, a sudden increase in the sample mass was observed when the equilibrium temperature was passed. The increase continued until the temperature was again over the equilibrium temperature. The start of carbon formation was observed at a slightly lower temperature than the temperature at which the increase in mass stopped. This behavior was also observed by Rostrup-Nielsen [79]. The temperature at which the mass increase stopped during heating is reported as the experimental equilibrium temperature.

For the first sample, the reported value is based on cooling and a cooling rate of 14 °C min^{-1}. However, it could be seen that the obtained value was far from the expected. This was believed to be caused be very high applied cooling rate of the experiments, which probably did not allow for sufficient temperature equilibration between the furnace and the sample. The heating and cooling rate was therefore changed to the aforementioned 1 °C min^{-1}, for the remaining samples.

Fig. 3.7 shows the typical relationship between the temperature and the sample weight during the experiments, as described above, for sample 6. From the figure, it can be seen that the sample weight is constant until the equilibrium condition is passed (t=0.7 h). Then the weight starts to rapidly increase and a weight increasement of approx. 2 % is observed within 1 h. When the temperature is increased above the equilibrium, the weight increase stopped (and started to decrease, due to the reversibility of the Boudouard reaction). The temperature at which the weight starts to increase is labeled $T_{B,c}$ and the temperature at which the weight increase stopped is labeled $T_{B,h}$. As described above, $T_{B,h}$ is reported as the experimental equilibrium temperature.

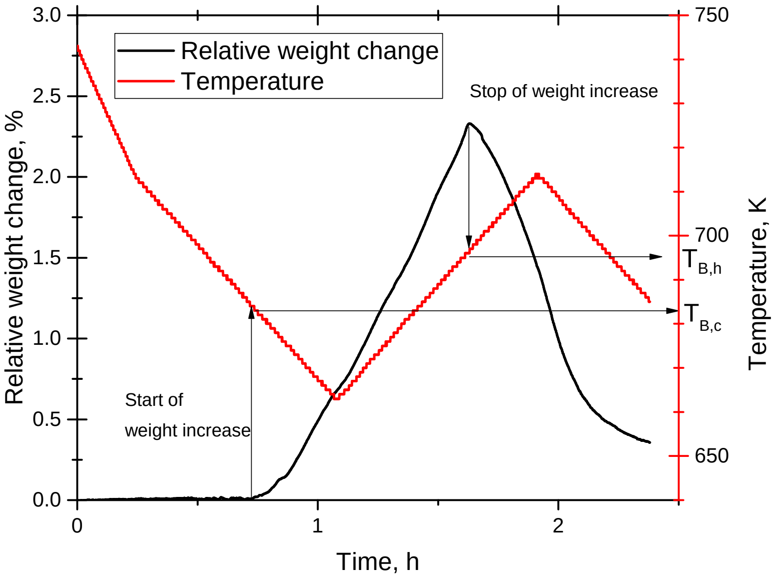

Figure 3.7: Typical relationship between the temperature and the sample weight during the TGA experiments. $T_{B,c}$: Temperature at which the weight starts to increase. $T_{B,h}$: Temperature at which the weight stop to increase

Fig. 3.8 shows pictures obtained with tunneling electron microscopy (TEM) of sample 1 and 2. The pictures shows that a huge amount of whisker carbon has formed. In addition, some encapsulation carbon has also formed (for both samples). The reason for this, is that the experiments is performed down to 30 K below the equilibrium for whisker carbon, and therefore also crosses the equilibrium for graphite formation. Analysis of the black whisker forming particle (in TEM by Haldor Topsoe A/S), showed that the particle was Ni (as expected).

3.3.2 Results and discussion

Table 3.2 shows the experimental condition and obtained experimental equilibrium temperature. The obtained experimental equilibrium points are plotted in Fig. 3.9 and Fig. 3.10 (showed as points). The lines represent the thermodynamics from the literature (Table 3.1). It can be seen from the plot that the experimental equilibrium points fit well with the Rostrup-Nielsen and Snoeck et al. thermodynamics from 600-700 °C (1-1.15 K^{-1}). At the lowest investigated temperature (at approx. 475 °C), Rostrup-Nielsen's thermodynamics are closer than Snoeck et al.'s thermodynamics. As noted in Table 3.1 and in the previous section, the temperature rate of this point was very high. Thus, the uncertainty of this measurement is probably high and the point will therefore be disregarded. The experimental data points were fitted and the following enthalpy and entropy were obtained,$\Delta H = -128\text{kJ}\,\text{mol}^{-1}$ and $\Delta S = -133\text{kJ}\,\text{mol}^{-1}\,\text{K}^{-1}$. The fitted line is plotted in Fig. 3.9.

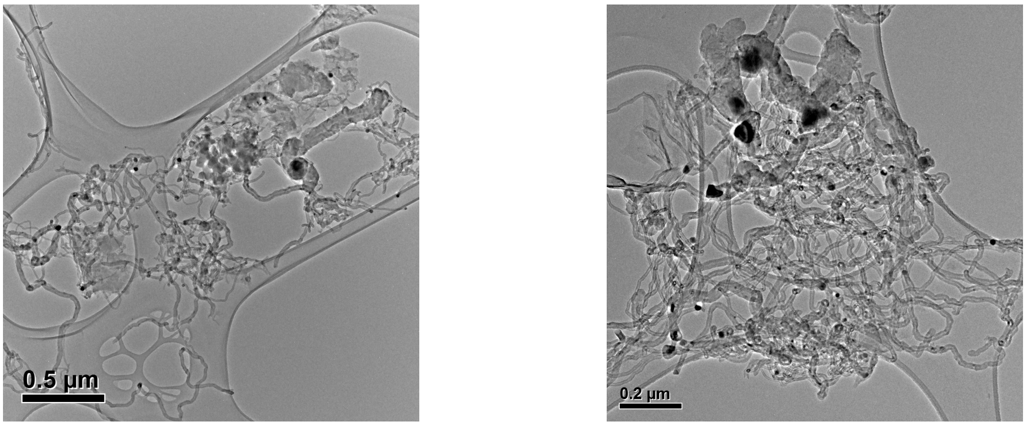

(a) Sample 1 **(b)** Sample 1

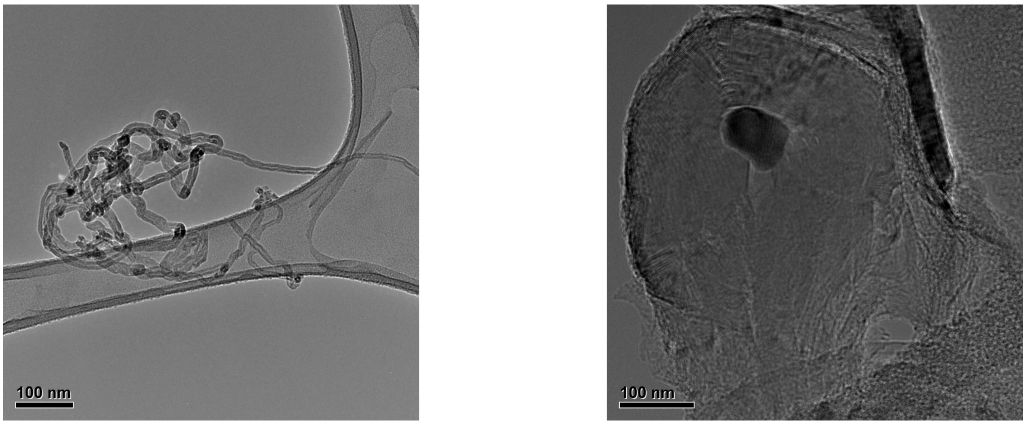

(c) Sample 2 **(d)** Sample 2

Figure 3.8: TEM pictures of samples used in TGA experiment showing whisker carbon (a-c) and encapsulation carbon (d). The black in front of the whisker carbon is a Ni particle.

With the limited number of experimental data points, it is hard to recommend the use of any of the whisker carbon thermodynamic data set over the others. However, it can definitely be seen, that the use of thermodynamic data for graphite will significantly underestimate the boundary for carbon formation. It appears that the use of the thermodynamics published by Rostrup-Nielsen and Snoeck et al. follow the trend of the data points from 640 °C to 700 °C best. Based on this, the thermodynamics published by Rostrup-Nielsen will be used in the rest of this thesis. As noted above, the thermodynamics for the whisker carbon depends on the Ni-particle size, but the large particle sizes used in SOCs means that the thermodynamic values will not change significantly for other manufactured solid oxide cells.

Table 3.2: Samples, test flow and results.

Sample	F, NmL min^{-1} CO	CO_2	N_2	CO/CO_2	$\ln K$	T, K	TGA setup
1	16.7	83.3	83.3	0.20	4.001	746*	TGA-1
2	32.0	4.4	83.3	7.21	-0.643	973	TGA-1
3	129.7	66.2	83.3	1.96	0.094	954	TGA-1
4	60.0	63.0	50.0	0.95	1.107	889	TGA-2
4	60.0	63.0	50.0	0.95	1.107	893	TGA-2
5	9.0	5.9	10.0	1.52	0.603	915	TGA-2
5	9.0	13.0	10.0	0.69	1.634	879	TGA-2
6	60.0	20.0	50.0	3.00	-0.325	969	TGA-2
6	60.0	29.4	50.0	2.04	0.130	952	TGA-2
7	60.0	63.0	50.0	0.95	1.107	908	TGA-2

*: The temperature rate was 14 °C min^{-1}, all others were 1 °C min^{-1}.

3.4 Conclusion

Carbon will form as graphite or whisker carbon on SOCs via the Boudouard reaction. The formed whisker carbon has the potential to delaminate the cells and ultimately destroys the cells in the process. The formation of carbon is only avoided when the reaction is thermodynamic equilibrium unfavored. The equilibrium is different from graphite and whisker carbon, and whisker carbon will be thermodynamically favored before graphite. Three studies have published thermodynamic values for whisker carbon. The values can not be directly transferred to SOCs, without experimental validation, because the thermodynamics also depends on the Ni particle size. Thermo-gravimetry experiments were therefore performed on SOCs material supplied by Haldor Topsoe A/S. The experiments showed that the thermodynamics published by Rostrup-Nielsen (obtained on smaller particles than used in SOCs, but larger than other published thermodynamic values) can be used to describe the equilibrium of whisker carbon on SOCs. The thermodynamics obtained is believed to be directly transferable to other manufactured SOCs, because the Ni particle size of SOCs are so large that the change in thermodynamic, due to the Ni particle size, can be neglected.

Only the formation of carbon on Ni is included in this thesis. However, future studies of the electrochemical formation of carbon and whisker carbon formation with zirconia should be conducted (e.g. if it only occur at high current densities, or also at more modest current densities). The carbon formation can be suppressed by using other materials or possibly the use of e.g. sulfur addition to the feed. However, these solutions are still not fully comparative with fuel electrodes based on Ni-YSZ with respect to performance and economy. It is an active research area, but outside the scope of this thesis.

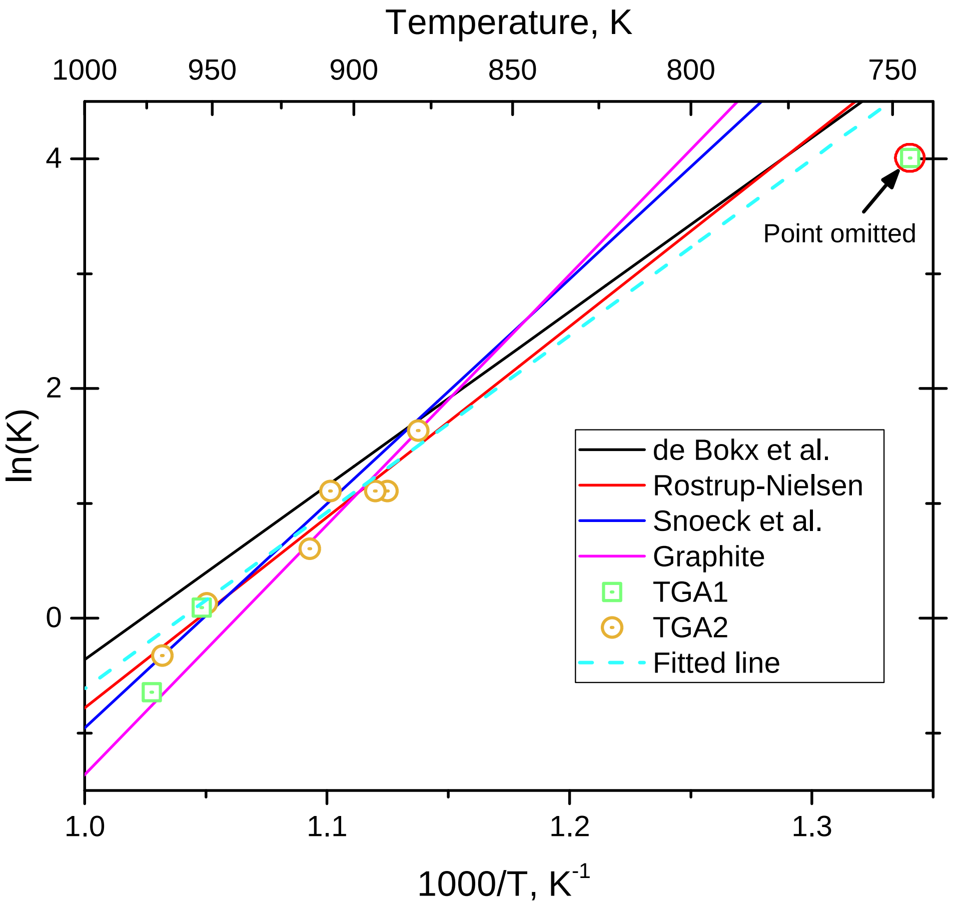

Figure 3.9: Experimental points (squares and circles) - plotted as ln(K) vs 1000/T. The lines represent the thermodynamics from the literature. Note that the dashed lines used for “Rostrup-Nielsen” and “Snoeck et al” in Fig. 3.1 has been converted to solid lines, in order to increase the readability.

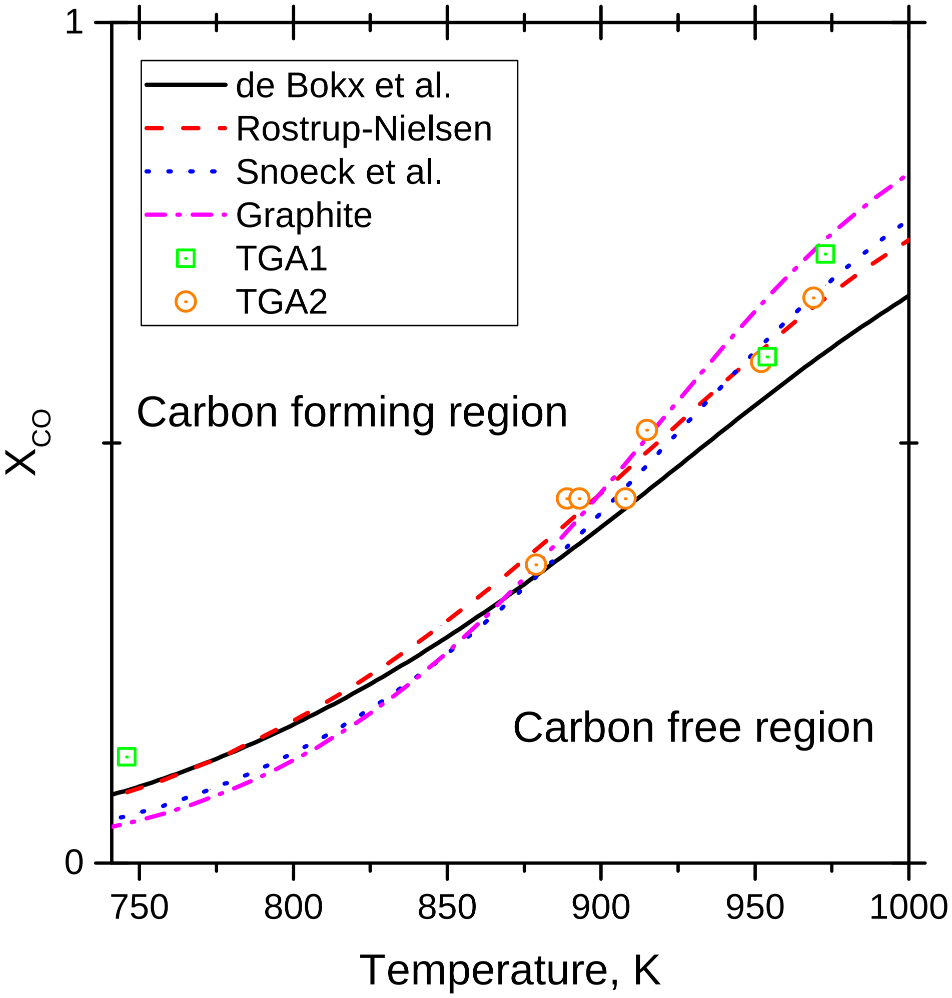

Figure 3.10: Experimental points (squares and circles) - plotted as X_{CO} in CO_2 vs T. The lines represent the thermodynamics from the literature

CHAPTER 4

Flow investigation and optimization

In this chapter the flow in the fuel channels are investigated and optimized. In the first section, the need for flow optimization is justified from post mortem analysis of cells performed by Haldor Topsoe A/S and modeling results. Afterwards, the flow is first optimized by changing the operation conditions and then by changing the geometry of a distributor.

4.1 Model calculations and observed phenomena

In several stack tests (performed by Haldor Topsoe A/S) delamination between the layers in the cell, because of carbon formation, was observed. The delamination occured in the same areas of the cells and it was therefore reasonable to suspect the flow distribution to play an important role. Fig. 4.1a shows the areas affected by delamination. It can be seen that the areas affected are at the edges, corners and between the outlet holes. In Fig. 4.1b it can be seen that the flow at the area affected by carbon formation (the edges, corners and between the outlet holes) is low, compared to the rest of the cell. Because of the low flow, the conversion in these areas is higher than at the rest of the cell, and thus the mole fraction of CO is locally very high. In Fig. 4.1c the margin to the Boudouard equilibrium temperature is calculated, using values of local gas composition and temperature obtained with the internal 3d stack model presented in Section 2.5. It can clearly be seen that there is a high similarity between the experimentally observed areas of carbon formation (Fig. 4.1a) and the estimated areas (Fig. 4.1c). Since the flow caused areas with high CO concentrations, the flow was sought optimized in the next two subsections.

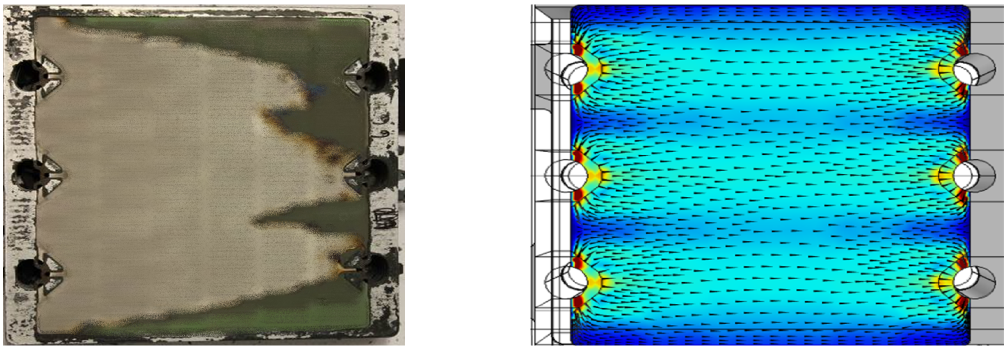

(a) Greenish areas to the right are affected by delamination due to carbon formation. Courtesy of Haldor Topsoe A/S

(b) Flow velocity ($\mathrm{m\,s^{-1}}$) of the fuel gas (CO_2) in the cells.

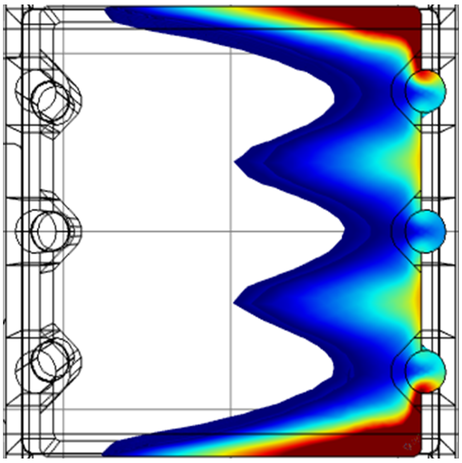

(c) Predicted areas with carbon formation based on the calculated gas composition and temperature. The plot only shows the areas with a negative temperature margin to the Boudouard equilibrium temperature. Thus, it is the area where carbon formation is thermodynamic favored.

Figure 4.1: Figures showing the a) actual areas affected by carbon formation, b) the flow velocity of the fuel gas, and c) the predicted areas with carbon formation. In all figures, the fuel gas enters from the holes at the left and exits through the holes to the right. Due to confidentiality, figure a) has been blurred and the scales for b) and c) has been omitted.

4.2 Flow optimization through change of operating conditions

A parameter study was performed to investigate the risk of carbon deposition due to the flow distribution at different operation conditions. Four parameters (temperature, current density, fuel utilization and air flow) was investigated at 2-3 levels (see Table 4.1). The upper limit for the temperature was fixed from limitations in the heaters and the upper limit of the air flow was fixed from considerations of the pressure drop. The current density was selected at values lower than 6882 $\mathrm{A\,m^{-2}}$ (The "odd" number is caused by the normalization with the cell area: 6882 $\mathrm{A\,m^{-2}}$ corresponds to 75 A). At high current densities ($> 10\,000\,\mathrm{A\,m^{-2}}$), a higher degradation of the cell has been observed, due to the nucleation and growth of oxygen in the YSZ grain boundaries near the air electrode [110]. To avoid this, a maximum current density of $6882\,\mathrm{A\,m^{-2}}$ was used. With a current density of $2294\,\mathrm{A\,m^{-2}}$, the cell is operated at very endothermic conditions. At $4588\,\mathrm{A\,m^{-2}}$ the cell is operated at slightly endothermic conditions and at $6882\,\mathrm{A\,m^{-2}}$, the cell is operated close to thermoneutral, i.e. the Joule heat ($Q_j = U\vec{i}A_{cell}n_{cell}$, see Section 2.3 on page 15) match the reaction enthalpy, and the temperature is therefore constant, see Section 2.2.. The fuel utilization (FU -see Chapter 2 for definition of fuel utilization) was selected at levels covering a large range. Since FU and $\vec{i}_t$ dictates the flow to the fuel electrode, the fuel flow is not explicitly given in Table 4.1. It can be calculated from equation Eq. (2.13) on page 16.

Table 4.1: Values used for the parameter study

Parameter Level	Low	Medium	High
T, °C	700	750	800
$\vec{i}_t$, $\mathrm{A\,m^{-2}}$	2294	4588	6882
Fuel Utilization (FU), %	20	35	50
Air Flow ($\dot{F}_{air}$), $\mathrm{NL\,min^{-1}\,cell^{-1}}$	0.5	-	1.4

The risk of carbon formation was evaluated by comparing the calculated local temperature within the cell with the calculated local equilibrium temperature of the Boudouard reaction, based on the gas composition. The parameter study showed that there was a risk of carbon formation at all combinations of the parameters, except for $T = 800\,°\mathrm{C}$, $\vec{i}_t = 2294\,\mathrm{A\,m^{-2}}$ and $FU = 20\%$ at both the investigated levels of $\dot{F}_{air}$.The margin, $T_{calc} - T_B$, was 10 °C and 33 °C, for $\dot{F}_{air} = 0.5\,\mathrm{NL\,min^{-1}\,cell^{-1}}$ and $\dot{F}_{air} = 1.4\,\mathrm{NL\,min^{-1}\,cell^{-1}}$, respectively. As explained in Section 2.5, the used stack model did not include the diffusion limitations in the fuel electrode (see later in the thesis, Chapter 6). This means that the margin towards the Boudouard reaction will be lower, than the calculated values above.

The parameter study revealed that FU was least limited at a value below 35 %, in order to avoid the risk of carbon formation. By increasing FU from 20 % in small steps, it was found that a maximal fuel utilization of 22 % could be used, before the margin towards the Boudouard equilibrium temperature became negative. As described in Section 4.1, the main issue is the poor flow distribution at the edges, between the outlet holes and especially at the corners. Therefore, since the cell could only be operated in the carbon-free region at low FU, the possibility of flow optimization was investigated.

4.3 Flow optimization through geometric changes

Fig. 4.2 shows a 3d sketch of the cell structure. The flow in the fuel channels are controlled by the shape of a gas distributor and the channels, formed by the interconnect. Fuel gas is entering through a manifold of three tubes (which are formed when single cells are assembled to form the stack) to the left in Fig. 4.2, moves through a barrier structure, called gas distributor, and is distributed to all the parallel channels (see insert of Fig. 4.2). Purge flow (typically air) is entering through holes at the left side of the cell and exiting through holes at the right side of the cell. The flow to the channels can be changed, by altering the shape of the gas distributor. The shape of the distributor was optimized in this study, for an cell/interconnect structure with square channels, in the article "Optimization of a new flow design for solid oxide cells using computational fluid dynamics modelling" [111]. The article is enclosed in the appendix for convenience, see Appendix D.1.

In the article, the flow index of uniformity was defined as:

$$F_u = \frac{N \min(u_1 \ldots u_N)}{\sum_{i=1}^{N} u_i} \tag{4.1}$$

where N is the number of channels and u is the velocity in the channel. For a perfectly uniform flow, the flow uniformity index will be 1, and it will be less than 1 for a non-perfect uniform flow.

Assuming that each channel received the same current density and has the same temperature, it was found that the overall allowed conversion could be calculated from the flow index and the maximum allowed conversion (based on the Boudouard equilibrium) by:

$$X_{overall} = X_{max} F_u \tag{4.2}$$

X_{max} is calculated from the Boudouard equilibrium constant based on the temperature in the stack. From the equation, it can be seen that poor flow uniformity is directly related to the allowed overall conversion in the cell. In the article, it was found that the flow could be improved and a flow index of 0.978 could be obtained.

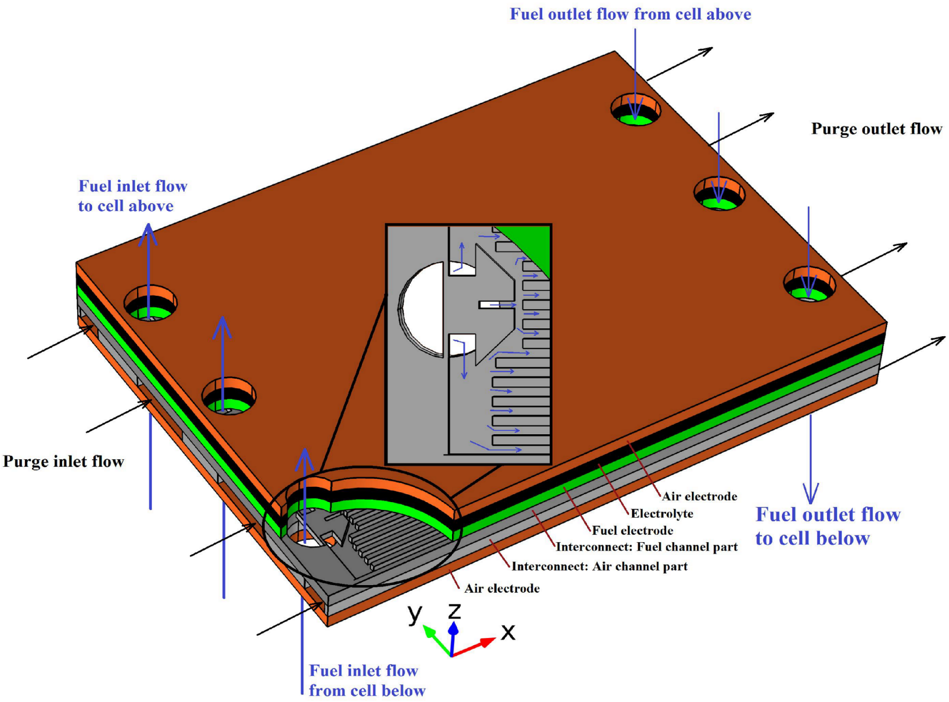

Figure 4.2: Sketch of the cell geometry. The insert shows the gas distributor and the parallel channels. From [111]

The design of the channels used by Haldor Topsoe A/S is slightly different (the actual design is confidential), than the presented channels in the article, whereas the design of the gas distributor is the same as in the article (patented in [112]). The procedure as described in the article [111] (see Appendix D.1) was applied to Haldor Topsoe A/S's design and an improvement of the flow index from 0.88 to 0.92 was calculated (based on a internal develop model, similar to the one presented in the article). The improvement was implemented in the production and are being tested by Haldor Topsoe A/S. The main reason why higher flow index values could not be obtained for Haldor Topsoe A/S's design, is the design of the channels and the location of inlet and outlet holes. In general, the flow uniformity increase, when the pressure drop in the channels, compared to the total pressure drop of the cell increase. This can e.g. be obtained be decreasing the cross-section of the channels.

The new flow design for Haldor Topsoe A/S's cell was implemented in the in-house 3d stack by Haldor Topsoe A/S (instead of using Eq. (4.2), with its limitations, due to the made assumptions). With the implementation of the new flow design, the gas composition and temperature in the cell was calculated, which allowed for the calculation of the Boudouard margin. Fig. 4.3 shows the Boudouard margin with respect to the old and new flow design. From the figure, it can be seen that the fuel utilization at which the Boudouard margin becomes negative is increased from 22 % with the old design to 32 % with the new design.

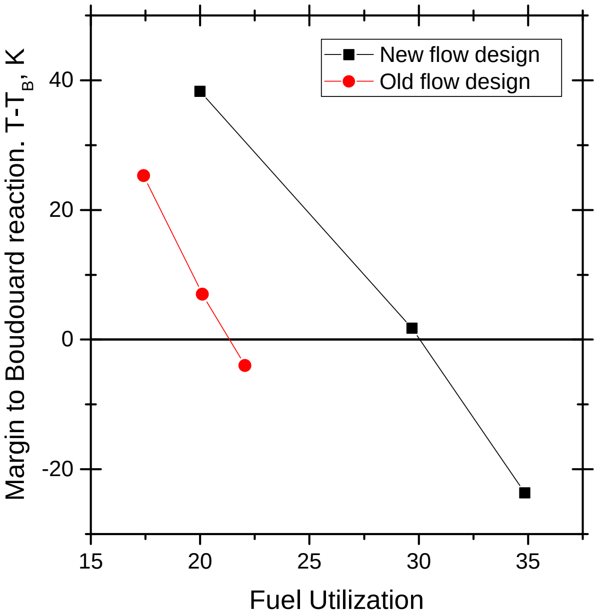

Figure 4.3: Boudouard margin as function of the fuel utilization for both the old and new flow design. Parameters: $T = 750\,°\mathrm{C}$, $\vec{i}_t = 4588\,\mathrm{A\,m^{-2}}$ and $\dot{F}_{air} = 0.5\mathrm{NL\,min^{-1}\,cell^{-1}}$.

4.4 Conclusion

It was found that poor flow distribution in the cells lead to local areas with high levels of CO and consequently carbon formation and delamination. A parameter study showed that only low levels (<22 %) of *FU* could be used with the current flow design if carbon deposition should be avoided. With rigorous CFD modeling, the flow was optimized for a model structure (published) and for Haldor Topsoe A/S's design. The flow optimization showed a clear improvement in the possible conversion of CO_2 in Haldor Topsoe A/S's flow design. However, the flow is not nearly uniform since the flow index value is only 0.92. This shows that the flow uniformity can still be improved, which would allow for an even higher conversion. It is recommended that Haldor Topsoe A/S continues to improve the flow design, if necessary by more radical design changes.

CHAPTER 5

Measurement of effective diffusion

In this chapter the effective diffusion of gas species through the fuel electrode and fuel electrode support is measured using a Wicke-Kallenbach setup. In the literature, several different models for diffusion in porous media has been used in connection with Wicke-Kallenbach diffusion cells and SOECs. Therefore in the first part of the chapter the theory behind diffusion, different diffusion models for porous media, and the choice of diffusion model for the calculation of effective diffusion parameters in this work will be described. In the second part the experimental Wicke-Kallenbach setup is described in detail. The third section describes the modeling of the Wicke-Kallenbach diffusion cell, which will be used to fit the effective diffusion parameters and the fourth section describes the characterization of the investigated samples. The fifth section describes the results of the measurement and modeling.

Two types of samples were obtained from Haldor Topsoe A/S: A sample type with only the fuel electrode support layer and a sample type with both the fuel electrode support layer and the fuel electrode. It was not possible to obtain a sample type with only the fuel electrode. The reason for this is due to the manufacturing process, in which the fuel electrode support is first produced and the fuel electrode is subsequently added. The samples with only the fuel electrode support will be designated “ES” in the following, the samples with both the fuel electrode and the fuel electrode support will be designated “E+ES” and the electrode itself will be designated “E”.

5.1 Introduction to diffusion

Diffusion is the spontaneously process in which species are transported from regions with high concentrations to regions with low concentration, i.e. the species are transported down a concentration gradient. In porous media the diffusion can be divided into four types: Bulk diffusion, Knudsen diffusion, viscous flow and surface diffusion.

Bulk diffusion describes the diffusion limited by gas-gas collisions and is mathematically described with Fick’s law:

$$\vec{N}_i^d = -D \nabla C_i \tag{5.1}$$

where $\vec{N}_i^d$ is the diffusion flux, D is the diffusion coefficient and ∇C_i is the concentration gradient.

For a binary gas mixture the diffusion flux can be described by Eq. (5.2) where $D_{i,j}$ is the binary diffusion flux, defined assuming no pressure gradient and no net gas flow. The calculation of the binary diffusion coefficient is described in the next subsection.

$$\vec{N}_i^d = -D_{i,j}\nabla C_i \tag{5.2}$$

With Graham's Law (Eq. (5.3)) the diffusion flux for the second gas species in a binary gas mixture can be calculated:

$$\vec{N}_i^d = \sqrt{\frac{M_j}{M_i}}\vec{N}_j^d \tag{5.3}$$

Where M is the molar mass of species i and j, respectively.

Knudsen diffusion describes the diffusion limited by gas-wall collisions and can be expressed as:

$$\vec{N}_i^K = -D_{K,i}\nabla C_i \tag{5.4}$$

The Knudsen diffusion coefficient, $D_{K,i}$, can be derived from kinetic theory:

$$D_{K,i} = \frac{2\bar{r}_{pore}}{3}\sqrt{\frac{8RT}{\pi M_i}} \tag{5.5}$$

where $\bar{r}_{pore}$ is the average pore radius, R is the gas constant and T is temperature.

Viscous gas flux describes the transport of species due to a pressure gradient:

$$\vec{N}_i^{vics} = -\frac{X_i P\kappa}{RT\mu}\nabla P \tag{5.6}$$

where X is the mole fraction of i and κ is the permeability

Surface diffusion describe the diffusion of species on the surface of the porous media. The surface diffusion is often neglected in diffusion modeling of SOC's [113] and this will also be the case in this thesis.

5.1.1 Calculation of Binary diffusion coefficient

The binary diffusion coefficient can be calculated with different theoretical and empirical correlations or experimental measurements can be used. In SOC modeling, the Chapman-Enskog theory and Fuller-Schettler-Giddings (FSG) model has been widely used [20]. The Chapman-Enskog theory is based on a rigorous solution of the Boltzmann equation for particle clouds from the kinetic theory. Based on the Chapman-Enskog theory, the binary diffusion coefficient can be approximated as:

$$D_{i,j} \approx 1.858 \frac{\sqrt{T^3 \left(\frac{1}{M_i} + \frac{1}{M_j}\right)}}{P \sigma_{i,j}^2 \Omega_D} \tag{5.7}$$

where $\sigma_{i,j}$ is the average collision diameter calculated by Eq. (5.8) in angstroms and Ω_D is the dimensionless collision intergral in the "Lennard-Jones (12-6) potential model" given by Eq. (5.9) [114].

$$\sigma_{i,j} = \frac{\sigma_i + \sigma_j}{2} \tag{5.8}$$

$$\Omega_D = \frac{1.06036}{T^{*0.15610}} + \frac{0.193}{\exp(0.47635T^*)} + \frac{1.03587}{\exp(1.52996T^*)} + \frac{1.76474}{\exp(3.89411T^*)} \tag{5.9}$$

$T^* = k_B T/e_{i,j}$ where k_B is Boltzmann constant and $e_{i,j} = \sqrt{e_i e_j}$, where e_i and e_j is the characteristic Lennard-Jones energy of species i and j, respectively. The Lennard-Jones energies, e_i, and the average collision diameters, $\sigma_{i,j}$, can be found in the literature [115].

The FSG model is based on the Chapman-Enskog approximation, Eq. (5.7). However, the Lennard-Jones characteristics lengths are replaced with lengths calculated from an empirical molar diffusion volume, $\sum v$. The diffusion volume is a constant property of a given gas and values for the diffusion volumes was found by least square estimates from known experimental values of $D_{i,j}$. The empirical correlation for the binary diffusion coefficient in the FSG model for non-polar gases at low pressure is given as [116]:

$$D_{i,j} \approx 0.001 \frac{T^{1.75} \left(\frac{1}{M_i} + \frac{1}{M_j}\right)^{0.5}}{P \left(\left(\sum v\right)_i^{1/3} \left(\sum v\right)_j^{1/3} \right)^2 \Omega_D} \tag{5.10}$$

where the molar diffusion volumes, $\left(\sum v\right)_i$ for relevant species in this thesis are given in Table 5.1.

Table 5.1: Molar diffusion volumes,$\left(\sum v\right)_i$ for the FSG model [116]

Species	Value
CO	18.9
CO_2	26.9
H_2	7.07
H_2O	12.7
N_2	17.9
O_2	16.6
Air	20.1

For the species involved in SOCs, Todd and Young [117] found that the FSG method has the lowest mean deviation (4.47 %) from experimental data and was accurate over a temperature range of 273 to >1000 K. It should be noted that the experimental data is sparse, especially at high temperatures. Based on [117], the FSG model is used to calculated the binary diffusion coefficient in this thesis, except for the Wicke-Kallenbach setup. Here a more accurate value can be calculated from Eq. (5.11), based on experimental measurements in the temperature range 194.7 K to 373 K, with a stated deviation of ±1% [118]. From Eq. (5.11) the binary diffusion constant at the temperature used in the experimental work (T=295 K) are $0.213 \times 10^{-5}\,\mathrm{m^2\,s^{-1}}$

$$D_{CO,N_2} = 10^{-4.8606+1.6959\cdot\log_{10}(T)} \tag{5.11}$$

where T is the temperature in K and the binary diffusion coefficient is given in $\mathrm{cm^2\,s^{-1}}$.

5.1.2 Diffusion models for porous media

Several different theories for diffusion has been proposed for gaseous diffusion in porous solids. In this thesis the following five models are considered:

- Cross-linked pore model
- Rothfeld-Scott model
- Dusty gas model (DGM)
- Binary friction model (BFM)
- Cylindrical pore interpolation model (CPIM)

Common for the porous media diffusion models are the inclusion of the ordinary bulk diffusion and Knudsen diffusion. For the DGM, BFM and CPIM the viscous flow is also included. All five models are used in the experimental investigation of the effective diffusion, however special focus is placed on the DGM. The reason for this is that the DGM model has been widely used for SOCs [61, 63, 119–121], and the fitted values from the Wicke-Kallenbach setup can thus be compared to literature values. The Cross-linked pore model and Rothfeld-Scott model are only derived for binary and isobaric conditions. This is sufficient for the Wicke-Kallenbach setup, but not for modeling SOC's, since the diffusion model for SOCs needs to be able to model a multicomponent mixture at non-isobaric conditions. The formal derivation of the DGM has been criticized [122, 123]. Instead the BFM [122] and the CPIM [123] have been proposed. Studies have shown that there is no significant difference between these three models [124, 125]. Since there is no significant different between the calculated fluxes between the models, only the DGM is used in this thesis.

Common for the five models is the use of a tortuosity factor to correct for the fact that the solid phase in the porous electrode causes the transport paths for gas to deviate from straight lines. The deviation from straight pores is called "tortuosity", τ, and is defined as $\tau = L_{eff}/L_0$ (see Fig. 5.1). The tortousity factor is the square of the tortuosity. The definition of τ implies that it can be calculated from rigorous measurement of the porous structure. However, since it is not trivial to obtain τ, the tortuosity factor is often used as a fitting parameter in diffusion models. Because of this, the fitted values for τ^2 will also contain the effect of deviation from the ideal cylinder geometry and pores with dead ends [126] as well as the diffusion models insufficiency in describing the actual diffusion and experimental errors. Based on the Cross-linked pore model, a theoretical value of $\tau^2 = 3$ was derived for an ideal isotropic pore structure [126]. In the literature

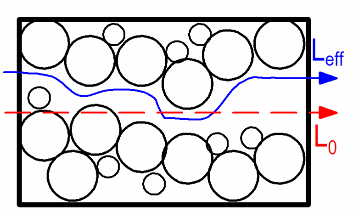

Figure 5.1: Illustration of tortuosity defined as $\tau = L_{eff}/L_0$. Because of the porous media the gas has to move a longer distance, L_{eff}, than the shortest distance, L_0.

the term "tortuosity" and "tortuosity factor" is sometimes intermingled [125, 127, 128] resulting in τ being defined as the "tortuosity" in some studies and as the "tortuosity factor" in others. As described above, τ is defined as the "tortuosity" in this thesis and τ^2 as the "tortuosity factor".

5.1.3 Cross-linked pore model

In the Cross-linked pore model (developed by Johnson and Stewart, also referred to as the Johnson and Stewart model [129]) the porous medium is substituted with cylindrical capillaries with radii following the pore volume distribution function, $v'(r_{pore})$. With the Cross-linked pore model, the total diffusion flux is given by [126, 129, 130]:

$$N_i^d = -\frac{c_t \rho_{app}}{\tau^2} \left[\int_0^{\inf} \left(\frac{1 - X_i \alpha}{D_{ij}} + \frac{1}{D_{K,i}} \right)^{-1} v'(r_{pore}) dr_{pore} \right] \frac{dX_i}{dx_L} \tag{5.12}$$

where N_i^d is the diffusion flux, c_t is the total gas concentration, ρ_{app} is the apparent particle density (which can be found from the porosity and true density: (1-ϵ)$\cdot\rho_{true}$), X_i is the mole fraction of i, v' is the pore volume distribution density for the pore structure, r_{pore}, is the radii of the pores and x_L is the diffusion length. α is defined as:

$$\alpha = 1 - \sqrt{\frac{M_i}{M_j}} \tag{5.13}$$

For steady-state conditions, integration of equation Eq. (5.12) from x_L=0 to x_L=L yields [130]:

$$N_i^d = -\frac{c_t \rho_{app} D_{ij}}{\alpha \tau^2 L} \int_0^{\inf} \ln \left[\frac{1 - X_{i,L}\alpha + D_{ij}/D_{K,i}}{1 - X_{i,0}\alpha + D_{ij}/D_{K,i}} \right] v' dr_{pore} \tag{5.14}$$

The model requires that the pore volume distribution function, $v'(r_{pore})$ is obtained, e.g. via Hg-porosimetry.

5.1.4 Rothfeld-Scott

In the Rothfeld-Scott model the diffusion flux in the model is given by [129]. :

$$N_i^d = -D_{ij,k}^{eff} \left(\frac{dC_i}{dx_L} \right) + \delta_i X_i N_t \tag{5.15}$$

where N_t is the sum of diffusion fluxes, and $D_{ij,k}$ and δ_i are given as:

$$D_{ij,k}^{eff} = \frac{\epsilon}{\tau^2} D_{ij,k} = \frac{\epsilon}{\tau^2} \left(\frac{1}{\frac{1}{D_{ij}} + \frac{1}{D_{K,i}}} \right) \tag{5.16}$$

$$\delta_i^{-1} = 1 + \frac{D_{ij}}{D_{K,i}} \tag{5.17}$$

Integration of Eq. (5.15) from $x_L = 0$ to $x_L = L$ yields [129]:

$$N_i^d = \frac{D_{ij,k}^{eff} C_t}{L\alpha} \ln \left[\frac{1 - X_{i,L}\alpha + D_{ij}/D_{K,i}}{1 - X_{i,0}\alpha + D_{ij}/D_{K,i}} \right] \tag{5.18}$$

where $X_{i,0}$ and $X_{i,L}$ are the mole fraction of i at $x_L = 0$ and $x_L = L$, respectively.

5.1.5 Dusty gas model

The dusty gas model (DGM) view the porous media structure as a $(n+1)^{th}$ component. The component differs from the gas components, since it is stagnant with respect to the stationary coordinates. The dusty gas model is comprehensively treated by Mason and Malinauskas [131] and Jackson [132]. In the dusty gas model, the Knudsen diffusion coefficient appears as a binary diffusion coefficient with the solid as one component. In molar units the DGM has the form:

$$\sum_{j \neq i}^{n} \frac{X_j N_i^d - X_i N_j^d}{D_{ij}^{eff}} + \frac{N_i}{D_{K,i}^{eff}} = -\frac{P}{RT} \nabla X_i - \frac{X_i}{RT} \left(1 + \frac{\kappa P}{\mu D_{K,i}^{eff}} \right) \nabla P \tag{5.19}$$

where P is the pressure, R the universal gas constant, T the temperature, κ the permeability coefficient, μ the viscosity, D_{ij}^{eff} and $D_{K,i}^{eff}$ are the effective binary diffusion coefficient and effective Knudsen diffusion coefficient, calculated by:

$$D_{ij}^{eff} = \frac{\epsilon}{\tau^2} D_{ij} \tag{5.20}$$

$$D_{K,i}^{eff} = \frac{\epsilon}{\tau^2} D_{K,i} \tag{5.21}$$

5.2 Experimental measurement of diffusion

The effective diffusion can be measured with diffusion cells based on the concept developed by Wicke and Kallenbach in 1941 [133]. This diffusion cell has a long standing history and is still frequently used [134–138]. The diffusion cell consists of two compartments separated by the sample. Gas A flows through one of the compartments and gas B through the other compartment. The pressure in the two compartments are adjusted so that the pressure difference is minimized (very close to 0), thereby ensuring that a pressure driven flow through the sample can be neglected. The low pressure difference can e.g. be ensured if both compartments are opened to atmosphere or, as in this case, to a common analyzer and ventilation. By measuring the flow rates of gas A and B, and the gas concentrations of the inlet and outlet flows, one can calculate the molar diffusion fluxes, N_i^d and N_j^d, related to the cross-section of the sample. Combined with knowledge of the porosity and pore distribution (e.g. Hg-porosimetry) the measurement of the effective diffusion can be used to calculate the tortuosity.

A newer diffusion cell is the Graham-diffusion cell (GDC) [139]. In a Graham-diffusion cell two compartments are again separated by the sample and flush with gas A and B, respectively. After steady-state has been reached, the gas flow to one of the compartment are closed and a connection from that compartment to a burette (or bubble flowmeter [140]) is opened. The flow to the opposite compartment remains open. From Graham's law it can be seen that the molar diffusion fluxes are not equal when the molar mass of species i and j are different.

$$N_i^d / N_j^d = -\sqrt{M_j / M_i} \tag{5.22}$$

This means that the number of moles in the closed compartment will change and this can be measured as a volumetric change by the burette/bubble flowmeter. From this volumetric diffusion flux the molar flux, N^d, can be calculated.

Soukup et al. [140] compared the WK and GDC and found that the differences in diffusion fluxes from both methods did not exceed 5 % and was below the experimental error for a series of porous samples (with pore radii from 78 nm to 10 µm). Since a WK setup was available, and the difference between the two diffusion cells are low, the WK setup was used.

5.2.1 Experimental setup

A Wicke-Kallenbach test setup was used to measure the effective diffusion, see Fig. 5.2. Gas was supplied to each compartment via a three-way valve and a mass flow controller. After the diffusion cell, outlet gas from each compartment flow through a needle valve to a gas analyzer. The needle valve was used to adjust the pressure difference between the two compartments. Before and after the diffusion cell, the pressure difference was measured with digital differential pressure gauges. A fine resolution gauge (Delta OHM HD 2114.2, measurement range 0 – 2 kPa, resolution 0.1 Pa accuracy ± 0.3% of fuel scala (f.s.)) was used to adjust the pressure difference for the effective diffusion measurements, while a coarse resolution gauge (Cole-Parmer 68370-02, measurement range 0 – 50 kPa, resolution 10 Pa, accuracy ± 0.1% of f.s.) was used to adjust the pressure during permeability measurements, see Section 5.5.6. When the pressure difference had been adjusted with pure N_2 on both sides, the three-way valve on one side was used to switch to the test gas (1% CO in N_2). Due to the similarities between N_2 and the test gas, further adjustment of the pressure difference was not necessary. The outlet gas was analyzer with an ABB AO2000 equipped with an infrared photometer (Uras26, measurement range 0-1000 ppm CO, resolution 1 ppm, accuracy ± 0.5% of f.s.)

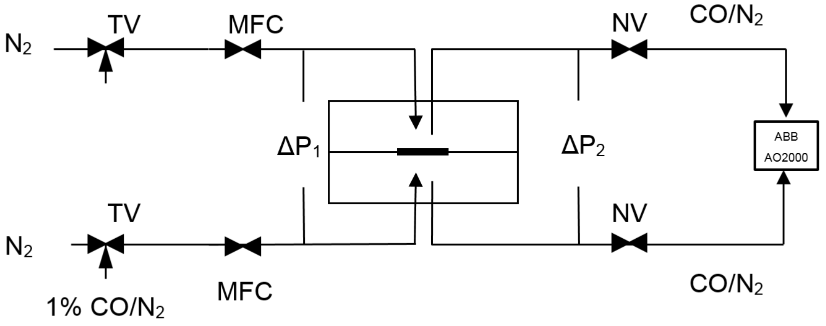

Figure 5.2: Schematic illustration of the experimental setup. Details of the Wicke-Kallenbach cell in figure Fig. 5.3. Symbols: TV: Three-way valve, NV: Needle valve, linear response Cv=0 to 1.8. MFC: Mass flow controller. ΔP_1: Digital differential pressure gauge, 0.1Pa resolution (Delta-ohm HD 2114.2). ΔP_1: Digital differential pressure gauge, 0.1 mbar resolution (Cole-Parmer 68370.02). ABB AO2000: Gas analyzer. Modified from an internal document

Figure 5.3 and Fig. 5.4 shows the details of the diffusion cell. The samples with a diameter of 25 mm were laser cut from the Ni/YSZ material and placed between silicon seals. Gas is supplied to the two compartments via 1/4" inch tubes placed inside a 1/2" inch tube. The gas flows over the sample and out via the 1/2" inch tube. The diffusion cell is held together by bolts, shown as arrows on Fig. 5.3.

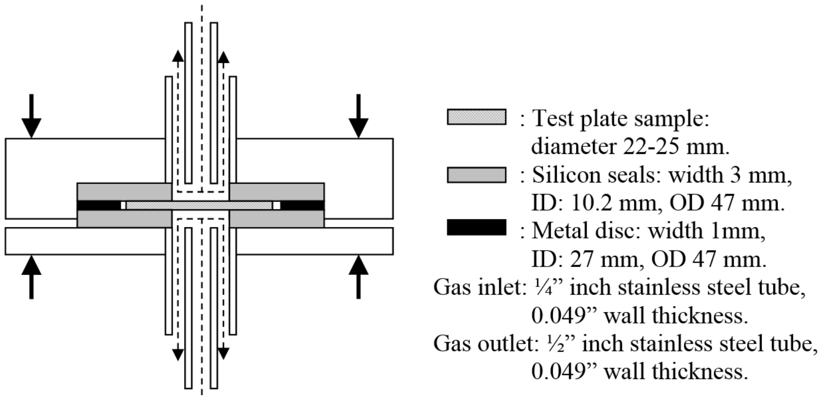

Figure 5.3: Details of the Wicke-Kallenbach cell used in the experimental setup. Picture from an internal document.

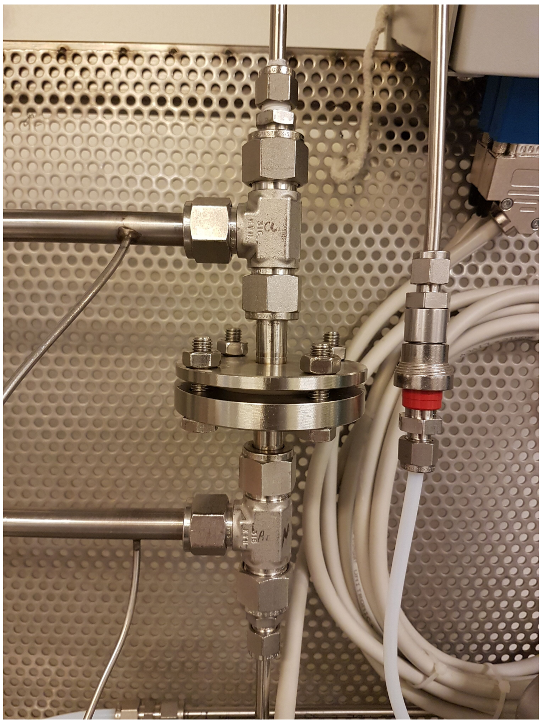

Figure 5.4: Picture of the Wicke-Kallenbach cell used in the experimental setup

5.2.2 Pressure in the Wicke-Kallenbach diffusion cell

The pressure in each compartment must be (close to) identical in order to avoid a pressure driven flow. For porous samples with radii above 7 µm significant deviations of diffusion fluxes has been observed for pressure differences as low as 7 Pa [141]. The pore radii for the tested samples were well below 7 µm (see Section 5.4), so a larger acceptable pressure difference range is expected. Later, in the permeability experiment (Section 5.5.6), it can be seen that pressure differences in the 1000 Pa order of magnitude are necessary to influence the diffusion fluxes. Since the pressure difference is adjusted with a precision of ±6 Pa, the pressure difference will not affect the measurement of the effective diffusion.

The Wicke-Kallenbach diffusion cell is run at atmospheric pressure (P_{atm} was measured to be 1019.9 hPa). However, when the flow rate to the Wicke-Kallenbach diffusion cell is increased, the pressure drop in the downstream tubes will also increase. To overcome this increased pressure drop, the absolute pressure in the diffusion cell is also increased. In order to evaluate if this can be neglected, the absolute pressure was estimated in the following experiment:

A sample was placed in the diffusion cell. The needle valve after chamber A was fully opened and the flow rate to chamber A was set to $0\,\text{mL}\,\text{min}^{-1}$. The needle valve after chamber B was also opened and the flow rate stepwise increased from $150\,\text{mL}\,\text{min}^{-1}$ to $900\,\text{mL}\,\text{min}^{-1}$ and the pressure difference was recorded. Since chamber A is open and the low permeability of the sample ensures a very low flow from chamber B to A through the sample, the absolute pressure in chamber A will be very close to P_{atm}. After the stepwise increase in flow rate to chamber B, the conditions were changed so that the flow was applied to chamber A while a zero flow was applied to chamber B.

Fig. 5.5 shows the measured pressure difference at the different applied flow rates. The pressure difference increase linearly with the flow rate. This is also expected, since the largest Reynolds number in the tubes from the diffusion cell is calculated with Eq. (5.23) to be 619, which is in the laminar flow regime (since it is below 2300 [142]), and the pressure drop can be calculated by the Darcy–Weisbach equation (Eq. (5.24) [142]), where a linear relationship between the pressure drop and the flow rate can be seen.

$$Re = \frac{\rho \bar{u} d_{tube}}{\mu} = 619 \tag{5.23}$$

$$\Delta P = \frac{128 \mu F L}{\pi d_{tube}^4} \tag{5.24}$$

where ρ is the density, $\bar{u}$ is the average velocity, d_{tube} is the diameter of the tube, μ is the viscosity, F is the volumetric flow rate and L is the length of the tube. Since the flow rate to both chambers in the measurement of the effective diffusion and permeability is equal, the pressure increase in each chamber will be identical. The absolute pressure of the diffusion cell can thus be calculated by Eq. (5.25). At a flow rate of $1400\,\text{ml}\,\text{min}^{-1}$, the maximum flow rate used in the experiments, the increase in pressure can be estimated to be 18.6 mbar. The increase in P_{cell} corresponds to an increase in the total gas concentration, C_t, of a factor $(P_{\text{cell}} + P_{\text{atm}})/P_{\text{atm}}$. The impact of the increased gas concentration on the diffusion flux, N^d, can directly be seen in the Cross-linked pore model (Eq. (5.14)) and Rothfeld-Scott model (Eq. (5.18)). Since τ^2 is used to fit the measured data with the equations, this will correspond to a change in the fitted τ^2 by a factor of $(P_{\text{cell}} + P_{\text{atm}})/P_{\text{atm}}$. At a flow rate of $1400\,\text{ml}\,\text{min}^{-1}$ the factor is $18.6\,\text{mbar}/P_{\text{atm}} \approx 1.018$. For the other diffusion models the correlation between τ^2 and the pressure is less clear, but will probably be in the same range. Thus in order to increase the accuracy of the

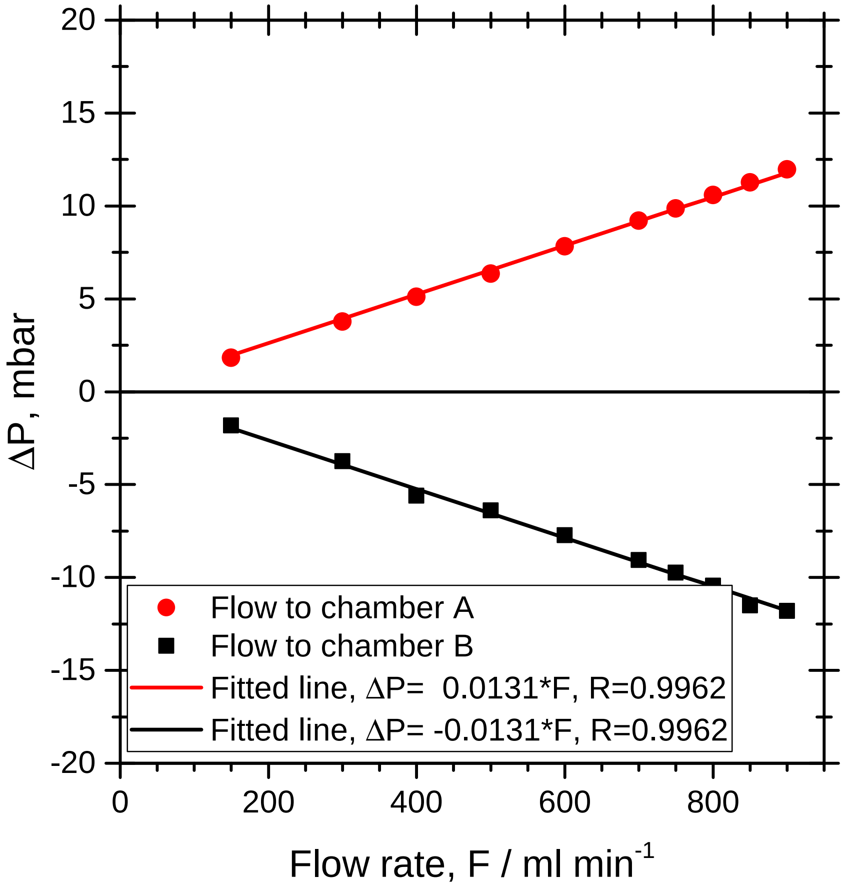

Figure 5.5: Pressure in the diffusion cell at different flow rates with linear fitted lines

estimations of τ^2, the experimental fit must include the effect of the varying pressure in the diffusion cell, P_{cell}.

$$P_{\text{cell}} = 0.0133 \cdot F + P_{\text{atm}} \tag{5.25}$$

5.3 Modeling of the experimental setup

The Wicke-Kallenbach setup was modeled with both a 1d model and a 2d axisymmetric model using COMSOL in order to fit the tortuosity, τ^2, and permeability, κ. This section will describe the two models and the solution procedure.

5.3.1 1d model

Figure 5.6 shows a schematic model of the Wicke-Kallenbach setup. In the 1d model, each chamber is assumed to be well mixed, transfer limitations between the sample chambers and the sample are neglected and only diffusion in the x-direction is modeled.

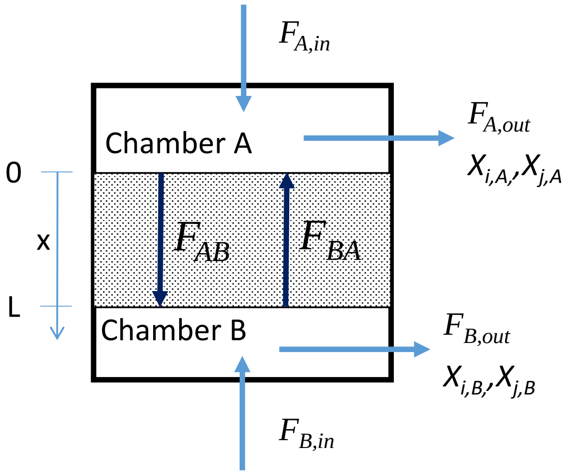

Figure 5.6: Schematic illustration of the 1d model of the Wicke-Kallenbach cell. X is the mole fraction of species i or j from chamber A or B. $F_{A,in}$ and $F_{B,in}$ is the flow to chamber A and B, respectively, F_{AB} and F_{BA} is the flow from chamber A to B and B to A, respectively, and $F_{A,out}$ and $F_{B,out}$ is the flow out the diffusion cell from chamber A and B, respectively

The boundary conditions in the model using the Cross-linked pore model and the Rothfeld-Scott model are:

$$X_{CO}|_{x_L=0} = X_{CO,A} \tag{5.26}$$

$$X_{CO}|_{x_L=L} = X_{CO,B} \tag{5.27}$$

where $X_{CO,A}$ is equal to the measured CO in the analyzer and $X_{CO,B}$ can be calculated from the known inlet concentration of the test gas, $X_{CO,B,in}$, (1 % CO in N_2) and the CO transferred from chamber B to A:

$$X_{CO,B} = \frac{X_{CO,B,in}F_{B,in} - F_{BA}}{F_{B,out}} \tag{5.28}$$

where F_{BA} is the volumetric flow from chamber B to A, and $F_{B,in}$ and $F_{B,out}$ is the volumetric flow entering and leaving chamber B, respectively. With the applied gasses (Pure N_2 to chamber A and 1 % CO in N_2 to chamber B), the flow rate from chamber B to A, F_{BA}, will only contain pure CO. F_{AB} will contain N_2 from chamber A to chamber B.

The flow rates $F_{B,in}$, F_{BA}, and $F_{B,out}$ can be calculated from mass and mole balances of the system:

$$F_{BA} = \frac{F_{A,in}}{\frac{1}{X_{CO,A,mea}} + 1 - \sqrt{\frac{M_{\mathrm{N2}}}{M_{\mathrm{CO}}}}} \tag{5.29}$$

$$F_{AB} = \sqrt{\left(\frac{M_{CO}}{M_{\mathrm{N}_2}}\right)} F_{BA} \tag{5.30}$$

$$F_{B,out} = F_{B,in} - F_{BA} + F_{AB} \tag{5.31}$$

where $X_{CO,A,mea}$ is the measured value of CO measured in the gas analyzer. For detailed derivation of these equations, see Appendix A. The total concentration was calculated with the ideal gas law with the pressure of the diffusion cell P_{cell}:

$$C_t = \frac{P_{\mathrm{cell}}}{RT} \tag{5.32}$$

In the Cross-linked pore model the integral is numerically calculated with the commonly known trapezoid method of integration. The diffusion flux is then calculated by multiplying the integration sum with $-C_t \rho_{app} D_{i,j}/(\alpha\tau^2 L)$ (see Eq. (5.14). In the Rothfeld-Scott model, the diffusion flux can be directly calculated from Eq. (5.18).

For the DGM, the boundary conditions are:

$$X_C O|_{x=0} = X_{CO,A} \tag{5.33}$$

$$X_C O|_{x=L} = X_{CO,B} \tag{5.34}$$

$$P|_{x=L} = P_{\mathrm{cell}} \tag{5.35}$$

In the Cross-linked pore model and the Rothfeld-Scott model, the pressure is assumed to be constant, while in the DGM model the pressure can vary through the sample. However, since M_{N_2} and M_{CO} are almost identical, the pressure gradient through the sample will be very close to zero. So, even though the pressure is strictly only fixed at x=L to the measured P_{cell}, the pressure in the sample will also be (extremely close to) P_{cell} for the DGM model and does not influence the results.

5.3.2 2d axisymmetric model

The 2d axisymmetric model consist of modeling the flow and mass transfer in the two chambers and the sample. A 2d axisymmetric model was chosen because the Wicke-Kallenbach setup is symmetric around the z-axis. This means that fewer elements are necessary, compared to a full 3d model. Figure 5.7 shows the geometry of the 2d axisymmetric model. On the inlet boundary to each chamber (labeled 1 and 2 on Fig. 5.7) the mole fractions of the gas and the flow rate is specified as boundary conditions:

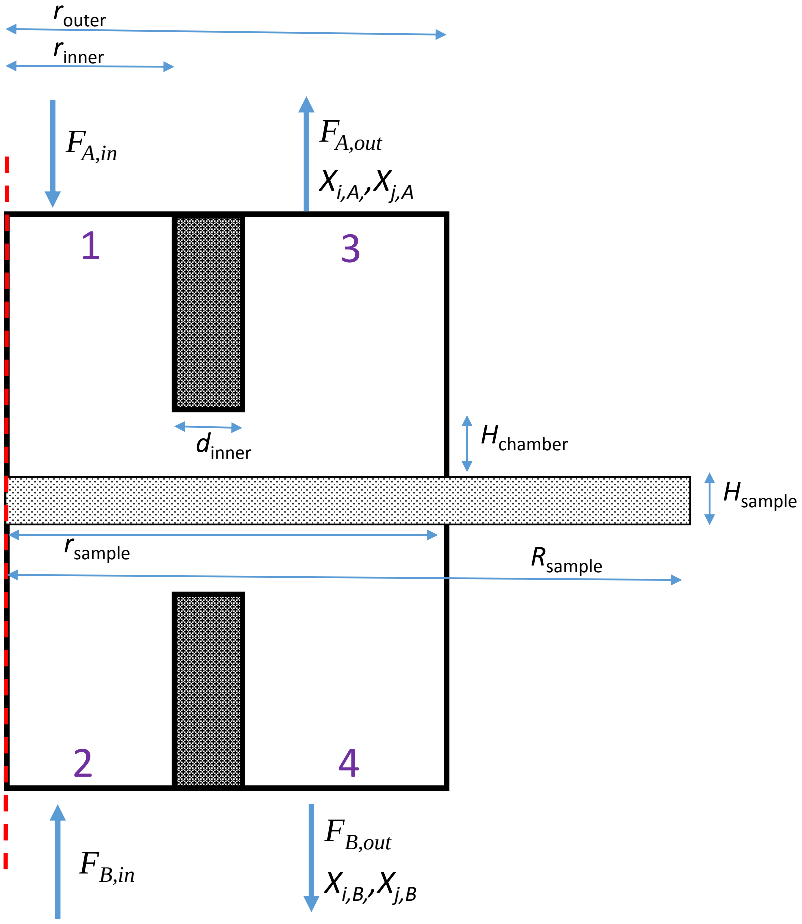

Figure 5.7: 2d axisymmetric model of the Wicke-Kallenbach cell. The gas to chamber A is entering at boundary 1 (inner tube) and existing at boundary 3. Similar the flow to chamber B is entering at boundary 2 and existing at boundary 4. The dark gray areas are the thickness of the inner tube and the light gray area is the sample. With the test gasses used in the experimental work, the species i and j are CO and N_2, respectively.

$$X_{\mathrm{CO}}|_1 = X_{\mathrm{CO},A,in} = 0 \tag{5.36}$$

$$X_{\mathrm{N}_2}|_1 = 1 - X_{\mathrm{CO}}|_1 \tag{5.37}$$

$$X_{\mathrm{CO}}|_2 = X_{\mathrm{CO},B,in} \tag{5.38}$$

$$X_{\mathrm{N}_2}|_2 = 1 - X_{\mathrm{CO}}|_2 \tag{5.39}$$

$$F|_1 = F_{A,in} \tag{5.40}$$

$$F|_2 = F_{B,in} \tag{5.41}$$

where $F_{A,in}$ and $F_{B,in}$ is the volumetric flow rate of test gas A and B into chamber A and B, respectively. $X_{i,A,in}$ and $X_{i,B,in}$ is the mole fraction of gas species i in test gas A and B, respectively. The inlet flow was assumed to be laminar. This assumption can be justified by calculating the Reynolds number:

The mass flow controller is capable of delivering a maximal flow of 2000 ml/ min, thus the maximum Reynolds number of the inner tube is:

$$d_{i,t} = (0.25\,\text{inch} - 2 \cdot 0.049\,\text{inch}) \cdot 2.54\,\text{cm}\,\text{inch}^{-1} = 0.386\,\text{cm} \tag{5.42}$$

$$\bar{u} = \frac{F_{A,in}}{A_{tube}} = \frac{F_{A,in}}{\pi(d_{i,t}/2)^2} = \frac{2\,\text{dm}^3\text{min}^{-1}}{\pi(0.386\,\text{cm}/2)^2} = \tag{5.43}$$

$$Re = \frac{\rho \bar{u} d_{i,t}}{\mu} = 734 \tag{5.44}$$

Since Re<2100 a steady fully developed flow will be laminar [115]. The entry length for laminar flow, $L_{h,laminar}$, can be calculated to be [142]:

$$\frac{L_{h,laminar}}{d_{i,t}} \cong Re \Rightarrow L_{h,laminar} = 14\,\text{cm} \tag{5.45}$$

Since the length of the tubes to the diffusion cell is 16 and 20 cm, respectively, and Re is 734, the assumption of laminar inlet flow is valid.

The flow in the chambers is assumed steady and is modeled with the steady state form of the continuity equation and momentum equation:

$$\nabla(\rho\vec{u}) = 0 \tag{5.46}$$

$$\rho(\vec{u} \cdot \nabla)u = \nabla \cdot (-P\boldsymbol{I} + \boldsymbol{\tau_s}) \tag{5.47}$$

where u is the velocity vector, $\boldsymbol{I}$ is the unity tensor, and $\boldsymbol{\tau_s}$ is the viscous stress tensor. The viscosity and density was fixed at the values of N_2 at 298 K.

The transport of species in the chambers was calculated with Eq. (5.48):

$$\nabla\dot{N}_i^d + \rho(\vec{u} \cdot \nabla)w_i = 0 \tag{5.48}$$

where $\dot{N}_i^d$ is the diffusion flux in $\text{kg}\,\text{m}^{-2}\,\text{s}^{-1}$ and $\rho(\vec{u} \cdot \nabla)w_i$ is the transport of species due to convection (w_i is mass fraction). The DGM was implemented and used for calculation of the diffusion in the sample.

The mesh of the sample consisted of quadrilaterals with a height of $H_{sample}/10$ and a length of $r_{sample}/30$ in the section of the sample directly exposed to the gas (from $r = 0$ to $r = r_{sample}$). In the section of the sample not directly exposed to the gas ($r = r_{sample}$ to $r = R_{sample}$) the height remained $H_{sample}/10$, but the length was increased to $(R_{sample} - r_{sample})/10$. At the boundary between the sample part exposed to the gas and the sample part not exposed to the gas (from z=0 to z=H_{sample} at $r = r_{sample}$), the mesh was refined with boundary layers (40 layers, stretching factor 1.1) because diffusion in the r-direction is observed here, whereas the diffusion in the r-direction is basically zero in the rest of the sample.

The mesh in the two chambers consisted of triangular generated with a element size between 2.5×10^{-7} m and 7.16×10^{-6} m. The maximum size, h_{max}, of the triangulars was selected so that the element Peclet number was always below 1, since the Galerkin method (used in COMSOL) becomes unstable when Pe>1 [143]:

$$Pe = \frac{\|u_{max}\|\, h_{max}}{2D_{ij}} < 1 \Rightarrow h_{max} < 7.16 \times 10^{-6}\,\mathrm{m} \tag{5.49}$$

where u_{max} is the maximal flow velocity, which occurs in the inner tube. Since there is a laminar flow in the inner tube, the maximal velocity can be calculated by $u_{max} = 2\bar{u}$.

With the very low value for h_{max} the number of elements becomes well above 3×10^6. Instead of using such a fine mesh, stabilization techniques can be used. The stabilization techniques added were streamline diffusion and crosswind diffusion. The stabilization techniques reduce the need for a fine mesh, but introduces artificial diffusion which reduces the accuracy of the calculation. The details of the techniques are outside the scope of the thesis, and the reader is referred to [143, 144].

In order to verify that the stabilization techniques can be used without affecting the results, the outlet concentration were calculated with and without the stabilization techniques for a model with the following parameters: $H_{sample} = 300\,\mu\mathrm{m}$, $\epsilon = 0.35$, $\tau^2 = 5$, $\bar{r}_{pore} = 0.25\,\mu\mathrm{m}$, $X_{CO,0} = 0.01$, $P = 1\,\mathrm{atm}$ and $\Delta P = 0\,\mathrm{Pa}$*. Different flow rates were used: $F_{A,in} = F_{B,in} = (0.3, 1.0, 1.5, 2.0) \cdot \mathrm{dm^3 min^{-1}}$.

The results are summarized in Table 5.2. In the table the outlet concentration has been divided with the outlet concentration from the non-stabilized model, with a h_{max} calculated from Eq. (5.49). From the table it can be seen that a higher flow rate requires a finer mesh. An extra fine mesh ($h_{min} = 1.88 \times 10^{-6}\,\mathrm{m}$, $h_{max} = 1.6 \times 10^{-4}\,\mathrm{m}$) is sufficient to achieve solutions within 1 % difference from the non-stabilized model for flow range below $2\,\mathrm{dm^3 min^{-1}}$. The calculation time for the stabilized models were in the range of 30 s, whereas it was over 30 min for the non-stabilized models. Based on the above, the model equations were stabilized with streamline diffusion and crosswind diffusion, and an “extra fine” mesh was used.

5.4 Sample characterization

In order to estimate τ^2 and κ, it is necessary to known the thickness, porosity and average pore radius/pore distribution of the sample. The thickness of the samples were measured with a Scanning Electron Microscope (SEM - model TM3030 from Hitachi), see Fig. 5.8. The samples where measured at seven different locations and the average and standard deviation for each sample type was calculated, see Table 5.3.

Based on the measurements, the average thickness of the fuel electrode (E) was

---

[*] Since $\Delta P = 0\,\mathrm{Pa}$ the viscous flow in the DGM can be ignored

Table 5.2: Mesh effect on the stabilized model versus the non-stabilized model. Values in the table are outlet concentration from the stabilized model divided with outlet concentration from the non-stabilized model

Mesh	h_{max}	Flow rate, ml min^{-1}		
		300	1000	2000
Coarse	8.38×10^{-4} m	1.002	0.986	
Normal	5.63×10^{-4} m	1.001	0.997	
Fine	4.38×10^{-4} m	1.000	1.000	1.133
Finer	3.50×10^{-4} m	1.001	1.001	1.097
Extra fine	1.60×10^{-4} m	1.000	1.000	1.002

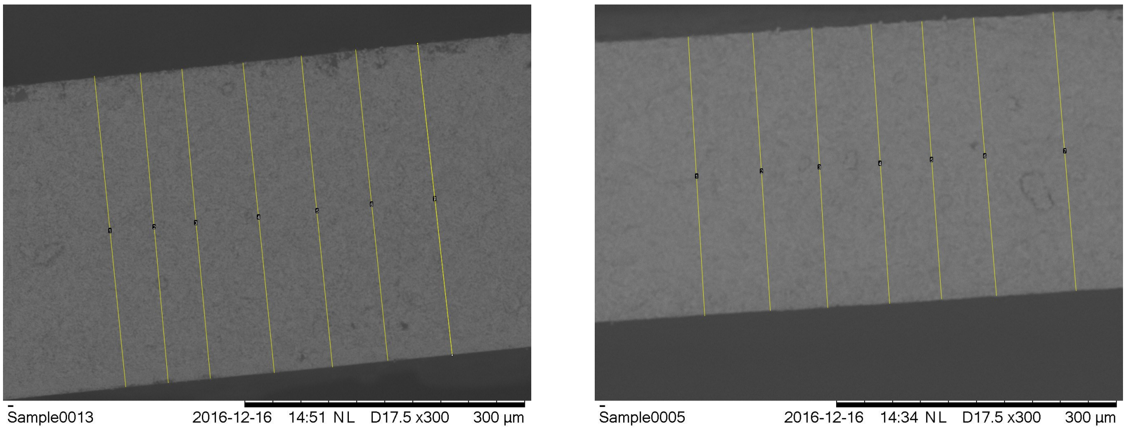

(a) Fuel electrode and fuel electrode support. **(b)** Fuel electrode support.

Figure 5.8: Example of SEM pictures used to measure the thickness of the samples. The thickness was measured with the program “ImageJ”, where the number of pixels per µm was calculated from the scale bar. Seven measurement for each sample was performed.

Table 5.3: Sample thickness measured with SEM

	ES	E+ES	E
mean	300.7	335.6	34.8
std	1.2	1.6	2.0

calculated by:

$$\bar{d}_E = \bar{d}_{E+ES} - \bar{d}_{ES} = 34.8\,\mu\mathrm{m} \tag{5.50}$$

And the standard deviation:

$$\sigma_E = \sqrt{\frac{\sigma_{E+ES}^2}{N_{E+ES}} - \frac{\sigma_{ES}^2}{N_{ES}}} = 2.0\,\mu\text{m} \tag{5.51}$$

where σ is the standard variation and N is the sample size.

The porosity and pore distribution were measured with Hg-porosimetry (using a Micromeritics Autopore IV 9520 and a contact angle of 140° at Haldor Topsoe A/S). Table 5.4 shows the measured porosity for the fuel electrode support (ES) and the fuel electrode support + fuel electrode (E+ES). Since the analysis required a sample mass greater than the samples used for the Wicke-Kallenbach setup, new samples were prepared from the same original cell as the Wicke-Kallenbach samples. From Table 5.4 it can be seen that the porosity appears to be slightly lower for E+ES samples, which can be explained by the presence of the electrode.

Based on the thickness of the layers, the porosity for E can be calculated:

$$\epsilon_E = \frac{\epsilon_{E+ES} d_{E+ES} - \epsilon_{ES} d_{ES}}{d_E} = 0.48\% \tag{5.52}$$

From SEM pictures, the very low porosity calculated for E could not be verified. Fig. 5.9 shows close-ups of the two side of a E+ES sample. From the pictures no clear difference in porosity can be seen. Therefore, a porosity of only 0.48 % for E does not seem likely.

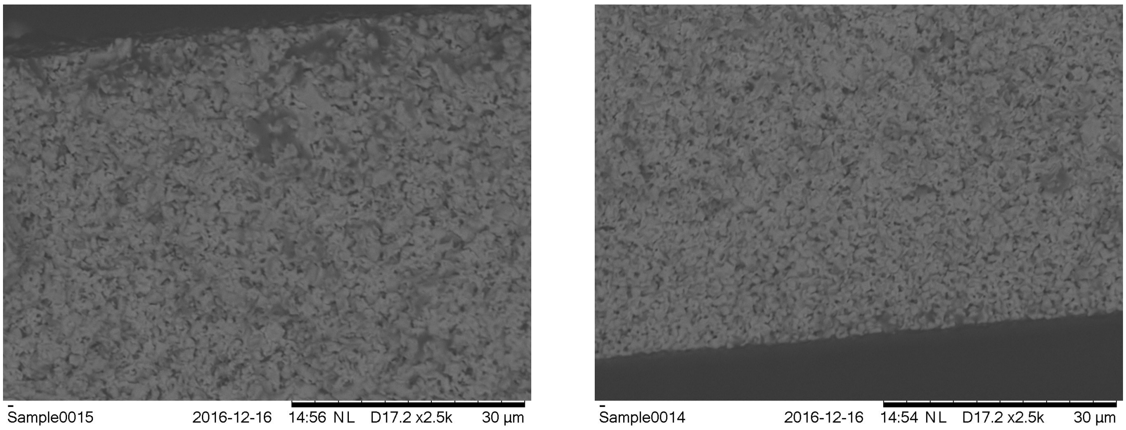

(a) Top **(b)** Bottom

Figure 5.9: SEM picture showing a close up of a sample with fuel electrode and fuel electrode support used to investigate the porosity. No clear difference in porosity can be seen from the pictures.

The relative standard deviation of the measurement method, stated by the laboratory at Haldor Topsoe A/S, is 3.8 %. Based on this, an unpaired t-test showed that the

H_0 hypothesis of equal means for the two sample types, could not be rejected[†]. Thus in the following, an average porosity of 30 % is used for both the fuel electrode and the fuel support. The pore size, $\bar{r}_{pore}$ for the fuel electrode + support is smaller than for the support alone (see Fig. 5.10). The reason for this can be explained by the fact that smaller Ni particles are used for the production of the electrode and the use of pore-forming agents in the manufacturing process of the support [145]. Smaller particles are used, since this increase the number of reaction sites (TPB's) [146]. The lower pore radius will affect the Knudsen diffusion, but could also increase the tortuosity. The average pore size of the sample, $\bar{r}_{pore}$, was calculated by:

$$\bar{r}_{pore} = 2\frac{V_{pore}}{S_{pore}} \tag{5.53}$$

where V_{pore} and S_{pore} is the pore volume and surface area, respectively.

Since it was not possible to measure the fuel electrode without the support, the pore size of the fuel electrode was fixed at the measured value for the combined electrode and support. However, this will likely slightly overestimate $\bar{r}_{pore}$ for the electrode.

Table 5.4: Hg-porosimetry measurement

	Porosity ϵ, %	$\bar{r}_{pore}$, Å
E+ES	29.3	1613
E+ES	28.6	1510
E+ES	29.2	1548
Average	29.0	1557
ES	32.6	1693
ES	32.0	1675
Average	32.3	1684

5.5 Results and discussion

Two experiments were conducted: One to estimate the effective diffusion and τ^2, and a second to estimate the permeability. In the first experiment the flow was varied from $150\,\mathrm{ml\,min^{-1}}$ to $1400\,\mathrm{ml\,min^{-1}}$ (it was not possible to obtain a stable higher flow) and the flow ratio between the two sides of the diffusion cell was kept at 1. With the needle valves (shown in Fig. 5.2) the pressure difference between the chambers were adjusted to within $\pm 0.005\,\mathrm{mbar}$. Due to the low pressure difference, the pressure driven flow is neglected and the measured values can therefore be directly used to calculate the effective diffusion.

[†] Based on a significance level of 0.05

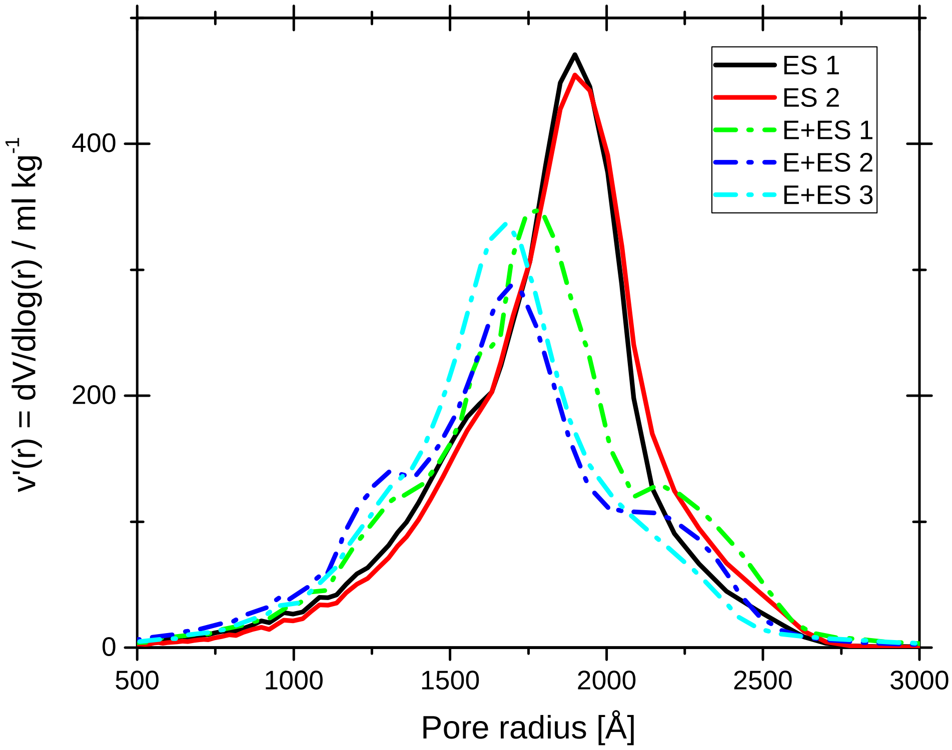

Figure 5.10: Pore distribution volume function $v'(r_{pore})$ from Hg-Porosimetry measurement

In the second experiment both flows were first fixed at 150 ml min^{-1} and then at 1000 ml min^{-1}. At both flow rates the pressure difference between the two sample were varied ±130 mbar. The low flow rate was selected, since the CO concentration at a low flow rate is high and the uncertainty of the CO analyzer would therefore affect the result to a lesser extend than at the high flow. On the other hand, at the high flow rate, the mass transfer resistance between the chamber and the sample would be less, due to the higher velocity and thus a higher Sherwood number, see Eq. (5.59). Some times, at high pressure differences, sudden changes in the measured CO concentration was observed (either towards 0 ppm or above the measurement scale, dependent on the direction of the pressure). This is ascribed to small leakages between the silicone seals and the sample. When this was observed, the experiment run was stopped and the sample was replaced with the next one.

The uncertainty of measured parameters in the experiment is given in Table 5.5.

5.5.1 Wicke-Kallenbach experimental results

Fig. 5.11 shows the measured CO concentration as function of the flow rate for three samples of each types. When possible each samples was tested multiple times (designated run 1, 2, and 3, respectively). From the figure, it can be seen that there is a difference between the ES samples and the E+ES samples and that the measured CO concentration

Table 5.5: Uncertainty of measured parameters

Parameter	Measurement device	Uncertainty
d_{sample}	Vernier caliper (DS/EN ISO 13385-1:2011)	$\pm0.02\,\mathrm{mm}$
$F_{A,in}$, $F_{B,in}$	Mass flow controllers (Brooks)	1%
ΔP (0-20 mbar)	Delta-ohm HD 2114.2	0.3% f.s. (20 mbar)
ΔP (20-300 mbar)	Cole-Parmer 68370.02	0.1% f.s. ± 0.1% of reading ±1 digit
$X_{CO,mea}$	Gas analyzer ABB AO2000	5 ppm
$X_{CO,gas}$	Certificate	2%
ϵ	Micromeritics Autopore IV 9520	3.8%

decreases with increasing flow rate. The difference between the two sample types are likely caused by the active layer present in E+ES, since this is the only difference between the samples. If the film resistance is ignored, the CO concentration should decrease linearly with the flow rate (the CO is diluted due to the increased gas flow). However, this is not the case at low flow rates, and film resistance can therefore not be ignored at low flow rates.

The rate of CO transfer through the samples can be calculated by Eq. (5.55) (see Appendix A for derivation) and are plotted in Fig. 5.12. In this figure it is easier to see the difference between the two sample types than in Fig. 5.11. The error bars in Fig. 5.12 increases significant with the flow rate. The reason for this is that the CO concentration here is low and thus the absolute 5 ppm uncertainty of the analyzer cause the relative uncertainty to increase.

$$F_{CO} = \frac{F_{A,in}}{\left[\frac{1}{X_{CO,0}} + \sqrt{\left(\frac{M_{CO}}{M_{N_2}}\right)} - 1\right]} \tag{5.54}$$

$$N_{CO}^{d} = \frac{F_{CO}}{\pi(d_{sample}/2)^2} \tag{5.55}$$

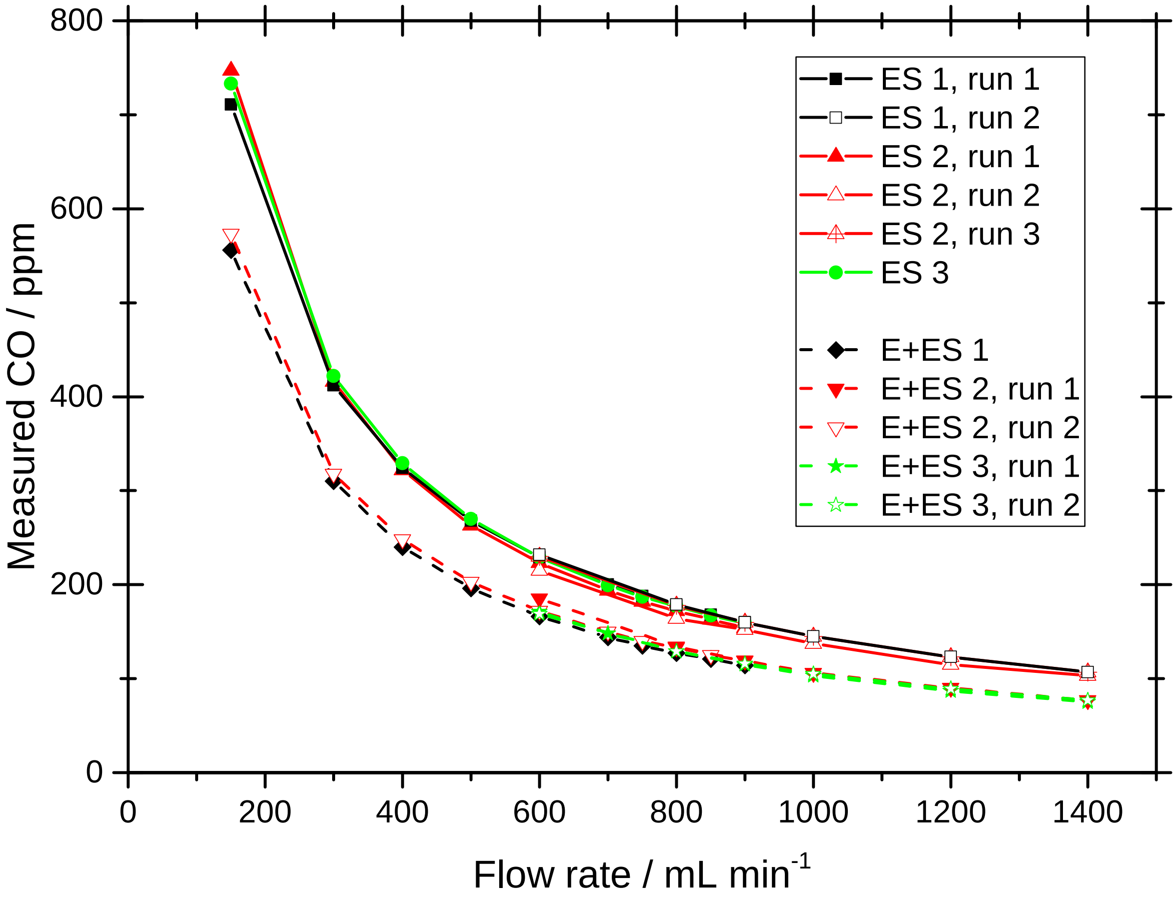

Figure 5.11: Measured CO concentration obtained from the Wicke-Kallenbach setup at different flow rates. The flow rates to both chambers were identical. The lines are for guiding the eye.

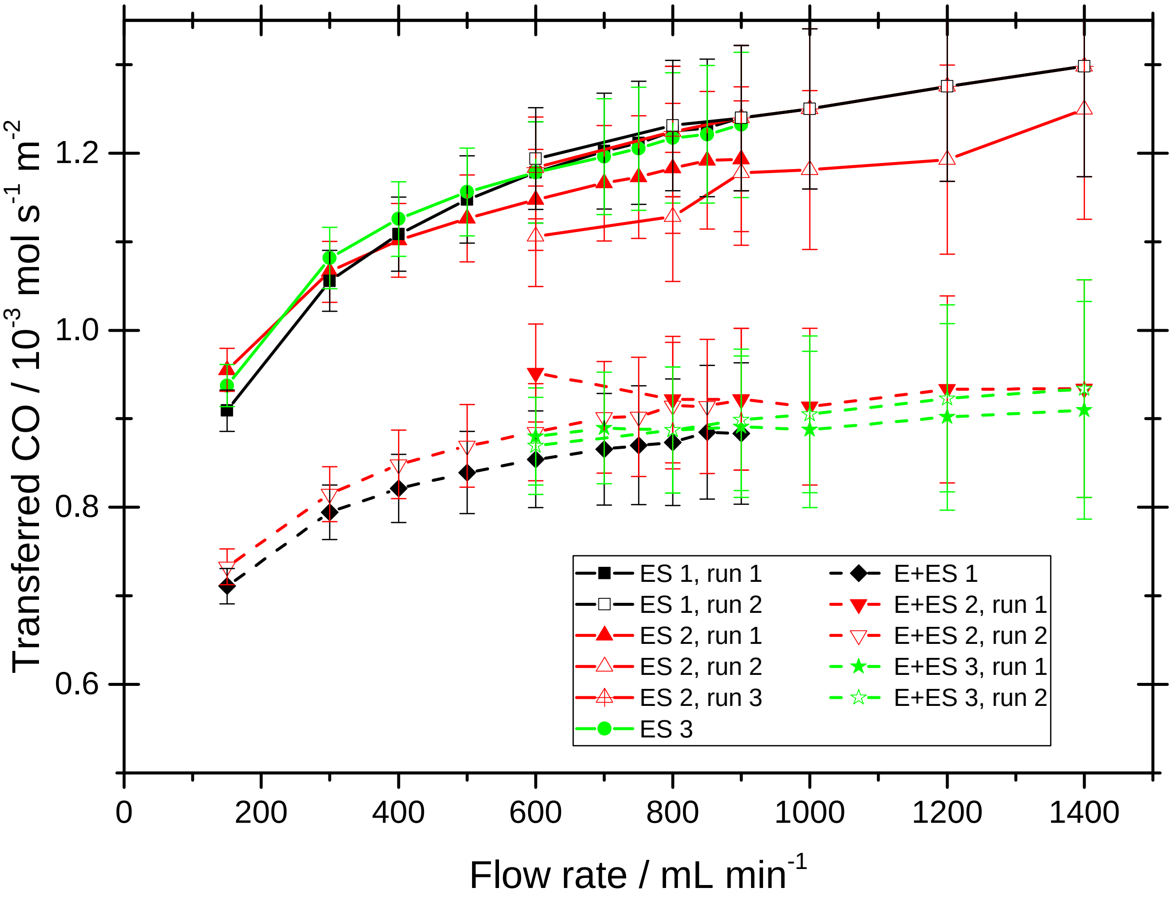

Figure 5.12: Transferred CO at different flow rates. The error bars (95 % confidence interval) are based on the uncertainty of measurements, see Table 5.5. The lines are for guiding the eye.

5.5.2 Calculation of tortuosity - 1d model

Based on the measurement of the CO flux, thickness, porosity and pore radius, the tortuosity factor was fitted for the ES samples. For the 1d model the model was fitted to the experimental values by minimization of the squared difference of the diffusion flux:

$$f_{N^d}(\theta^0) = \min_{\tau^2 \in \Re} \left(\left(N^d_{CO,calc}(\theta^0) - N^d_{CO,mea} \right)^2 \right) \tag{5.56}$$

where θ^0 denotes the measured input parameters, $\theta^0 = (d_{sample}, F_{A,in}, F_{B,in}, H_{sample}, X_{CO,mea}, X_{CO,gas}, \epsilon)$, as given in Table 5.6. $f_{N^d}(\theta^0)$ denotes the minimization function of the diffusion flux evaluated at θ^0. The function was fitted with a tolerance of 0.01 with respect to τ^2. The function was fitted for all the measured points with the ES samples. The measured flux is calculated by Eq. (5.55).

Table 5.6: Values for θ^0 used to calculate τ^2 for the support layer and standard variation, σ

Parameter	mean	σ
d_{sample}	10.2 mm	0.02 mm
$F_{A,in}$, $F_{B,in}$	$\mathbf{F}_{mea,k}$	$1\% \cdot \mathbf{F}_{mea,k}$
H_{sample}	300.7 µm	1.2 µm
$X_{CO,mea}$	$\mathbf{X}_{CO,mea,k}$	5 ppm
$X_{CO,gas}$	10000 ppm	200 ppm
ϵ	0.3	0.0114

The fitted values for τ^2 was 4.8, 3.8, and 5.3 for the Cross-linked pore model, Rothfeld-Scott model and DGM, respectively. All the diffusion models gave very poor fits for the anode support samples, especially at lower flow rates. The calculated diffusion flux, N^d, was to high at low flow rates and to low at high flow rates, see Fig. 5.13. The reason for this can likely be explained by the fact that the mass transfer resistance from the gas to the sample has been neglected and that both chambers are assumed to be well mixed. The former cause the mass transfer limitations to be included in the fit of τ^2. Since the mass transfer resistance is dependent on the gas velocity, the influence on τ^2 will also be dependent on the flow rate. The problem with the well mixed assumption is that, if it is not valid, the surface on the sample could be exposed to significantly different CO concentrations.

The mass transfer can be approximated by the film model, in which the entire concentration difference between the bulk flow and the surface is considered to be localized in a thin viscous film/layer adjacent to the surface [115]. In the film layer, the mass transfer takes place via molecular diffusion and is modeled with Fick's law:

$$N_d = \frac{D_{i,j}}{\delta}(C_i^{surf} - C_i^{bulk}) \tag{5.57}$$

where δ is the thickness of the film layer, C_i^{surf} is the concentration of species i at the surface and C_i^{bulk} is the concentration of the species in the bulk. In stead of evaluating δ,

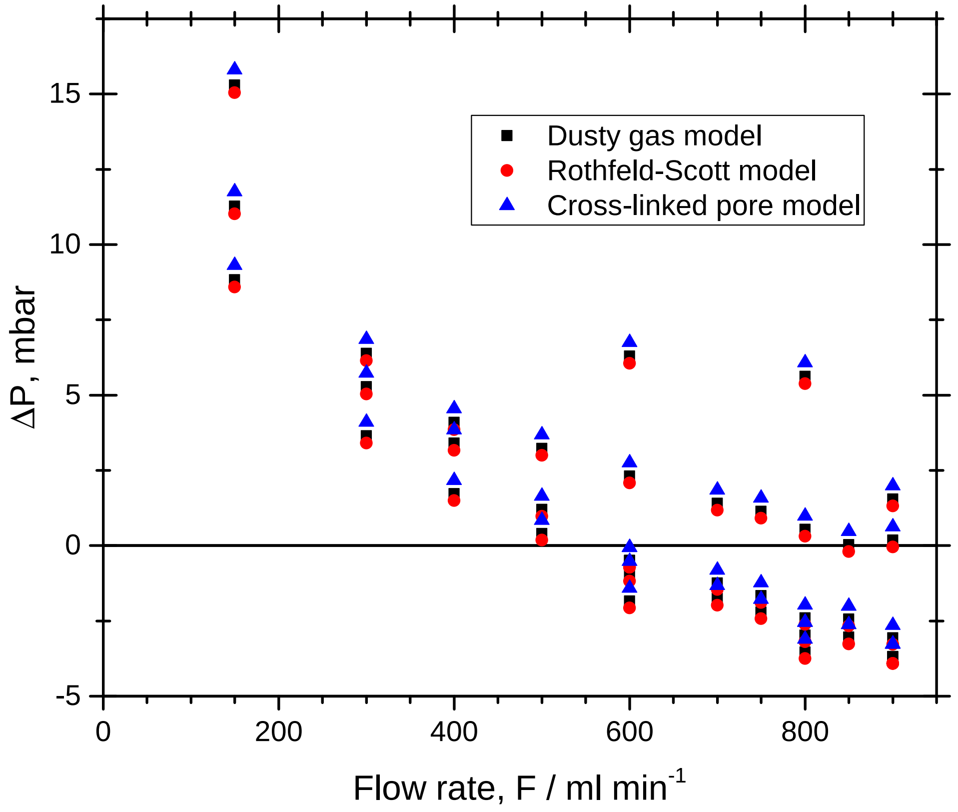

Figure 5.13: Deviation between calculated and measured diffusion flux, $(N^d_{calc} - N^d_{mea})/N^d_{mea}$, with the diffusion models without taking mass transfer limitations into account. The fitted values for τ^2 (4.8, 3.8 and 5.3 for the Cross-linked pore model, Rothfeld-Scott model and DGM, respectively) was used to calculate the deviation

a mass transfer coefficient, k_{mt}, is defined as $k_{mt} = \frac{D_{i,j}}{\delta}$ and Eq. (5.57) is rewritten to:

$$N_d = k_{mt}(C_i^{surf} - C_i^{bulk}) \tag{5.58}$$

k_{mt} can be calculated form the Sherwood number, Sh, defined as $Sh = \frac{k_{mt}l}{D_{i,j}}$. The Sherwood number can be expressed as a function of Reynolds number, Re, and Schmidt number, Sc, see Eq. (5.59). Since all the parameters in the function, except the velocity, is identical for all the experiment conducted on the Wicke-Kallenbach setup (neglecting the small pressure effect on μ,ρ and $D_{i,j}$), it should be possible to fit k_{mt} with a function depending only on the average velocity $\bar{u}$ which, in turn, depends on the inlet flow rate.

$$Sh = f(Re, Sc) = f(\frac{\rho \bar{u} l}{\mu}, \frac{\mu}{\rho D_{i,j}}) \tag{5.59}$$

To see if the mass transfer resistance could explain the poor result of the 1d model, the mass transfer coefficient was fitted as a function of the inlet flow rates $F_{A,in}$ and

$F_{B,in}$ (they were equal in all sample points) using the experimental data and results from the 2d model. The flux was calculated with Eq. (5.55). The average concentration at the surface on each side of the sample was computed in the 2d model by integration over the surface and dividing with the surface area. Assuming that the well-mixed assumption was valid, the concentration in chamber A was taken as the measured outlet concentration, $C_A^{surf} = X_{CO,mea} \cdot C_t$. The concentration in chamber B was taken as the outlet concentration calculated from the known inlet concentration and the CO transfer from chamber B to A (as given in Eq. (5.28)).

With the flux and CO concentrations, the mass transfer coefficient was calculated with Eq. (5.58). Fig. 5.14 shows the calculated mass transfer coefficient versus the flow rate for both chamber A and chamber B. From the figure, it can be seen that the mass transfer coefficient can be estimated from the flow rate using a logarithmic function. Since there will only be very small differences in μ and ρ between the two chambers (because of the difference in CO concentration), it is expected from Eq. (5.59) that k_{mt} should not vary between the two chambers. This is also the case, since only minor differences can be seen in Fig. 5.14.

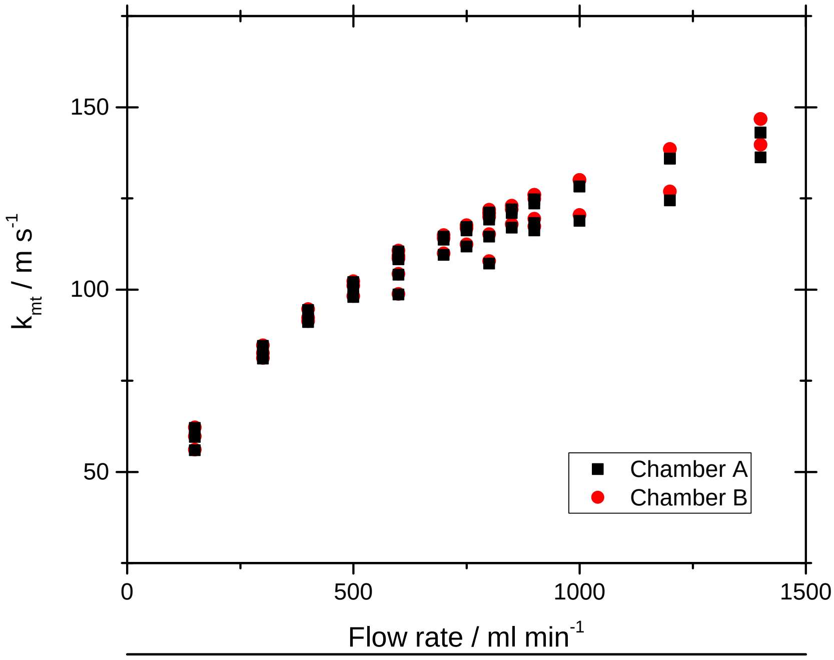

Figure 5.14: Mass transfer coefficient as function of the flow rate for chamber A and B.

The calculated mass transfer resistance from bulk gas phase to sample surface was incorporated in the 1d model by replacing $X_{CO,gas}$ with $C_{\mathrm{CO}}^{surf}/C_t$ from Eq. (5.58):

$$N_d = k_{mt} \cdot (C_{\mathrm{CO}}^{surf} - C_{\mathrm{CO}}^{bulk}) \tag{5.60}$$

$$X_{CO,gas} = \frac{C_{\mathrm{CO}}^{surf}}{C_t} = \frac{N_d + k_{mt} \cdot \frac{C_{\mathrm{CO}}^{bulk}}{C_t}}{k_{mt}} \tag{5.61}$$

and replacing $X_{CO,mea}$ with:

$$N_d = k_{mt} \cdot (C_{\mathrm{CO}}^{surf} - C_{\mathrm{CO}}^{bulk}) \tag{5.62}$$

$$X_{CO,mea} = C_{\mathrm{CO}}^{bulk}/C_t = -\frac{N_d - k_{mt} \cdot \frac{C_{\mathrm{CO}}^{surf}}{C_t}}{k_{mt}} \tag{5.63}$$

With the new “effective” mole fractions, τ^2 was once again fitted with the different diffusion models using the 1d model. However, no differences in the diffusion flux was observed (difference less than 1×10^{-12}. The results shows that the 1d model with the well-mixed assumption cannot model the Wicke-Kallenbach setup satisfying. In the next section, where the 2d model is discussed, the flow patterns in the two chambers and the “well-mixed” assumption, will be investigated as a explanation for the 1d model’s lack of applicability.

5.5.3 Calculation of tortuosity - 2d model

In the 2d model τ^2 was fitted using Eq. (5.64):

$$f_{X_{CO}}(\theta^0) = \min_{\tau^2 \in \Re} \left(\sum_k \left(\frac{X_{CO,calc,k} - X_{CO,mea,k}}{X_{CO,mea,k}} \right)^2 \right) \tag{5.64}$$

First τ_{ES}^2 for the ES samples was fitted to a value of 4.81, using the DGM, and subsequently τ_E^2 for the E+ES samples were fitted to a value of 11.9 assuming that the support layer had a τ_{ES}^2-value of 4.81. Fig. 5.15 shows the measured CO mole fraction and the CO mole fraction calculated with the fitted values for τ_{ES}^2 and τ_E^2, and Fig. 5.16 shows the measured and calculated rate of CO transfer (Fig. 5.17 is similar to Fig. 5.16, except that error bars are added). From the figures it can be seen that the fit is reasonable. In order to evaluate the effect of the uncertainties related to the experiment a sensitivity and uncertainty analysis with respect to τ_{ES}^2 and τ_E^2 was carried out and is presented in the following.

5.5.4 Sensitivity and uncertainty analysis

Based on the uncertainties of the parameters (see Table 5.5 on page 61) the uncertainty of the estimate of τ_{ES}^2 can be estimated with a Monte Carlo procedure [147] (see Appendix B).

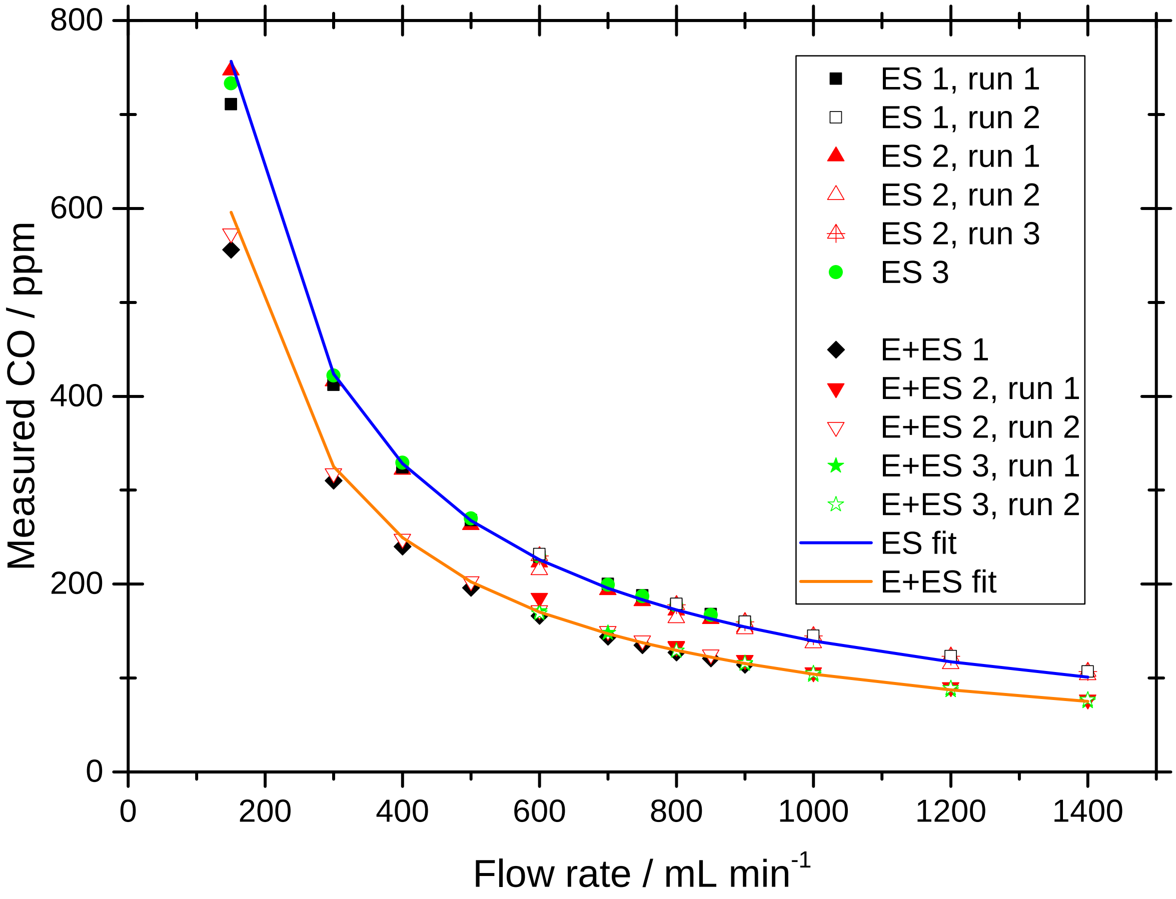

Figure 5.15: Calculated (lines) and measured (points) $X_{CO,mea}$ values. The calculated lines are calculated with the estimated τ^2 values: $\tau^2_{ES} = 4.81$ and $\tau^2_E = 11.9$.

However, before conducting the uncertainty analysis, a sensitivity analysis was performed. The purpose of the sensitivity analysis was to determine which parameters had the largest effect on τ^2_{ES} and which had the smallest effect, and could therefore be neglected.

The performed sensitivity analysis was a one-at-a-time (OAT) analysis where a single variable is varied while the others are held constant:

$$s_m = \frac{f(\theta_{mean,m} \pm \sigma_m, \theta^0)}{\tau^{2,0}_{ES}} \tag{5.65}$$

Here, f denotes the minimization function given in Eq. (5.64) assuming that only parameter m is changed, and the remaining parameters are fixed. $\tau^{2,0}_{ES}$ is the value of τ^2_{ES} computed at ϕ^0 (see Table 5.6) and s_m is the relative sensitivity of a variation of one σ on τ^2_{ES}.

Table 5.7 shows the result of the sensitivity analysis. It can be seen that the uncertainty of $F_{A,in}$, $F_{B,in}$,$X_{CO,mea}$, $X_{CO,gas}$ and ϵ has the largest effect on τ^2 and d_{sample} and H_{sample} has the lowest effect on τ^2. Based on this, d_{sample} and H_{sample} was omitted from the uncertainty analysis.

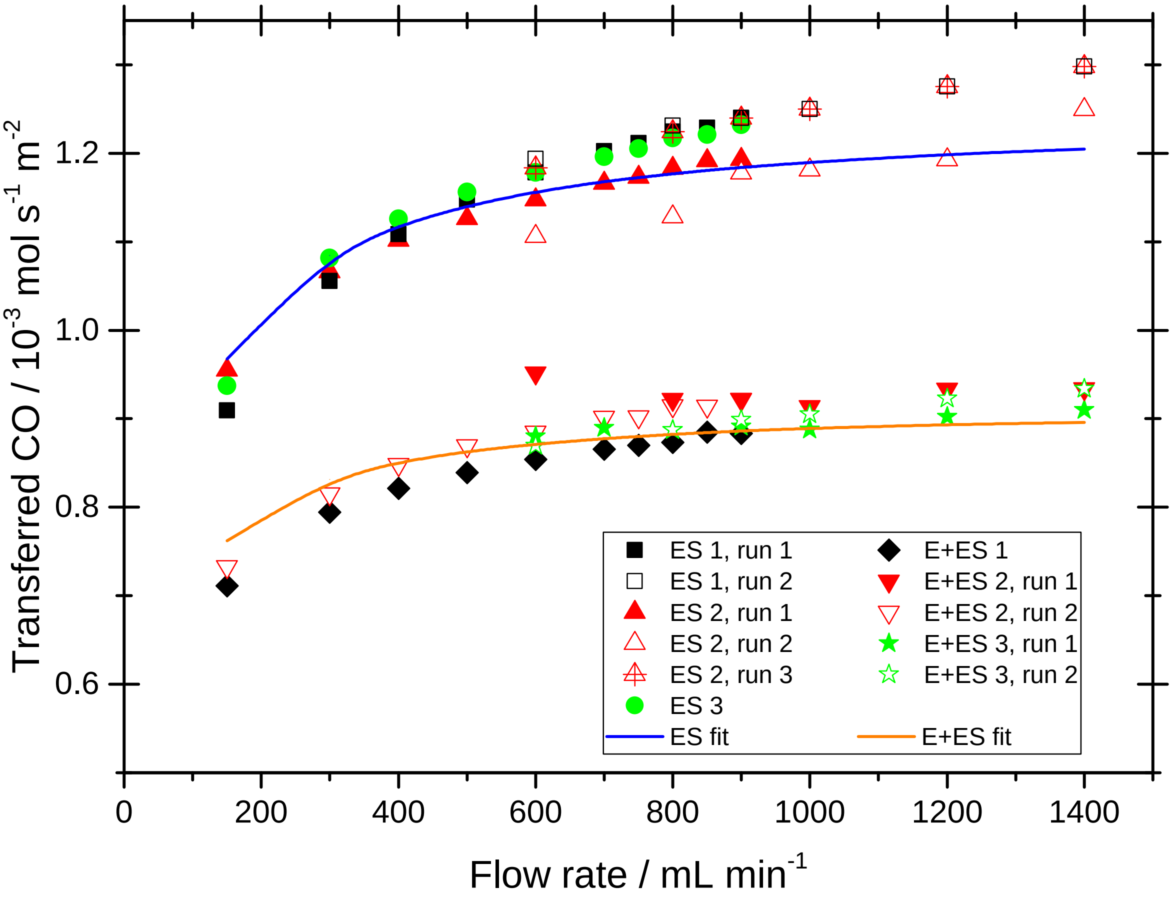

Figure 5.16: Calculated (lines) and measured (points) rate of CO transfer through the sample. The calculated lines are based on the estimated τ^2 values: $\tau^2_{ES} = 4.81$ and $\tau^2_E = 11.9$.

An uncertainty analysis was performed using the Monte Carlo procedure with latin hypercube sampling [148] described by Sin et al. [147] (see Appendix B). A relative low total number of 150 samples where used, due to a high calculation time. Using only a subset of 100 out of the total 150 samples showed no impact on the obtained statistics. This implies that the sample size was large enough. From the description of the DGM (Section 5.1.5) it can be seen that τ^2 and ϵ can be replaced with a constant, η_{diff}, so that $\eta_{diff} = \epsilon/\tau^2$. In doing this, the uncertainty connected to the measurement of ϵ can be disregarded in the modeling of diffusion within the electrode (Chapter 6) and the uncertainty analysis was therefore performed with respect to η_{diff}. Fig. 5.18 shows the measured CO concentration and the calculated CO concentration with the 95% confidence intervals, calculated from the uncertainty analysis. From the uncertainty analysis, η_{diff} is found to have a mean of 0.0645 and a standard deviation of 0.003 (a relative deviation of 4.61 %). The corresponding mean value of τ^2_{ES} and the uncertainty

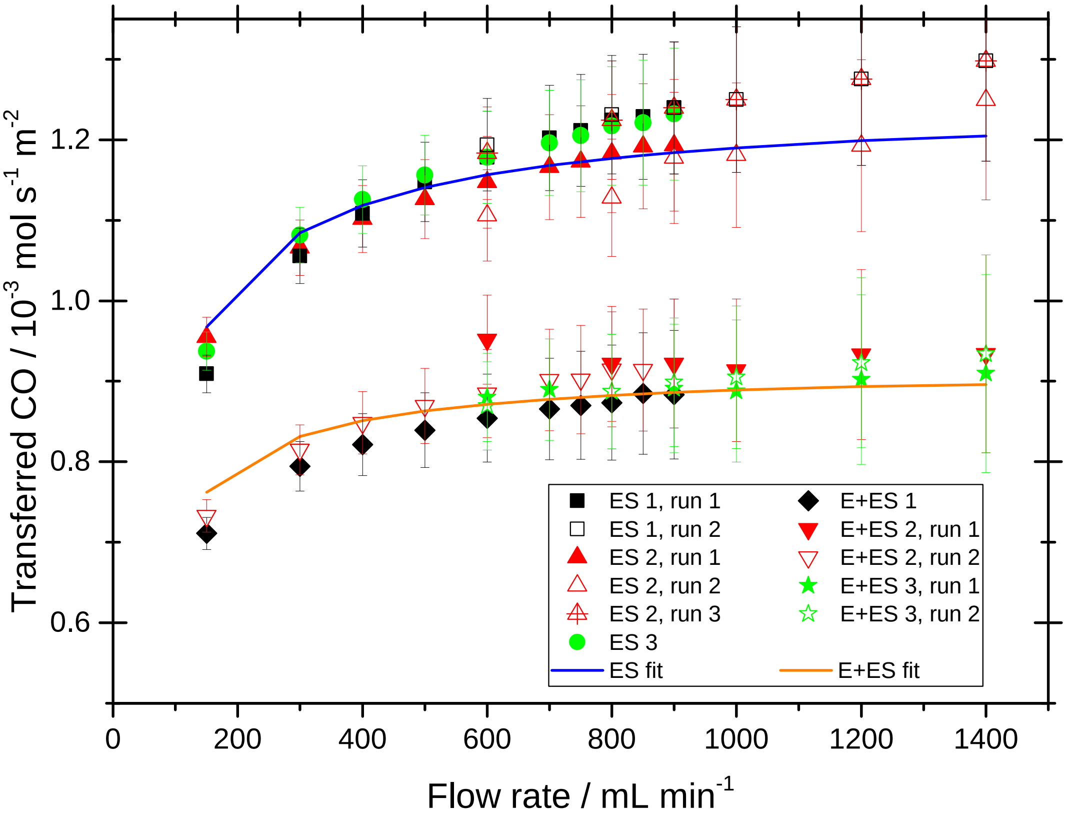

Figure 5.17: Similar to Fig. 5.16, but with error bars.

Table 5.7: Result of sensitivity analysis. The table shows the sensitivity value, s_m, when parameter m is increased or decreased with one σ.

Parameter m	$+\sigma$	$-\sigma$
d_{sample}	1.004	0.995
$F_{A,in}$, $F_{B,in}$	0.989	1.011
H_{sample}	0.995	1.002
$X_{CO,mea}$	0.970	1.320
$X_{CO,gas}$	1.024	0.976
ϵ	1.037	0.961

of τ_{ES}^2 can be calculated from the values and uncertainty of η_{diff} and ϵ:

$$\tau_{ES}^2 = \frac{\epsilon}{\eta_{diff,ES}} = 4.65 \tag{5.66}$$

$$\delta\tau_{ES}^2 = \tau_{ES}^2 \sqrt{\left(\frac{\delta\eta_{diff,ES}}{\eta_{diff,ES}}\right)^2 + \left(\frac{\delta\epsilon}{\epsilon}\right)^2} = 0.278 \tag{5.67}$$

$$\frac{\delta\tau_{ES}^2}{\tau_{ES}^2} = 5.97\% \tag{5.68}$$

The difference in relative uncertainty of $\eta_{diff,ES}$ and τ^2_{ES} (respectively 4.61 % and 5.97 %) shows the improvement in using η_{diff} instead of τ^2_{ES} in the diffusion modeling in the subsequent chapter. The mean value of τ^2_{ES} from the uncertainty analysis was lower than the value calculated without including the uncertainty. The value calculated from the uncertainty analysis will be used, because it includes the uncertainties of the measured parameters.

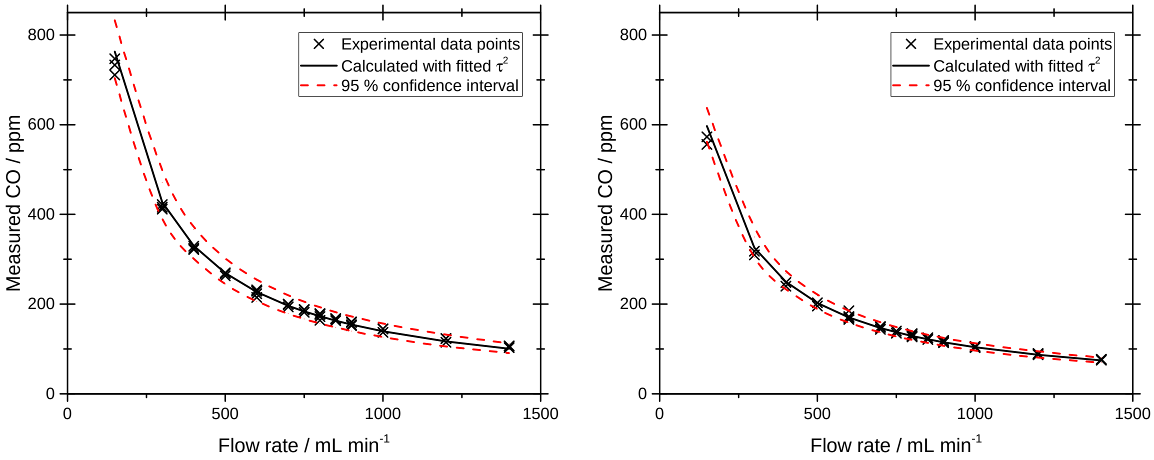

(a) τ^2_{ES} **(b)** τ^2_{E+ES}

Figure 5.18: Measured CO and calculated CO with 95 % confidence interval.

Similar for $\eta^2_{diff,E}$ an uncertainty analysis was performed. Together with the parameters used in the uncertainty study of $\eta^2_{diff,ES}$, the uncertainty of $\eta^2_{diff,ES}$ was also included. With these uncertainty factors, the average $\eta^2_{diff,E}$ was calculated to be 0.020 with a standard deviation of 0.003 (a relative standard deviation of 14.9 %). This corresponds to an average τ^2_E of 14.8 with a standard deviation of 2.27. The average $\eta^2_{diff,E}$ from the uncertainty analysis was higher than the value calculated without the uncertainty (11.9). The main reason for this, is that the value used for τ^2_{ES} in the uncertainty analysis was based on the uncertainty analysis of τ^2_{ES}, which was lower than the τ^2_{ES} value found without including the uncertainty. Physically, this corresponds to an increase in the diffusion resistance for E when the diffusion resistance in ES is decrease. The high standard deviation of 2.27 shows that the uncertainty of τ^2_E is high. This is due to the low thickness of E.

5.5.5 Comparison with literature values for τ^2

Several different techniques have been used in the literature to calculate the tortuosity. Table 5.8 list the techniques and resulting tortuosity for different Ni/YSZ samples. In tomography an image of the sample is obtained and the tortuosity is in general calculated from $\tau = L_{eff}/L$ where L_{eff} is the effective length and L is the shortest length between two points. Typical tomography techniques includes Focused Ion Beam Scanning Electron Microscope (FIB-SEM) and X-rays. An disadvantage with the tomography methods is that only a small part of the sample is investigated and care must therefore be taken to ensure that the selected part is representative for the whole sample. Furthermore, as previously mentioned, when τ^2 is fitted to experimental data, it also includes effect from dead-end pores and the variation in pore diameter as well as any shortcomings of the diffusion model.

In the overpotential method, the fact that a loss of cell voltage will occur when there is a difference between the gas bulk concentration and the gas concentration at the reaction sites (i.e. TPBs) is used. E.g. during fuel cell operation with H_2 the overpotential can be calculated with [124]:

$$\eta_{conc} = -\frac{RT}{2F} \ln \left(\frac{P_{\mathrm{H_2},TPB} P_{\mathrm{H_2O},bulk}}{P_{\mathrm{H_2},bulk} P_{\mathrm{H_2O},TPB}} \right) \tag{5.69}$$

where η_{conc} is the overpotential loss due to concentration differences caused by the diffusion limitations and P is the partial pressure of the gas species at the reaction sites (TPB) and bulk, respectively.

From Table 5.8 it can be seen that τ^2_{ES} range from 2 to 9 depending on the method and composition of the Ni/YSZ support and if a reaction layer is included. A single value for the reaction layer, τ^2_E, was found ($\tau^2_E = 10.15$), but with a lower porosity than that of the reaction layer used in this thesis. These values corresponds well with the values obtained from the 2d modeling in this thesis.

5.5.6 Permeability measurement

The pressure difference was obtained by manually adjusting the needle valves, and it was therefore not possible to obtain the same pressure differences for each experimental run. Fig. 5.19 shows the measured $X_{CO,mea}$ versus the pressure difference, ΔP, for the two investigated flow rates. A negative ΔP indicates that the pressure in chamber A is lower than chamber B and vice versa. The pressure difference was obtained by increasing the pressure in either chamber A or B, while the pressure in the opposite chamber was maintained at P_{atm}. $X_{CO,calc}$ was calculated with the Wicke-Kallenbach model presented in Section 5.3.2. The permeability, κ, for all the experimental runs was fitted by minimizing the relative difference between the calculated CO concentration $X_{CO,calc}$, and the measured CO concentration, $X_{CO,mea}$. $X_{CO,calc}$ was calculated using the 2d model and the fitted values for τ^2_E and τ^2_{E+ES}.

$$g(\theta) = \min_{\kappa \in \Re} \left(\left(\frac{X_{CO,calc} - X_{CO,mea}}{X_{CO,mea}} \right)^2 \right) \tag{5.70}$$

The fitted value of the permeability was $\kappa_{ES} = 1.1 \times 10^{-15}\,\mathrm{m}^2$ for the support material and $\kappa E = 0.40 \times 10^{-15}\,\mathrm{m}^2$. Fig. 5.19 shows the experimental data (points) and the fitted values (lines).

Table 5.8: Tortuosity values from the literature. In the table τ denotes the tortuosity and τ^2 the tortuosity factor. TG, OP, WK, and Eq. stands for Tomography, Overpotential, Wicke-Kallenbach and Equation, respectively.

Method	Tortuosity	Source	Note
TG	$\tau_x = 2.05, \tau_y = 1.99, \tau_z = 1.78$	[149]	FIB-SEM measurements, $\epsilon = 47.5 - 49.6\%$, NI:YSZ 50:50
TG	$\tau_x^2 = 3.26, 3.48, 6.17, \tau_y^2 = 2.71, 3.04, 3.92, \tau_z^2 = 2.27, 2.64, 10.8$	[150]	FIB-SEM measurements for three samples with the volume composition: Sample 1: 42.3 % Ni, 18.9 % YSZ, 38.8 % pore; Sample 2: 34.2 % Ni, 29.7 % YSZ, 36.1 % pore; Sample 3: 23.6 % Ni, 50.6 % YSZ, 25.8 % pore;
TG	$\tau^2_{electrode} = 2.22, \tau^2_{activelayer} = 10.15$	[145]	3d reconstructions obtained by X-ray nano-tomography for an electrode and the functional layer, $\epsilon_{electrode} = 46.6, \epsilon_{activelayer} = 22.8$, Ni:YSZ 50:50
TG	$\tau_1 = 3.01 - 3.15, \tau_2 = 1.9, \tau_3 = 2$	[128]	τ_1 obtained from limiting current experiments, τ_2 as 1 but with surface diffusion, τ_3 calculated from FIB-SEM. $\epsilon = 0.33$
TG	$\tau_1 \approx 2.5, \tau_2 \approx 3, \tau_3 \approx 4, \tau_4 = 5.77.$	[151]	FIB-SEM measurements, τ_1 obtained from sample with 40 wt% Ni, 60 wt% YSZ $\epsilon = 0.15$, τ_2: 50 wt% Ni, 50 wt% YSZ $\epsilon = 0.21$, τ_3: 60 wt% Ni, 40 wt% YSZ $\epsilon = 0.23$, τ_4:70 wt% Ni, 30 wt% YSZ $\epsilon = 0.27$
OP	$\tau^2_{SMM,CO-CO_2} = 4.79, \tau^2_{DGM,CO-CO_2} = 4.5, \tau^2_{BFM,CO-CO_2} = 5.49, \tau^2_{SMM,H_2-H_2O-Ar} = 5.0, \tau^2_{DGM,H_2-H_2O-Ar} = 4.5, \tau^2_{BFM,H_2-H_2O-Ar} = 5.29$	[124]	Experimental values of overpotential in a CO-CO_2 and a H_2-H_2O-Ar system. $\epsilon = 0.46$
WK	$\tau^2 = 2.5 - 3$	[136]	Fuel electrode layer (500 µm) with 40/60 % vol Ni/YSZ, active layer (5-10 µm) with 50/50 vol% Ni/YSZ $\epsilon = 0.3 - 0.6$
Eq	$\tau^2 = \epsilon^{-0.5}$	[152]	Bruggeman correction. Only valid for $\epsilon > 0.6$ [153]
Eq	$\tau^2 = \frac{(1+\epsilon)^2}{\epsilon(1+\epsilon)^2+4\epsilon^2(1-\epsilon)}$	[154]	Equation based on a 3d cube packing model and compared with experimental data.

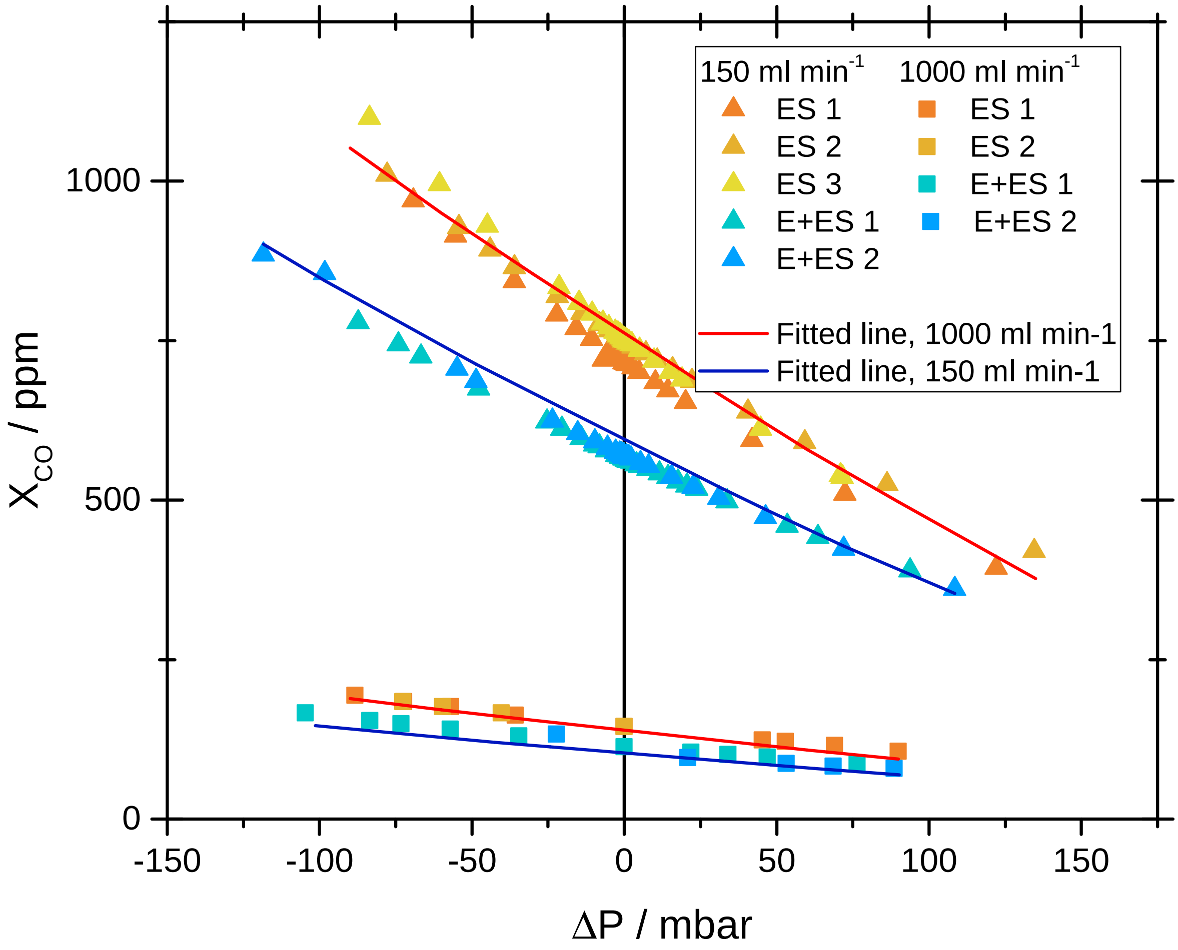

Figure 5.19: Permeability results. Squares are at $1000\,\mathrm{ml\,min^{-1}}$ and triangle are at $150\,\mathrm{ml\,min^{-1}}$

Similar to the calculation of τ^2, an uncertainty analysis of the permeability was performed. In addition to the parameters included in the uncertainty analysis of τ^2, ($F_{i,in}$, $F_{j,in}$,$X_{CO,mea}$, $X_{CO,gas}$), ΔP was added. The previously described Monte Carlo method was used with a total of 100 samples. Based on the uncertainty analysis, the standard deviation of the permeability was found to be $0.018 \times 10^{-15}\,\mathrm{m}^2$.

5.5.7 Comparison with literature value for κ

In the literature a wide range of values have been used for the permeability, see Table 5.9. In some studies a constant value is assumed (without specifying why the value was chosen) in the range of $10^{-7}\,\mathrm{m}^2$ to $10^{-12}\,\mathrm{m}^2$. Others have used the Kozeny-Carman equation (Eq. (5.71)) and calculated the permeability to be in the range $10^{-14}\,\mathrm{m}^2$ to $10^{-16}\,\mathrm{m}^2$. Finally, the permeability has been measured with permeametry and porosimetry methods to be in the range $10^{-14}\,\mathrm{m}^2$ to $10^{-15}\,\mathrm{m}^2$. In permeametry the flow rate through a sample is measured when a known pressure is applied, i.e. similar to the method used in this study. In porosimetry the opposing force due to surface tension is measured during intrusion of a non-wetting liquid (typically mercury) at high pressure into the sample. From the measurement of the force, the permeability can be calculated [155, 156].

$$\kappa = \alpha_{KC} \frac{\epsilon^3 d_{par}^2}{(1-\epsilon)^2} \tag{5.71}$$

where α_{KC} is a constant and d_{par} is the diameter of the particles that makes up the material.

Comparing the fitted values for κ ($\kappa_{ES} = 1.1 \times 10^{-15}\,\mathrm{m}^2$ and $\kappa_E = 0.40 \times 10^{-15}\,\mathrm{m}^2$) with the data in Table 5.9, it can be seen that the fitted values for κ is within the literature interval, but in the lower range. Comparing specifically to the data in row 4, 11, 13 and 15, which have a similar porosity to the investigated samples, they are all in good agreement with the fitted values for the permeability.

Table 5.9: Literature values for κ of Ni-YSZ. Compiled by [157]

No.	κ, m^2	Method	Microstructure	Source
1	$2-18 \times 10^{-14}$	Permeametry and porosimetry	$\epsilon \approx 0.4, 1\,\mu\mathrm{m} < d_p < 5\,\mu\mathrm{m}$	[155]
2	$1-4 \times 10^{-14}$	Permeametry	$\epsilon > 0.3$	[158]
3	9.83×10^{-15}	Permeametry	$d_p \approx 0.5 - 10\,\mu\mathrm{m}$	[156]
4	$1-5 \times 10^{-15}$	Permeametry and porosimetry	$0.2 < \epsilon < 0.3$	[159]
5	1×10^{-12}	Constant parameter	$\epsilon = 0.38 - 0.5, d_p = 1 - 2\,\mu\mathrm{m}$	[160]
6	1.7×10^{-12}	Constant parameter	$\epsilon = 0.38, d_p = 1\,\mu\mathrm{m}$	[161]
7	1.57×10^{-12}	Constant parameter	$d_p = 1\,\mu\mathrm{m}$	[162]
8	1.76×10^{-11}	Constant parameter	$\epsilon = 0.5$	[163]
9	1.0×10^{-7}	Constant parameter	$\epsilon = 0.9$	[164]
10	2.18×10^{-14}	Kozeny-Carman	$\epsilon = 0.35, d_p = 0.5\,\mu\mathrm{m}$	[165]
11	1.27×10^{-15}	Kozeny-Carman	$\epsilon = 0.3, d_p = 0.5\,\mu\mathrm{m}$	[166]
12	9.237×10^{-15}	Kozeny-Carman	$\epsilon = 0.5, d_p = 2.5\,\mu\mathrm{m}$	[167]
13	1.9×10^{-15}	Kozeny-Carman	$\epsilon = 0.3, d_p = 1\,\mu\mathrm{m}$	[168]
14	8×10^{-16}	Kozeny-Carman	$\epsilon = 0.4, d_p = 0.9\,\mu\mathrm{m}$	[169]
15	1.27×10^{-15}	Kozeny-Carman	$\epsilon = 0.3, d_p = 0.5\,\mu\mathrm{m}$	[170]

5.5.8 Investigation of well-mixed assumption

In the calculation of τ^2 with the 1d model, it was speculated that the disagreement with the model and the measured values was due to the assumption of a well-mixed gas phase within the two chambers of the diffusion cell. With the 2d model it was possible to extract the flow pattern and CO concentration, both in the chambers and the sample, for investigation of this.

Fig. 5.20 shows the flow velocity in the two chambers for the lowest inlet flow rate ($150\,\mathrm{ml\,min^{-1}}$) and the highest flow rate ($1400\,\mathrm{ml\,min^{-1}}$). The white lines are the stream lines and the red arrows are the two components of the velocity, u_r and u_z. From the figure it can be seen that a recycling zone is present at both low and high flow rates. However, because of the location of the recycling zone, the sample surface will not be exposed to a well-mixed gas composition, since the inlet gas is not mixed with the outlet gas before the inlet gas reached the sample. This can also be seen in Fig. 5.21 were the CO mole fraction is plotted in both chambers at the low flow rate (the two figures left) and at the high flow rate (the two figures right). From the figures it can be seen that the CO mole fraction in chamber A (the two top figures) increases significantly from $r = 0$ to $r = r_{sample}$ just above the sample surface, due to the flow profile (see Fig. 5.20). The increase is most clearly seen at the low flow rate, but is also present at the high flow rate. In chamber B (the two bottom figures) a decrease in CO is seen from $r = 0$ to $r = r_{sample}$ just below the sample surface, again most significant for the low flow rate.

These figures clearly shows that the two chambers of the diffusion cell are not well-mixed and this is why the 1d model (with this assumption) cannot be used to model the cell. Similar observations has been reported by Perdana et al. [171] for a Wicke-Kallenbach setup with a different inlet and outlet geometry.

5.6 Conclusion

The analysis and modeling of the setup reveal that mass transfer from the bulk gas to the sample, and the influence of the flow pattern within the setup, was significant. A simple 1d model approach, which is usually used to model Wicke-Kallenbach diffusion cells, was therefore insufficient to model the diffusion cell. Instead a 2d axisymmetric model, including the mass transfer and flow pattern, was used. With the 2d model, the tortuosity of the support material was calculated to be $\tau^2_{ES} = 4.65$ with a standard deviation of 0.287 (corresponding to a relative uncertainty of 5.97 %) and for the reaction layer material $\tau^2_E = 14.8 \pm 2.27$, relative uncertainty 15.4%.

The porosity and tortuosity was combined into a new parameter: $\eta_{diff} = \epsilon/\tau^2$. When performing the uncertainty analysis with respect to η_{diff} rather than τ^2, the uncertainty of ϵ can be ignored. In this way, the relative uncertainty is reduced to 4.61 % for $\eta_{diff,ES}$ and to 14.9 % for $\eta_{diff,E}$.

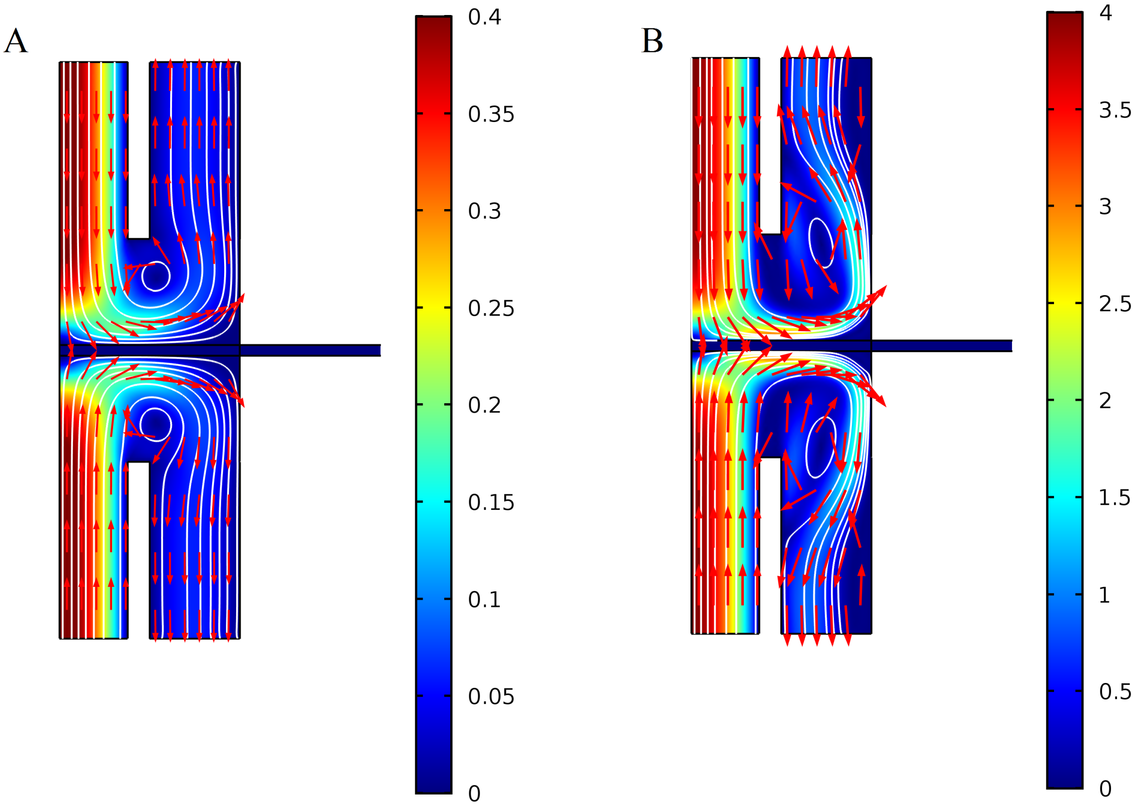

Figure 5.20: Flow magnitude within the Wicke-Kallenbach diffusion cell. A (left): Flow magnitude at 150 ml min^{-1} and B (right): Flow magnitude at 1400 ml min^{-1}. Based on the values given in Fig. 5.3 and Table 5.6, $\eta_{diff,ES} = 0.0645$ and κ=1.14 m^2. Noted the difference in scale of the two figures

The permeability was fitted to $\kappa_{ES} = 1.1 \times 10^{-15}\,\mathrm{m}^2$ for the support material and $\kappa_E = 0.40 \times 10^{-15}\,\mathrm{m}^2$ for the reaction layer material. An uncertainty analysis reveal a low experimental uncertainty of $0.018 \times 10^{-15}\,\mathrm{m}^2$.

Both the values for τ^2 and κ are within reasonable ranges, compared to the literature.

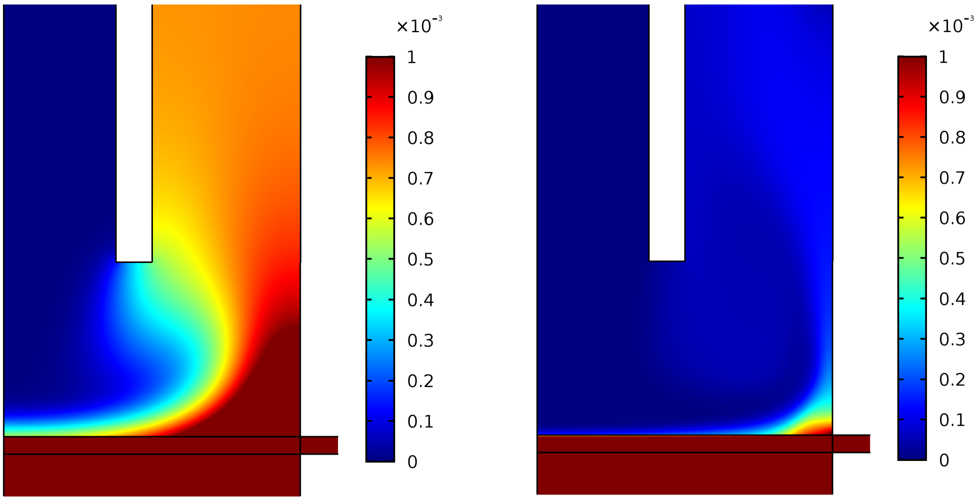

(a) Chamber A, flow rate 150 ml min^{-1} **(b)** Chamber A, flow rate 1400 ml min^{-1}

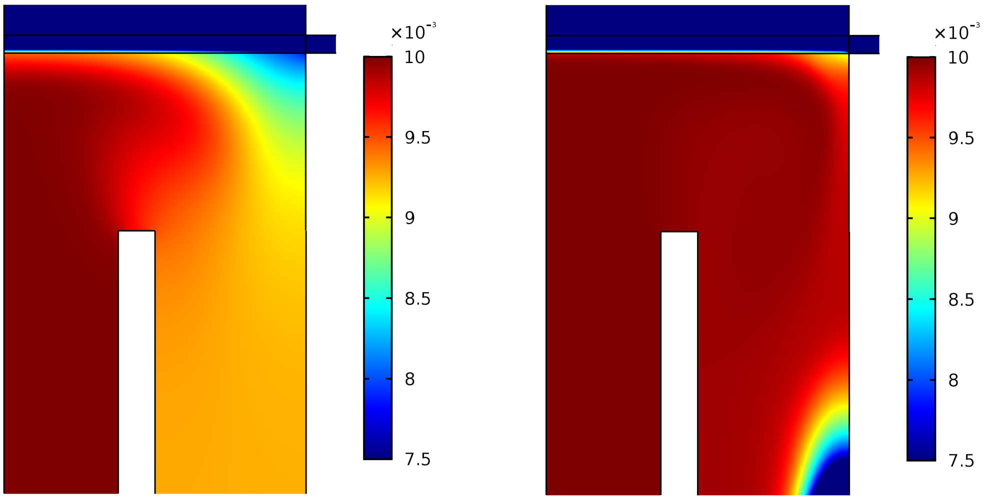

(c) Chamber B, flow rate 150 ml min^{-1} **(d)** Chamber B, flow rate 1400 ml min^{-1}

Figure 5.21: Mole fraction in the diffusion cell compartments at two different inlet flow rates. The top figures are chamber A and the two bottom figures are chamber B. The left figures are the low flow rate (150 ml min^{-1}) and the right figures are at a high flow rate (1400 ml min^{-1}). Noted the scale in the top figures goes from 0 to 10^{-3} and from 7.5×10^{-3} to 10×10^{-3} in the two bottom figures

CHAPTER 6

Modeling of diffusion limitations in fuel electrode and impact on carbon formation risk

---

The diffusion of gas species in the fuel electrode is important, since the reactants (CO_2 and H_2O) has to diffuse from the fuel channel to the reaction sites (the triple phase boundaries, see Section 1.2). Afterwards, the products (CO and H_2) has to diffuse from the reaction sites to the fuel channel. In this chapter, the diffusion through the fuel electrode is modeled and the gas composition and risk of carbon formation is evaluated. As described in Section 5.1.2 several models for the diffusion has been proposed, but the dusty gas model has been selected.

The diffusion is modeled with a 1d model and a 2d model. As described in Section 1.2 the planar SOC consist of cells and interconnects, where the interconnects distribute the flow across the cell and leads the current through the stack. At the points where the interconnects touch the cell, the cell will not be in contact with the gas channel (see Fig. 6.1). However, the electrochemical reactions will still take place in the cell underneath the intersection of the cell and interconnect. Consequently the gas has to diffusive a longer way to reach the reaction sites below the interconnect, compared to the reaction sites below the channel, and this leads to higher concentration gradients.

In the air electrode, the formed oxygen also has to diffuse from the reaction sites to the air channel. However, the air electrode is not investigated in this thesis. Instead the reader is referred to the literature, e.g. [172, 173].

The modeling work and results are published in the article “Modelling of Gas Diffusion in Ni/YSZ Electrodes in CO_2 and co-electrolysis“. The postprint of the article is included in the thesis appendix, see Appendix D.2.

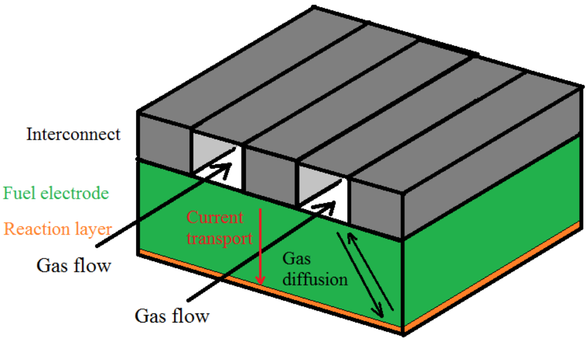

Figure 6.1: Sketch of diffusion and current transport. The gas is transported via diffusion from the boundary between the fuel electrode and the channel, to the TPBs at the bottom. Under the rib of the interconnect, the gas has to diffuse a longer distance, compared to under the channel.

6.1 Conclusion

A 1d and 2d model has been developed and the concentration and pressure gradient in the fuel electrode was calculated. The effect of the channel dimensions was investigated and found to have a significant influence on the mole fraction and pressure gradients. It was found that the CO mole fraction at the fuel electrode-electrolyte interface could be expressed as a simple linear function based on the current density (when the channel dimensions were fixed).

In the confidential version of the thesis, the linear functions were fitted to the obtained values for the effective diffusion in Chapter 5 and implemented in the in-house 3d stack model. With the altered 3d stack model the Boudouard margin was calculated with and without diffusion limitations. With diffusion limitations, the margin was significantly reduced. An uncertainty analysis including the η_{ES} and η_E showed that these parameters only induced a low uncertainty of the calculated Boudouard margin. The results shows that diffusion limitations are important in SOECs.

CHAPTER 7

Removal of formed carbon

The purpose of this chapter is to investigate if the formed carbon from the Boudouard reaction can be removed and ultimately if the carbon formation can be suppressed. If carbon can be removed without destroying the cells, the system can be operated at a higher conversion. This would decrease the load on a subsequent purification process and decrease the amount of recycle (which lowers the power consumption).

In this chapter, the background for carbon removal in the literature is reviewed with respect to solid oxide cells. Based on the literature, an experimental plan is designed and a test setup is build. The results are presented and discussed.

7.1 Carbon removal and suppression

No studies have been found for SOEC with respect to carbon removal or suppression. The removal of carbon has been studied for SOFC fueled with syngas, CH_4 and synthetic diesel reformate [174–178]. In a SOFC the CH_4 and synthetic diesel reformate fuel is either pre-reformed before entering the SOFC, or reformed within the fuel electrode, typically with H_2O, to give a mixture of CO and H_2. Carbon formation is thermodynamically favored when the oxygen-to-carbon and hydrogen-to-carbon ratio is low. However, for SOFC the addition of H_2O decreases the voltage of the cell (and thereby the power output), and it has therefore been investigated if the addition of H_2O could be omitted and the formed carbon subsequently removed. The formed carbon can be removed by using a gasification gas of either O_2, H_2O, CO_2 or H_2. The gasification gas will react with the solid carbon according to the following reactions:

$$\mathrm{C\,(s) + O_2 \rightleftharpoons CO_2} \tag{7.1}$$
$$\mathrm{C\,(s) + H_2O \rightleftharpoons CO + H_2} \tag{7.2}$$
$$\mathrm{C\,(s) + H_2 \rightleftharpoons CH_4} \tag{7.3}$$
$$\mathrm{C\,(s) + CO_2 \rightleftharpoons CO} \tag{7.4}$$

For gasification with H_2O, the formed CO might react further, via the water-gas shift reaction ($\mathrm{H_2O + CO \rightleftharpoons H_2 + CO_2}$).

The rate of gasification depends on the type of gasification gas. However, the gasification gas (except H_2) might also oxidize Ni:

$$2\,\mathrm{Ni} + \mathrm{O_2} \rightleftharpoons 2\,\mathrm{NiO} \tag{7.5}$$

$$\mathrm{Ni} + \mathrm{H_2O} \rightleftharpoons \mathrm{NiO} + \mathrm{H_2} \tag{7.6}$$

$$\mathrm{Ni} + \mathrm{CO_2} \rightleftharpoons \mathrm{NiO} + \mathrm{CO} \tag{7.7}$$

During manufacturing of the fuel electrode, NiO and YSZ are sintered together (Fig. 7.1a). The cermet is then heated and reduced with H_2 ($\mathrm{NiO} + \mathrm{H_2} \rightleftharpoons \mathrm{Ni} + \mathrm{H_2O}$, Fig. 7.1b) . During operation, Ni agglomerates and forms fewer but larger particles (Fig. 7.1c). If the Ni is later re-oxidized, the NiO can not fit the original space and a locale tensile stress is induced in the YSZ network [179]. This tensile stress can cause failure and ultimately cracks in the electrolyte (Fig. 7.1d).

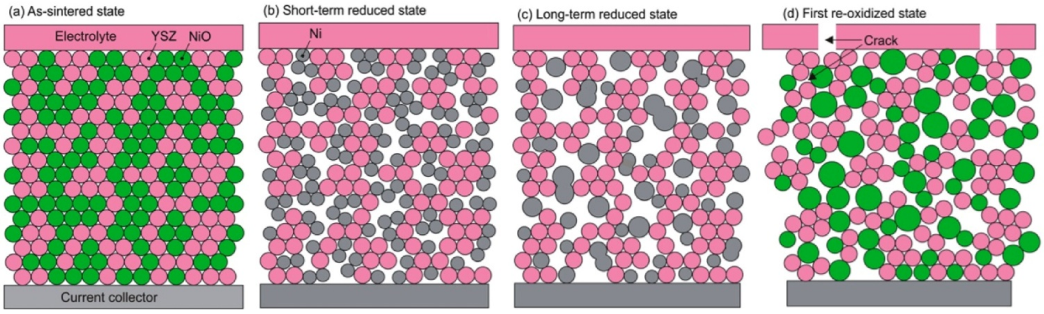

Figure 7.1: Cartoon illustrating the microstructural changes in the NI/YSZ cermet upon the different redox steps. Pink particles represent YSZ, and green and gray particles represent respectively NiO and Ni. a) As-sintered state. (b) Short-term reduced state. (c) Long-term reduced state. (d) First re-oxidized state. The two arrows point to a crack in the electrolyte and a failure in the ceramic network in the cermet, respectively. Modified from [179].

To ensure that the fuel electrode is not oxidized, it is necessary to choose a gasification gas, temperature, and exposure time, that ensures carbon removal but does not allows for Ni oxidation. This can e.g. be obtained with adding a small amount of H_2 or CO. The equilibrium constant for Ni oxidation with H_2O or CO_2 (Eq. (7.6) and Eq. (7.7)) is around 10^{-5} at 750 °C [176]. Using 5 % H_2, the reaction quotient is 0.05, which is much larger than the equilibrium constant. Re-oxidation of Ni should therefore not occur.

The literature will now be examined and a gasification strategy will be developed.

7.1.1 Literature survey

As described above, studies on carbon removal on SOEC's have not been published. A few studies on carbon removal on SOFC's have been published and are reviewed in the following.

Kirtley et al. [175] have used in situ Raman to study the formation and removal of carbon on Ni/YSZ. The carbon was formed at 730 °C when the electrode was exposed to dry methane at open circuit voltage (OCV). The removal of carbon was tested with H_2O, CO_2, and O_2 and monitored in situ with Raman spectroscopy. They found that carbon started to form within seconds after being exposed to dry methane and reached an asymptotic limit after 7-8 min. The asymptotic limit is ascribed to the limits of the penetration depth of the Raman excitation light. When exposed to H_2O, CO_2, and O_2, respectively, it was found that H_2O removed the carbon (observed as loss of signal) within 20 s, O_2 removed carbon within 60 s and CO_2 removed carbon within 120 s. After the loss of carbon signal, a NiO signal appear after 0 - 23 s for O_2, 60 - 150 s for CO_2, and 140 - 185 s for H_2O. The increase in NiO signal continued for O_2, while it reached an asymptotic limit when H_2O or CO_2 was supplied to the cell. The asymptotic limit, when H_2O or CO_2 was used, is reached because an equilibrium between the H_2O/H_2 and CO_2/CO, respectively, is obtained. The result of the study thus suggests that H_2O is faster than CO_2 and O_2 to remove carbon, while the risk of oxidizing Ni is highest when O_2 is used.

Kuhn and Kesler [176] tested a cell with a Ni/YSZ support layer and a Ni/ScSZ reaction layer. A carbon deposition gas (0.4 % of CH_4, C_2H_6, and CO, respectively in N_2) was used to form carbon over a period of 100 hr and afterward a gasification gas was used to remove the carbon. Fig. 7.2 shows the mass change when the sample was exposed to carbon deposition from CH_4 and CO-gas, and subsequently exposed to either a H_2 or CO_2-gasification gas. It can be seen that the mass is increasing over the first 100 hr at 600 °C and when the gasification gas is used (t>100 hr), the carbon is rapidly removed. At 700 °C the Boudouard reaction is thermodynamically limited by the small amount of formed CO_2 [176] (turquoise line in Fig. 7.2), and therefore no increase in the mass was observed. The study suggests that the carbon formation rate is linear (for at least the first 100 h) for carbon formation from CO, whereas the carbon formation rate for CH_4 is higher initially and then decreases. In Fig. 7.2a, the gas used for the black line (700/CH_4/CO_2) was 0.5 % CH_4 in N_2, whereas it was 0.375 % CH_4 for the blue, red, and green line. Comparing the black, red and green line in Fig. 7.2 it can be seen that the carbon formation rate is highly dependent on reactant concentration (black and red line), but the temperature only has a minor influence (red and green line). The result of this study suggests that carbon can be fully removed, even when a substantial amount has been formed. However, it does not specify the amount of carbon that can be formed before affecting the cell performance.

Subotić et al. [177, 178] studied the carbon removal from Ni/YSZ electrodes. First carbon was formed by exposing the electrode to a diesel reformat (15.4 % H_2, 13.7 % CO, 9.8 % CO_2, 20.3 % CH_4, 11 % H_2O and 29.8 % N_2) for 30 min, which caused massive carbon deposition. After the first 15 min, the cell performance deteriorated significantly faster, indicating that the catalytic active Ni-surface was covered with carbon and thus deactivating Ni for further reforming reactions (in SOFC, methane needs to be reformed to H_2 and CO). The cell was regenerated by exposing it to a wet H_2/N_2 mixture (45.6 %

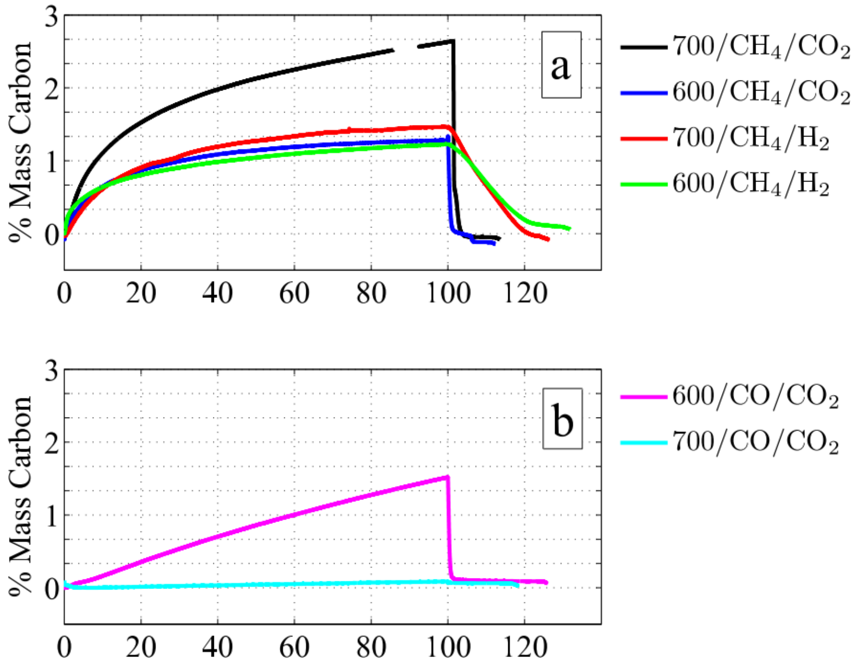

Figure 7.2: Carbon deposition and gasification results for 100 h chemical reversibility testing for carbon deposition from CH_4 (a) and CO (b), and subsequently gasification by H_2 or CO_2 at 600 and 700 °C. The legend states the temperature, the gas used during carbon deposition and the gas used to gasify the deposited carbon. E.g. 700/CH_4/CO_2 means that the temperature was 700 °C, CH_4 was used during the carbon depositon step and CO_2 was used to gasify the deposited carbon. Condition at carbon deposition for the top figure was: (Black line) 0.5 % CH_4 in N_2 201 sccm, (Blue, red and green line) 0.375 % CH_4 in N_2 at a total gas flow rate of 200.75 sccm. For the bottom figure: 0.4 % CO in N_2 at a total gas flow rate of 200.75 sccm . For gasification with CO_2, the gas composition was 95 % CO_2 and 5 % H_2 with a total flow rate of 156 sccm, and for gasification with H_2 the gas composition was 5 % H_2 in N_2. Figure modified from [176].

H_2, 11 % H_2O, and 43.4% N_2) for 24 hr and subsequently a dry H_2/N_2 mixture (45.6 % H_2 and 54.4% N_2) for another 20 hr. Fig. 7.3 shows the Ui-curve (Voltage, U vs current density, i.) before and after the carbon deposition as well as after the regeneration. From the figure, it can be seen that the gray curve (case 2 - after carbon deposition) is below the blue line (case 1 - carbon-free), meaning that the cell voltage and power density is decreased. After regeneration, the orange points (representing case 3 - after regeneration) are on top of the blue line. This shows that the original performance of the cell has been recovered. A total of three carbon formation and regeneration cycles was performed without any sign of degradation.

In continuation of Subotić et al.'s experimental work, a model describing the surface coverage of species was developed and the regeneration with wet and dry hydrogen was simulated [180]. It was found that elementary adsorbed carbon was removed within less than 5 min, which was substantially less than the experimentally found 44 hr. However, the formation of other carbon phases was not included due to lack of reaction kinetics and “discrepancies in the numerical handling of these separate phases and their interactions” [180]. Regeneration with CO_2/N_2-mixture and a $CO_2/O_2/N_2$-mixture was also simulated. It was found that when a CO_2/N_2-mixture was used, both C(s) and adsorbed CO could not be completely removed. When a $CO_2/O_2/N_2$-mixture was used, very high carbon gasification rates were observed. However, within seconds a potential for Ni oxidation was established.

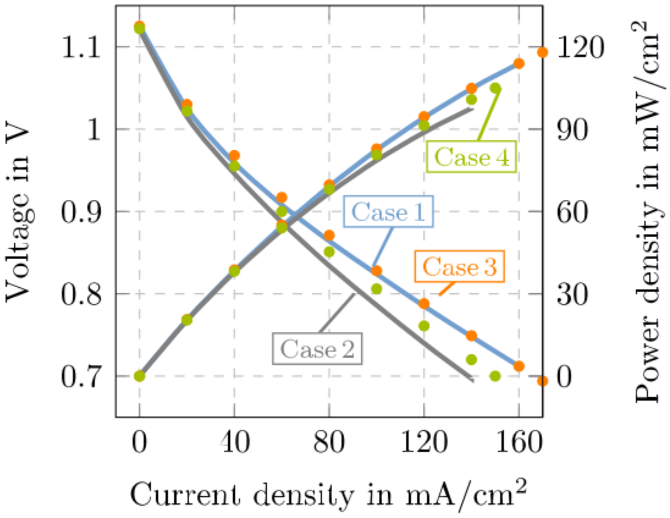

Figure 7.3: Electrochemical cell performance before and after carbon deposition and regeneration experiments: Case 1: Carbon-free anode; Case 2: After carbon deposition experiment; Case 3: After regeneration procedure; Case 4: After cathode degradation with compressor air (not commented further in this thesis). Figure modified from [178].

The studies by Subotić et al. suggest that carbon formed within the first 15 min of exposure to a carbon forming gas, affected the performance of the cells. Furthermore, it suggests that a regeneration step of 44 h is needed to fully regenerate the cell. Based on the study, a short period with carbon forming conditions will be used in the experiment. However, a regeneration step of 44 h is unfeasible for a commercial CO_2-electrolysis plant. Instead, the CO_2 concentration during gasification will be measured and the duration of the gasification step chosen based on these measurements.

The suppression of carbon formation by removal of deposited carbon has been reported for Ni/Al_2O_3 [181] and $Ni/CaAl_2O_4$ [182]. Both studies investigated the CO_2 reforming of CH_4, where carbon is a problem due to a low steam to carbon ratio. After a period of reforming and carbon deposition on the sample, the deposited carbon was removed with CO_2 (H_2 was also investigated in [182]). Fig. 7.4 shows the gain and loss of mass due to carbon deposition and gasification from [181], when the carbon deposition/gasification cycle was repeated multiple times. In Fig. 7.4A it can be seen that the relative increase in mass is largest for the first cycle and decreases for each subsequent cycle. Fig. 7.4B shows that when the temperature is increased, during a carbon removal step, the relative increase in mass decreases to zero. This suggest that all carbon have been removed. The rate for reforming of CH_4 does not decrease with the number of cycles. A similar observation was presented in [182].

The results presented above can not be directly transferred to the SOEC electrode used for electrolysis of CO_2: The carbon is formed from CO rather than CH_4, and due to the mechanical and thermal stresses in a cell, present in a stack, small amounts of formed carbon might deteriorate the cell within the first cycle. However, if it is possible to suppress the carbon formation on Ni/YSZ without deteriorating the cell, and the cell can sustain carbon removal, the time between carbon removal steps can be increased and the cells can be operated at higher CO concentrations.

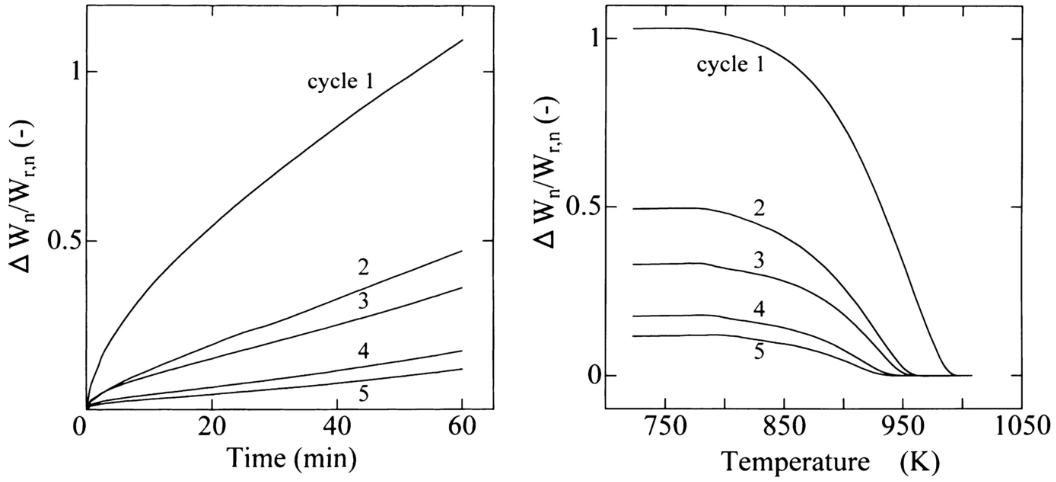

Figure 7.4: Left: A - Changes in the catalyst weight in methane flow (carbon deposition) T=1000 K, Methane flow $1.5 \times 10^{-5}\,\mathrm{mol\,s^{-1}}$. Right: B - Changes in catalyst weight in carbon dioxide (carbon removal step). ΔW_n is the difference in sample mass during the experiments and $\Delta W_{r,n}$ is the start mass for cycle r. Thus $\Delta W_n/W_{r,n}$ is the relative change in mass. The carbon removal step is started at 700 K and the temperature is continuously increased to 1000 K (5 K/ min). The CO_2 flow was $3.0 \times 10^{-5}\,\mathrm{mol\,s^{-1}}$. Figure modified from [181].

7.1.2 Input to experimental plan

Based on the literature study, H_2O will be used to remove the carbon. In addition, some H_2 will be added, so that the oxidation of Ni to NiO is thermodynamically limited. H_2O was chosen because the gasification of carbon with H_2O is relative fast, while the oxidation of Ni can be avoided with a small amount of H_2. The literature study showed that O_2 would be even faster to gasify carbon, but O_2 will also oxidize Ni. Small amount of H_2 can not be added to O_2, since it will be consumed rapidly and form H_2O (at the high operation temperature). CO_2 will be slow to gasify the carbon and a calculation study showed that CO_2 can not completely removed carbon [180]. A few studies on Ni catalyst suggest that the carbon formation can be inhibited by frequent cycles of carbon formation and removal. To investigate if this is the case, the CO_2 developed during the gasification step will be measured and used to evaluate the amount of carbon formed, as the number of regeneration cycles increases.

7.2 Experimental setup

A pilot unit for stack tests was built as part of this PhD study. The purpose of the pilot unit was to investigate the possibilities for carbon removal on SOEC stacks. This requires that the pilot unit must be able to supply a range of gasses (CO_2, CO, H_2, safety-gas (5% H_2 in N_2), air and steam), heat the gasses and stack, and supply the stack with current.

The pilot unit is outlined in Fig. 7.5 and consists of:

A: Mass-flow controllers (MFC) for addition of CO_2, CO, H_2, safety-gas (5% H_2 in N_2), and compressed air

B: Water mass-flow controller and evaporator

C: Electrical heaters (LE)

D: Furnace

E: Gas cooling with cooling water (CW) and sample extraction section (AP)

F: Power supply unit (PSU)

The addition of gas and water is controlled with mass-flow controllers (MFC). The gas to the fuel side of the cell (CO_2, CO, H_2, and safety-gas) is heated in the preheater LE 1, potentially mixed with H_2O evaporated in LE 5, and heated to 750 °C in LE 3. Similarly, the gas to the purge side (CO_2 and dry air) is heated in LE 2 and LE 4. The temperature in the furnace is controlled with LE 6. After the stack/furnace, the gas is cooled with cooling water (CW on Fig. 7.5) and points for gas sampling (AP) are placed. In case of trips, the valve before the needle valves at the safety gas line and the dry air line opens and a predetermined flow is obtained. The experimental setup was controlled with National Instruments' program Labview, which was also used as data acquisition system. During the regeneration step, occasionally continuous measurement of the released CO_2 was also taken with a "Guardian NG", which was capable of measuring CO_2 in the 0-3 % range. During the regeneration step, H_2O will oxidized solid carbon to CO, which is subsequently

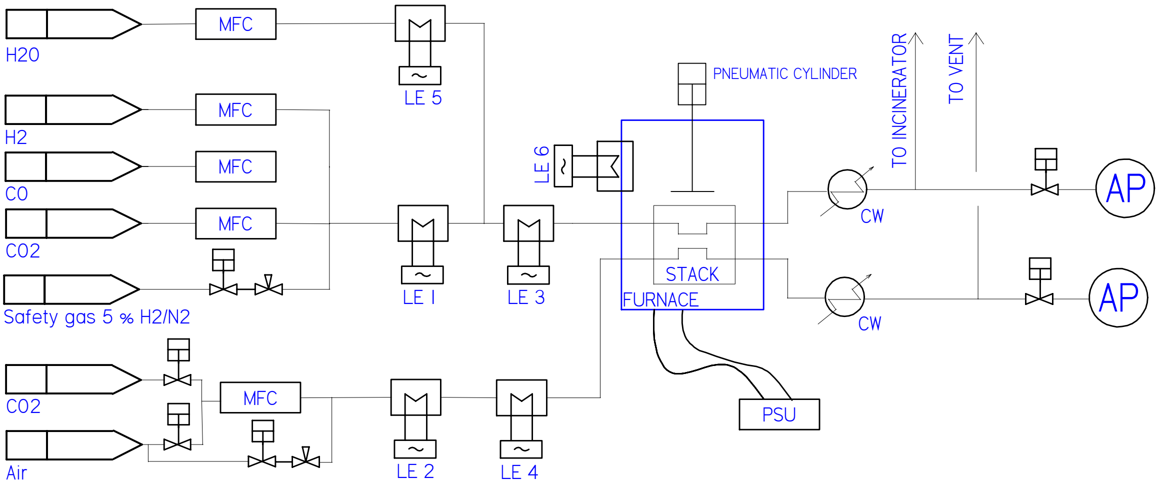

Figure 7.5: Schematic drawing of the experimental setup (the pilot plant).

reacted to CO_2 via the water-gas shift reaction. A thermodynamic calculation (using internal software at Haldor Topsoe A/S) showed that, at 750 °C, approx. two-third of the oxidize carbon will be present as CO_2 and one-third will be present as CO. The kinetics for the water-gas shift reaction are fast and it is therefore expected that the actual gas composition will be close to the thermodynamic equilibrium. The CO_2-detector can therefore be used to give a rough estimate of the amount of released carbon, and to compare the amount of released carbon during the experiment.

A 9-cell stack (supplied by Haldor Topsoe A/S) was placed in the furnace on a manifold and held in place by a compression system. Between the stack and the manifold a Statoterm gasket was placed, to ensure the gas tightness. The electrical heaters and the furnace were regulated with a maximum rate of 3 K/ min to ensure that the cells/stack were not damaged from thermal stress during heating and cooling.

The 9-cell stack was a 2.5G Ni/YSZ fuel electrode supported cell [108]. The active fuel electrode consisted of Ni/YSZ, the electrolyte consisted of YSZ and the air electrode consisted of LSCF (strontium doped lanthanum ferrite partially cobalt doped) with a CGO (gadolinia doped ceria) barrier layer between the air electrode and the electrolyte. The 9-cell stack was placed in a casing. Since the casing is primarily used for larger stacks, a void between the stack and the casing had to be filled with a compression mat. Between the mat and the stack, four thermocouples were placed and the stack and compression mat were squeezed into the casing, see Fig. 7.6.

7.3 Experimental plan

To test the possibility of frequent carbon removal by a water regeneration step, three stacks were tested in the experimental setup. The stacks were tested with the following

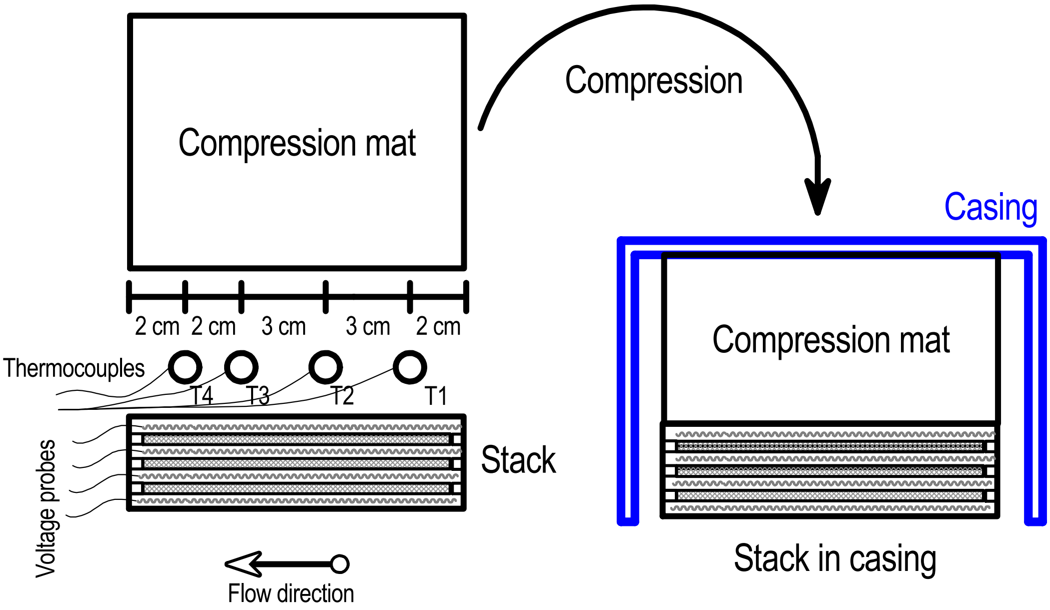

Figure 7.6: Placement of thermocouples and stack position within the casing. Four thermocouples were placed on top of the stack (separated from the stack with a thin Statoterm plate). On top of the stack and thermocouples, a large compression mat was placed. The parts were placed in the casing and compressed, so that the stack aligned with the bottom of the casing. This ensured that the space between the stack and casing became gas-tight. The thermocouples are referred to as T1, T2, T3 and T4. T1 is closest to the inlet of the gas flow, and T4 is closest to the outlet. Note that, due to readability, only 3 cells are shown in the stack and the stack/compression mat is not to scale. The gas flow to the stack is supplied via a manifold, which is fixed to the bottom of the casing.

steps, explained in details below:

1. Heat up + open circuit voltage (OCV) measurement
2. Voltage-current (Ui)-measurement (only stack A)
3. Initial degradation run
4. Stack A: Operation at carbon forming conditions with thermal cycling
   Stack B+C: Operation at carbon forming conditions with a water regeneration step and thermal cycling

The flow, temperature and applied current density for the steps are summarized in Table 7.1. The theory behind the OCV measurement and cell voltage is described in the introduction part, Section 2.1. Illustrations of the response to an OCV measurement, a

Table 7.1: Overview of the steps in the experiments. γ is the conversion, fuel flow is the flow to the fuel electrodes and purge flow is the flow to the air electrodes.

Test	t / h	T / °C	$\vec{i_t}$/ $\mathrm{A\,m^{-2}}$	γ / %	Fuel flow / $\mathrm{NL\,h^{-1}}$				Purge / $\mathrm{NL\,h^{-1}}$	
Step					CO_2	H_2	H_2O	5 % H_2/N_2	CO_2	Air
1.0 Heating	3.6	25→750	–	–	500	–	–	400	–	1000
1.1. OCV measurement	1.5	750	–	–	–	330	–	400	–	1000
2.0 Ui-measurement, stack A only	12	750	918–7800		1000	50	–	–	741	–
3.0 Initial degradation	≈ 200	750	7800	32	1000	50	–	–	741	–
3.1 Regeneration step (similar to 4.1-4.4)										
3.2 OCV measurement	1.5	750	–	–	634	32	–	–	–	1000
4.0 Carbon forming operation										
4.0A Stack A	16.3	750	7800	65	492	25	–	–	741	–
4.0B Stack B	0.25	750	7800	65	492	25	–	–	741	–
4.0C Stack C	0.5–1.0	750	7800	65	492	25	–	–	741	–
Step 4.1-4.4 for stack B and C only										
4.1 Flush I	0.033	750	–	–	492	25	–	–	741	–
4.2 Flush II	0.016	750	–	–	0	25	–	400	741	–
4.3 Flush III	0.033	750	–	–	–	–	–	400	741	–
4.4 Water injection	0.083	750	–	–	–	–	80	400	741	–
Return to 4.0B (stack B)/4.0C (stack C)										
4.5. OCV measurement	1.5	750	–	–	634	32	–	–	–	1000
4.6. Cooling	3.3	750→100	–	–	500	–	–	400	–	1000
4.7. Heating	3.3	100→750	–	–	500	–	–	400	–	1000
4.8. OCV measurement	1.5	750	–	–	634	32	–	–	–	1000
5.0 Return to step 4										

trip, and a thermocycle, is illustrated in Appendix C. The Ui-measurement for stack A is described below in step 2.

1) After the stack had been mounted in the setup, it was heated from room temperature to 750 °C. After reaching the specified temperature, the flows were changed (according to Table 7.1) and an OCV measurement was taken by recording the cell voltage after 1.5 hr (at which the cell voltage and temperature were stabilized).

2) Ui-measurement was conducted for stack A. The Ui-measurement consisted of a series of measurements of the cell voltage, U, at different current densities, $\vec{i_t}$. The reason for the Ui-measurement was to test the functionality of the test setup with a real stack and to be able to compare the stack performance with some of Haldor Topsoe A/S's internal tests (not discussed further in the thesis). With the flow specified in Table 7.1, the current density was increased to 918, 1835, 2753, 3670, 4588, 5964, 6882, and 7800 $\mathrm{A\,m^{-2}}$, respectively. After a period of 1.5 hr (after which the cell voltage and temperature stabilized), the cell voltage and temperatures were recorded, and the current density was increased. The Ui-measurements should not cause a difference between stack A and B/C, since the Ui-measurements were conducted at conditions were carbon formation should be thermodynamically unfavored and the total time for the Ui-measurement was very short compared to step 3 – the initial degradation step.

3) During stack tests at Haldor Topsoe A/S it is commonly observed that a relative high initial degradation rate can be seen for SOECs. This has also been reported in the literature [183] and [11, pg. 88]. To separate this from the degradation observed from operating at carbon formation favored conditions, the stack was operated at unfavored carbon formation conditions for approx. 200 hr. With the in-house 3d stack model, Section 2.5, it was calculated that the initial degradation could be conducted at 7800 $\mathrm{A\,m^{-2}}$ with an overall conversion of 32 % without carbon deposition (the temperature margin was + 18 K). To test if carbon had formed anyhow, a carbon removal/regeneration step (similar to the one described in step 4) was performed before the operation at carbon forming condition was started.

4) After the initial degradation step, the overall conversion was increased to from 32 % to 65 % by decreasing the inlet flow. In this way, the carbon potential was increased and, with the in-house 3d model, it was calculated that the Boudouard equilibrium temperature at approx. half the active cell area was below the actual temperature within the stack. Thus, the stack was operated at conditions where carbon formation would certainly be expected. Stack A the stack was operated at the carbon formation conditions for 16 h, followed by an OCV measurement, a thermocycle, and another OCV measurement. In the thermocycle step the system was cooled to 100 °C, by lowering the set point of the heaters with a ramp of 3.3 °C/ min. Due to the thermal mass of the furnace and stack, the actual rate of temperature change was less than 3.3 °C/ min for a large part of the cooling step. When 100 °C was reached, the system was heated to 750 °C and an OCV measurement was performed. The flow was then changed and a current density of $7800\,\mathrm{A\,m^{-2}}$ was again applied for 16 h. 16 h was initially selected because the thermocycle was calculated to take 8 h, and a complete cycle could thus be performed each day. However, the addition of OCV measurements (2x1.5 h) and the extended cooling time, due to the high thermal mass, made the cycle last 32 h instead. However, the 16 h of operation at carbon formation conditions was kept.

For stack B and C, regeneration steps were performed frequently, to hopefully avoid a catastrophic build-up of carbon. In the test of stack B, regeneration step was performed after each 15 min of carbon forming operation. For stack C, the time at carbon forming operation, was 30 min for the first 6 thermocycles and then increased to 60 min for remaining thermocycles. The regeneration step consisted of flushing the setup with the operation gas mixture CO_2/H_2 with a current density $0\,\mathrm{A\,m^{-2}}$ for 2 min, followed by a gas mixture of H_2 mixed with the safety-gas for 1 min and ultimately pure safety-gas for 2 min. Then $64.3\,\mathrm{g\,h^{-1}}$ H_2O (equal to $80\,\mathrm{NL\,h^{-1}}$) was added for 5 min to the safety gas flow. The flushing of the setup was necessary to make the operation of the measurement safe and avoid saturation of the CO_2-analyzer. The first flush with CO_2/H_2 ensured that CO was flushed out of the system. Thus, if any leakage between the setup and the analyzer should occur, the amount of CO released would be low. The next two flushing steps brings the CO_2 concentration in the setup below 3 %, which is the upper range of the CO_2-analyzer. After the water injection step, an OCV measurement was performed.

After the experiments, a post-mortem analysis (PMA) was performed. The PMA consisted of dismantling the stack, separating and visual inspecting of each component in the stack. The visual inspection was conducted with both the naked eye and with SEM.

7.4 Results

First, the results of the initial degradation step (step 3.0) are presented and then the results from the regeneration step (step 3.1) are presented. Afterward, the results of the carbon forming and regeneration steps (step 4.0 to 4.7) are presented for each stack. Finally, the amount of carbon removed during the regeneration step are estimated.

An erroneous PLC (Programmable Logic Controller) caused several trips during the experiments. The PLC was responsible for the safety system of the pilot unit and despite thorough troubleshooting from Haldor Topsoe A/S's electricians, the problem was first identified and solved after the completion of the experiments. A small number of trips were caused by issues related to the laboratory at which the setup was located (loss of gas and power, shutdown of incinerator unit). Furthermore, the power supply unit also malfunctioned and was replaced with a spare. The effects of the trips are described in the appropriate subsections below.

7.4.1 Initial degradation - Step 2-3

Fig. 7.7 shows the average cell voltage and temperature of the three stacks during the initial degradation period. Unexpected shutdowns (trips) and OCV measurements are marked with symbols. From the figure, it can be seen that the average cell voltage, and temperature, of the three stacks are close to each other. The initial degradation period for all stacks was affected by a number of trips. To increase the readability of the presented measurements, the time on the x-axis is the effective time of operation. Thus, the downtime from trips and OCV measurement was removed.

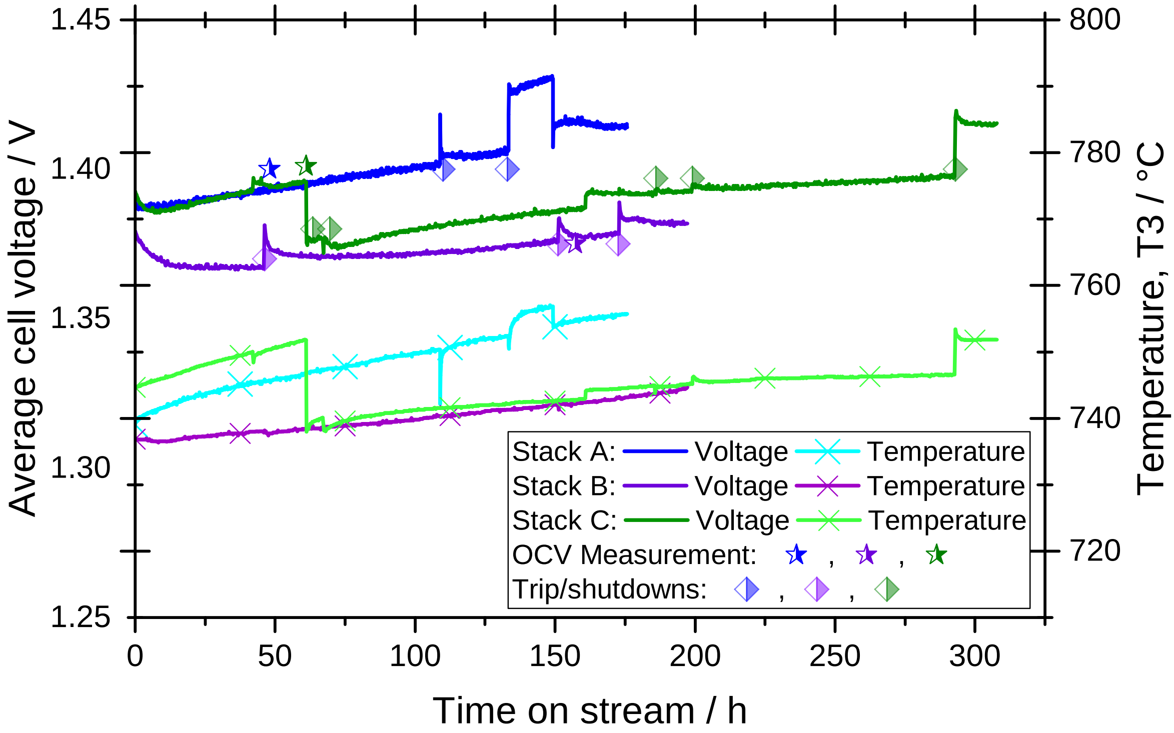

Figure 7.7: Average cell voltage and stack temperature (T3). OCV measurements and trips are shown with star and diamond symbols, respectively.

From the average cell voltage curve, the effect of the trips can be seen as small increasements in the voltage. All stacks ran at the conditions described in step 3 in Table 7.1, except for:

- Stack A from $t = 137\,\mathrm{h}$ to $t = 154\,\mathrm{h}$, where the safety gas was not turned off after a trip by a mistake.
- Stack C from $t = 61\,\mathrm{h}$ to $t = 294\,\mathrm{h}$, where the current density was decreased from $7800\,\mathrm{A\,m^{-2}}$ to $6882\,\mathrm{A\,m^{-2}}$.

The reason for the decrease in current density for stack C, was a large increase in the temperature observed for the first 61 h. To compensate for the decrease in the current density, the time was increased from ≈200 h to 294 h. After $t = 294$ h, the current density was increased to 7800 $\mathrm{A\,m^{-2}}$ and neither the cell voltage nor temperature exceeds the ranges observed from stack A. The OCV measurement all showed cell voltages of close to 1.2 V, which shows that the cells were not leaking during the initial degradation.

The deviation between the average cell voltage and temperature of the three stacks is probably cause by differences from the production of the cells.

7.4.2 Regeneration step - Step 3.1

After the initial degradation step, a regeneration step was performed to test if carbon had formed. Fig. 7.8 shows that CO_2 was formed when water was added to stack B and C after the initial degradation period, suggesting that solid carbon was gasified. The regeneration step was also applied to stack A, but the CO_2-analyzer was not installed at that time, and therefore stack A is not included in Fig. 7.8. The presence of solid carbon after the initial degradation step, which should have been running at thermodynamically unfavorable conditions, suggest that the model predictions are not accurate for the conditions used in the initial degradation step. In the previous chapter, it was shown that diffusion limitations may cause high concentration gradients in the fuel electrode, when the current density is high. This can explain the presence of carbon. The diffusion limitations was not included in the predictions made prior to the carbon removal experiments, because the diffusion experiments was not completed at that time. The diffusion was later included, and it was found that the Boudouard margin was negative at the conditions used for the initial degradation. The exact calculate is not included in the thesis, due to confidentiality. From the figure, it can be seen that the CO_2 peak is larger for stack C. When the peaks were integrated, the peak for stack B was approx. 11 g and the peak for stack C was approx 38 g (the mass was calculated with Eq. (7.8) on page 104). This suggests that carbon is forming at both 6882 and 7800 $\mathrm{A\,m^{-2}}$.

To test if the CO_2 signal was caused by release of adsorbed CO or CO_2, a simple test was performed. A gas consisting of 50 % CO and 50 % CO_2 was passed over stack C before the initial degradation step was started. The temperature of the stack was 750 °C and no current was applied. After 30 min the regeneration step was started. During the regeneration step no CO_2 peak was observed. This shows that the observed peak during the carbon formation/regeneration steps was not caused by adsorbed CO or CO_2, but due to deposited carbon.

7.4.3 Operating at carbon forming conditions, carbon removal, and thermocycling - Step 4

During the experiments, the voltage and temperature were continuously measured and logged. However, in order to facilitate an efficient data representation of the experiment,

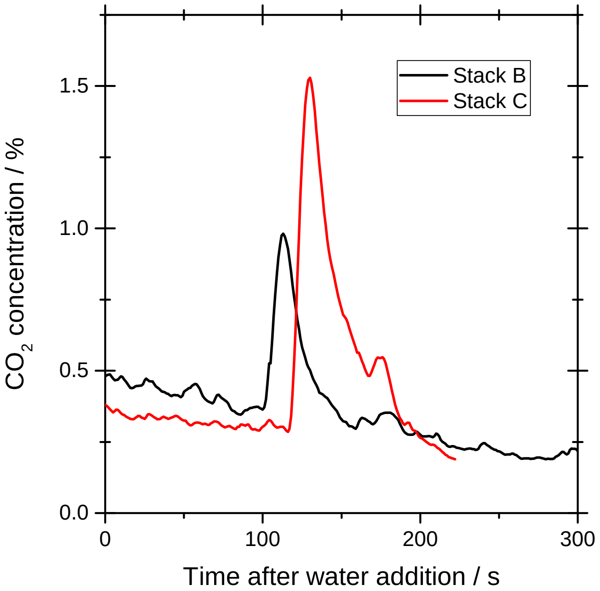

Figure 7.8: Measured CO_2 during the first regeneration step after the initial degradation step for stack B and C. Conditions: $T = 750\,°C$, Gas flow: 400 $NL\,h^{-1}$ of safety gas (5 % H_2/N_2) + 80 $NL\,h^{-1}$ H_2O.

the reported measurements are reduced to the following measurements during each cycle in step 4 (illustrated in Fig. 7.9). The first measurement is at the carbon formation conditions, right before the regeneration step starts (end of step 4.0B and 4.0C, for stack B and C only). These are marked $M_{1,1} \ldots M_{1,n}$ in Fig. 7.9. For stack B and C, the second measurement is at the carbon formation conditions, right before the last regeneration step before the thermocycle starts (marked M_2 in Fig. 7.9). For stack A, it is at the carbon formation conditions right before the thermocycle starts, since no regeneration steps are used for stack A in step 4. The third measurement is at the end of the OCV measurement (step 4.8) after the thermocycle (marked M_3 in Fig. 7.9). The first two measurement were chosen because they represent the measurement of the performance of the stack at pseudo-steady state. It can be seen from Fig. 7.9 that the voltage is high when the carbon formation conditions are applied, but reaches a pseudo steady state during the step length (due to the stabilization of the temperature). The third measurements were chosen because the OCV measurements can be used to identify if a cell has become leaking.

The effect of operating under carbon forming conditions are shown in Fig. 7.10, Fig. 7.13 and Fig. 7.15 for stack A, B, and C, respectively. The figures consist of subfigures showing cell voltage and temperature at the three different measurement points described above.

For stack A, it can be seen from Fig. 7.10a and c that the performance of the stack is not changed with the first four thermocycles, since the cell voltage and temperature are almost constant. However, after the fourth thermocycle, the cell voltage of cell 1, 6, 7,

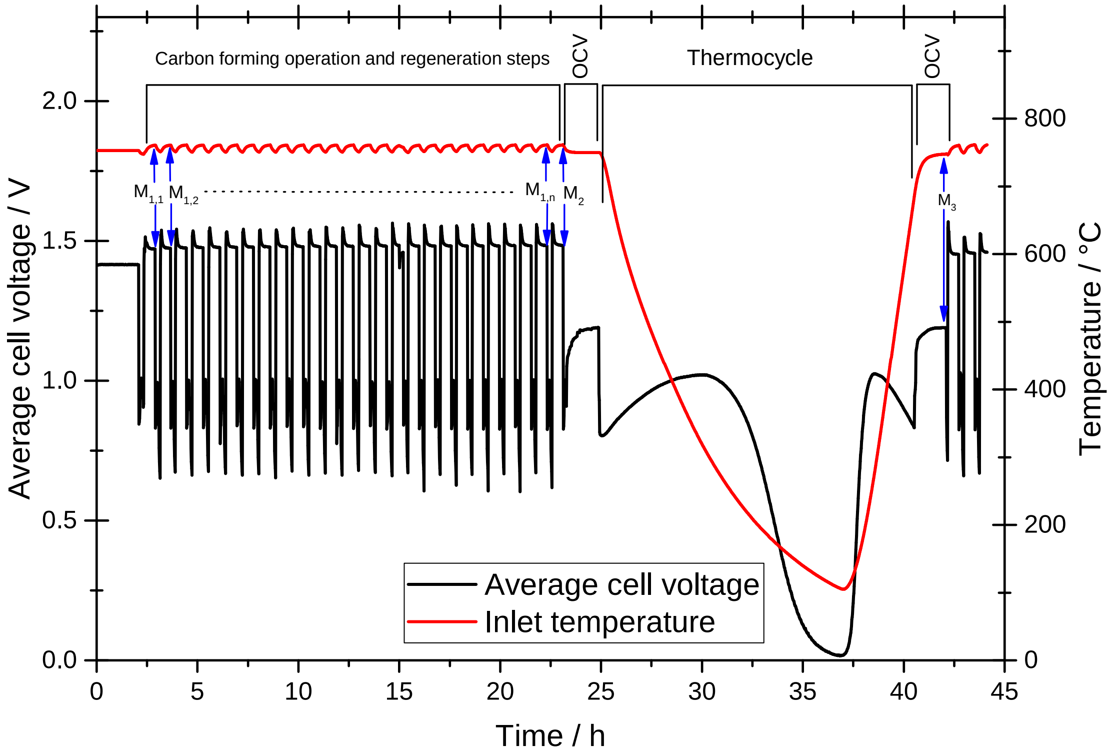

Figure 7.9: Illustration of the measurement points (marked M in the figure) at which data for step 4 are reported. The figure shows the carbon forming operation with regeneration steps (step 4-4.4, from t=3 h to t=23), a OCV measurement (step 4.5, t=23 – 25 h), a thermocycle (step 4.6-4.7, t=25 - 40 h), another OCV measurement (step 4.8, t=40-42 h) and the start of another set of carbon forming/regeneration steps (t>42 h).

and 8 increases. Because of the increase in cell voltage, the temperature of the stack also increases (described in Section 2.2). The rapid increase in cell voltage, especially for cell 8, after the fourth and sixth thermocycle suggest that a mechanical failure has occurred in the cell. The OCV measurement (Fig. 7.10b) shows that the OCV is very close to constant during the experiment. This suggests that the cells in the stack are not leaking. If the stack was leaking, the OCV should decrease and the temperature should increase (due to combustion of leaking H_2), compared to the initial values.

The cell voltage and stack temperature kept increasing until 17 thermocycles had been completed. To avoid a complete failure of the stack, the test was stopped and dismantled. The PMA showed that the fuel electrode and the electrolyte was severely delaminated for cell 8 at the fuel outlet (where the risk of carbon formation is highest), and also cell 6, 7 and 9 were delaminated to a lesser extend. Fig. 7.11 shows a photograph of cell 8 (purge side). The light gray areas are where the air electrode and electrolyte (dark gray) has delaminated from the fuel electrode. A piece of the cell was also investigated with SEM. From Fig. 7.12 it can also be seen that the fuel electrode and electrolyte has delaminated.

This clearly shows that delamination has taken place, and can also explain the sudden increase in cell voltage and temperature observed in Fig. 7.10.

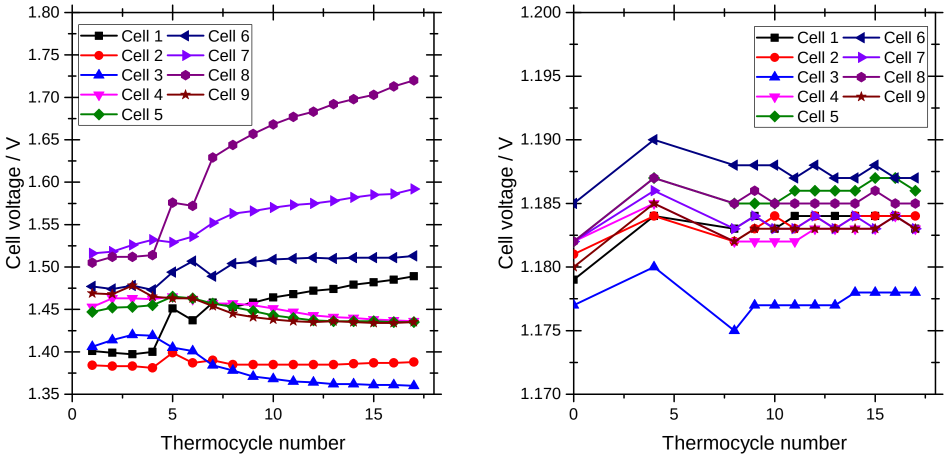

(a) Cell voltage before thermocycle **(b)** OCV after thermocycle

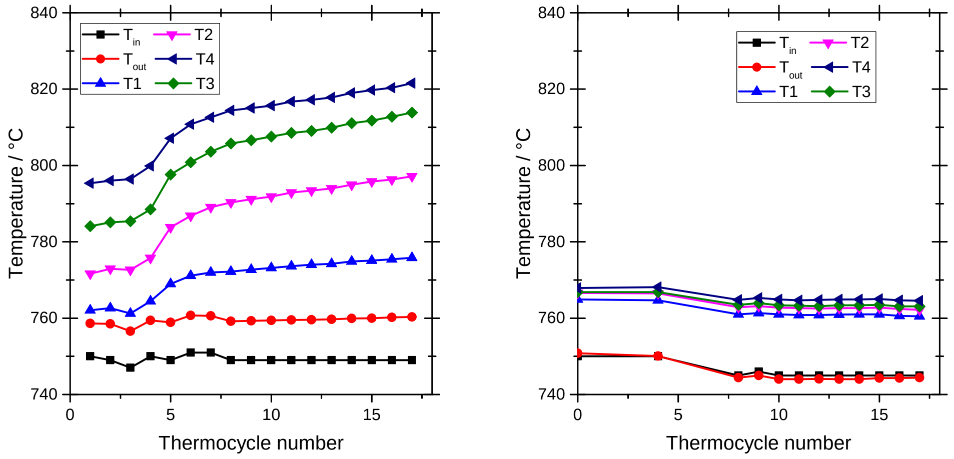

(c) Temperature at cell voltage measurement before thermocycle **(d)** Temperature at OCV-measurement after thermocycle

Figure 7.10: Cell voltage, temperature and OCV-measurement for stack A. a) Cell voltage before the thermocycle, b) OCV after the thermocycle, c) Temperature before the thermocycle, d) Temperature during OCV-measurement

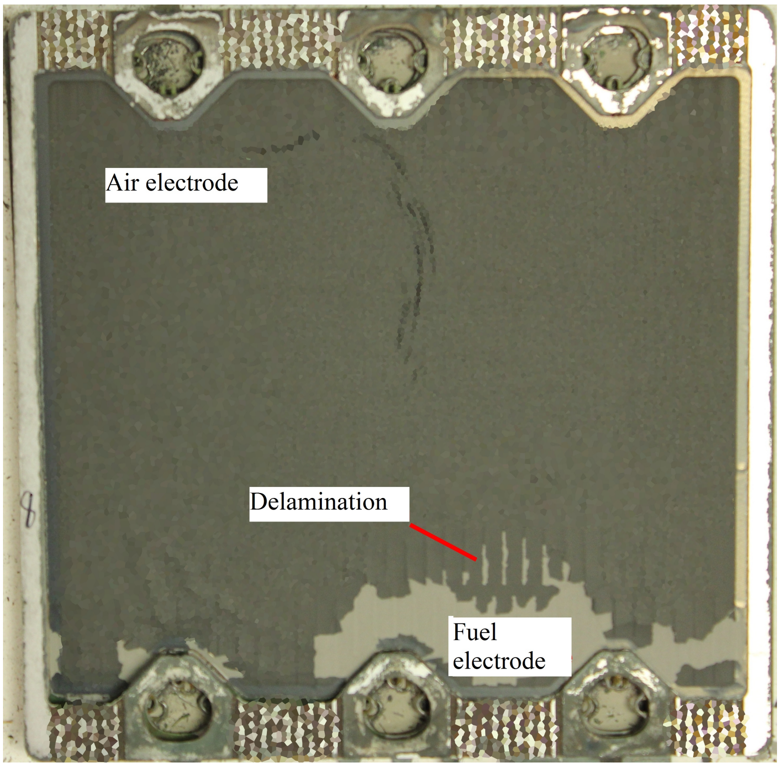

Figure 7.11: Picture of air-side of cell 8 from stack A after test. The flow is entering through the holes at the top and existing at the bottom holes, thus the highest CO concentration, and thus the highest carbon forming risk, is present at the bottom. The dark gray are the air-electrode and electrolyte, and the light gray is the fuel electrode. The picture shows clear delamination between the air electrode/electrolyte and the fuel electrode. The pictures has been blurred, due to confidentiality.

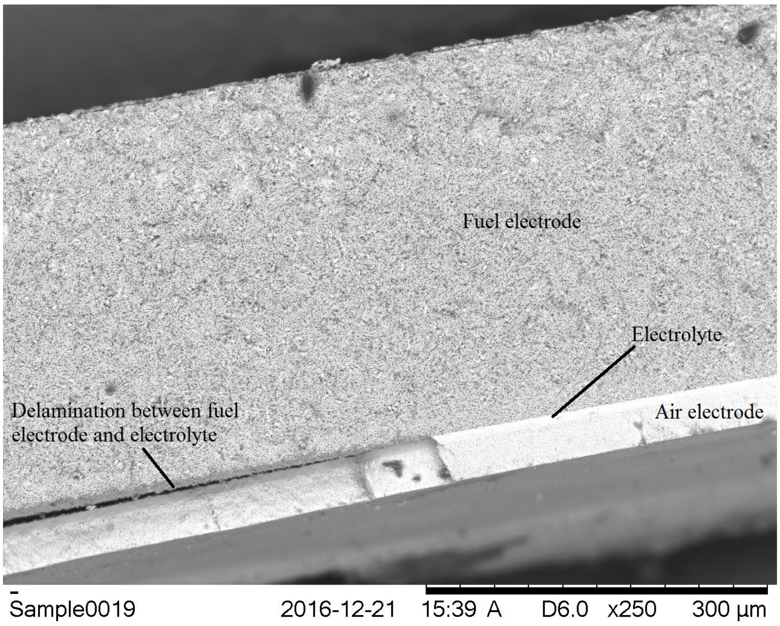

Figure 7.12: SEM picture of cell 9 from stack A. In the left of the picture a delamination between the fuel electrode and electrolyte can be seen.

The results for stack B are unfortunately very limited. Before the OCV measurement, after the second thermocycle was completed, the experimental setup tripped and was restarted. After the restart, the programmed experimental run was automatic started at the carbon forming step. However, the heaters (LE1, LE2, LE3, and LE4) were not properly restarted, so the temperature of the stack/furnace decreased slowly towards room temperature. The thermal mass of the experimental setup was quite large compared to the cooling of the setup, so the cooling rate was approximately the same as during the thermocycles and the stack should therefore not be exposed to thermal stress exceeding its design limits. However, as the stack cooled, the carbon formation conditions become more and more severe. In addition, during the regeneration step, the evaporated water was mixed with cold gas before entering the stack, instead of being heated to 750 °C. This caused the temperature within the stack to rapidly drop during the water addition step. After the water addition step, the internal of the stack was heated from conduction and convection of heat from the furnace, casing, and manifold. The stack was thus both exposed to severe carbon formation conditions and rapid cooling/heating. When the heaters were correctly restarted, and an OCV measurement was initialized, the highest temperature within the stack (T3) increased to 1000 °C within a minute. During the short time, the OCV was around 1.1 V for cell 1-4 and 0.9 V for cell 5-9. These two observations suggest that the stack was leaking, resulting in mixing of hydrogen and air, with a subsequent combustion within the stack.

From the PMA, it could be seen that a hole was formed from cell 1 all the way to cell 9 through the cells and interconnects. Fig. 7.14 shows the hole in cell 1 and cell 9. Furthermore, the green color of the fuel electrode shows that the fuel electrode had been exposed to an oxidizing atmosphere (NiO is greenish), which will occur when oxygen, from the air side, are transported to the fuel side and reacts with the hydrogen (which acts as a reducing species, preventing oxidation of NiO).

From the data that was obtained from stack B, it can be seen that the cell voltage of cell 8 increased during the carbon forming/regeneration steps. The cell performed poorly before the first regeneration step (1.75 V), so the increase in voltage during the carbon forming/regeneration steps are likely due to an inherent failure, rather than a pure result of the carbon forming/regeneration steps. For the remaining cells, no increase in cell voltage was observed. This suggest that the carbon forming/regeneration steps in them selves (without thermocycling), do not damage the cell in the short term.

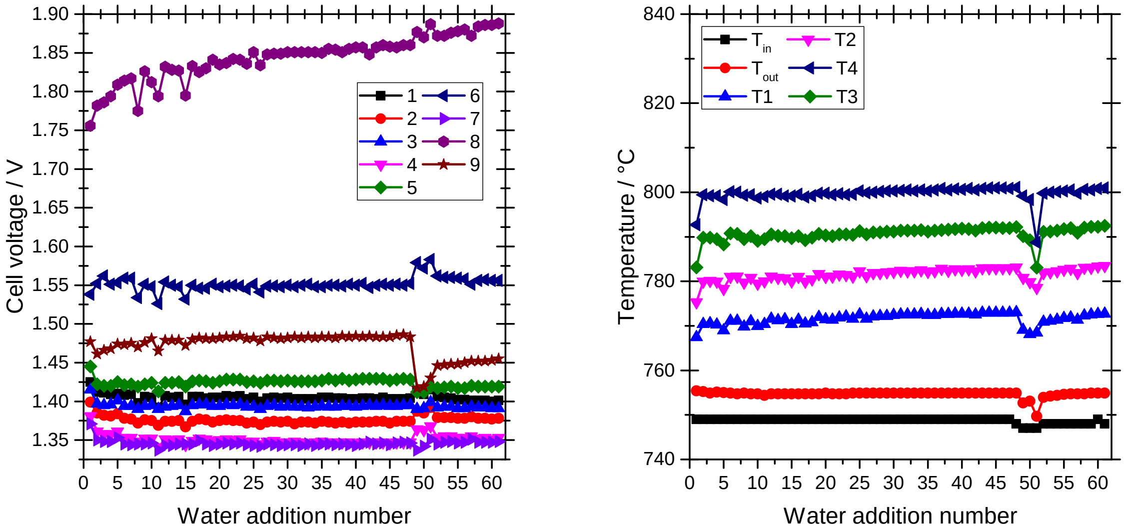

(a) Cell voltage before water regeneration step **(b)** Temperature at cell voltage measurement before water regeneration step

Figure 7.13: Cell voltage and temperature for stack B. a) Cell voltage before the water regeneration step and b) Temperature before the water regeneration step.

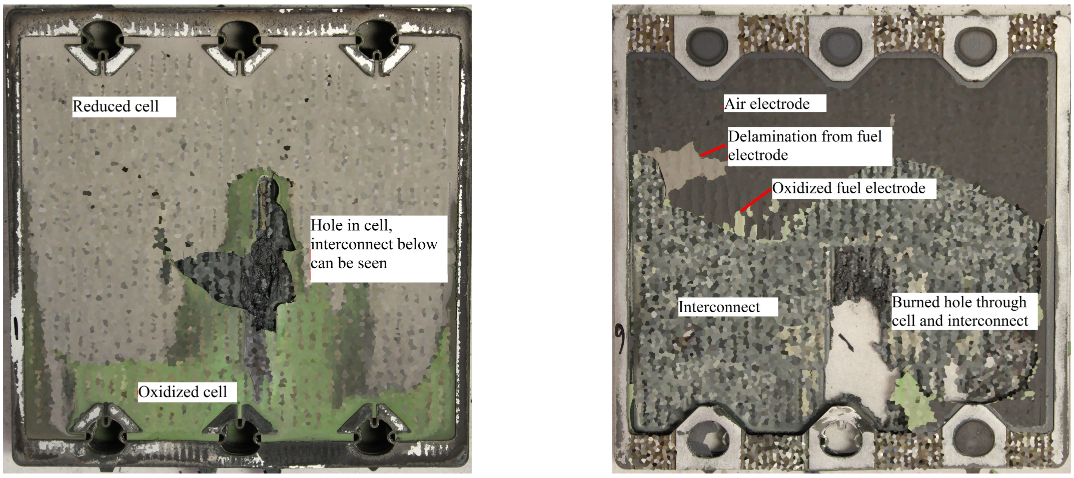

(a) View of the fuel-side of cell 1 **(b)** View of the air-side of cell 9

Figure 7.14: Pictures of cell 1 and 9 from stack B after test. The picture clearly shows a hole through the cells. In both pictures, it can also be seen that the Ni in the fuel electrode has been oxidized to NiO (greenish color). In the picture of cell 9, it can also be seen that the air-electrode/electrolyte has delaminated from the fuel electrode, since there are areas where the dark gray (air-electrode/electrolyte) has been removed from the light gray (fuel electrode). The pictures has been blurred, due to confidentiality.

Fig. 7.15 shows the results of stack C. From Fig. 7.15e it can be seen that the voltages of cell 1 and 2 are very high at the beginning of the experiment, and that the voltage of cell 2 is rapidly increasing to around 2 V within the first 20 carbon forming/regeneration steps, before the first thermocycle. After five thermocycles, the cell voltage of cell 1 and 2 starts to decrease. However, it can be seen from Fig. 7.15c that a large temperature increase also occurs after 5 thermocycles. This is likely caused by gas leakage, causing internal combustion of CO. The suspicion of gas leakage is further strengthened when looking at the OCV charts (Fig. 7.15b and Fig. 7.15d). From the OCV charts, it can be seen that the OCV for cell 2 is decreased to 1.1 V after 3 thermocycles and down to 0.85 V after 5 thermocycles. This clearly shows that the gas composition in cell 1 is different after 2 and 5 thermocycles. It can also be seen from the OCV charts that the temperature inside the stack is high and increases rapidly with each thermocycle. Since no current is drawn from the stack, and the gas inlet flows and heats are constant, this shows that gas is leaking and being combusted within the stack.

After 10 thermocycles, the cell voltages are rapidly decreasing and the temperature increasing. From Fig. 7.15b it can be seen that the OCV for cell 1, 2, and 3 after 10 thermocycles are all low. This suggest that cell 1, 2, and 3 are now leaking gas, causing a large internal combustion, which heats the cell. In the final measurement, the temperature at one of the thermocouples reached 980 °C, as a result of the internal combustion.

Indeed the PMA showed a hole all the way through the stack, severe re-oxidizing of Ni (meaning that the gas at the fuel electrode has been oxidizing, since the hydrogen had been combusted), and locations where the interconnect had melted. Fig. 7.16 shows the bottom and top cell, where the former mentioned observations can be seen.

The results are discussed in the discussion section.

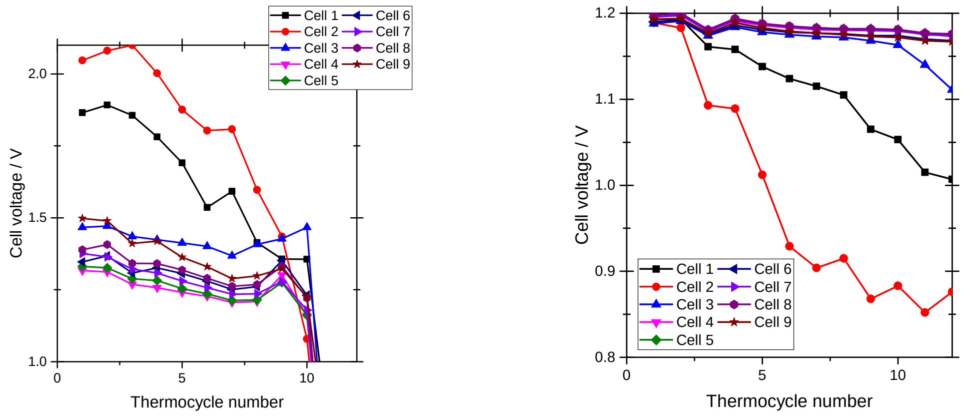

(a) Cell voltage before thermocycle **(b)** OCV after thermocycle

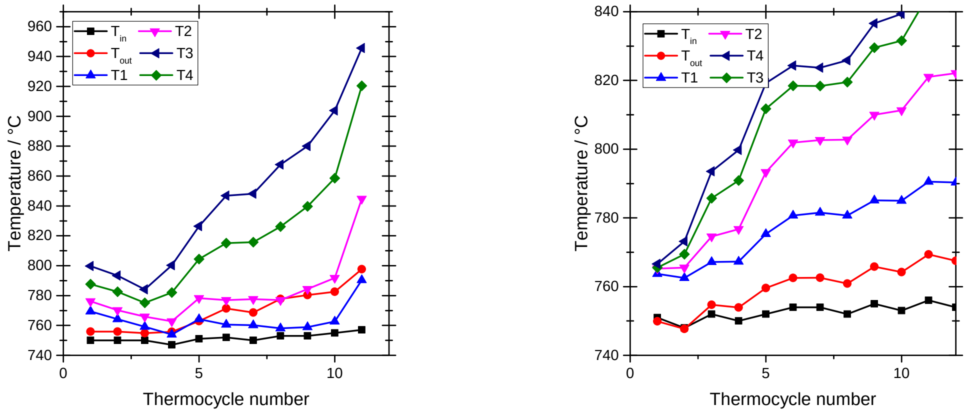

(c) T at cell voltage measurement before thermocycle **(d)** T at OCV-measurement after thermocycle

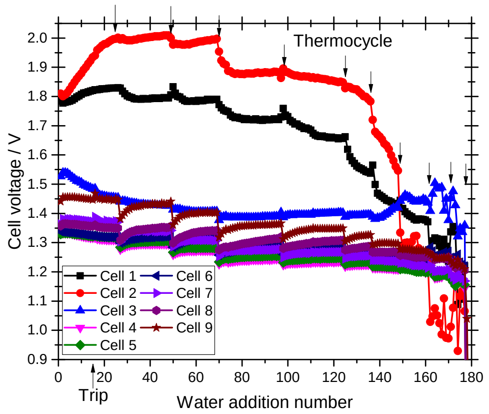

(e) Cell voltage before each water regeneration step. The measurement before a thermocycle is marked with arrows. The setup tripped before the first thermocycle (mark with an arrow on the abscissa).

Figure 7.15: Cell voltage, temperature and OCV-measurement for stack C. a) Cell voltage before the thermocycle, b) OCV after the thermocycle, c) Temperature before the thermocycle, d) Temperature during OCV-measurement, and e) Cell voltage before each water regeneration step. Note that different scales are used on all figures. The lines are for guiding the eye.

(a) View of fuel-side of cell 1 **(b)** View of fuel-side of cell 9

Figure 7.16: Pictures of cell 1 and 9 from stack C after test. The pictures clearly shows a hole through the cells (left corner). In both pictures, it can also be seen that the Ni in the fuel electrode has been oxidized to NiO (greenish color). The pictures has been blurred, due to confidentiality.

7.4.4 Amount of C(s) removed during the regeneration step

With the CO_2-analyzer it was possible to measure the CO_2 released during the regeneration step. Fig. 7.17 shows the measured CO_2 concentration as function of the time after water injection (Fig. 7.17a-Fig. 7.17b) and as a function of the number of water regeneration steps for stack B (Fig. 7.17c). The datapoint for cycle=0 is the regeneration step after the initial degradation step, before the carbon formation conditions are applied. From the figure, it can be seen that an increase in the CO_2 concentration is observed from 60 s to 150 s after the addition of water to the evaporator.

It can also be seen from the figure that the size of the peak decreases with the cycle number (except for cycle 6) . Fig. 7.17c shows the integrated area under the peaks (numerically integrated with the trapezoidal method and a grid size of 1 s), after the baseline has been subtracted (the baseline was fitted as a linear line using the data points from $t = 0\,\mathrm{s}$ to $t = 50\,\mathrm{s}$ and from $t = 160\,\mathrm{s}$ to $t = 200\,\mathrm{s}$). It can be seen that the integrated area decreases, except for cycle 5. After 9 cycles, the areas are so small that the signal can not be distinguished from the noise. In Fig. 7.17c the mass of removed carbon is also given in the second y-axis in Fig. 7.17cc. The mass of the removed carbon, m_C was estimated with:

$$m_C = \frac{3}{2} \int_{t=50\,s}^{t=160\,s} F_t \cdot X_{\mathrm{CO_2},mea} dt \cdot \frac{P}{RT} \cdot M_C \tag{7.8}$$

Where 3/2 accounts for the fact that approximate 2/3 of the removed carbon is present as CO_2 and 1/3 as CO (thus, only 2/3 of the gasified carbon is measured), F_t is the total flow to the fuel side (safety gas + H_2O, see step 4.4 in Table 7.1), $X_{\mathrm{CO_2},mea}$ is the measured CO_2, and M_C is the molar mass of carbon. The estimation of the mass of carbon deposted has a high uncertainty. The uncertainty of the gas analyzer is 2 %, and the uncertainty of the flow of the safety gas is probably around 5 % (The flow was measured with a rotameter).

A similar observation was done for stack C. In Fig. 7.18 the measured CO_2 and the value of the integrated peaks, as a function of the time after water injection and cycle number are shown. Again, it can be seen that the CO_2 peak is present between 60 s to 150 s after the addition of water to the evaporator.

Despite the high uncertainty of the estimated mass of deposited carbon, the estimation shows that the amount of carbon is not insignificantly low. The formation of several grams of carbon within 15 min (Fig. 7.17cc) also corresponds with the observations from the TGA experiments, where it is seen that the Boudouard reaction is fast.

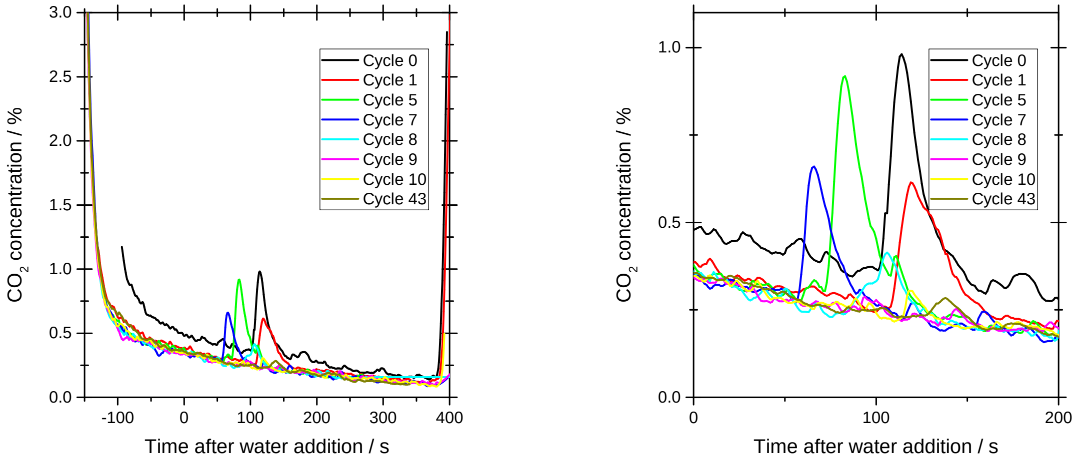

(a) Measurement of CO_2 as a function of time after water addition

(b) Close-up of Fig. 7.17a

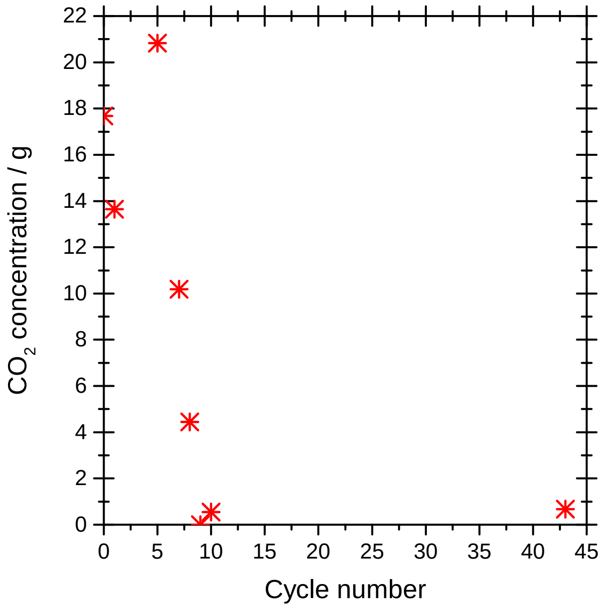

(c) Integrated peak area

Figure 7.17: CO_2 measurement from stack B. The measured CO_2 are plotted in a) and b) as function of the time after water addition. In c) the mass of the gasified carbon is found from the area of the peaks by numerical integration and plotted as the cycle number.

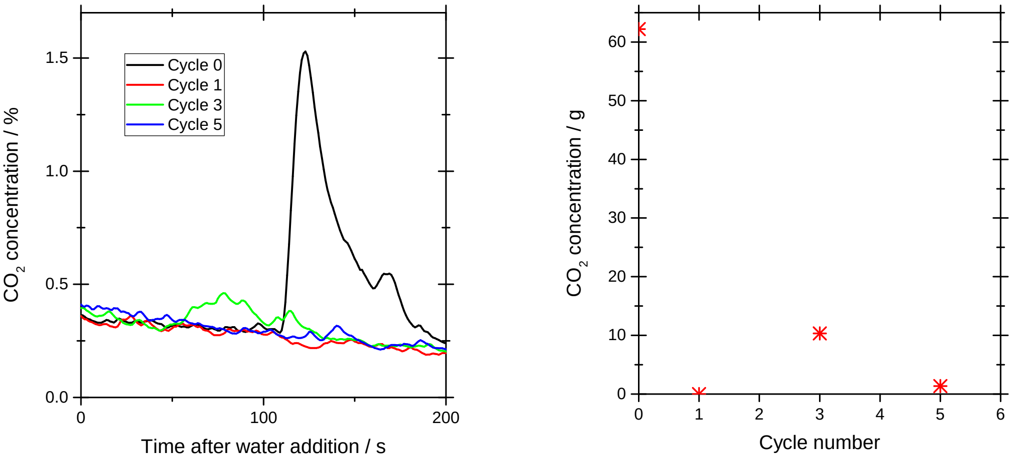

(a) Measurement of CO_2 as function of time after water addition

(b) Integrated peak area

Figure 7.18: CO_2 measurement from stack C. The measured CO_2 are plotted in a) as function of the time after water addition. In b) the mass of the gasified carbon is estimated from the peaks by numerical integration and plotted as the cycle number.

7.5 Discussion

Stack A acted as a base case for how the carbon formation and thermocycling steps affected the cells. From the stack test, it was clear that the cells delaminate when they were exposed to carbon formation conditions and thermocycling. Stack B showed good stability with respect to the regeneration step, but due to a trip, enough data to access to long-term stability was not obtained. Stack C showed that some of the cells were highly affected by the water regeneration steps. From Fig. 7.15 it could be seen that the cell voltage seems to increase more rapidly when the length of the carbon formation step is increased from 30 min to 60 min. Since the carbon formation step was only 15 min in stack B, it might be possible to remove the formed carbon with the regeneration step, if the carbon formation time is only 15 min and not extended to 30 min. If the above stands, the amount of carbon formed is crucial to design of a regeneration plan that will not destroy the cells. Cell test, performed by a fellow PhD student at Haldor Topsoe A/S [184], also showed that minor amounts of carbon did not cause permanent damage to the cell. However, an operation time of CO production below 30 min is not feasible for a whole system with the intent to produce highly pure CO. With should a short operation time, the system will likely not be able to flush out the used H_2 and H_2O. H_2 and H_2O will therefore either accumulate in the recycle, or end up in the product.

The measurement of released CO_2 suggests that the rate of carbon formation decreases with the number of regeneration steps. This has also been reported for Ni in the literature [181, 182] and explained as a change in the number of reaction sites. However, the lower amount of CO_2 could also be explained by the formation of different carbon phases (e.g. filamentous carbon and graphite), which will form with different rates. Another explanation is that the measured gas is not at equilibrium and a large fraction of the carbon is reacted to CO and not further to CO_2, via the water-gas shift reaction. This has been observed in the literature [176], where a main part of the gasified carbon was present as CO when H_2O was used as the gasification agent. However, since the stack has almost the same temperature for all the measurement with the CO_2-analyzer, the rate of the water-gas shift reaction in all the cases should be roughly the same. To test which carbon species are formed in the regeneration step, the CO_2-analyzer should be combined with gas samples measured with GC. A separate CO-analyzer, or a combined CO/CO_2-analyzer, could also be used. Time did not allow for this in this thesis.

The experiment showed that carbon was formed during the initial steps, where it should have been thermodynamically limited. Measurement and modeling of the diffusion, showed that the diffusion limitations cause high concentration gradients. Thus, the carbon formation observed during the initial degradation step can be explained by diffusion limitations. To validate further modeling, the CO_2-analyzer and regeneration steps, can be used as a final test to show if carbon is being formed.

The experiments should be repeated, if the water regeneration method is to be ruled completely out. Unfortunately the time did not allow to carry out more experiments within the scope of the PhD project. Should further experiments be carried out, the following points should be considered to improve the experiments:

1. Use of impedance spectroscopy
2. Use of Raman spectroscopy
3. Less severe carbon forming conditions

1. Impedance spectroscopy was used by Subotić et al. [177] and allowed for a good measurement of the change in performance for a new cell, a cell with carbon and a regenerated cell. Furthermore, impedance spectroscopy can be used to show when the cell is fully regenerated and has reached its original performance. Impedance spectroscopy can easily be installed in the experimental setup.

2. Raman spectroscopy has been used to follow the formation and removal of carbon [175, 177]. Raman spectroscopy is capable of distinguishing between the different carbon phases [89]. Raman spectroscopy can thus both be used to see the amount of formed carbon and the distribution between the different phases. However, Raman spectroscopy is hard or impossible to install in a stack, since the probe has to be inserted in the stack. Raman spectroscopy is therefore more suitable for single cell test.

3. The carbon forming conditions used in the experiment were quite harsh. If less severe carbon forming conditions are used, the amount of carbon formed, and the part of the cell affected would be lower. This could potentially be enough to ensure that the cell survives the carbon formation. In the experiment, it was measured that carbon had formed in the fuel electrodes during the initial degradation step. The fact that the stack survived several trips during the initial step, without deteriorating the cells, suggest that small amounts of carbon formed under less severe conditions do not destroy the cells.

7.6 Conclusion

With the experimental conditions used, it was not possible to show that carbon removal can be used to allow the stack to be operated at carbon formation conditions. Instead, it appears that small operation time, at severe carbon formation conditions with intermittent removal of solid carbon by injection of water, destroys the cells faster than without the water removal steps. There might be combinations of operation time and conditions where carbon formation can be tolerated, but the time did not allow to investigate this further.

CHAPTER 8

Overall discussion

The overall objective of the thesis was to investigate the limits for the allowed CO concentration during electrolysis of CO_2 and how the limit could be increased. The increase of CO concentration is desired because it lowers the strain on the separation unit and amount of recycle, when SOECs are used in systems like Haldor Topsoe A/S's eCOs. The CO concentration was limited by the carbon formation via the Boudouard reaction, a non-uniform flow, and the diffusion in the electrode. The thesis has focused on obtaining knowledge on the limiting causes and the overall status of this will be discussed in the following.

8.1 Carbon equilibrium curve (Chapter 3)

The Boudouard reaction was investigated and discussed in Chapter 3 of the thesis. The reaction was found to produce whisker carbon and graphite, which cause delamination of the cell between the fuel electrode and the electrolyte layer. From the literature and the TGA experiments conducted in this work, the reaction was found to occur when it was thermodynamic favored. From the literature, difference between the thermodynamics for graphite carbon and whisker carbon was observed.

Three different set of thermodynamic values for the Boudouard reaction was obtained from the literature, but all based on Ni with much lower particle size than the Ni used in SOCs. Experiments with TGAs were therefore performed and it was found that the thermodynamics published by Rostrup-Nielsen provides a good agreement with the measured values. The used TGAs had an upper temperature limit of 700 °C, and the experimental data has therefore only been obtained below this temperature. The operation temperature of SOEC are 600-800 °C, so experimental data points in the upper end of the range should also be obtained to strengthen the validation of the thermodynamic data.

An uncertainty analysis of the thermodynamic data was not performed. However, the average deviation between the experimental measured points and the calculated thermodynamics, was calculated to be 1.7 percentage point of X_{CO} in CO_2.

8.2 Flow limitations (Chapter 4)

The influence of operating conditions on the flow was investigated and found to have very little influence. Instead an optimization of the geometry of the gas inlet lead to improved flow distribution. The optimization was published for an ideal system and applied to Haldor Topsoe A/S confidential design. In both cases, it was shown that the flow optimization is important for CO_2 electrolysis. At 750 °C, it was found that the optimized design for Haldor Topsoe A/S increases the allowed CO concentration (without diffusion, but with the thermodynamics of Rostrup-Nielsen) from 22 % to 32 %. However, the flow index, F_u, only has a value of 0.92, so there is room for further improvement (although it might require a substantial change of the geometry). Other companies and research institutions are using designs without corners, e.g. tubular and circular planer designs, but also e.g. square planar designs such as the design used by Forschungszentrum Jülich, see Fig. 8.1. In the design by Forschungszentrum Jülich, a large mixing zone is placed before and after the cell (the quadratic light gray square in the cell frame is the cell and the dark gray areas before and after are mixing zones). If a similar large mixing zone is added to the design investigated in this thesis, the flow would probably be improved considerably. However, the active area would decrease and thereby decrease the production of CO per area and increase the capital cost (since the cost of the stack will be roughly the same). Since the capital cost and operation cost of the separation and recycle will decrease, when the CO concentration is increased, the addition of a larger mixing zone would be a economical balancing between the two effects.

In addition to the flow, a number of other factors must also be included when a potential new design is evaluated. The cost and ease of manufacturing, pressure drop, conductivity, and active area per total area are just some of these factors. However, since many SOECs are based on designs developed/optimized for SOFCs, there might by room for optimization of the design. E.g. SOFCs designed as auxiliary power units (APU) for use in vehicles must be able to withstand vibrations [185], while a stationary SOFC will not be exposed to such vibrations.

8.3 Diffusion limitations (Chapters 5 and 6)

The effective diffusion in two samples, consisting of fuel electrode support material and fuel electrode support + active fuel electrode, respectively, was measured with a Wicke-Kallenbach setup. Combined with measurement of the thickness of the samples, pore diameter, and porosity, it was possible to fit the tortuosity factor, τ^2, and the permeability, κ. The fitted value for the fuel electrode support was consistent with values from the literature on similar material. The fitted value for the tortuosity factor for active fuel electrode ($\tau_E^2 = 14.8$) was significantly higher than the electrode support layer ($\tau_{ES}^2 = 4.65$). In the literature, a single value ($\tau^2 = 10.15$) for a similar active layer with a higher porosity (and therefore an expected lower tortuosity factor) was found. The

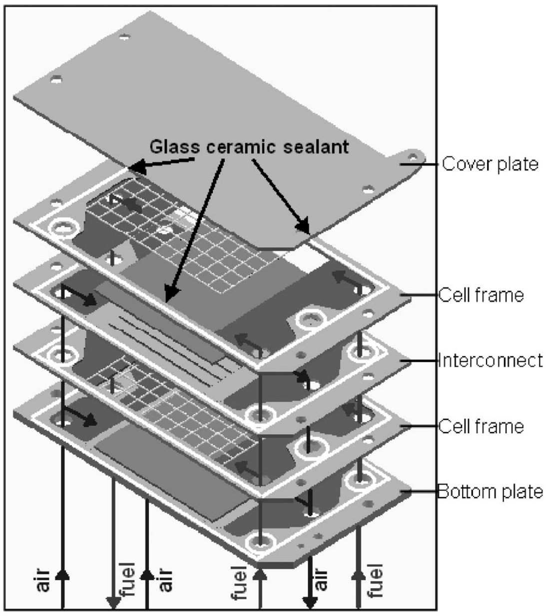

Figure 8.1: Planar design used by Forschungszentrum Jülich. Taken from [186]

high tortuosity factor calls for a further investigation of the active layer and optimization of the structure of the layer. However, since the fuel electrode layer is several times the thickness of the active layer, the fuel electrode layer accounts for the largest increase in CO mole fraction, despite its lower tortuosity factor.

It was only possible to obtain samples with either the fuel electrode support layer or samples with both the fuel electrode support and the active fuel electrode. This meant that it was not possible to obtain measurements of just the active electrode layer. The uncertainty in fitting τ_{ES}^2 is therefore contributing to the uncertainty of τ_E^2. Future experiments should be performed on samples with just the active electrode layer. However, such samples should probably be thicker than the active layer in the tested samples (34.8 µm), since thin samples might crack during mounting in the Wicke-Kallenbach setup or from the pressure difference during permeability measurement (these could of course be omitted, or at least performed after the tortuosity measurements).

A 1d and 2d model was developed and large concentration gradients from the cell channel through the fuel electrode to the active layer, especially under the rib, was found. With the 1d model, four parameters were found to be important for the concentration gradient: $\vec{i}_t$, η, d_p, and d_e. With the 2d model, the effect of the dimensions of the rib and channel was also investigated and it was found that the width of the rib, w_{rib}, had a large influence on the concentration gradient. Since four of the total five parameters are fixed once an SOEC cell has been designed and produced, it is very important to include thoughts on diffusion in the design of e.g. new SOCs designed as SOECs. With respect to limiting the impact of diffusion limitations, the cells should be designed with fuel electrodes that have a high porosity, large pores and low thickness. The interconnect should be designed with ribs as thin as possible. However, very thin and highly porous fuel electrodes are undesired for the type of SOECs used in this thesis (fuel electrode supported cells), since the fuel electrode support provide mechanical strength to the cell. Very thin ribs are also undesired, because smaller ribs cause the current density to increase in the ribs (the same amount of current has to flow through a smaller cross-area). The size of the ribs will also affect the flow in the fuel channel and will therefore require a new optimization of the flow, or at least a calculation of the impact. The diffusion models should therefore not stand alone, but rather be used as elements of a toolbox, which also includes models for flow, current distribution, mechanical strength etc.

In the confidential version of the thesis, the diffusion limitations were implemented in the in-house 3d stack model. From the model, it was found that the diffusion caused a large decrease in the allowed CO channel concentration, and thereby a large decrease in the average CO outlet concentration.

Since the relationship between the concentration in the channel and at the reaction interface could be expressed as a simple linear relationship, dependent only on the current density, the findings could also be implemented in other 3d stack models, without significantly increasing the complexity or calculation time. This is important, because it allows for modeling on very different scales (e.g. µm for diffusion to cm for flow in channels) within the same model.

8.4 Impact on operating space

Fig. 1.9 (presented on page 11) was used to illustrate the limitations of the operation space during electrolysis of CO_2. In the figure, the exact location and size of the equilibrium curve for the Boudouard reaction and the extend of the flow nonuniformity and diffusion limitations were not known. With the investigations performed in this thesis, the location of the equilibrium curve and impact of flow nonuniformity and diffusion limitations were quantified. The exact quantifications are confidential, and therefore not shown in the public version of the thesis.

8.5 Carbon removal (Chapter 7)

With the quantification of the flow nonuniformity and diffusion limitations, it could be seen that the operation space of SOEC was limited and operation at high CO concentrations was not possible. As a way to possibly operate SOECs with high CO concentrations (i.e. in the carbon forming region), the possibility for carbon removal, before irreversible damage are caused to the cell, was investigated. Even when the carbon was removed at intervals between 15 min to 1 h, irreversible damage and delamination of the cell was observed. The damage was worst for the cells subjected to the carbon removal via steam injections. A reason for this could be that the gas and temperature changes during the carbon removal step stresses the delaminated cell. A less severe carbon removal step with CO_2 (and some H_2 to avoid oxidation of Ni) could be used instead of steam. However, the literature reviewed in Chapter 7, suggest that during carbon removal with CO_2, it is not possible to completely remove the carbon. This requires further investigation

Although the possibility for succesful removal of carbon would be very beneficial, it seems that future work is probably best spend on the optimization of flow and diffusion on the short term and development of carbon resistant materials on the long term.

CHAPTER 9

Conclusion

The maximum CO concentration is highly affecting the efficiency and economics of CO production via SOEC. It was found that the maximum CO concentration was limited by carbon formation via the Boudouard reaction, a non-uniform flow, and the diffusion in the electrode. The thesis has focused on obtaining knowledge on the three limiting causes. From experimental work, the equilibrium for the Boudouard reaction on fuel electrode material was obtained and found to be in agreement with literature values for whisker carbon. The impact of the flow was quantified, the flow was optimized via CFD modeling and a significant improvement of the allowed CO concentration was calculated. The diffusion in the electrode was measured experimentically and was used as input for modeling of the diffusion in the fuel electrode. The diffusion was found to have a very limiting effect on the allowed CO concentration in the channel.

The investigations of carbon formation and their quantification using experiments and modeling showed that the range for carbon free operation is limited and particularly it is difficult to obtain sufficiently high CO conversion. It was therefore decided to investigate if a strategy where carbon was allowed to form, but subsequently removed before damaging the cell, was viable. A carbon removal strategy with carbon gasification by water was investigated. However, the cells was quickly damaged beyond reasonable operation with the removal strategy.

The developed models in the thesis, can be use to evaluate the carbon formation risk at different operation points. The effect on carbon formation risk when changes of the design parameters, such as the microstructure of the fuel electrode or flow geometry, are made, can also be assessed.

CHAPTER 10

Future work

The thesis has provided knowledge of the limiting factors for operating at high CO concentration in SOECs. However, a number of questions are still open and a number of findings needs to be further investigated.

As noted in the discussion, the equilibrium for the Boudoaurd reaction is investigated in TGAs capable of operation at temperatures up to 700 °C, but the SOECs are operated at temperatures up to 800 °C. It would therefore be beneficial to strengthen the investigation of the thermodynamic data for the equilibrium with experimental data obtained at temperatures between 700 and 800 °C.

There is still room to improve the flow design. Even though the flow index value is 0.92 for the optimized commercial cell, there is a lot to gain from increasing it further and this should be explored. However, it might require a complete redesign and other parameters, such as price and easy of manufacturing, pressure drop, conductivity, and active area per total area, must also be taken into account.

The diffusion investigations showed that the diffusion limitations in the fuel electrode were very high. The basis for the calculations of diffusion limitations are based on measurement of samples from only two cells. As such, it should be investigated if these two samples are representative. If they are representative, the possibility for changing the microstructure of the fuel electrode, to a more porous structure, should be investigated. A higher porosity will also in general decrease the tortuosity factor, and thus increase the effective diffusion factor ($\eta_{diff} = \epsilon/\tau^2$).

APPENDIX A

Wicke-Kallenbach

This appendix will describe the derivation of the mass balance equations for the Wicke-Kallenbach diffusion cell used in the thesis. Fig. A.1 shows a schematic drawing of the two chambers in the diffusion cell. In the experimental setup, the gas to chamber A is pure N_2 and the gas to chamber B is 0.01 % CO in N_2. In the following "i" will denote CO and "j" will denote "N_2".

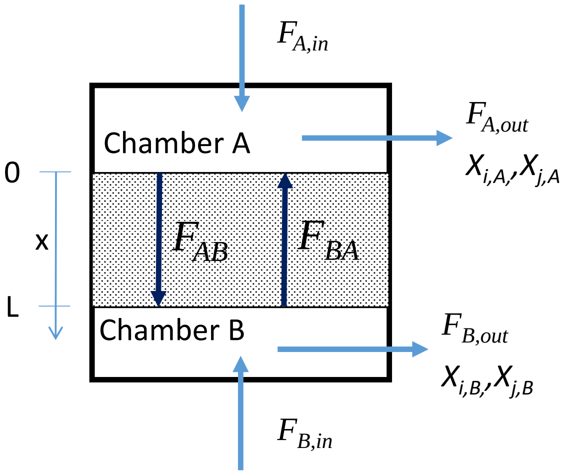

Figure A.1: Schematic illustration of the 1d model of the Wicke-Kallenbach cell

In order to calculate the diffusion flux, a mass balance is set up for chamber A of the diffusion cell:

$$F_{A,out} = F_{A,in} - F_{AB} + F_{BA} \tag{A.1}$$

where $F_{A,in}$ and $F_{A,out}$ is the flow rate of the gas entering and exiting chamber A via the pipes. F_{AB} and F_{BA} is the flow rate of the gas diffusion from from chamber A to B and vice-versa. For a two-component N_2/CO system, which is used in the diffusion experiment, F_{AB} and F_{BA} will be pure N_2 or CO, respectively.

According the Grahams law, F_{AB} can be calculated by:

$$F_{AB} = \sqrt{\left(\frac{M_i}{M_j}\right)} F_{BA} \tag{A.2}$$

Furthermore a mass balance for species i in chamber A yields:

$$F_{0,out}X_{j,A} = F_{BA} \tag{A.3}$$

$$\left[F_{A,in} + \left(-\sqrt{\left(\frac{M_j}{M_i}\right)} + 1\right) F_{BA}\right] X_{j,A} = F_{BA} \tag{A.4}$$

$$F_{A,in} = F_{BA}\left[\frac{1}{X_{j,A}} - \left(-\sqrt{\left(\frac{M_j}{M_i}\right)} + 1\right)\right] \tag{A.5}$$

$$F_{BA} = \frac{F_{i,in}}{\left[\frac{1}{X_{j,A}} + \sqrt{\left(\frac{M_j}{M_i}\right)} - 1\right]} \tag{A.6}$$

F_{AB} can be expressed as:

$$F_{AB} = \sqrt{\left(\frac{M_j}{M_i}\right)} F_{BA} \tag{A.7}$$

$$F_{AB} = \sqrt{\left(\frac{M_j}{M_i}\right)} \cdot \frac{F_{A,in}}{\left[\frac{1}{X_{j,A}} + \sqrt{\left(\frac{M_j}{M_i}\right)} - 1\right]} \tag{A.8}$$

The diffusion flux can now be calculated by dividing the flow rate of i with the area of the diffusion:

$$N_i^d = \frac{F_{BA}}{r_{sample}^2\pi} \tag{A.9}$$

APPENDIX B

Monte Carlo procedure for uncertainty analysis

This appendix will describe the Monte Carlo procedure used for uncertainty analysis in the thesis. The implementation of the Monte Carlo procedure is based on [147].

In the procedure a model structure, represented by **f**, is used to calculated the output **y** given the input parameter θ:

$$\mathbf{y} = \mathbf{f}(\theta) \tag{B.1}$$

The Monte Carlo procedure consist of three steps: 1) Specifying the input uncertainty, 2) sampling the input uncertainty, and 3) propagating the sampled input uncertainty through **f** to obtain the uncertainty of **y** [147].

1) The uncertainty of the input parameters where found from datasheet and calculations (see the main part of the thesis). The uncertainty of the input parameters was assumed to have a normal probability distribution.

2) The Latin Hypercube Sampling method (LHS) [148] was used for probabilistic sampling of the input space. For each sample, θ_l contains one value of each input parameter:

$$\theta_n = [\theta_{1,n}, \theta_{2,n} \ldots \theta_{L,n}], \quad \text{for } n = 1, 2 \ldots N \tag{B.2}$$

where l is the parameter, L is the total number of parameters and N is the number of samples. The value of θ_l was found by dividing the cumulative normal distribution in N evenly distributed parts and use the inverse of the cumulative normal distribution function to calculate the limits of the associated parameter values. A random value between the two parameter values were then obtained:

$$\theta_{n-1} = \text{inverse-CDF}\left(\frac{n-1}{N} + 10^{-6}, \mu_n, \sigma^2\right) \tag{B.3}$$

$$\theta_n = \text{inverse-CDF}\left(\frac{n}{N} - 10^{-6}, \mu_n, \sigma^2\right) \tag{B.4}$$

$$\theta_{l,n} = \text{rand}\left(\theta_{n-1}, \theta_n\right) \tag{B.5}$$

where μ_n is the mean value of the parameter, σ^2 is the variance, “inverse-CDF” is the inverse of the cumulative normal distribution function, “rand” is the function returning a number value within the given interval, n is the sample number and N is the total number of samples. The 10^{-6} value was added/subtracted, since the inverse cumulative normal distribution function is not defined for 0 or 1. The order of the input vector θ_l was randomly mixed. When there was correlation between the input parameters, the rank-based method of Iman and Conover [187] was used together with the LHS.

3) The sampled input matrix $\theta_{L \times N}$ was propagated through $\mathbf{f}$ by performing one calculation for each input parameter sample. The output, $\mathbf{y}$, was assumed to be normally distributed and characterized with the mean value and the variance.

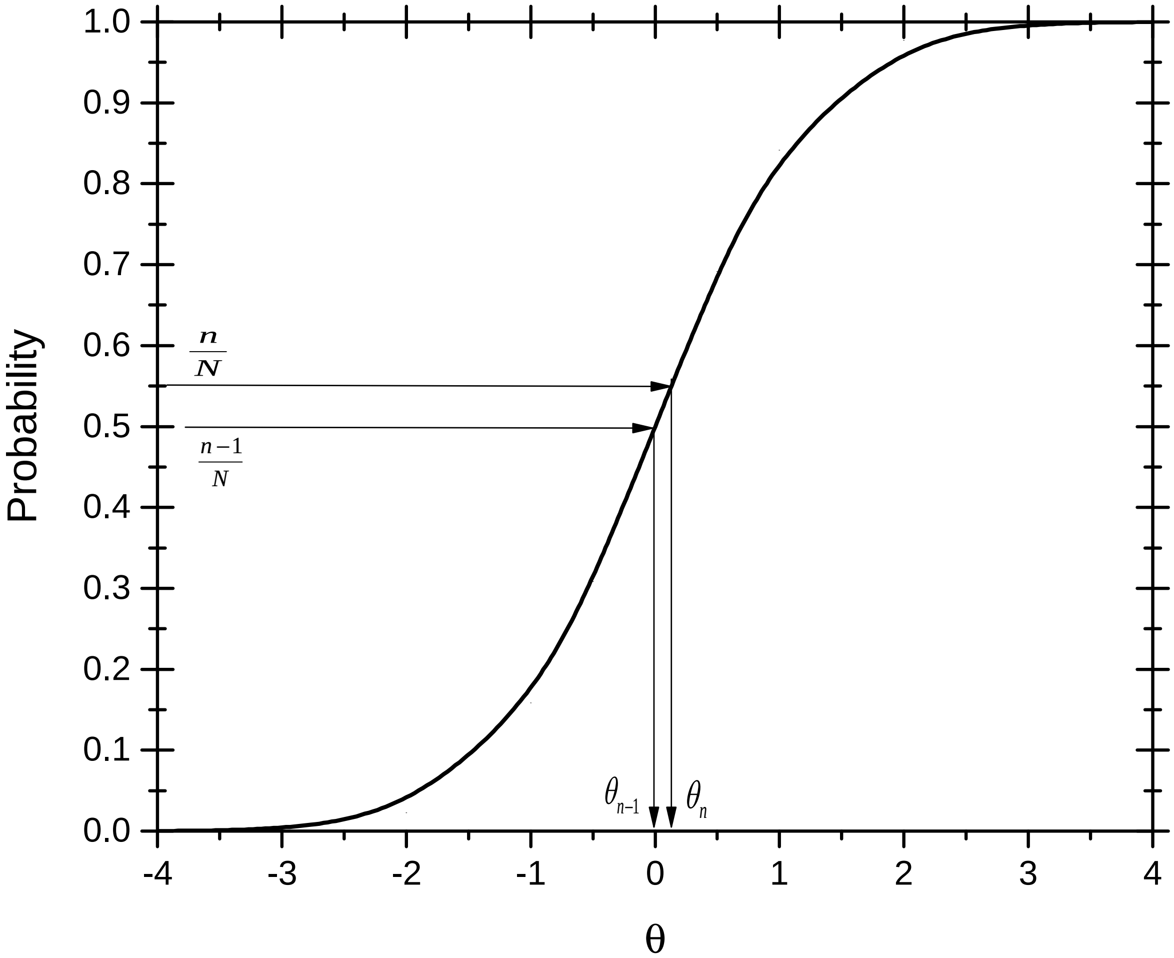

Figure B.1: The cumulative normal distribution for $\mu_n = 0, \sigma^2 = 1$. The figure illustrates how θ_{n-1} and θ_n in Eq. (B.3) and Eq. (B.4) are found.

APPENDIX C

Illustrations of voltage and temperature response during stack experiments

In this appendix, the voltage and temperature of the 9-cell stack used in Chapter 7 during various scenarios are plotted.

Fig. C.1 shows the typical response to an OCV measurement. It can be seen that steady state with respect to the voltage is obtained after 0.5 h. The temperatures do not reach steady state within the tested 1.5 h, but do no longer affect the voltage measurement.

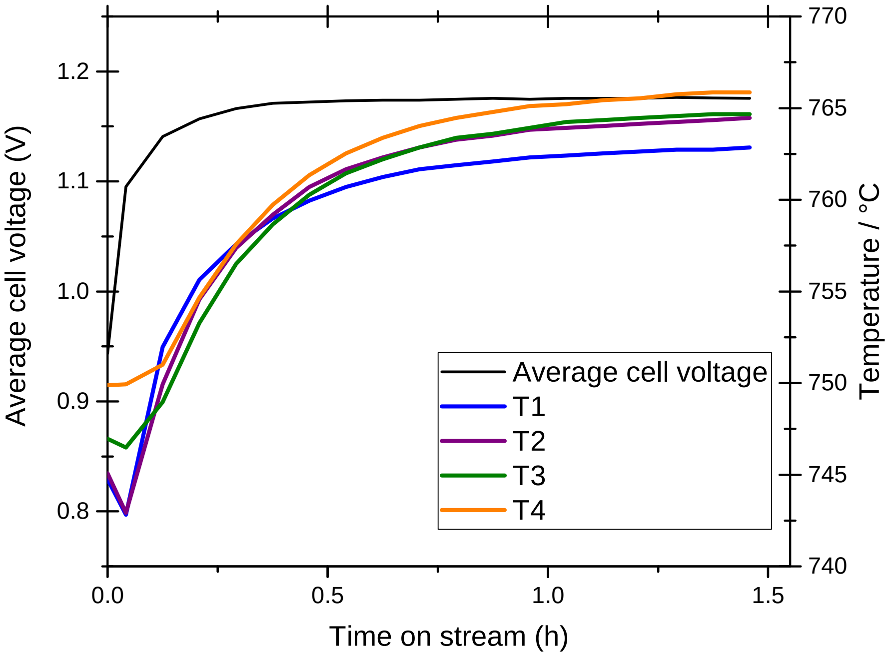

Figure C.1: Responds of the temperature and average cell voltage during OCV measurement.

Fig. C.2 shows the typical response to a thermocycle. At $t = 0$ h, the set point of the heaters are decreased with 3.3 °C/ min and the power unit is turned off. Due to the high thermal mass of the setup, compared to the low thermal mass of the gas, the actual cooling rate of the stack is about four times lower than 3.3 °C/ min

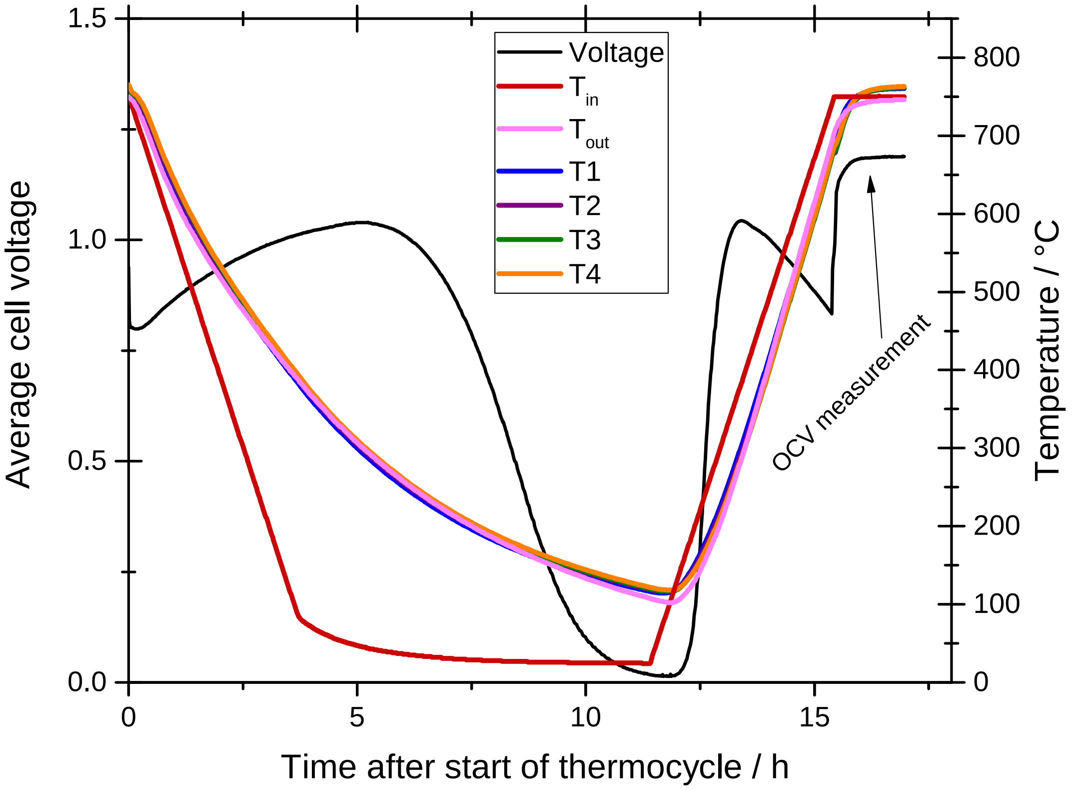

Figure C.2: Plot of temperature and average cell voltage respond to a thermocycle. T_{in} and T_{out} is the temperature of the inlet and outlet gas, respectively.

Fig. C.3 shows the typical response to a trip where the setup is restarted shortly after the trip event. It can be seen from the figure, that the temperature of the stack only decreases slowly (due to a high thermal mass of the setup and a low gas flow with a small heat capacity). During trip, the setup is flushed with safety gas to the fuel electrode and air to the air electrode. When the setup is restarted, a CO_2 flow is added to the safety gas flow. This increases the thermal mass of the inlet gas. A higher thermal mass means that the setup is heated faster. Furthermore, the electrical heaters need a certain minimum flow to maintain their performance. The change in gas composition when restarting the setup, can also be seen in cell voltage.

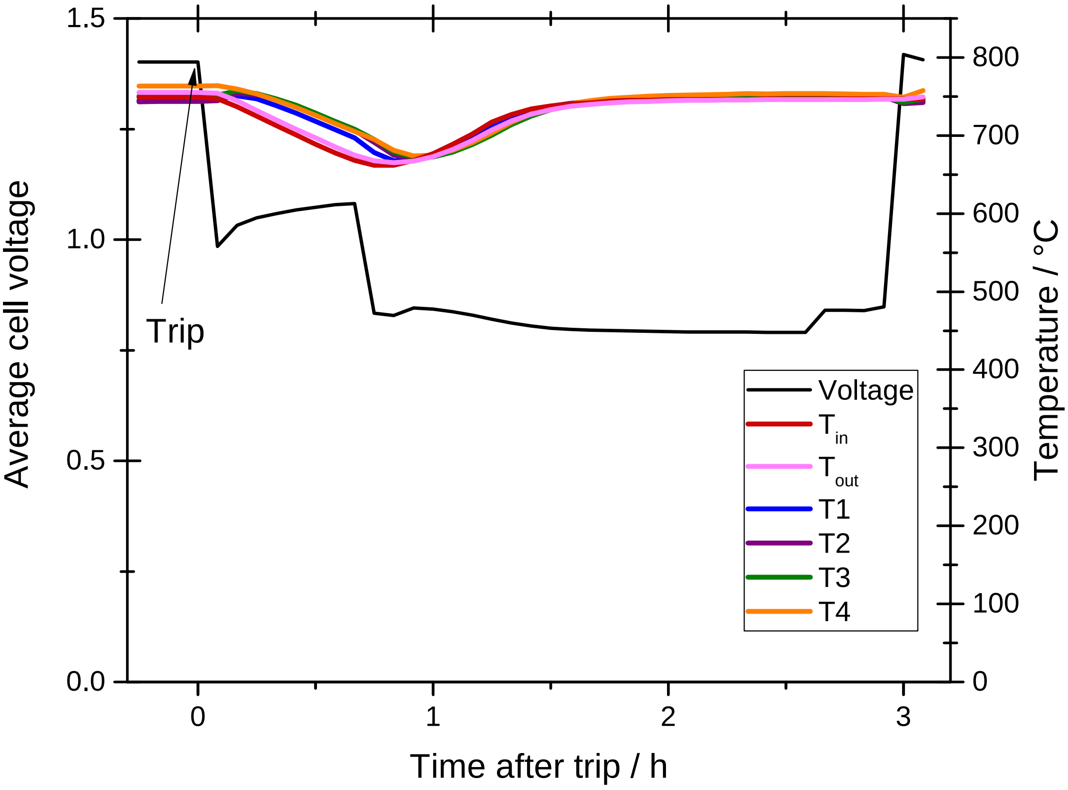

Figure C.3: Plot of temperature and average cell voltage responds to a trip event at $t = 0$ h. In this example, the setup is restarted after 0.75 h and heater to the operation temperature (750 °C.

Fig. C.4 shows the typical response to a trip where the setup is restarted when the setup has reached room temperature. Since the restart received a manual control of the system (e.g. to check the reason for the trip), trip event that occurred out of office hours was first restarted the next day. From the figure, it can be seen that the temperature of the stack only decreases slowly (due to a high thermal mass of the setup and a low gas flow with a small heat capacity). The trip should therefore be gently to the stack, with respect to thermal stresses. With that being said, the trips was designed with personal safety as the top priority and equipment/stack safety as the secondary priority.

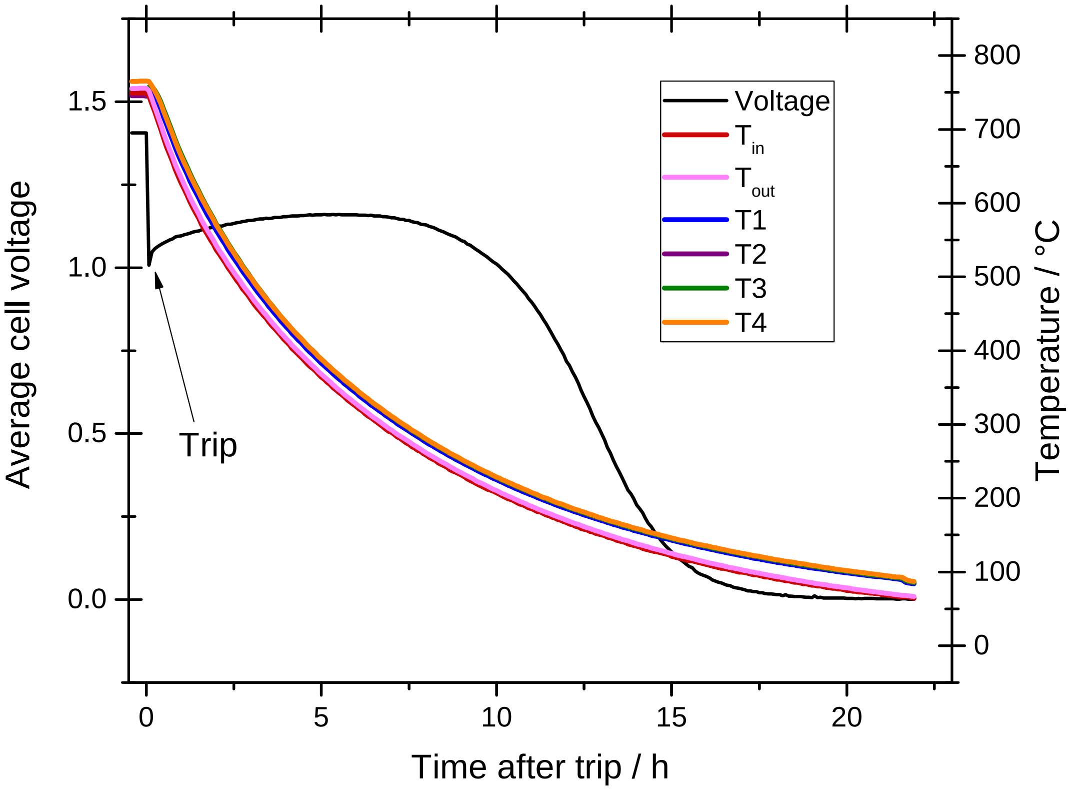

Figure C.4: Plot of temperature and average cell voltage responds to a trip event at $t = 0$ h. In this example, the setup was not restarted, before the setup had reached room temperature.

APPENDIX D

Articles

D.1 Optimization of a new flow design for solid oxide cells using computational fluid dynamics modelling

Journal of Power Sources 336 (2016) 261–271

Contents lists available at ScienceDirect

Journal of Power Sources

journal homepage: www.elsevier.com/locate/jpowsour

Optimization of a new flow design for solid oxide cells using computational fluid dynamics modelling

Jakob Dragsbæk Duhn [a, b, *], Anker Degn Jensen [a], Stig Wedel [a], Christian Wix [b]

[a] Department of Chemical and Biochemical Engineering, Technical University of Denmark, Building 229, DK-2800 Kgs, Lyngby, Denmark
[b] Haldor Topsoe A/S, Haldor Topsøes Allé 1, DK-2800, Kgs, Lyngby, Denmark

HIGHLIGHTS

- A novel geometric design for flow distribution in solid oxide cells is modelled.
- The optimized design is robust towards normal tolerances in manufacturing.
- The optimized design maintains high flow uniformity for different flow rates.
- The effect of temperature gradients on the flow uniformity is investigated.

ARTICLE INFO

Article history:
Received 20 May 2016
Received in revised form
17 October 2016
Accepted 18 October 2016

Keywords:
Solid oxide cell
Flow distribution
Fuel utilization rate
Planar fuel cells
Geometry optimization
Parallel channels

ABSTRACT

Design of a gas distributor to distribute gas flow into parallel channels for Solid Oxide Cells (SOC) is optimized, with respect to flow distribution, using Computational Fluid Dynamics (CFD) modelling. The CFD model is based on a 3d geometric model and the optimized structural parameters include the width of the channels in the gas distributor and the area in front of the parallel channels. The flow of the optimized design is found to have a flow uniformity index value of 0.978. The effects of deviations from the assumptions used in the modelling (isothermal and non-reacting flow) are evaluated and it is found that a temperature gradient along the parallel channels does not affect the flow uniformity, whereas a temperature difference between the channels does. The impact of the flow distribution on the maximum obtainable conversion during operation is also investigated and the obtainable overall conversion is found to be directly proportional to the flow uniformity. Finally the effect of manufacturing errors is investigated. The design is shown to be robust towards deviations from design dimensions of at least ±0.1 mm which is well within obtainable tolerances.

1. Introduction

Solid oxide cells (SOC) are electrochemical systems capable of operating in fuel cell mode (solid oxide fuel cell - SOFC) and electrolyzer mode (solid oxide electrolyzer cell - SOEC). In SOFC mode hydrogen, carbon monoxide, or hydrocarbons are oxidized, thereby generating electricity, whereas, in SOEC mode, water or carbon dioxide are reduced to fuels/chemicals by consuming electricity.

Solid oxide cells are considered a promising energy technology because of their high theoretical efficiency (due to the high operating temperature of 850–1200 K) in both SOFC and SOEC mode [1]. In order to achieve the high theoretical efficiency, the flow in the cells must be close to uniform. If the flow is not uniform, the conversion in some channels/areas of the cell will be higher than others. If the SOFC is running on hydrogen, Ni might oxidize to NiO due to high local concentrations of water [2]. In SOEC mode, during CO_2-electrolysis or CO_2/H_2O co-electrolysis, carbon might be formed via the Boudouard reaction due to high local concentrations of CO [3]. Additionally, a non-uniform flow also contributes to thermal stress within the cell since the heat effects of reaction become unevenly distributed [4–6].

The flow in SOCs has been widely studied, with U- and Z-type manifold and parallel channels being favored by most researchers [7–17]. In U- and Z-type SOCs the parallel channels are fed from a single manifold. In U-type flow, the channels nearest the inlet/outlet receive more flow than the channel farthest away from the inlet/outlet. In Z-type flow, the parallel channels nearest and

---

[*] Corresponding author. Department of Chemical and Biochemical Engineering, Technical University of Denmark, Building 229, DK-2800 Kgs, Lyngby, Denmark.
E-mail address: JADU@kt.dtu.dk (J.D. Duhn).

http://dx.doi.org/10.1016/j.jpowsour.2016.10.060
0378-7753/

Nomenclature

$A_{channel}$	Cross-sectional area (cm^2)
A_{active}	Active cell area (cm^2)
a	Change transfer coefficient
E_{act}	Activation energy ($J\ mol^{-1}$)
$\mathscr{F}$	Faraday's constant (96487 $C\ mol^{-1}$)
F_{nu}	Flow non-uniformity index
F_u	Flow uniformity index
h	Height of cell (mm)
j	Current density ($A\ cm^{-2}$)
j_o	Exchange current density ($A\ cm^{-2}$)
M_i	Molar mass of component i ($g\ mol^{-1}$)
$\dot{m}$	Mass flow rate ($kg\ s^{-1}$)
N	Number of channels
n	Number of moles per second ($mol\ s^{-1}$)
n_{act}	Activation overpotential (V)
p	Pressure (Pa)
p^{ϕ}	Pressure at normal conditions (101.325 kPa)
R	Universal gas constant (8.3144 $J\ K^{-1}\ mol^{-1}$)
T^{ϕ}	Temperature at normal conditions (273.15 K)
u	Velocity ($m\ s^{-1}$)
$\dot{v}$	Volumetric flow rate per time unit ($NL\ s^{-1}$)
$\ddot{v}$	Volumetric flow rate per time unit and active cell area ($NL\ s^{-1}\ cm^{-2}$)
w_b	Width of the header before the parallel channels (mm)
w_{cc}	Width of the center channel of the distributor (mm)
w_{sc}	Width of side channel of the distributor (mm)
X	Conversion of the reactant
z	Number of electrons transferred
α	Ratio of w_{sc} to w_{cc}
γ	Pre-exponential factor ($A\ cm^{-2}$)
ρ	Density ($kg\ m^{-3}$)
μ	Gas viscosity ($kg\ m^{-1}\ s^{-1}$)
τ	Viscous stress tensor (Pa)
χ_{H_2}	Mass fraction of H_2 in inlet flow
ΔP	Pressure drop (Pa)

farthest away from the inlet receive roughly the same flow, whereas the center channels will receive a lesser flow than the outer channels [12]. To improve the inherently poor flow distribution with these designs, the cross section of each parallel channel can be changed [18,19] or the manifold geometry can be changed [12].

An alternative design to the U- and Z-types is to have gas inlet/outlet holes in front of the parallel channels and adding barriers that distributes the gas into the parallel channels [20–22]. In this article the flow distribution in a commercial SOC cell design [22] using barriers to distribute the gas flow is investigated and optimized using CFD modelling. The effect of the flow non-uniformity on the maximum overall conversion is also investigated. We show that such a design can be optimized to obtain a more optimal design than achievable by Z or U type designs.

Other designs than U- and Z-type, such as serpentine, interdigitated flows [23,24], subset of U- and Z-type geometries [25] and pin type flow cells [26] has also been investigated in the literature [27–30]. However, the pressure drop in serpentine and interdigitated flow quickly increases to the order of a few bars for larger fuel cells [31,32], and the pressure drop in geometries using subset of U- and Z-type is generally higher than single U- and Z-type [25]. In general parallel channels has the lowest pressure drop [33] and parallel channels are therefore of higher interest than the other designs for SOCs.

For low-temperature fuel cell technologies, like Proton Exchange Membranes (PEM), another important aspect is water management, in order to assure that the fuel cell is not flooded [7,30,34–38]. In this article we have focused on SOCs where water flooding is not an issue, and thus we will not investigate water management in our design.

2. Model description

2.1. Geometric model

Fig. 1 shows the structure of the SOFC/SOEC cell used in this study. The cell consists of 5 layers: Air electrode, air channel, fuel channel, fuel electrode and electrolyte. An interconnect is placed between the air and fuel channel with the purpose to connect the air and fuel electrode electrically and to distribute the gas evenly to the entire electrode. In this study an interconnect shape with parallel channels is used. Here the gas is divided into the parallel channels, and the ribs ensure electrical contact between the interconnect and the electrode. In this paper we are only concerned with the fuel flow. The fuel channel layer consists of 45 parallel channels, each 1 mm wide and with a height of h = 0.3 mm, separated by 1 mm wide ribs.

Fuel gas (typically CH_4 or H_2 in SOFC and H_2O/CO_2 in SOEC) is entering through a manifold of three tubes (which are formed when single cells are assembled to form the stack) to the left in Fig. 2, moves through a barrier, hereafter called gas distributor, and is distributed to all the parallel channels (see insert of Fig. 1). Purge flow (typically air) is entering through holes at the left side of the cell and exiting through holes at the right side of the cell. In a stack several cells are placed on top of each other, however only the flow in the fuel channel layer is modelled in this study. Furthermore, the flow in the stack manifold (the pipes with in the cell shown in Fig. 1) is not included in the model.

Fig. 2 shows the geometry of the model implemented in COMSOL 5.1 together with the parameters w_{sc}, w_{cc}, w_b. In order to decrease computational time, the model consists of one third of the cell. The channels are numbered sequentially starting from the bottom. Note that the number of channels on each side of the distributor is not identical. The dimension of the active area is 90 mm × 111 mm (H x B), giving a total active area of 99.9 cm^2. The model is a 3d model where the height (z-dimension) of the interconnect is 0.3 mm. Previously, 2d models with different approximations have been used [8,31,32], while other have applied 3d models in order to avoid the uncertainty introduced by the approximations when reducing to a 2d model [11,16,39]. Since the computational time of our model was relatively low (2–5 min on an Intel Xeon E5-2637 CPU with 3.5 GHz), we only considered the 3d model.

2.2. Computational methods

The flow in SOCs under operation is affected by electrochemical reactions and temperature gradients (causing density and viscosity changes). These changes are often disregarded in studies of the flow uniformity [8,32,39,40], and we will also assume isothermal and non-reacting incompressible flow. The validity of these

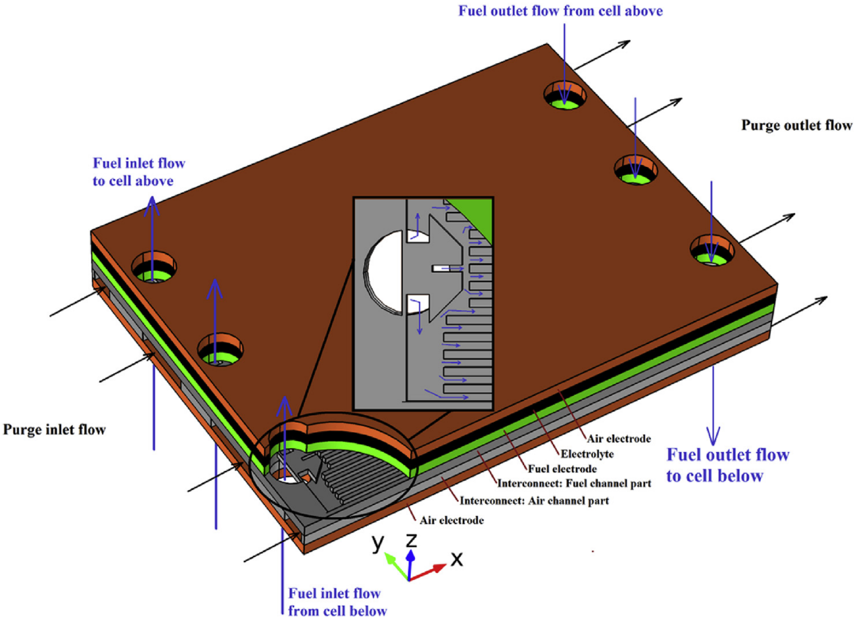

Fig. 1. Sketch of the cell geometry. The insert shows the gas distributor and the parallel channels.

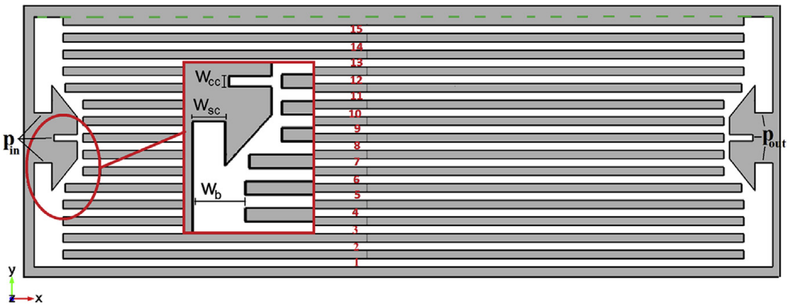

Fig. 2. The flow domain modelled in COMSOL. The cross section is extruded 0.3 mm. An inlet pressure, p_{in}, is applied to the left and an outlet pressure, p_{out}, to the right. On the dotted horizontal line a symmetry condition is applied.

assumptions is evaluated in section 3.8.

2.2.1. Flow

The flow is assumed steady and is modelled with the steady state form of the continuity equation and momentum equation:

$$\text{Continuity equation} \quad \nabla\cdot(\rho u) = 0 \tag{1}$$

$$\text{Momentum equation} \quad \rho(u\cdot\nabla)u = \nabla\cdot(-pI+\tau) \tag{2}$$

Here ρ is the density, u is the velocity vector, p is the pressure, I is the unity tensor, and τ is the viscous stress tensor. The viscosity and density are fixed at the values of air at 1000 K (ρ = 0.35 kg m^{-3}, μ = 4.1 × 10^{-5} kg m^{-1} s^{-1}).

2.2.2. Boundary conditions

An inlet gauge pressure, p_{in}, of 150 Pa is specified at the inlet surfaces and on the outlet surfaces a gauge pressure of $p_{out} = 0$ Pa is specified (see Fig. 2). On all solid walls, a no slip condition is applied, except for the surfaces touching the horizontal line in Fig. 2. Here a symmetry condition is applied. The symmetry condition was validated by modelling two-third of the cell with the parameters for the optimized design presented in section 3.4, and the two models were found to give identical flow profiles.

2.2.3. Measure of flow uniformity

Different measures of the flow uniformity/non-uniformity have been used in the literature. Flow uniformity indices, defined by either (3) [16] or (4) [39] have been used by some authors, whereas others have used a non-uniformity index, F_{nu} [12,32]. The flow uniformity indices F_u and F_{u2} are identical if all single channel areas (and the density of the gas in each channel) are the same.

For a perfectly uniform flow, the flow uniformity index will be 1 and the non-uniformity index will zero. For non-uniform flow, the indices will be in the interval]0,1[.

$$\text{Flow uniformity index} \quad F_u = \frac{N\min(u_1\ldots u_n)}{\sum_{i=i}^{n} u_i} \tag{3}$$

$$\text{Flow uniformity index} \quad F_{u2} = \min\left(\frac{m_i}{\overline{m}}\right) = \min\left(\frac{\rho A_{channel_i} u_i}{\overline{\rho A_{channel} u}}\right)\overline{u_i} = \frac{\sum \rho_i A_{channel,i} u_i}{N} \tag{4}$$

$$\text{Flow non-uniformity index} \quad F_{nu} = \frac{\max(u_1 \ldots u_n) - \min(u_1 \ldots u_n)}{\max(u_1 \ldots u_n)} \tag{5}$$

Which flow index to use depends on the purpose of the optimization. If it is important that all reactants entering the channel are converted, the operating limits would be determined from the channel with the highest flow. In this case F_u should not be used. A high flow in a single channel would only affect F_u to a minor degree, whereas F_{nu} would be highly affected. If unwanted side reactions take place at high product concentrations, the operating limits would be determined by the channel with the lowest flow. In this case, F_u should be used because it is directly affected by the minimum flow.

In SOFC with pure H_2, the produced H_2O might oxidize Ni to NiO at high H_2O concentrations and in SOEC mode, during CO_2 and co-electrolysis, solid carbon might form via the Boudouard reaction at high product concentrations [3,41–43]. The current model is therefore optimized with respect to F_u.

2.3. Mesh and solver settings

The mesh was build using cuboids in the parallel channels and tetrahedrons everywhere else. The cross-sections of the parallel channels were divided into squares, from which the cuboids were created by sweeping the channels. The size of the squares was found by dividing the height and the width of the channel with an integer, where a value greater than 7 was found not to influence the results. The sweeping was conducted using COMSOL's built-in sweep function with the predefined "Coarser" setting. This resulted in cuboids with a size of approx. 5.3 mm × 0.14 mm x 0.04 mm.

The tetrahedrons were created using COMSOL's built-in tetrahedral function with the predefined "Finer" setting and a z-direction scale of 2. All other settings were kept at standard values.

The mesh was tested by coarsening and refining the predefined settings, and it was found that a further refining than the above resulted in change of less than 0.05% to the F_u value.

The simulations were carried out with the MUMPS solver with the fully coupled constant Newton method (damping factor = 1). All other solver settings were kept at their default values (e.g. the relative tolerance was 0.001).

The average velocity in each channel was extracted using COMSOL's built-in average component coupling function

3. Results and discussion

3.1. Scope of optimization

The geometry presented in Fig. 1 has a large range of optimizations. The number of inlet holes and channels could be changed, the geometry of the distributor and channels could be changed and a completely different design of the distributor could also be used. In order to limit the optimization possibilities, the scope of the optimization was restricted to values of the parameters w_{cc}, w_{sc} and w_b. This has several advantages: The purge flow is unaffected and the same cells, seals and external pipe connections can be used. In the following, the effect of the parameters will be illustrated, an optimized design will be constructed, the effect on reaction extent will be calculated and the effect of manufacturing tolerances on the optimized design will be evaluated. Figures showing the velocity field and pressure distribution are available as supplementary material.

3.2. Effect of gas distributor dimensions

The influence of the dimensions of the gas distributor was investigated by changing w_{sc} and w_{cc} (see insert on Fig. 3). From the geometry, it is clear that when $w_{sc} < w_{cc}$, the outer channels will obtain a significantly lower flow than the center channels, leading to a poor flow distribution. The parameter α is therefore introduced, with the constraint $\alpha > 1$:

$$\alpha = w_{sc}/w_{cc} \tag{6}$$

Fig. 3a shows the effect on F_u of changing w_{cc} and α. The figure shows that a maximum in the flow uniformity exists for an intermediate value of α. The reason for this is that at lower α levels, the outer channels (channel 1–4) obtain less flow than the center channels. Increasing α increases the flow to the outer channels and reduces the flow to the center channels. However, as α increase above a certain value the flow reduction in the center channels only causes an increase of the flow to channel 5 and 12 (Fig. 3b). The value of α at which the flow uniformity is maximized, decreases with w_{cc} from 4 to 5 at w_{cc} = 0.4 mm, to 2 at w_{cc} = 1 mm. For w_{cc} = 0.2 and 0.3 mm the optimum α is lower than that at 0.4 mm. Furthermore, for w_{cc} = 0.2 mm, a sharp optimum is observed ($\alpha = 2.5$) and for w_{cc} = 0.3 and 0.4 mm the flow uniformity reached a plateau. However, if α is further increased, the flow uniformity decreases for w_{cc} = 0.3 and 0.4 mm as well (not shown). The sharp optimum for w_{cc} = 0.2 mm is explained by the fact that at such small width the inlet pressure is not enough to push sufficient gas to the center channels when $\alpha > 2.5$, even though some gas will be forced from the side channels, around the distributor, into the center channels. The resulting flow in the center channels is therefore lower than that of the side channels (especially channel 5).

Overall, the maximum obtainable value of F_u is located at w_{cc} 0.3 and $\alpha = 3.5$ when w_b is fixed at 2 mm.

3.3. Effect of increasing the header width

To further increase the flow uniformity the influence of header width, $w_{b,}$ before channels 1–4 and 13–15 (see insert on Fig. 3), was investigated (Fig. 4a). The ribs between channel 5 and 6 and between 11 and 12 are not changed. This means that these two ribs act as constrictions for the side channel flow to enter the center channels. The combinations of w_{cc} and α were based on the maximum points in Fig. 3 and the optimum value of w_b was found to vary with w_{cc} and α. Increasing w_b leads to more flow in channel 1–4 and channel 12–15 (Fig. 4b). Since especially the flow in the outer channels is low when w_b is equal to 2 mm, increasing w_b increases the flow uniformity, until the flow in channel 6–11 becomes lower than the flow in channel 1–4.

3.4. Optimal design

To investigate the combined effect of the three parameters, bounds for the three parameters were defined (Table 1) and the parameter space was explored using Monte Carlo simulations. The Monte Carlo method was selected to reduce the risk of finding a local maximum point and additionally has the advantage that all the calculations could be performed in parallel, i.e. using a

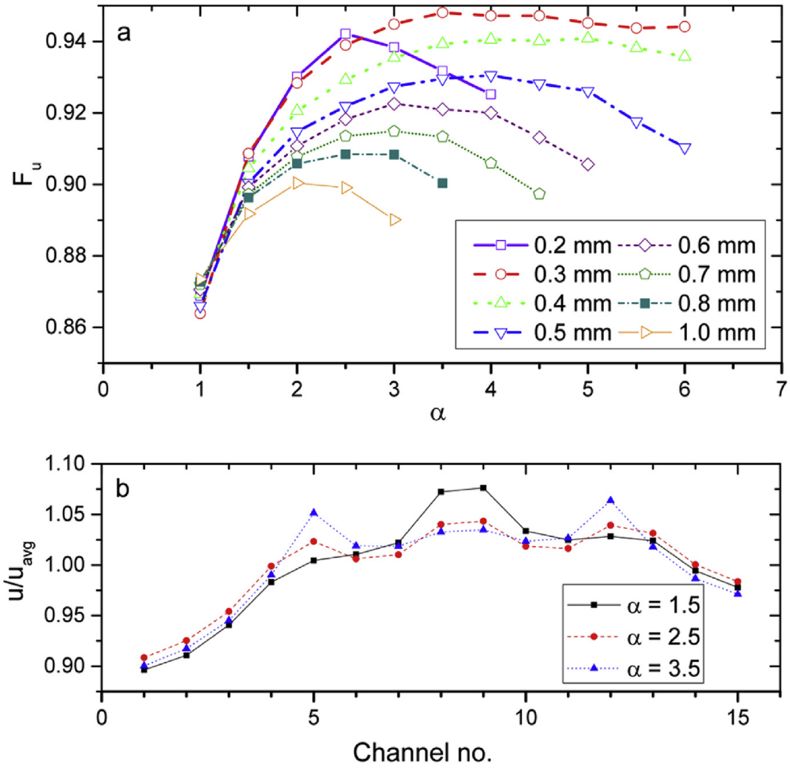

Fig. 3. Effect of gas distributor dimensions. a) F_u as function of α for different w_{cc} values (0.20 mm–1 mm). b) Normalized flow in each channel for $w_{cc} = 0.6$ mm at different values of *α*. In both figure a and b, w_b was fixed at 2 mm.

computer cluster.

300 Monte Carlo simulations were performed and the optimal design (highest F_u value) was found to be located at w_{cc}, α and w_b equal to 0.9 mm, 4.66 and 7.2 mm, respectively, with $F_u = 0.978$. The normalized flow in each channel is plotted in Fig. 5. It can be seen that the flow is close to being identical for all channels. Channel 1 still receives the least amount of flow and channel 5, 12–13 the most. However, the deviations are now very small compared to those in Figs. 3b and 4b.

The uniformity in flow can also be seen in the pressure. Fig. 6 shows the pressure drop across channel 1 and the differences between channel 1 and channel 5, 8 and 15, respectively. It can be seen that the pressure differences for the channels are small. It can also be seen that approximately one-tenth of the pressure drop is taking place in the inlet and outlet manifold (approx. 10 Pa pressure drop in each). The pressure is investigated further in the next section.

Other designs with similar F_u values were also found. To illustrate this, the designs were plotted in Fig. 7. In the figure, the data points are projected onto two-dimensional planes. Fig. 7a contains all 300 data points, and Fig. 7b contains only the data points with $F_U > 0.97$. The value of 0.97 was selected to include a sufficient number of data points to illustrate the correlation between the parameters, while the rest of the data points was excluded for clarity. From the figure it can be seen that there is a correlation between w_{cc} and w_b and to a minor extent between w_{sc} and w_b. The figure shows that an increase in w_{cc} (which leads to more flow in the center channels), can be compensated for by an increase in w_b. When w_b is around 4 mm, the optimum w_{sc} value is around 2.5–3 mm. As w_b increase, the span of optimum values for w_{sc} increases to 2.5–4.5 mm. This means that as long as the combination of w_{cc} and w_b is reasonable, the exact value of w_{sc} is of less importance (as long as it is within the span defined above).

The model is simplified (isothermal, non-reacting and incompressible flow), meshed with a certain refinement and geometrically restricted to the cell, thus an optimal design for non-isothermal, reacting and compressible flow may differ somewhat from the optimized result under simplified conditions Also, since the performance in terms of flow uniformity is almost identical for the local maxima, a preferred design can be chosen by evaluating other properties than the flow uniformity, such as the total pressure drop over the cell.

3.5. Underlying factors

As stated previously the purpose of the distributor (and also header width) is to distribute the gas evenly to all the parallel channels. For the optimized design, it can be seen (Fig. 6b) that the lengths of all the channels are approx. the same and that the pressure difference within the header section (i.e. excluding the gas distributor) is less than 4 Pa (Fig. 6a). Since the pressure applied to each channel and the channel length is approx. the same, the resulting flow will also be close to identical and a high F_u value will be obtained.

When the parallel channels have a varying length, the pressure in the header must be higher for long channels compared to short channels. However, it is hard/sometimes impossible to get a precise non-uniform pressure distribution in the header section. Fig. 3 illustrates how only a local-maximum, for the design shown in Fig. 1, can be achieved with parallel channels of uneven length. Parallel

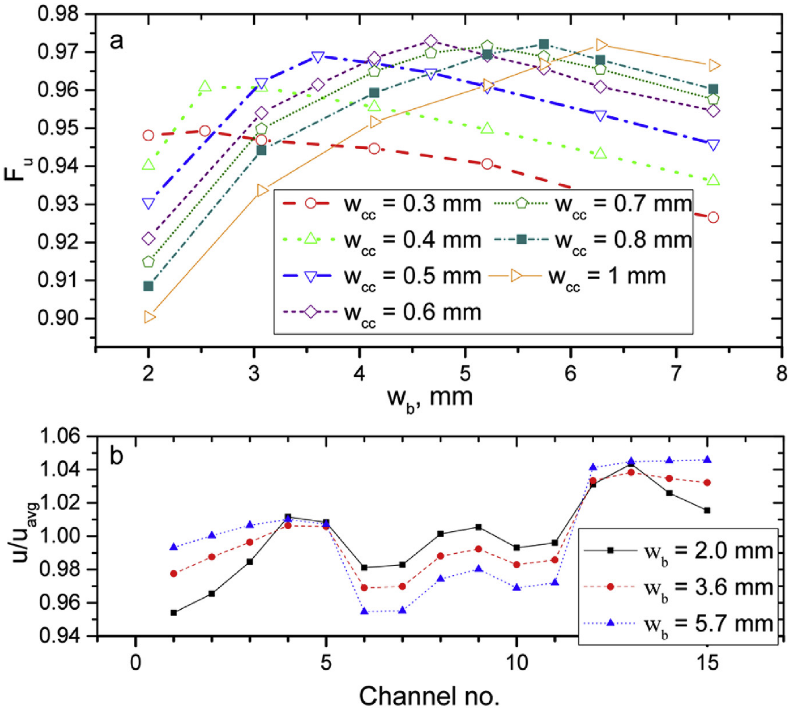

Fig. 4. Effect of w_b. a) F_u as function of w_b for the optimum points ($\{w_{cc}, \alpha\} = \{0.2$ mm, 2.5; 0.3 mm, 3.5; 0.4 mm, 4; 0.5 mm, 4; 0.6 mm, 3; 0.7 mm, 3; 0.8 mm, 2.5; 1 mm, 2$\}$) found in Fig. 3 b) Normalized flow in each channel for $w_{cc} = 0.6$ mm, $\alpha = 2.5$ and different values of w_b.

Table 1
Parameter space.

Parameter	Lower bound	Upper bound
$w_{cc,\ mm}$	0.2	1.2
α	1.5	6
$w_{b,\ mm}$	2	8.5

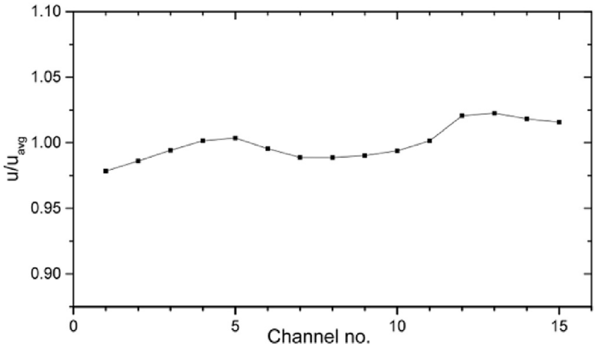

Fig. 5. Normalized flow in each channel for the optimized design (w_{cc}, α and w_b = 0.9 mm, 4.66, 7.2 mm).

channels of uneven length may be necessary when maximizing the active area, but from a flow point-of-view parallel channels with identical length are preferred.

Table 2 lists the average pressure, standard deviation of the inlet pressure to each channel relative to the average pressure ($\sum(p_{c,i} - p_{avg})/N$), pressure drop ratio (pressure drop in the parallel channels over the total pressure drop) and F_u for several cases (rows 1–6 are also shown in Figs. 3b and 4b).

It can be seen that when α is increased (row 1–3), the average pressure before the channels is also increased. This increase the $\Delta P_{channels}/\Delta P_{total}$ ratio and also F_u. The reason for this is that the cross section of the distributor becomes larger and the pressure drop over it therefore decreases. From row 4–7 it can be seen that when the header width is increased, the pressure drop ratio does not change much, but the relative standard deviation decreases and F_u increases, until a certain value of w_b (here between 5.7 and 7.35 mm). This is because the length of the channels becomes more uniform and the flow resistance in the header decreases due to the larger value of w_b. After a certain value of w_b, the pressure drop ratio decreases (since more flow is going through the side channel, the pressure drop in the header section increases). This can also be seen more generally in Fig. 7 and section 3.4, where a correlation between w_{cc} and w_b is described. To reach an optimized design (row 8), the pressure must be uniform (low standard deviation) and the $\Delta P_{channels}/\Delta P_{total}$ must be high.

It is commonly acknowledged that the pressure drop in the manifold should be significantly lower than that over the cells in a stack to ensure a uniform flow distribution to the cells [16,32,39,40]. This is analogous to obtaining a uniform flow in industrial fixed bed reactors and multiple tubular reactors (after the pressure drop in each tube has been adjusted to a common value). For such reactors, a uniform flow can be obtained as long as the pressure drop in the inlet and outlet hood is lower (more than one order of magnitude) than the pressure drop in the tubes [44–46]. Plotting F_U as function of pressure drop ratio (added as supplementary material) shows that high F_u values can only be obtained with high pressure drop ratio and that the length of the channels should be approx. identical (W_b should be high).

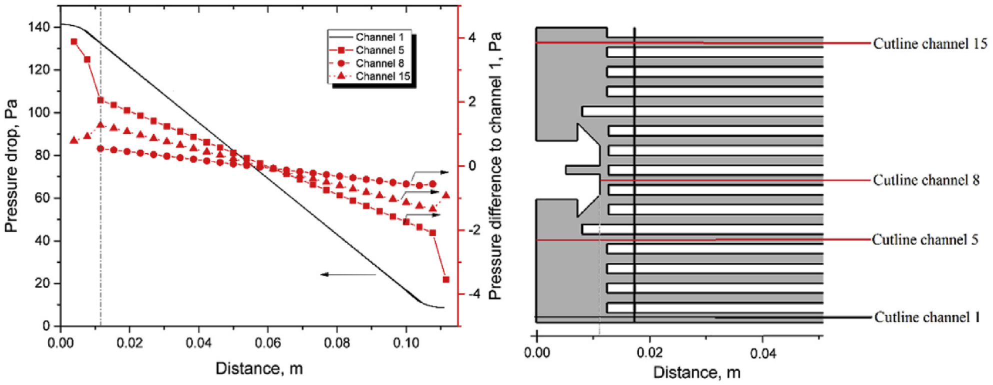

Fig. 6. a) Left: Pressure profile for the optimized design (w_{cc}, α and w_b equal to 0.9 mm, 4.66 and 7.2 mm, respectively and $F_u = 0.978$) for channel 1 (left ordinate). The pressure differences between channel 1 and channel 5, 8, 15, respectively, are also plotted (right ordinate). b) Right: Illustration of the cutlines used to create the pressure profiles.

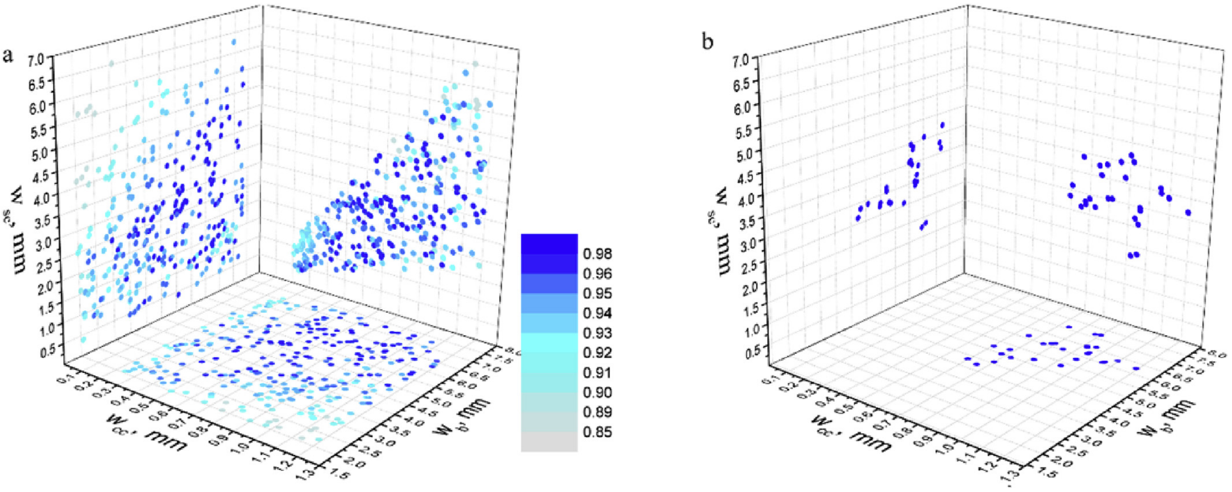

Fig. 7. Data points from the Monte Carlo optimization projected onto two-dimensional planes: a) all data points shown, the color map shows the F_u value of each data point. b) Only the data points with $F_u > 0.97$.

Table 2
Pressure and flow uniformity parameters for different designs. wcc, wsc and wb in mm, pressure and relative standard deviation in Pa, all others are unitless.

Case				Average pressure before parallel channels	Relative Standard deviation	$\Delta P_{\text{channels}}/\Delta P_{\text{total}}$	F_u
w_{cc}	w_{sc}	α	w_b				
0.6	0.9	1.5	2.0	121	1.8	0.61	0.899
0.6	1.5	2.5	2.0	127	2.6	0.69	0.918
0.6	2.1	3.5	2.0	130	2.9	0.74	0.921
0.6	1.5	2.5	2.0	125	2.6	0.67	0.918
0.6	1.5	2.5	3.6	126	2.3	0.68	0.957
0.6	1.5	2.5	5.7	127	1.8	0.69	0.967
0.6	1.5	2.5	7.35	125	1.5	0.65	0.955
Optimized design				139	0.9	0.85	0.978

Based on this, our recommendation for designing a distributor for parallel channels is to use parallel channels with equal length and ensure that the pressure drop ratio is high (preferably the pressure drop in the channels should be one order of magnitude higher can that of the distributor). Similarly, for U- and Z-type designs, the pressure drop in the channels should be significantly higher compared to the manifold/header section.

3.6. *Tolerance to errors in manufacturing*

During manufacturing the production of the geometries will be within certain tolerances, e.g. defined in industry standards such as ISO 2768-1. However, minor changes in the dimensions of the distributor might alter the flow significantly. According to ISO 2768-1 a tolerance of ±0.05 mm is normally a permissible deviation when working with linear dimensions up to 3 mm in the “fine” tolerance class. Based on the optimized design (w_{cc}, α and w_b equal to 0.9 mm, 4.66 and 7.2 mm, respectively) all combinations of w_{cc}, w_{sc}, and w_b ±0.05 mm were tested and the lowest value of F_u was found to be 0.976. When the uncertainty was increased to ±0.1 and ± 0.2 mm, the lowest value of F_u was found to be 0.975 and 0.970, respectively. The design of the gas distributor is therefore robust towards deviations in the geometry caused by tolerance errors in the manufacturing of up to twice of the value allowed in ISO 2768-1.

3.7. *Effect of flow rate*

The effect of flow rate on the flow uniformity and pressure drop was investigated (Fig. 8) and it was found that the effect on flow uniformity was small, whereas the pressure drop increased linearly with the flow rate. The result shows that the design is capable of handling quite different flows without significant changes in the flow uniformity. This is important for an SOC operating under varying conditions. Examples of this include SOFCs operating with changing load depending on the demand or SOECs used for storing excess electrical energy in chemical species. A similar response was observed for the other designs (not shown). Investigation of the pressure profiles at the high flow rates (not shown) showed that the decline in flow uniformity was due to different changes in the pressure drop in the center channel and side channel of the distributor. The pressure drop in the center channel increased more than in the side channels and this caused a large fraction of the flow to move through the side channels and thus relatively less flow is supplied to channels 8 and 9 (see Fig. 2) through the center channel of the distributor. So, if the design is to be used at higher flow rates than approx. 1 NL min^{-1} per cell the distributor should be re-optimized.

3.8. *Effect of assumptions and flow property parameters*

The simulations have been performed assuming an isothermal, non-reactive and incompressible flow (which is similar to others [8,32,39,40]). In this section we will explore the validity of results based on these assumptions.

3.8.1. *Effect of the flow parameters (viscosity and gas)*

The optimization was performing using the viscosity and density of air at 1000 K. To verify that the optimized design is also good for other gasses and temperatures, the flow property parameters were calculated at 900, 1000, and 1100 K for air, H_2 and CO_2 and corresponding F_u values were computed. H_2 and CO_2 were selected because these are respectively the lightest and heaviest gasses commonly used in SOCs (disregarding hydrocarbons higher than methane). The simulations showed no change in the F_u values.

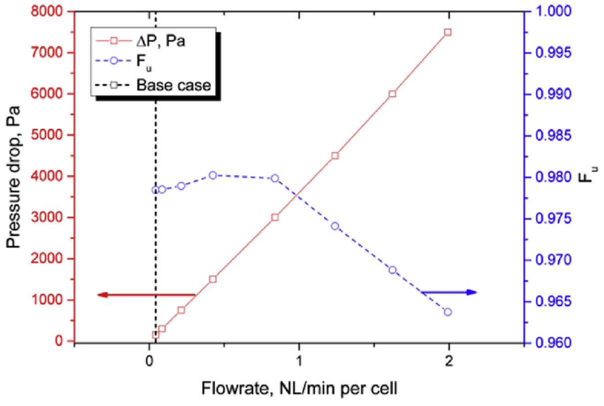

Fig. 8. Effect of flow rate on the flow non-uniformity and pressure drop. Vertical line shows optimization base case.

3.8.2. *Effect of non-isothermal conditions*

Bi et al. [39] found that, when applying a linear temperature increase of 200 K between the inlet and the outlet of a SOFC and assuming a uniform rate of the chemical reactions across the channels, the difference in flow rate distribution compared to the isothermal and non-reacting flow case was less than 1%. Using similar conditions as Bi et al. ($\Delta T = 200$ K from 650 °C to 850 °C, 65% w/w H_2, 35% w/w H_2O, 85% conversion and an uniform rate) we found a difference of F_u of less than 0.03%.

Often a non-linear temperature profile between the inlet and outlet is observed in SOC, especially if a cross- or counter flow is used, or if the heat transfer from side of the cell to the surroundings is significant [47–50]. In the literature temperature differences between the edge and the center of the cell has been reported to be in the range of 5–10 K cm^{-1} depending on the operating conditions and design in SOFC mode [49–52]. In SOEC mode the cell can be run endothermic, thermo-neutral, and exothermic which means that the temperature in the center of the cell can either be lower, the same or higher than the edge. In the literature values in the range of −2 to 10 K cm^{-1} has been reported [53]. Using an in-house model (not presented) we obtained values in the same range.

3.8.3. *Effect of reaction present*

To investigate if the temperature difference in the *y*-direction (see Figs. 1 and 2 for axis orientation) is affecting the flow uniformity, we applied a temperature gradient of −5 to 15 K cm^{-1} in the y-direction for the channels and fixed the temperature at the edge to 1000 K. When air was used as the fluid the effect on F_u was less than 1%. It would be more correct to include the effect of the temperature on the current density also. However, the relationship between the current density and temperature is not straightforward and a rigorous calculation of the current density is outside the scope of this article. Instead of a rigorous calculation, we have used the Butler-Volmer equation to approximately calculate the increase of the current density w. r.t. temperature.

The Butler-Volmer equation is given as [54]:

$$j = j_0\left[exp\left(\frac{azFn_{act}}{RT}\right) - exp\left(\frac{-azFn_{act}}{RT}\right)\right] \tag{7}$$

where J_o is the exchange current density, a is the charge transfer coefficient, z is the number of electrons transferred and n_{act} is the activation overpotential. J_o can be expressed as [54].

$$j_0 = \gamma\exp\left(-\frac{E_{act}}{RT}\right) \tag{8}$$

Using the values given in the literature for the hydrogen-water reaction [54,55], an increase in the current density of 14% was found when increasing the temperature from 1000 K to 1010 K and maintaining the same activation overpotential (0.25 V based on [54]).

In order to include the effect of the temperature on the current distribution, we assumed that the fuel cell was fed with a 65% w/w H_2, 35% w/w H_2O gas mixture and 50% conversion of H_2 in SOFC mode. In SOEC mode we assumed a feed with 35% w/w H_2, 65% w/w H_2O gas mixture and 50% conversion of H_2O. The maximum change in F_u given these operating conditions was less 1%. This number is based on the assumptions above and the model presented in section 2. It therefore appears that violation of the assumptions does not change the flow significantly.

However, if an entire cell is modelled instead, a temperature gradient of only 5 K cm^{-1} in the y-direction (from $y = 0$ mm 45 mm (half the cell width) and -5 K cm^{-1} from $y = 45$ mm–90 mm) results in a change in the flow uniformity of more than 1% (using the same conditions as for the 1/3 of the cell above). The reason for this is that the absolute temperature difference for a whole cell is higher than for 1/3 of the cell.

We therefore advise that the results found in this study are only applied to cells operating with low temperature gradients in the y-direction. Such operation is possible. Work regarding the understanding and reducing of heat transfer from the stack to the surroundings has been carried out and is of critical importance when designing SOC systems [6,56–59]. Forschungszentrum Jülich also demonstrated a 5 kW SOFC stack with very low temperature gradients in the y-direction [47]. In SOEC mode, the stack can be operated thermo-neutral, which means that the net heat generation is zero and no temperature gradient in either the x- or y-direction is present [60,61] (assuming sufficient insulation of the sides or that the stack is operating in an oven).

3.9. *Effect of flow non-uniformity on possible reaction extent*

The level of flow uniformity limits the maximum allowable extent of conversion of reactants in the cell, before unwanted side-reactions take place. In SOFC the unwanted side-reactions are oxidations of Ni to NiO and in SOEC unwanted side-reactions cause carbon formation (Table 3). Since the current density is (almost) constant in the y-direction when the cell is run in co- or counter-flow configuration and temperature effects from the side of the stack are ignored, the number of moles converted in each channel will be the same.

The number of moles per unit time entering a channel is given by (9). By using this equation, the conversion in each channel and the overall conversion can be expressed by the flow uniformity index and the maximum conversion allowed in the channel with the lowest flow, X_{max}.

$$\text{Moles reactant per time fed to channel i } n_i = \frac{u_i}{\bar{u}} \cdot \frac{1}{N} \cdot n_{total} \tag{9}$$

$$\text{Conversion in channel i } X_{channel,i} = \frac{X_{max} \cdot \min(n_i)}{n_i} = \frac{X_{max} \cdot \min\left(\frac{u_i}{\bar{u}}\right)}{\frac{u_i}{\bar{u}}} = \frac{X_{max} F_u}{\frac{u_i}{\bar{u}}} \tag{10}$$

$$\text{Overall conversion } X_{overall} = \frac{N \cdot X_{max} \cdot \min(n_i)}{n_{total}} = X_{max}\mathrm{F_u} \tag{11}$$

When side-reactions are ignored, the maximum conversion allowed is 100%. With the optimized gas distributor design (flow uniformity index equal to 0.978) the conversion in the channel with the highest flow is 95.6% (calc. with (10)) and the overall conversion is 97.8% (calculated with (11)).

Table 3
Unwanted side-reactions in SOFC/SOEC.

Reactions generating NiO	Reactions generating C
$Ni + CO_2 \rightleftarrows NiO + CO$	$2CO \rightleftarrows C(s) + CO_2$
$2Ni + CO_2 \rightleftarrows 2NiO + C(s)$	$CH_4 \rightleftarrows C(s) + 2H_2$
$Ni + CO \rightleftarrows NiO + C(s)$	$CO + H_2 \rightleftarrows C(s) + H_2O$
$2Ni + O_2 \rightleftarrows 2NiO$	$CO_2 + 2H_2 \rightleftarrows C(s) + 2H_2O$
$Ni + H_2O \rightleftarrows NiO + H_2$	

In SOFC the conversion is limited by the risk of oxidizing Ni to NiO by the formed products [62]. Oxidation would damage the electrode due to volume expansion, eventually destroying the cell. The oxidation is thermodynamically unfavored when a small amount of reducing species (CO or H_2) is present. At 1000 K the Ni oxidizing reaction by H_2O is thermodynamically unfavored when the gas mixture contains at least 0.5% H_2 (using the thermodynamics given in Ref. [63]). This means that, for a pure hydrogen fueled SOFC, X_{max} is equal to 99.5%, the overall conversion (calculated with (11 and using the flow uniformity index of the optimized gas distributor design) is 97.3% and the conversion in the channel with the highest flow is 95.2%.

During CO_2- and co-electrolysis solid carbon can be formed. The carbon is typically whisker carbon, causing delamination of the electrode and electrolyte. In CO_2 electrolysis the carbon formation is thermodynamically favored for conversions above 74.5% at 1000 K (using the thermodynamics given in Ref. [64]). This means that the overall conversion is limited to 72.9% and the conversion in the channel with the highest flow is only 71.2%. If a design with less uniform flow is used, e.g. the design in Bi et al. [39], the overall conversion is limited to 67.8% (for $F_u = 0.91$). This shows that the flow uniformity has a significant effect on the possible overall conversion.

The above calculations are only strictly valid under the assumption of isothermal and non-reacting flow. However, as shown in section 3.8 the results are nevertheless applicable as long as there is no temperature gradient in the y-direction.

4. Conclusion

The optimal design of a special gas distributor to distribute the feed gas into parallel channels of a solid oxide cell has been investigated with CFD modelling. An optimized design was achieved by changing three geometrical parameters ($w_{cc} = 0.9$ mm, $\alpha = 4.66$, $w_b = 7.2$ mm) in the gas distributor reaching a flow uniformity index of 0.978. The optimization was performed using 300 Monte Carlo simulations and a soft maximum was found. Since the maximum is soft, the optimized design can be further tuned by including e.g. pressure drop in the optimization penalty function.

A temperature gradient of 5 K cm^{-1} in the direction perpendicular to the flow in the channels was found to influence the calculated flow uniformity, whereas a temperature gradient in the x-direction of up to 15 K cm^{-1} did not affect the flow uniformity. Thus, the findings in this study are only valid for cells with low temperature gradients in the y-direction.

The design is robust towards variations in the manufacturing process since variations in the optimized parameters of ±0.05 mm only lower the flow uniformity marginally from 0.978 to not less than 0.976.

Since flow uniformity dictates the possible overall conversion, the optimized design allows for a higher overall conversion than the non-optimized design. In the optimized gas distributor design, the maximum allowable average conversion (to avoid carbon formation) is only reduced by 2.3 percentage point compared to the situation with ideal flow distribution. In CO_2 electrolysis this corresponds to an overall conversion of 72.9% with the optimized design compared to the theoretical maximum of 74.5%.

Acknowledgments

This project is a collaboration between the CHEC Research center at DTU Chemical Engineering and Haldor Topsoe A/S and is partially funded by the Danish Industrial Ph.D. Fellowship

Programme (grant no. 1355-00140) administered by Innovation Fund Denmark.

Appendix A. Supplementary data

Supplementary data related to this article can be found at http://dx.doi.org/10.1016/j.jpowsour.2016.10.060.

References

[1] J.B. Hansen, Fuel processing for fuel cells and power to fuels as seen from an industrial perspective, J. Catal. 328 (2015) 280–296, http://dx.doi.org/10.1016/j.jcat.2015.04.014.

[2] C.M. Huang, S.S. Shy, H.H. Li, C.H. Lee, The impact of flow distributors on the performance of planar solid oxide fuel cell, J. Power Sources 195 (2010) 6280–6286, http://dx.doi.org/10.1016/j.jpowsour.2010.04.073.

[3] Y. Tao, S.D. Ebbesen, M.B. Mogensen, Carbon deposition in solid oxide cells during Co-Electrolysis of H2O and CO2, J. Electrochem. Soc. 161 (2014) F337–F343, http://dx.doi.org/10.1149/2.079403jes.

[4] K. Kendall, N.Q. Minh, S.C. Singhal, Chapter 08-Cell and Stack Designs, High Temp. Solid Oxide Fuel Cells, 2003, pp. 197–228. http://dx.doi.org/10.1016/B978-185617387-2/50025-8.

[5] L.G.J. De Haart, M. Spiller, Fuel cells – solid oxide fuel cells | gas distribution, in: J. Garche (Ed.), Encycl. Electrochem. Power Sources, Elsevier, Amsterdam, 2009, pp. 77–87. http://dx.doi.org/10.1016/B978-044452745-5.00253-7.

[6] N.Q. Minh, System designs and applications, in: M. Kendall, Kevin, Kendall (Eds.), High-temperature Solid Oxide Fuel Cells 21st Century, second ed., Elsevier Ltd., 2016, pp. 283–327, http://dx.doi.org/10.1016/B978-0-12-410453-2.00009-9.

[7] J. Jang, W. Yan, H. Li, W. Tsai, Three-dimensional numerical study on cell performance and transport phenomena of PEM fuel cells with conventional flow fields, Int. J. Hydrogen Energy 33 (2008) 156–164, http://dx.doi.org/10.1016/j.ijhydene.2007.09.005.

[8] W.L. Huang, Q. Zhu, Flow distribution in U-type layers or stacks of planar fuel cells, J. Power Sources 178 (2008) 353–362, http://dx.doi.org/10.1016/j.jpowsour.2007.12.003.

[9] G. Hu, J. Fan, S. Chen, Y. Liu, K. Cen, Three-dimensional numerical analysis of proton exchange membrane fuel cells (PEMFCs) with conventional and interdigitated flow fields, J. Power Sources 136 (2004) 1–9, http://dx.doi.org/10.1016/j.jpowsour.2004.05.010.

[10] C.-H. Cheng, H.-H. Lin, Numerical analysis of effects of flow channel size on reactant transport in a proton exchange membrane fuel cell stack, J. Power Sources 194 (2009) 349–359, http://dx.doi.org/10.1016/j.jpowsour.2009.04.075.

[11] M. Hyun, S.-K. Kim, D. Jung, B. Lee, D. Peck, T. Kim, et al., Prediction of anode performances of direct methanol fuel cells with different flow-field design using computational simulation, J. Power Sources 157 (2006) 875–885, http://dx.doi.org/10.1016/j.jpowsour.2006.02.023.

[12] J.M. Jackson, M.L. Hupert, S.A. Soper, Discrete geometry optimization for reducing flow non-uniformity, asymmetry, and parasitic minor loss pressure drops in Z-type configurations of fuel cells, J. Power Sources 269 (2014) 274–283, http://dx.doi.org/10.1016/j.jpowsour.2014.06.136.

[13] W. Xia, Y. Yang, Q. Wang, Effects of operations and structural parameters on the one-cell stack performance of planar solid oxide fuel cell, J. Power Sources 194 (2009) 886–898, http://dx.doi.org/10.1016/j.jpowsour.2009.06.009.

[14] S. Su, H. He, D. Chen, W. Zhu, Y. Wu, W. Kong, et al., Flow distribution analyzing for the solid oxide fuel cell short stacks with rectangular and discrete cylindrical rib configurations, Int. J. Hydrogen Energy 40 (2015) 577–592, http://dx.doi.org/10.1016/j.ijhydene.2014.10.125.

[15] H.H. He, S.D. Zhang, Q. Zhang, S.C. Su, B. Wang, W.L. Zhang, Investigating on the flow distribution of a planar solid oxide fuel cell stack, Adv. Mater. Res. 986–987 (2014) 97–100, http://dx.doi.org/10.4028/www.scientific.net/AMR.986-987.97.

[16] W. Bi, D. Chen, Z. Lin, A key geometric parameter for the flow uniformity in planar solid oxide fuel cell stacks, Int. J. Hydrogen Energy 34 (2009) 3873–3884, http://dx.doi.org/10.1016/j.ijhydene.2009.02.071.

[17] J. Duquette, A. Petric, Silver wire seal design for planar solid oxide fuel cell stack, J. Power Sources 137 (2004) 71–75, http://dx.doi.org/10.1016/j.jpowsour.2004.05.038.

[18] J.A. Salvatore, V. Rajamani, A. Dutta, EP2377190 (B1) Unif. Gas Distribution through Channels of SOFC, 2012. http://worldwide.espacenet.com/publicationDetails/description?CC=EP&NR=2377190B1&KC=B1&FT=D&ND=4&date=20140806&DB=worldwide.espacenet.com&locale=en_EP (accessed November 26, 2015).

[19] W. Zhang, P. Hu, X. Lai, L. Peng, Analysis and optimization of flow distribution in parallel-channel configurations for proton exchange membrane fuel cells, J. Power Sources 194 (2009) 931–940, http://dx.doi.org/10.1016/j.jpowsour.2009.05.033.

[20] Y.-P. Chyou, Y.-N. Cheng, K.-F. Lin, US 20070207363 A1 Interconnect set of planar solid oxide fuel cell having flow paths, 2007. https://www.google.com/patents/US20070207363 (accessed November 27, 2015).

[21] C.M. Huang, S.S. Shy, C.H. Lee, On flow uniformity in various interconnects and its influence to cell performance of planar SOFC, J. Power Sources 183 (2008) 205–213, http://dx.doi.org/10.1016/j.jpowsour.2008.04.059.

[22] T. Heiredal-Clausen, C. Buchholtz Frederiksen, Gas Inlet for SOEC Unit, (2014). https://patentscope.wipo.int/search/en/detail.jsf?docId=WO2014177212&recNum=1&maxRec=&office=&prevFilter=&sortOption=&queryString=&tab=PCT+Biblio (accessed July 13, 2015).

[23] L. Wang, H. Liu, Performance studies of PEM fuel cells with interdigitated flow fields, J. Power Sources 134 (2004) 185–196, http://dx.doi.org/10.1016/j.jpowsour.2004.03.055.

[24] W. Yan, S. Mei, C. Soong, Z. Liu, D. Song, Experimental Study on the Performance of PEM Fuel Cells with Interdigitated Flow Channels vol. 160, 2006, pp. 116–122, http://dx.doi.org/10.1016/j.jpowsour.2006.01.063.

[25] S. Maharudrayya, S. Jayanti, A.P. Deshpande, Pressure drop and flow distribution in multiple parallel-channel configurations used in proton-exchange membrane fuel cell stacks, J. Power Sources 157 (2006) 358–367, http://dx.doi.org/10.1016/j.jpowsour.2005.07.064.

[26] N. Guo, M.C. Leu, U.O. Koylu, Network based optimization model for pin-type flow field of polymer electrolyte membrane fuel cell, Int. J. Hydrogen Energy 38 (2013) 6750–6761, http://dx.doi.org/10.1016/j.ijhydene.2013.03.066.

[27] X. Li, I. Sabir, Review of bipolar plates in PEM fuel cells: flow-field designs, Int. J. Hydrogen Energy 30 (2005) 359–371, http://dx.doi.org/10.1016/j.ijhydene.2004.09.019.

[28] A. Hermann, T. Chaudhuri, P. Spagnol, Bipolar plates for PEM fuel cells: a review, Int. J. Hydrogen Energy 30 (2005) 1297–1302, http://dx.doi.org/10.1016/j.ijhydene.2005.04.016.

[29] H. Tawfik, Y. Hung, D. Mahajan, Metal bipolar plates for PEM fuel cell-A review, J. Power Sources 163 (2007) 755–767, http://dx.doi.org/10.1016/j.jpowsour.2006.09.088.

[30] J. Wang, Theory and practice of flow field designs for fuel cell scaling-up: a critical review, Appl. Energy 157 (2015) 640–663, http://dx.doi.org/10.1016/j.apenergy.2015.01.032.

[31] J. Wang, Pressure drop and flow distribution in parallel-channel configurations of fuel cells: U-type arrangement, Int. J. Hydrogen Energy 33 (2008) 6339–6350, http://dx.doi.org/10.1016/j.ijhydene.2008.08.020.

[32] S. Maharudrayya, S. Jayanti, A.P. Deshpande, Flow distribution and pressure drop in parallel-channel configurations of planar fuel cells, J. Power Sources 144 (2005) 94–106, http://dx.doi.org/10.1016/j.jpowsour.2004.12.018.

[33] J. Wang, H. Wang, Flow-field designs of bipolar plates in PEM fuel cells: theory and applications, Fuel Cells 12 (2012) 989–1003, http://dx.doi.org/10.1002/fuce.201200074.

[34] A. Arvay, J. French, J.-C. Wang, X.-H. Peng, A.M. Kannan, Nature inspired flow field designs for proton exchange membrane fuel cell, Int. J. Hydrogen Energy 38 (2013) 3717–3726, http://dx.doi.org/10.1016/j.ijhydene.2012.12.149.

[35] C.-H. Chen, S.-P. Jung, S.-C. Yen, Flow distribution in the manifold of PEM fuel cell stack, J. Power Sources 173 (2007) 249–263, http://dx.doi.org/10.1016/j.jpowsour.2007.05.007.

[36] X. Yu, B. Zhou, A. Sobiesiak, Water and thermal management for Ballard PEM fuel cell stack, J. Power Sources 147 (2005) 184–195, http://dx.doi.org/10.1016/j.jpowsour.2005.01.030.

[37] Y. Zong, B. Zhou, A. Sobiesiak, Water and thermal management in a single PEM fuel cell with non-uniform stack temperature, J. Power Sources 161 (2006) 143–159, http://dx.doi.org/10.1016/j.jpowsour.2006.02.107.

[38] A. Faghri, Z. Guo, Challenges and opportunities of thermal management issues related to fuel cell technology and modeling, Int. J. Heat. Mass Transf. 48 (2005) 3891–3920, http://dx.doi.org/10.1016/j.ijheatmasstransfer.2005.04.014.

[39] W. Bi, J. Li, Z. Lin, Flow uniformity optimization for large size planar solid oxide fuel cells with U-type parallel channel designs, J. Power Sources 195 (2010) 3207–3214, http://dx.doi.org/10.1016/j.jpowsour.2009.11.127.

[40] J.-H. Koh, H.-K. Seo, C.G. Lee, Y.-S. Yoo, H.C. Lim, Pressure and flow distribution in internal gas manifolds of a fuel-cell stack, J. Power Sources 115 (2003) 54–65, http://dx.doi.org/10.1016/S0378-7753(02)00615-8.

[41] J. Kirtley, A. Singh, D. Halat, T. Oswell, J.M. Hill, R.A. Walker, Situ raman studies of carbon removal from high temperature Ni–YSZ cermet anodes by gas phase reforming agents, J. Phys. Chem. C 117 (2013) 25908–25916, http://dx.doi.org/10.1021/jp408192e.

[42] V. Alzate-Restrepo, J.M. Hill, Carbon deposition on Ni/YSZ anodes exposed to CO/H2 feeds, J. Power Sources 195 (2010) 1344–1351, http://dx.doi.org/10.1016/j.jpowsour.2009.09.014.

[43] A. Faes, A. Hessler-Wyser, A. Zryd, J. Van Herle, A review of RedOx cycling of solid oxide fuel cells anode, Membr. (Basel) 2 (2012) 585–664, http://dx.doi.org/10.3390/membranes2030585.

[44] V.E. Senecal, Fluid distribution in process equipment, Ind. Eng. Chem. 49 (1957) 993–997, http://dx.doi.org/10.1021/ie50570a031.

[45] A. Cybulski, G. Eigenberger, A. Stankiewicz, Operational and structural nonidealities in modeling and design of multitubular catalytic reactors, Ind. Eng. Chem. Res. 36 (1997) 3140–3148, http://dx.doi.org/10.1021/ie960596s.

[46] G. Eigenberger, W. Ruppel, Catalytic Fixed-bed Reactors, in: Ullmann's Encycl. Ind. Chem, 2012, http://dx.doi.org/10.1002/14356007.b04_199.pub2.

[47] B. Emonts, IWV-3 Report 2005: Future as a Challenge, Schriften Des Forschungszentrums Jülich. R. Energietechnik/Energy Technol., Forschungszentrum, Zentralbibliothek, Jülich, 2005. http://juser.fz-juelich.de/record/46935.

[48] K.P. Recknagle, R.E. Williford, L.A. Chick, D.R. Rector, M.A. Khaleel, Three-dimensional thermo-fluid electrochemical modeling of planar SOFC stacks,

J. Power Sources 113 (2003) 109–114, http://dx.doi.org/10.1016/S0378-7753(02)00487-1.

[49] Y.P. Chyou, T.D. Chung, J.S. Chen, R.F. Shie, Integrated thermal engineering analyses with heat transfer at periphery of planar solid oxide fuel cell, J. Power Sources 139 (2005) 126–140, http://dx.doi.org/10.1016/j.jpowsour.2004.07.001.

[50] J.S. Herring, J.E. O'Brien, C.M. Stoots, G.L. Hawkes, J.J. Hartvigsen, M. Shahnam, Progress in high-temperature electrolysis for hydrogen production using planar SOFC technology, Int. J. Hydrogen Energy 32 (2007) 440–450, http://dx.doi.org/10.1016/j.ijhydene.2006.06.061.

[51] C.-K. Lin, T.-T. Chen, Y.-P. Chyou, L.-K. Chiang, Thermal stress analysis of a planar SOFC stack, J. Power Sources 164 (2007) 238–251, http://dx.doi.org/10.1016/j.jpowsour.2006.10.089.

[52] M. Peksen, A. Al-Masri, L. Blum, D. Stolten, 3D transient thermomechanical behaviour of a full scale SOFC short stack, Int. J. Hydrogen Energy 38 (2013) 4099–4107, http://dx.doi.org/10.1016/j.ijhydene.2013.01.072.

[53] G. Hawkes, J. O'Brien, C. Stoots, S. Herring, M. Shahnam, Thermal and electrochemical three dimensional CFD model of a planar solid oxide electrolysis cell, Heat. Transf. 4 (2005) 27–36, http://dx.doi.org/10.1115/HT2005-72565.

[54] M. Ni, M. Leung, D. Leung, Parametric study of solid oxide steam electrolyzer for hydrogen production, Int. J. Hydrogen Energy 32 (2007) 2305–2313, http://dx.doi.org/10.1016/j.ijhydene.2007.03.001.

[55] S.H. Chan, Z.T. Xia, Polarization effects in electrolyte/electrode-supported solid oxide fuel cells, J. Appl. Electrochem 32 (2002) 339–347, http://dx.doi.org/10.1023/A:1015593326549.

[56] D.L. Damm, A.G. Fedorov, Radiation heat transfer in SOFC materials and components, J. Power Sources 143 (2005) 158–165, http://dx.doi.org/10.1016/j.jpowsour.2004.11.063.

[57] S. Tang, A. Amiri, P. Vijay, M.O. Tadé, Development and validation of a computationally efficient pseudo 3D model for planar SOFC integrated with a heating furnace, Chem. Eng. J. 290 (2016) 252–262, http://dx.doi.org/10.1016/j.cej.2016.01.040.

[58] M. Spinnler, Studies on high-temperature multilayer thermal insulations, Int. J. Heat. Mass Transf. 47 (2004) 1305–1312, http://dx.doi.org/10.1016/j.ijheatmasstransfer.2003.08.012.

[59] M. Spinnler, E.R.F. Winter, R. Viskanta, T. Sattelmayer, Theoretical studies of high-temperature multilayer thermal insulations using radiation scaling, J. Quant. Spectrosc. Radiat. Transf. 84 (2004) 477–491, http://dx.doi.org/10.1016/S0022-4073(03)00264-4.

[60] M. Ni, Computational fluid dynamics modeling of a solid oxide electrolyzer cell for hydrogen production, Int. J. Hydrogen Energy 34 (2009) 7795–7806, http://dx.doi.org/10.1016/j.ijhydene.2009.07.080.

[61] M. Ni, Modeling of a solid oxide electrolysis cell for carbon dioxide electrolysis, Chem. Eng. J. 164 (2010) 246–254, http://dx.doi.org/10.1016/j.cej.2010.08.032.

[62] J. Kuhn, O. Kesler, Method for in situ carbon deposition measurement for solid oxide fuel cells, J. Power Sources 246 (2014) 430–437, http://dx.doi.org/10.1016/j.jpowsour.2013.07.106.

[63] P. Nehter, A high fuel utilizing solid oxide fuel cell cycle with regard to the formation of nickel oxide and power density, J. Power Sources 164 (2007) 252–259, http://dx.doi.org/10.1016/j.jpowsour.2006.08.037.

[64] J.R. Rostrup-Nielsen, Equilibria of decomposition reactions of carbon monoxide and methane over nickel catalysts, J. Catal. 27 (1972) 343–356, http://dx.doi.org/10.1016/0021-9517(72)90170-4.

D.2 Modelling of Gas Diffusion in Ni/YSZ Electrodes in CO2 and co-electrolysis (postprint)

Modelling of Gas Diffusion in Ni/YSZ Electrodes in CO_2 and co-electrolysis

Jakob Dragsbæk Duhn[1*], Anker Degn Jensen[1], Stig Wedel[1], Christian Wix[2]
[1]DTU Chemical Engineering, Søltofts Plads 229, 2800 Kgs. Lyngby/Denmark
[2]Haldor Topsoe A/S; Haldor Topsøes Allé 1, 2800 Kgs. Lyngby/Denmark
[*] Corresponding author: jadu@kt.dtu.dk

Abstract

Carbon formation may occur during CO_2 and CO_2/H_2O electrolysis using solid oxide electrolyzer cells due to the Boudouard reaction ($2CO \rightarrow CO_2 + C(s)$). Formed carbon may disintegrate the cell structure and it is therefore of importance to be able to predict when carbon is formed, and take actions to prevent its formation.
For prediction of carbon formation, the gas composition in the electrode must be known. In this work, the diffusion of gases in the electrode has been modelled with the dusty gas model in 1 and 2 dimensions, and the effect of tortuosity, porosity, temperature, electrode thickness, pore diameter, current density, pitch and rib width has been investigated. It is shown that diffusion limitations on reactant/product transport may lead to carbon formation.

The parameters describing the microstructure and the dimensions of the cathode channels and interconnect ribs are found to have a large effect on the carbon formation propensity. Given a set of parameters, a simple correlation between the CO mole fraction in the channel and under the interconnect rib, and current density during CO_2-electrolysis can be derived. This correlation makes it possible to efficiently integrate the calculation of carbon formation risk in existing electrolyzer cell models.

Keywords: Boudouard reaction, Carbon Formation, Diffusive Mass Transport, Electrolysis, Fuel cell, Mathematical Modeling, Solid Oxide Electrolysis Cell.

1 Introduction

Solid oxide electrolyzer cells (SOEC) are electrochemical devices capable of converting H_2O and CO_2 to H_2 and CO. The electrolysis of H_2O and CO_2 is important since it is capable of producing H_2, CO or syngas directly from electrical energy from e.g. renewable energy sources. These compounds can be used to produce synthetic hydrocarbon fuels as a solution to reduce oil consumption and carbon dioxide emissions.

However, the formation of carbon has been observed during electrolysis of CO_2 and CO_2 and H_2 co-electrolysis [1,2]. The carbon can block pores and reaction sites [3], cause the Ni structure in the electrode to change [4], and cause local fractures in the cermet [5]. It is therefore of great importance to avoid carbon formation. During both CO_2 and co-electrolysis carbon formation has been observed at operating conditions where it should be thermodynamically unfavored based on the gas composition in the bulk of the gas phase (i.e. in the gas channels of a stack) [2,6]. In the literature it has been presumed that this is caused by diffusion limitations within the electrode [2,6]. In this study we investigate this presumption by calculating the concentration profiles in the electrode and evaluate the risk of carbon formation based on the actual gas composition in the electrode, rather than the composition in the gas bulk.

Different models for diffusion in the electrode material have been used in the literature, including Fick's law, Stefan-Maxwell model, dusty gas model, binary friction model, and the cylindrical pore interpolation model [7–9]. The most frequently used models are Fick's law and dusty gas model [9]. Suwanwarangkul et al. [10] compared the performance of Fick's law, the Stefan-Maxwell model, and the dusty gas model in predicting the experimental measured concentration overpotentials in SOFC anodes for H_2-H_2O-Ar and CO-CO_2 systems. The concentration overpotential depends on the gas concentrations in both the gas channel and at the interface between the electrode and electrolyte. With the diffusion models, the gas composition at the interface can be calculated and thus also the concentration overpotential can be calculated and compared to the measured value.
Using this approach, Suwanwarangkul et al. [10] found that the dusty gas model was better at predicting the concentration overpotential. For the CO-CO_2 system Fick's law could also be used to model the system with acceptable accuracy (within 15 % of the results obtained by the dusty gas model) when the current density was low (0.1 A cm^{-2}) and at low (25 %) to intermediate (40%) CO concentrations. At a higher current density (0.3 A cm^{-2}) Fick's law could only be used for intermediate CO concentrations. Suwanwarangkul et al. [10] also found that the dusty gas model was the only suitable model for the H_2-H_2O-CO-CO_2 system. Vural et al. [8] found that the dusty gas model, Stefan-Maxwell model and the binary friction model all gave similar predictions for the concentration overpotential for H_2-H_2O-Ar and CO-CO_2 systems up to high current densities (1.5 A cm^{-2}) and small pore radius (0.27 µm). Wang et al. [11] compared the dusty gas model with the binary friction model and the cylindrical pore interpolation model and found that they gave similar results. In this study, the diffusion has been modelled with the dusty gas model. This model was chosen because 1) the investigated situations span a wide range of current density and CO concentrations, 2) the H_2-H_2O-CO-CO_2 system is also investigated.

Ni containing catalysts are used in different industrial processes such as reforming and high temperature methanation. The carbon formation on Ni has therefore been thoroughly studied [3,12–16]. Carbonaceous gas species might form solid carbon through the Boudouard reaction (Reaction 1) and methane decomposition (Reaction 2) [3,17]. The carbon can be in the form of graphite [18], pyrolytic carbon, carbides [19,20], and filamentous carbon (also called whisker carbon) [14,21]. At the high temperatures used in SOECs, filamentous carbon and graphite will be formed [22,23], see Figure 1.

Boudouard reaction $2CO \rightleftharpoons CO_2 + C(s)$ (1)

Methane decomposition $CH_4 \rightleftharpoons 2H_2 + C(s)$ (2)

When both carbon and hydrogen species are present, the water-gas shift reaction and methanation reaction will also take place.

Water-gas shift $CO + H_2O \rightleftharpoons CO_2 + H_2$ (3)
Methanation reactions $CO + 3H_2 \rightleftharpoons CH_4 + H_2O$ (4)

Carbon deposition on solid oxide cells running in fuel cell mode, with methane [23,24] and other hydrocarbons [25] as the carbon source, has been widely studied. However, only a few studies have focused on solid oxide cells running in electrolysis mode with either H_2O+CO_2 or CO_2 as the process feed [26–29]. In co-electrolysis carbon deposition has been observed and is believed to cause delamination of the electrode from the solid electrolyte after long-time testing (≤ 700 hr.) [1]. In CO_2-electrolysis it has been observed that just crossing the equilibrium (forming small amounts of carbon) is a reversible process [2]. It is generally accepted that carbon formation is to be expected when there is a nickel catalyst present and the gas shows affinity for carbon formation after the establishment of methanation and shift equilibria [30]. The affinity for carbon formation, a_c, is given as the equilibrium constant, divided with the reaction quotient:

$$a_c = K_1/Q_1 \quad (5)$$

$$Q_1 = \frac{X_{CO_2}}{X_{\mathrm{CO}}^2 p_t} \quad (6)$$

K_1 is the equilibrium constant for reaction 1, Q_1 is the reaction quotient, X is the mole fraction of CO_2 and CO, respectively, and p_t is the total pressure in atm.

When $a_c > 1$, the gas shows affinity for carbon formation. Since the equilibrium constant is a function of temperature, the temperature at which the gas mixture starts to show affinity to carbon formation via the Boudouard reaction, T_B, can be calculated. If the equilibrium temperature is less than the actual temperature, the formation of carbon is thermodynamically unfavorable and if the equilibrium temperature is above the actual temperature, the formation of carbon is thermodynamically favorable. Calculating the equilibrium temperature is advantageous since the necessary temperature increase to avoid carbon formation can easily be calculated as $T_B - T_{cell}$.

Some studies have used the thermodynamic data for graphite when calculating the equilibrium constant for the Boudouard reaction [1,31,32]. However, there is a significant difference between the thermodynamic data for graphite and filamentous carbon [13,14,33]. Figure 1 shows the equilibrium curves for carbide (Ni_3C), graphite and filamentous carbon. It can be seen that for temperatures above 650 °C, the equilibrium constant is higher for filamentous carbon than graphite. Thus, the gas mixture will show affinity to filamentous carbon, rather than graphite carbon, at a higher temperature. Since we want to investigate situations where the gas composition has just crossed the equilibrium, we will use the thermodynamic data for filamentous carbon, which are based on experimental studies [3,13,14]. The studies present somewhat different values for the equilibrium constant. In this study we have used the thermodynamic data given by Rostrup-Nielsen [13], since they are based on experiments up to 700 °C, whereas the others are based on temperatures below 575 °C [3] and 627 °C [14], respectively.

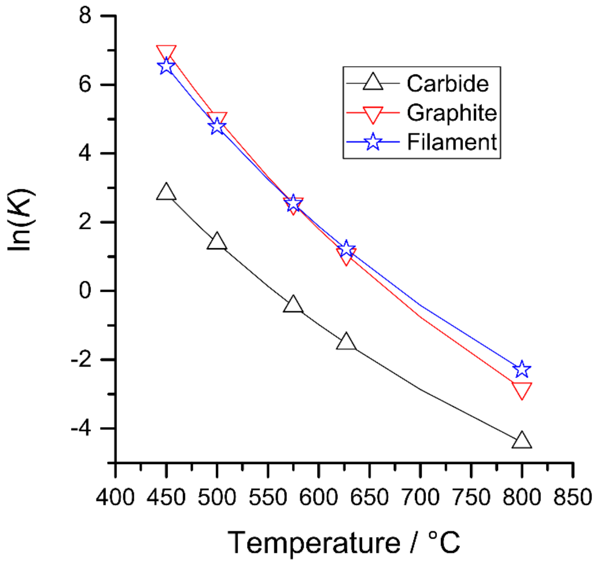

Figure 1. Equilibrium constant for different forms of carbon formation as function of temperature. Based on data from [3]**.**

2 Models

Figure 2a and 2b shows a schematic view of the SOEC. Starting from the top on figure 2a, gas is entering at the cathode gas channel and flows over the cathode. Gas species are diffusing through the porous cathode towards the electrode-electrolyte interface driven by a concentration gradient. At the electrode-electrolyte reaction interface the electrochemical reduction of CO_2 and H_2O takes place (reaction 14 and 15, see section 2.4). The thickness of this layer, d_i, is between a few µm and 20 µm [34–36]. In our modelling, we have selected a thickness of 10 µm. The specific number does not influence the results significantly, since the major part of the diffusion take place in the support layer, which is several times thicker than the reaction layer. The products of the electrochemical reactions, respectively CO and H_2, diffuse back to the channel and are swept out by the channel flow. During co-electrolysis, the water-gas shift reaction (reaction 3) as well as the methanation reaction (reaction 4) will also take place in the electrode.

The formed oxygen ions diffuse through the electrolyte and react to oxygen molecules at the anode. The formed oxygen molecules are transported out of the cell via the sweep flow in the anode channel. Figure 2b shows the cell in the x-z dimension, where the interconnect can be seen. The interconnect forms the cathode channels, which help distribute the fluid uniformly [37], and the rib, which ensures that there is electrical contact between adjacent cells.

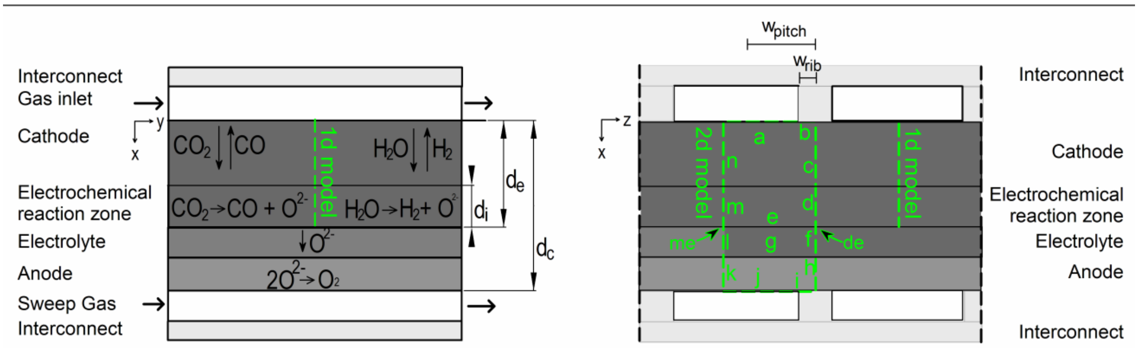

Figure 2a (left) and 2b (right). Figure 2a is a schematic xy-plane view of the cell and 2b is the a xz view of the cell. The 1d model is marked on both figures and the 2d model is marked on figure 2b. The single letters on figure 2b are used to label the boundaries and the double letters are used to label the points, which are referred to in the text.

Two models are used in this study: A 1d model and a 2d model (see figure 2a and 2b). The 1d model consists of the cathode and electrochemical reaction zone along the line shown in figure 2. The 2d model consists of the cathode, electrochemical reaction zone, electrolyte and anode (the rectangle shown in figure 2b). In the 2d model, the cathode and anode consist of parts with contact to the gas channel and with contact to the interconnect rib. In this way, the effect of the interconnect rib on the gas transfer and current density distribution is included. The letters in figure 2b are used to label the boundaries and are referred to in the following text. The point where "d" and "e" intersect (the point under the center of the rib) is labelled "de" in the following text. Likewise, the point where "m" and "e" intersect (the point under the center of the channel) is labelled "me"

The governing equations for both models are given in the following. The 1d model only considers the changes in the x direction and 2d model only considers the changes in the x and z direction.

The following assumptions have been made: 1) the total pressure in the channel is 1 atm, 2) the system is at steady state, 3) the part of the cell that is modeled is at isothermal conditions, 4) the material is isotropic, 5) the surface diffusion and thermal diffusion can be neglected. The assumption of isothermal condition is justified since the thickness of the cell is relatively thin and the thermal conductivities of the materials are high. Very small temperature gradients in the x-direction have previously been calculated [38] and are therefore disregarded in this work. The isothermal assumption is furthermore justified by a rough evaluation of the difference between the cell temperature and the gas temperature, presented in the appendix.

2.1 Mass Transport

The mass balance at steady state is given by

$$\nabla \vec{N}_i = r_i \qquad (7)$$

where $\vec{N}_i$ *is* the flux of species *i*, and r_i is the rate of reaction of species *i*.

2.2 Diffusion

In the dusty gas model, the molar flux of compound *i* is given as an implicit function of the other molar fluxes the molar fractions, and the gradients of pressure and molar fractions:

$$\sum_{j=1,j\neq i}^{n}\frac{X_i\vec{N}_j-X_j\vec{N}_i}{D_{ij}^{eff}}-\frac{\vec{N}_i}{D_{i,k}^{eff}}=\frac{\mathrm{p}}{RT}\nabla X_i+\frac{X_i}{RT}\left(1+\frac{Bp}{\mu_m D_{i,k}^{eff}}\right)\nabla p \quad (8)$$

where X_i is the molar fraction of species i, $D_{i,k}^{eff}$ is the effective Knudsen diffusion coefficient of species i, $D_{i,j}^{eff}$ is the effective binary diffusion coefficient of species *i* in *j*, *p* is the pressure; $\vec{N}_i$ is the flux of species *i*, *B* is the permeability and μ_m is the viscosity of the mixture

The binary diffusion coefficient is calculated by the Chapman–Enskog correlation and the Knudsen diffusion coefficient is calculated by kinetic theory of gases [39].

$$D_{i,j}^{eff}=\frac{\epsilon}{\tau}D_{i,j}=\frac{\epsilon}{\tau}0.001858T^{1.5}\cdot\frac{\left(\frac{1}{M_i}+\frac{1}{M_j}\right)^{0.5}}{p\sigma_{i,j}^2\Omega_D} \quad (9)$$

$$D_{i,K}^{eff}=\frac{\epsilon}{\tau}D_{i,K}=\frac{\epsilon}{\tau}\cdot\frac{d_p}{3}\sqrt{\frac{8RT}{\pi M_i}} \quad (10)$$

where M_i is the molecular weight of component *i*, $\sigma_{i,j}$ is the average collision diameter between component i and j and Ω_D is the dimensionless collision integral in the Lennard-Jones potential model, ϵ is electrode porosity, τ is the tortuosity, d_p is the pore diameter. σ and Ω_D are available in the literature [39,40]. Based on [41] where permeabilities for Ni-YSZ electrodes are summarized, we have selected a permeability of $B=5\cdot10^{-15}\ \mathrm{m}^2$.

2.3 Transport of electrons and oxygen ions

In the 2d model two charged particles are modelled, electrons and oxygen ions. The electrodes and electrolyte is assumed to be pure electronic and ionic conductors, respectively. Ohms law is used to calculate the current distribution in the 2d model.

$$\nabla(\sigma_{el}\nabla\Phi_{\mathrm{el}})=0 \quad (11)$$
$$\nabla(\sigma_{io}\nabla\Phi_{\mathrm{io}})=0 \quad (12)$$

The electronic conductivity, σ_{el}, of the electrodes is high compared to the ionic conductivity of the electrolyte, σ_{io}, and is therefore assumed to be temperature independent in the investigated temperature regime. The electronic conductivity is 800 $\mathrm{S\,cm^{-1}}$ for the cathode (Ni-8YSZ) and 72 $\mathrm{S\,cm^{-1}}$ for the anode (LSM) [42–44]. The ionic conductivity for the electrolyte is temperature dependent and given as [45]:

$$\sigma_{io}=466\cdot\exp\left(-\frac{9934}{T}\right) \quad (13)$$

where T is inserted in K and σ_{io} is in $\Omega^{-1}\mathrm{cm}^{-1}$. In the 1d model, the current density is assumed to be uniform and thus equations 11 and 12 are not used.

2.4 Reactions

Two electrochemical reactions take place at the cathode-electrolyte interface, namely the reduction of CO_2 to CO and of H_2O to H_2:

$$\mathrm{CO_2}+2\mathrm{e}^-\rightarrow\mathrm{CO}+\mathrm{O}^{2-} \quad (14)$$
$$\mathrm{H_2O}+2\mathrm{e}^-\rightarrow\mathrm{H_2}+\mathrm{O}^{2-} \quad (15)$$

The rates of reactions 14, and 15 are given as functions of the current density, see Table 1. During co-electrolysis both reaction 14 and reaction 15 may occur at the interface. In this case the current density will consist of the current arising from each of the two reactions:

$$\vec{i} = \vec{i}_{H_2O} + \vec{i}_{CO_2} \tag{16}$$

One approach to model co-electrolysis is to assume that only reaction 15 occurs at the interface and that subsequently CO_2 is converted to CO via the water-gas shift reaction [46]. Another approach is to assume that both reactions occur at the interface and include a parameter β, that determines the fraction of the interface surface available for H_2O electrolysis [47–49]. In this approach, the electrical current is divided between the two reactions depending on the mole fraction of CO_2 and H_2O at the interface.

$$\beta = \frac{x_{H_2O}^{int}}{x_{CO_2}^{int} + x_{H_2O}^{int}} \tag{17}$$

In this study we will use the latter method, where both reaction 14 and 15 take place at the interface.In the water-gas shift reaction occur infinite fast, the two methods should give the same. However, since the water-gas shift reaction might not reach equilibrium within the reaction zone, the latter method is used.

In the entire electrode three reactions might take place: 1) the water-gas shift reaction, 2) methanation reaction, and 3) the Boudouard reaction. Only the water-gas shift reaction is included in the model as a reaction with finite rate. The rate expression is given in Table 1. The reason for excluding the methanation reactions is that the formation of methane is severely limited by thermodynamics at the high temperature and low pressure in the electrode (calculated with in-house thermodynamics software). The carbon formation reactions are excluded because we only want to identify if carbon formation if thermodynamic feasible. It is generally accepted that carbon formation will take place when the carbon affinity a_c is above 1 [12,50]. Since SOECs are normally operated at steady state for long periods of time, any affinity for carbon is likely to cause accumulation of carbon, regardless of the reaction rate, and will eventually cause problems for the cell.

The rate expressions for reactions 14, 15 and 3 and the thermodynamic equilibrium constants for the Boudouard reaction (reaction 1) are given in Table 1.

Table 1. Reaction rates and equilibrium.

Reaction	Thermodynamic equilibrium or rate expression	Source
14	$r_{CO_2,electrolysis} = \frac{\vec{i}}{2F} \cdot (1-\beta) \cdot \frac{1}{d_i}$	
15	$r_{H_2O,electrolysis} = \frac{\vec{i}}{2F} \cdot \beta \cdot \frac{1}{d_i}$	
3	$r_{wgs} = k_{sf}\left(P_{H_2O}P_{CO} - \frac{P_{H_2}P_{CO_2}}{K_{ps}}\right)$ $k_{sf} = 0.0171 \exp\left(-\frac{103191}{RT}\right)\ \mathrm{mol\ m^{-3}\ Pa^{-2}\ s^{-1}}$ $K_{ps} = \exp(-0.2935Z^3 + 0.635Z^2 + 4.1788Z + 0.3169)$ $Z = \frac{1000}{T} - 1$	[38]

1	$K_B = \exp\left(\frac{138100 - 144.6T}{RT}\right) \cdot 1\ \mathrm{atm}^{-1}$	[13]

In Table 1 *F* is Faradays constant, p_i is the partial pressure of species *i*, *R* is the universal gas constant and, *T* is the temperature.

The reaction rate for the four species in the cathode and reaction interface can be written as:

$$r_{H_2} = r_{wgs} + r_{H_2O,electrolysis} \quad (18)$$

$$r_{H_2O} = -r_{wgs} - r_{H_2O,electrolysis} \quad (19)$$

$$r_{CO} = -r_{wgs} + r_{CO_2,electrolysis} \quad (20)$$

$$r_{CO_2} = r_{wgs} - r_{CO_2,electrolysis} \quad (21)$$

Where r_{wgs} is the reaction rate for the water-gas shift reaction. $r_{H_2O,electrolysis}$ and $r_{CO_2,electrolysis}$ are 0 in the cathode support.

In the 2d model the oxidation of the oxygen ion takes place at the anode-electrolyte interface:

$$2\,\mathrm{O}^{-2} \rightarrow \mathrm{O}_2 + 4\mathrm{e}^- \quad (22)$$

$$r_{O_2} = \frac{\vec{\mathrm{i}}}{4F} \quad (23)$$

The transfer of the oxygen molecules to the anode channel is calculated with the mass transfer equation (eq. 7) and the dusty gas model (eq. 8).

2.5 Boundary Conditions and Numerical Solution

It follows from the assumption of negligible mass transfer between the bulk gas in the channel and the sample, that the mole fractions of all species at the boundary between the fuel electrode and the bulk gas is identical to the bulk gas. The pressure is also the same. Thus, the boundary conditions at x = 0 for the 1d model are:

$$X_i|_{x=0} = X_{(i,channel)} \quad (24)$$

$$p|_{x=0} = p_{(t,channel)} \quad (25)$$

Where $X_{(i,channel)}$ is the mole fractions in the channel, and $p_{(t,channel)}$ is the channel pressure. $X_{(i,channel)}$ and $p_{(t,channel)}$ must be specified as input to the model.

Similar for the 2d model the boundary conditions at x=0 for the part of the cathode in contact with the cathode channel (labelled “a” on figure 2b) is given by equation 24 and 25.

Furthermore, no current is transferred from the electrode to the channel.

$$\vec{n} \cdot \vec{\mathrm{i}}|_{x=0} = 0 \quad (28)$$

Where $\vec{n}$ is the normal vector to the boundary.

For the part of the cathode in contact with the interconnect (labelled “b” on figure 2b), the potential, Φ, is specified and the mass flux across the boundary is zero.:

$$\Phi|_{x=0} = 0 \tag{29}$$

$$\vec{n} \cdot \vec{N_i}|_{x=0} = 0 \tag{30}$$

The boundary conditions at the anode, x=d_c, in contact with the anode channel (labelled “j” on figure 2b) are:

$$X_i|_{x=\mathrm{d_c}} = X_{(i,channel)} \tag{31}$$

$$p|_{x=\mathrm{d_c}} = p_{(t,channel)} \tag{32}$$

$$\vec{n} \cdot \vec{\mathrm{i}}|_{x=0} = 0 \tag{33}$$

For the anode in contact with the interconnect (labelled “i” on figure 2b), the current density is specified and a zero mass flux.

$$\vec{N_i} = 0 \tag{34}$$

$$\vec{\imath} = \vec{\imath}_\mathrm{t} \cdot \frac{w_{pitch}}{w_{rib}} \tag{35}$$

where $\vec{\imath}_\mathrm{t}$ is the applied current density with respect to the entire cell cross-section.

For the other boundaries in the 2d model a symmetry/insulation condition is applied:

$$\vec{n} \cdot \vec{N_i}|_{x=0} = 0 \tag{36}$$

$$\vec{n} \cdot \vec{\mathrm{i}}|_{x=0} = 0 \tag{37}$$

The equations were solved in COMSOL Multiphysics (finite element method) using a damped Newton solver. The 1d model was divided into 200 elements. For the 2d model the cathode and electrode-electrolyte interface was meshed with a triangular mesh using COMSOL’s in-build “finer” mesh setting for fluid dynamics. In the electrode-electrolyte interface the mesh was refined in the x-direction by a factor of 10 and in the y-direction by a factor of 5. The electrolyte and anode were meshed with a triangular mesh using COMSOL’s in-build “extra fine” mesh setting for general physics. The actual number of elements varied with w_{pitch} and $\mathrm{d_c}$. Further refinement of the mesh (changing the in-build settings to “very fine” and “extremely fine“, respectively, showed no difference in the obtained results.

3 Results and Discussion

The result and discussion section is divided into four main parts. First the results from the 1d model are presented. Subsequently the results from the 2d model are presented and compared to the 1d model. Afterwards, the 1d model is used to investigate if diffusion limitations can explain observed carbon formation in some recent studies and, lastly, it is shown that the calculated CO mole fraction from the 2d model can be approximated by a simple linear correlation between the mole fraction in the channel and the current density. Thus makes it possible to include diffusion in current SOEC models without significant increase in calculation time.

3.1 1d model

3.1.1 Electrolysis of CO_2

Figure 3a shows the mole fraction of CO and CO_2 through the cathode layer and Figure 3b shows the corresponding equilibrium temperature for carbon formation, T_B, for a channel gas composition of 60 % CO and 40 % CO_2 and current densities of 0.4 A cm^{-2} and 0.5 A cm^{-2}, respectively. Since there is neither H_2 nor H_2O in the system, the water-gas shift reaction can be ignored. From Figure 3b it can be seen that the change in mole fraction through the cathode layer caused by the diffusion limitations, causes the equilibrium temperature to rise above the cell temperature (in this case 973 K, marked with a horizontal line in Figure 3b) and the Boudouard reaction will therefore be thermodynamically favored close to the electrode-electrolyte interface. In order to avoid the carbon formation, the temperature should either be increased by at least 10 or 20 K, for 0.4 A cm^{-2} and 0.5 A cm^{-2}, respectively or the current density must be decreased below 0.4 A cm^{-2}. With the given parameters (T, $\vec{i}_t$, ϵ, τ, d_e, d_p, X_{CO2}), gas diffusion limitations becomes an important phenomenon in relation to carbon formation even at moderate current densities.

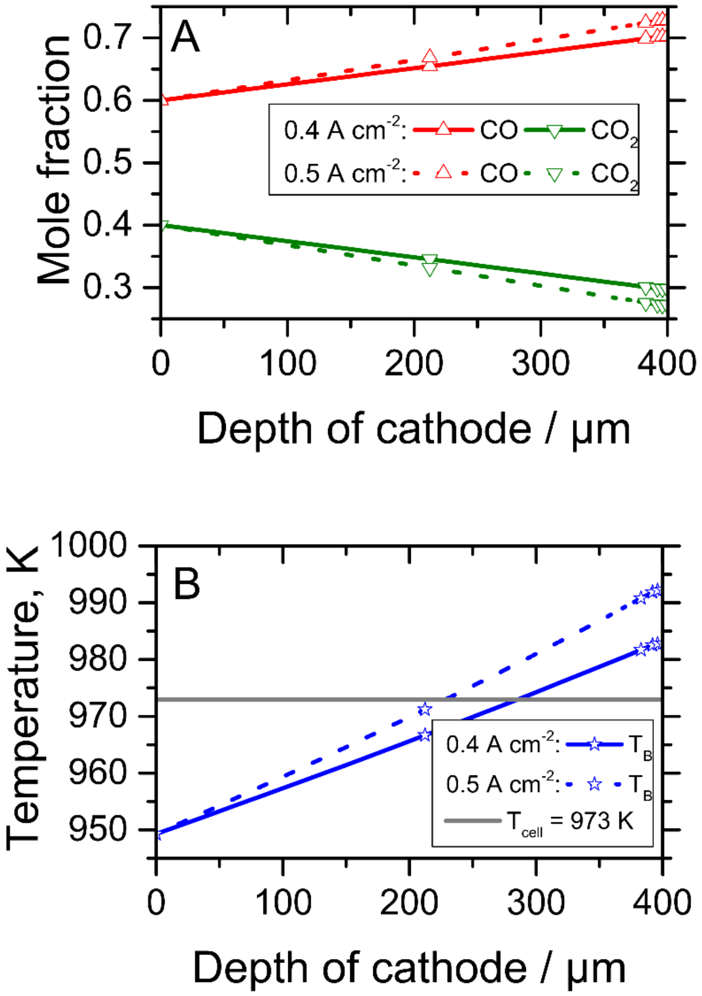

Figure 3. Mole fraction (a) and equilibrium temperature, T_B (b) profiles during CO_2 electrolysis for *T*=973 K, $\vec{i}_t$=0.4 and 0.5 A cm^{-2}, ϵ = 0.3, τ = 3, d_e = 400 μm and a CO mole fraction of 60 %. The depth of the electrode is from the gas channel, i.e. x=0 is at the gas channel and x=400 μm is at the electrode-electrolyte interface. The cell

temperature, 973 K, is marked with a gray horizontal line to clearly illustrate where the Boudouard equilibrium temperature crosses the cell temperature.

3.1.2 Electrolysis of CO_2 and H_2O (co-electrolysis)

Figure 4a shows the mole fraction of H_2 and CO (H_2O and CO_2 are omitted for clarity) through the electrode layer for $\vec{i}$= 0.5 and 1.0 A cm^{-2} and an overall conversion of 60 %. It is assumed that the SOEC is fed with a 40:60 mixture of H_2O and CO_2 and that the gas in the fuel channel has reached the water-gas shift equilibrium. Thus, the gas composition in the gas channel is 33% CO, 27% CO_2, 26% H_2 and 14% H_2O. The Boudouard equilibrium temperature, T_B is also shown in Figure 4b. Since the equilibrium temperature is below T_{cell} at 0.5 A cm^{-2}, but slightly above at 1.0 A cm^{-2}, carbon formation is thermodynamically unfavorable at the low current density, but favorable at the high current density. The difference in diffusion coefficients of H_2 and CO can clearly be seen in the different slopes of the CO and H_2 gradients through the electrode.

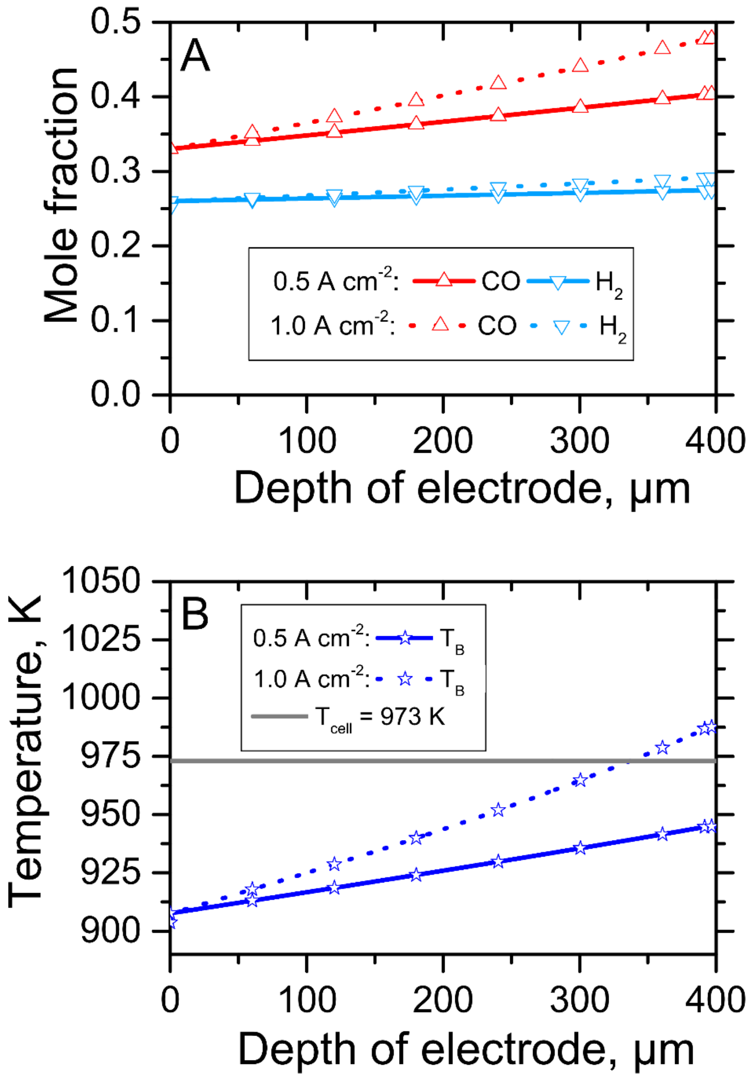

Figure 4. Mole fraction (a) and equilibrium temperature, T_B (b) profiles during co-electrolysis at *T*=973 K, $\vec{i}_t$=0.5 and 1.0 A cm^{-2}, ε = 0.3, τ = 3, de = 400 μm and an gas

channel composition of 33% CO, 27% CO_2 26% H_2 and 14% H_2O. The temperature of the cell (T_{cell} = 973 K) is marked with a gray horizontal line.

3.2 Sensitivity analysis

The parameters in the model can be divided into operating parameters (temperature, conversion and current density) and property parameters (porosity, tortuosity, electrode depth, and pore diameter). By changing only one parameter, while holding all others constant, the effect of that parameter can be investigated. In Figure 5 the effect of the parameters on the CO mole fraction at the electrode-electrolyte interface for CO_2 electrolysis is shown. All parameters, except the one being changed, were held constant at the values given in table 2

Table 2. Parameter values used for the parameter study

Parameter	Value	Unit
Current density, $\vec{\imath}_t$	0.75	A cm^{-2}
CO mole fraction, X_{CO}	0.5	-
Temperature, T_{cell}	1000	K
Cathode depth, d_e	400	µm
Porosity, ε	0.3	-
Tortuosity, τ	3	-
Pore diameter, d_p	0.5	µm

The results shows that 1) the effect of changing T is small, 2) changing ε/τ or d_p has a large effect when the parameter has a low value, but a low effect when they are above about 0.2 and 1 µm respectively, i.e. at about the standard values they are assigned (common values for the ε/τ fraction is 0.1 to 0.2 [29,38,51–54] and for the pore diameter it is 0.13 µm to 1.5 µm [47,51,53–55]), 3) the CO mole fraction is proportional to the CO mole fraction in the channel, current density and electrode depth. Thus, in order to minimize the CO mole fraction at the electrode-electrolyte interface, ε/τ and d_p must be above a certain value while d_e should be small. If this is not the case the CO mole fraction in the channel and the current density must be limited.

The high effect of ε/τ or d_p on the mole fraction shows that for an accurate prediction of the diffusion limitations, these parameters must be determined with good accuracy.

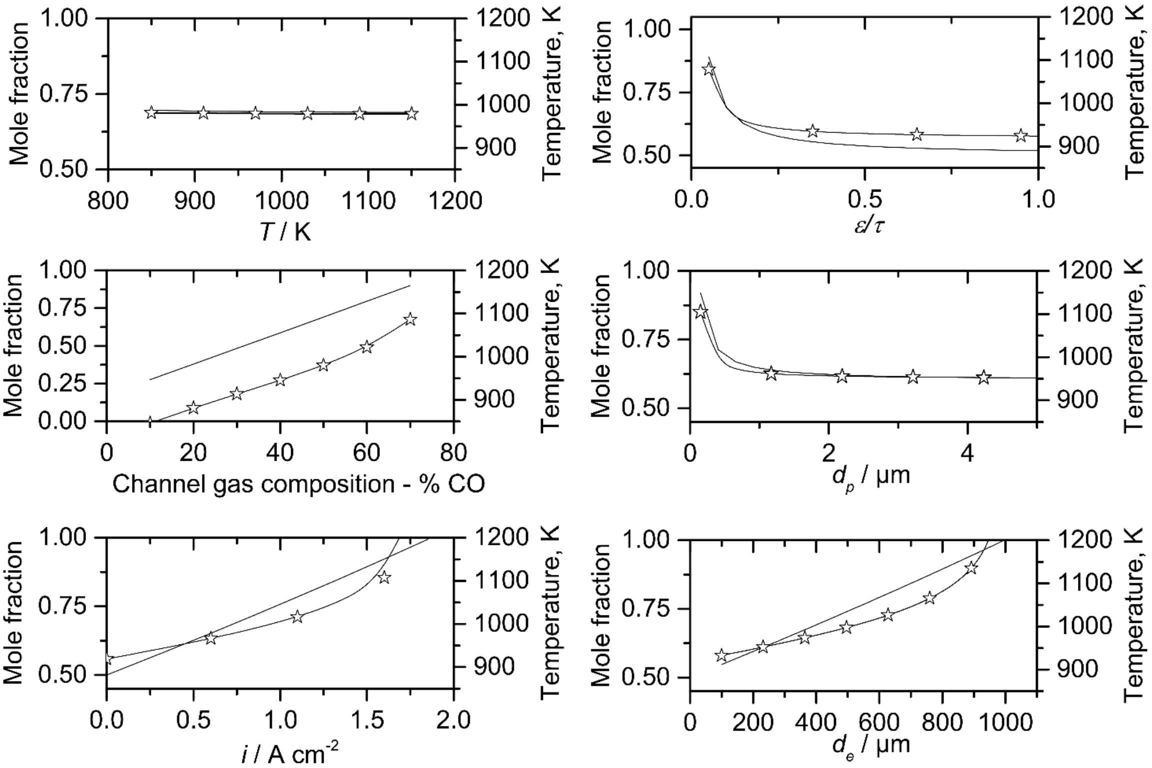

Figure 5. Effect of operating (T, X_{CO}, $\vec{i_t}$) and property (ε/τ, d_e, d_p) parameters on the mole fraction of CO (lines) and the equilibrium temperature for the Boudouard reaction, T_b, (lines with stars) at the electrode-electrolyte interface during CO_2-electrolysis. Standard conditions are listed in table 2.

3.3 2d model

3.3.1 Electrolysis of CO2

Figure 6 shows the mole fraction of CO for a case with w_{pitch} = 1 mm and w_{rib} = 0.5 mm (similar conditions as used in section 3.1.1. for the 1d model). At point “me” the CO mole fraction is 0.75 at the electrode-electrolyte interface, which is close to the 1d model (where it is 0.72, see figure 3). Moving to the right, the CO mole fraction increase, especially under the rib (from z=0.5 mm) and reaches a mole fraction of 0.89 at point “de”. This increase corresponds to an increase in the Boudouard equilibrium temperature from 1000 K to 1071 K. This is a large increase compared to the 995 K calculated with the 1d model and shows the importance of including the effect of the rib on gas transfer. The increase in Boudouard equilibrium temperature means that the temperature of the cell must be increased above 1071 K in order to thermodynamically suppress the formation of carbon.

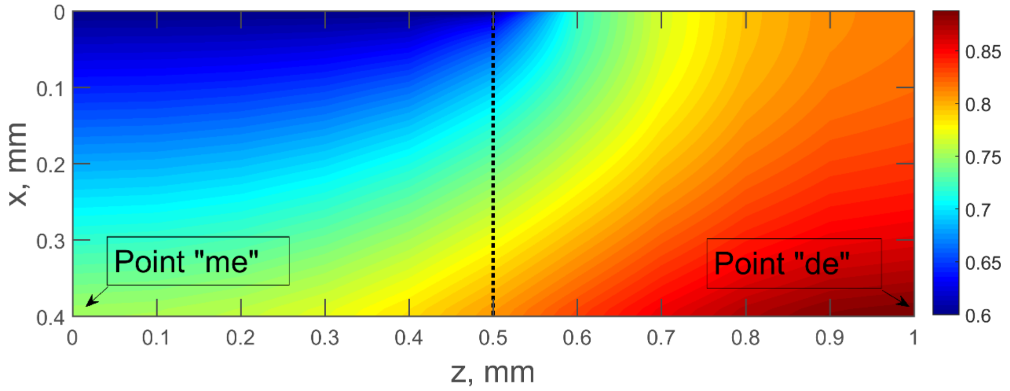

Figure 6. CO mole fraction in the cathode and reaction interface layers. The vertical line at z= w_{rib} **= 0.5 mm separates the domain under the channel (left of the vertical line) and the domain under the rib (right of the line). Conditions:** T**=973 K,** $\vec{\imath}_t$**=0.5 A cm**$^{-2}$**,** ϵ **= 0.3,** τ **= 3,** d_e **= 400 µm** X_{CO} **= 0.6,** w_{pitch} **= 1 mm and** w_{rib} **= 0.5 mm.**

3.3.2 Electrolysis of CO_2 and H_2O (co-electrolysis)

Figure 7 shows the mole fraction and Boudouard equilibrium temperature for a case with w_{pitch} = 1 mm and w_{rib} = 0.5 mm with a gas channel composition of 33% CO, 27% CO_2 26% H_2 and 14% H_2O at 0.5 A cm^{-2} (similar to figure 4). At point “me” the CO mole fraction is 0.425, which is slightly above the 0.40 obtained with the 1d model (see figure 4). At the right side the CO mole fraction increases to 0.52 at point “de”. This corresponds to an increase in the Boudouard equilibrium temperature from 947 K to 988 K. In the 1d model the equilibrium temperature is calculated to be 970 K.

The reason for the lower Boudouard equilibrium temperature for the 2d model at point “me” is that the absolute pressure is lower than in the 1d model (not shown).

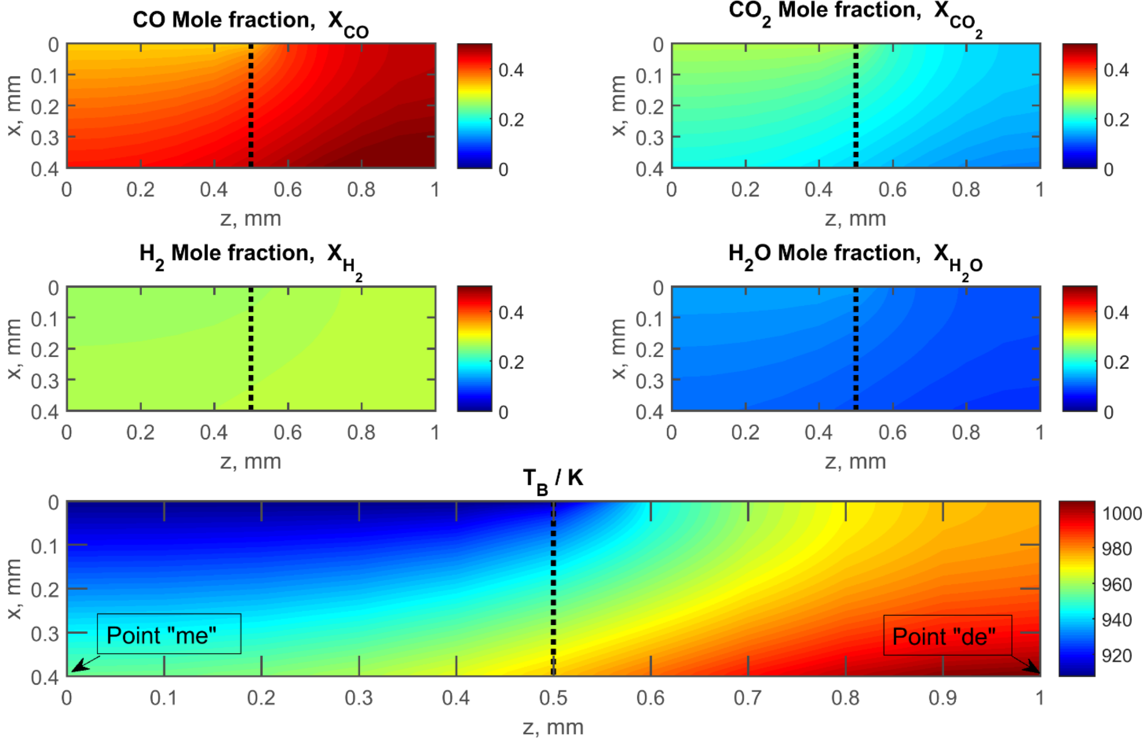

Figure 7. Mole fraction and Boudouard equilibrium temperature in the cathode and reaction interface layers. The vertical line at z= w_{rib} = **0.5 mm separates the domain under the channel (left of the line) and the domain under the rib (right of the line). Conditions:** T**=973 K,** $\vec{i}_t$**=0.5, ε = 0.3,** τ **= 3,** d_e **= 400 µm, gas composition: 33% CO, 27%** CO_2 **26%** H_2 **and 14%** H_2O**,** w_{pitch} **= 1 mm and** w_{rib} **= 0.5 mm.**

3.3.3 Effect of w_{pitch} and w_{rib}.

The effect of w_{pitch} and w_{rib} is illustrated on Figure 8 for electrolysis of CO_2 in terms the difference between the CO concentration under the rib and under the channel. From the figure it can be seen that the difference between the mole fraction beneath the rib (point "de") and the mole fraction beneath the channel (point "me") increase as w_{pitch} and w_{rib} are increased. Especially an increase of the mole fraction difference is observed when w_{rib} is increased.

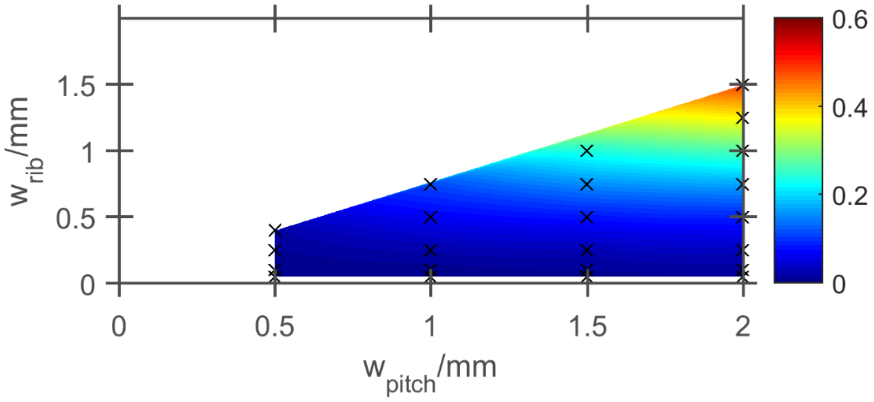

Figure 8: Difference in CO concentration (as mole fraction) between point "de" and "me" at different combinations of w_{pitch} **and** w_{rib}**. The surface is linear interpolated based on the data points marked with black x's.** T **= 1000 K, ε =0.3,** τ **=3,** d_e **= 400 µm,** d_p **= 0.5 µm,** $\vec{i}_t$ **= 0.25 A** cm^{-2}**,** X_{CO} **= 0.25**

3.4 Comparison with Literature

During an experimental study of carbon formation in CO_2-electrolysis, Skafte et al. [2] found that carbon was formed at CO/CO_2 ratios in the gas channel thermodynamically unfavorable for the reaction. In one case, carbon was observed at 1023 K with a current density of 0.39 A cm^{-2} and an outlet mole fraction of 73 % CO (calculated from the article).
The size of the cell was 53 mm by 53 mm with an active area of 40 mm by 40 mm. We have assumed that the current density and flow is uniform across the cell, and thus modelled the diffusion with the 1d model (ignoring the effect of ribs from interconnects). The physical properties of the cell are not given; however, assuming an electrode thickness of 310 µm, a porosity of 30 % and a tortuosity of 3 (based on data on similar cells used by the same authors) the equilibrium temperature for the Boudouard reaction is calculated to be 5 K above the actual temperature. This indicates that diffusion limitations in the electrode can explain why carbon was formed in their study.

In a recent study by Tao et al. [6] carbon formation was observed during co-electrolysis at 67 % conversion, where the formation should be thermodynamically unfavored up to above 99 % conversion. A total of five cells with different current densities and porosities were tested (Table 3). The electrode thickness was ~315 µm, the tortuosity was around 3 (based on the model fitting in the article) and the temperature was 1123 K at open circuit voltage and increased to 1148 K at current densities of 2.0 A cm^{-2}. The size of the cells was 50 mm by 50 mm with an active area of 40 mm by 40 mm.

For cell 4 and 5 carbon formation was observed, while no carbon was observed for cell 1-3. From impedance spectroscopy an increase in both the conversion impedance and diffusion impedance was observed for cell 4 and 5. Furthermore the porosity was lower in cells 4 and 5. An increase in conversion impedance means a higher mole fraction of either $CO+H_2$ or CO_2+H_2O. The increase in diffusion impedance is caused by a change between the bulk gas and the gas composition at the interface. Based on this, the authors suggest that the carbon formation is caused by diffusion limitations. This is also in agreement with figure 5, where it can be seen that a change in porosity can cause a significant increase in the product mole fraction at the interface due to diffusion limitations.

Table 3. Properties of the five cells tested by Tao et al. [1]

Cell	Current density $\vec{i}_t$ / A cm^{-2}	Gas conversion γ / %	Estimated porosity / %	Carbon observed
1	1.5	45	30-40	No
2	2.0	59	30-40	No
3	2.0	59	30-40	No
4	2.0	59	20	Yes
5	2.25	67	25	Yes

The hypothesis that diffusion limitations caused the carbon formation was tested with the 1d diffusion model. Again, we have assumed that the flow and current is distributed uniformly across the cell and have thus used the 1d model (ignoring the effect of ribs from interconnects). This was selected due to the small dimensions of the cell. Furthermore, if the 1d model predicts risk of carbon formation, the 2d model would certainly also predict risk of carbon formation. The gas channel composition was computed by bringing the gas to the water-gas shift equilibrium. Figure 9 shows the equilibrium temperature for the Boudouard reaction as a function of current density and porosity at the electrode-electrolyte interface.

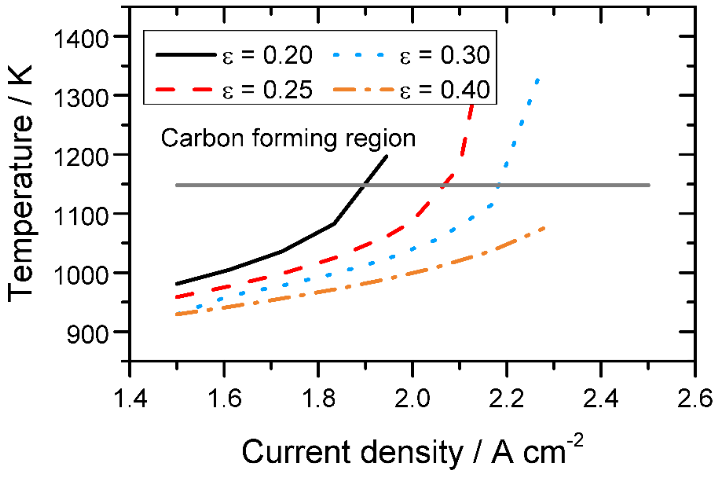

Figure 9. Equilibrium temperature for the Boudouard reaction at the electrode-electrolyte interface as function of the current density at different levels of porosity. The horizontal line is the temperature of the cell (1148 K) in the test in [[1]].

Conditions: T=1148 K, ε = 0.3, d_e = 315 μm. The gas composition was 0.45(1-γ) H_2O, 0.45(1-γ) CO_2, 0.10+0.45(γ) H_2, 0.45(γ) CO, where the conversion γ is a function of $\vec{\imath}_t$ and interpolated from table 3.

Since the porosity for cell 1-3 was 30-40 %, it can be seen from the blue and yellow curve in figure 9 that T_B for these cells lie below the temperature of cell at i = 1.5 to 2.0 A cm^{-2} (the reaction is thermodynamically unfavored). However, for cell 4 with a porosity of 20 %, it can be seen that the corresponding black line in Figure 9 crosses T_{cell} at a current density of 1.9 A cm^{-2} i.e. below 2.0 A cm^{-2} used in the experiment. Similarly, for cell 5, the red line shows that T_B crosses T_{cell} at a current density below 2.5 A cm^{-2}, thus suggesting that carbon formation locally in the cell is thermodynamically favorable. The diffusion limitations thus seem to explain the observed carbon formation in cells 4 and 5.

3.5 Implementation of the rib effect in existing models

Several existing models of SOEC only calculate the gas composition in the gas channel [56,57] or neglect the effect of the ribs on the gas concentration within the electrode [38,42,51,58]. For such models it would be advantageous if the gas composition under the rib could be found directly from the gas composition within the gas channel and operational parameters ($\vec{\imath}$, T), since this will not significantly increase the computational time. When the gas composition has been calculated, the carbon affinity can be calculated and the risk of carbon formation can be assessed.

For large 3d models of entire stacks, the difference in scale of the involved structures (e.g. mm to cm for inlet manifolds and interconnect channels and μm for the electrode) makes the detailed modelling of the diffusion under the interconnect ribs infeasible. Homogenization techniques are already used in some models to reduce the number of degrees of freedom from billions to tens of thousands [59], so including a detailed modelling of the diffusion in the electrode in each cell in the stack would be undesirable. To investigate if the gas composition beneath the rib could be expressed as a simple function of gas composition in the channel and the operational parameters, we used the 2d model to calculate the gas composition with the parameters given in Table 4. The parameters describing the microstructure and the interconnect structure were fixed. Those parameters will not vary significantly across the cell and from cell-to-cell. The temperature influence is omitted due to the small influence observed in Figure 5.

Table 4. Parameter values used for figure 10

Parameter	Value	Unit
Current density, $\vec{\imath}_t$	0.1, 0.25, 0.5, 0.75	A cm^{-2}
CO mole fraction, X_{CO}	0.13, 0.25, 0.46, 0.63	-
Temperature, T_{cell}	1023	K
Pitch width, w_{pitch}	1	mm
Rib width, w_{rib}	0.5	mm
Cathode depth, d_e	400	μm
Porosity, ε	0.3	-
Tortuosity, τ	3	-
Pore diameter	0.5	μm

Figure 10 shows the difference between the CO mole fraction in the gas channel and point "me" (beneath the center of the channel) and point "de" (beneath the center of the rib), respectively. The difference between the CO mole fraction in the channel and the average CO mole fraction at the boundary labelled "e" in figure 2b is also shown. The average mole fraction is calculated using elementwise integration with numeric quadrature of 4th order (standard in COMSOL).

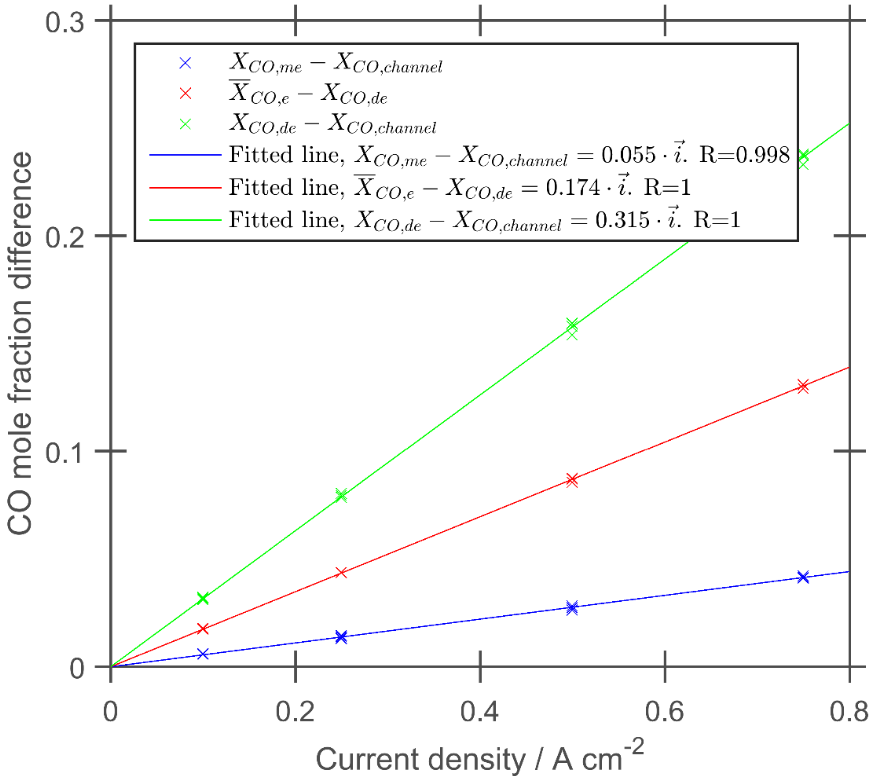

Figure 10 CO mole fractions difference between the channel and the point beneath the middle of the channel (point "me"), the point beneath the middle of the rib (point "de"), and the average mole fraction on boundary "e". Conditions are given in table 4.

The figure shows that the CO mole fraction at the points and at the boundary "e" can be calculated directly from the current density and the CO mole fraction in the channel:

$$X_{CO}|_{point\ me} - X_{CO}|_{channel} = 0.055 \cdot \vec{\imath}_t \tag{38}$$
$$\overline{X_{CO}}|_{boundary\ e} - X_{CO}|_{channel} = 0.174 \cdot \vec{\imath}_t \tag{39}$$
$$X_{CO}|_{point\ de} - X_{CO}|_{channel} = 0.315 \cdot \vec{\imath}_t \tag{40}$$

The function will change when the parameters relating to the cell (ε, τ, d_e, d_p, w_{pitch}, w_{rib}) are changed, or if the temperature is changed significantly. However, it is relatively simple to calculate a new correlation based on a 2d simulation with new parameters.

The credibility of the perfect linear fits can be investigated by examine the dusty gas model. For a binary gas mixture (CO-CO_2 as present in Figure 10) equation (8) reduces to:

$$\frac{X_{CO}\vec{N}_{CO_2}-X_{CO_2}\vec{N}_{CO}}{D^{eff}_{CO-CO_2}}-\frac{\vec{N}_{CO}}{D^{eff}_{CO,k}}=\frac{\mathrm{p}}{RT}\nabla X_{CO}+\frac{X_{CO}}{RT}\left(1+\frac{Bp}{\mu_m D^{eff}_{CO,k}}\right)\nabla p \qquad (41)$$

Using Graham's law, $\vec{N}_{CO_2}/\vec{N}_{CO}=\sqrt(M_{CO}/M_{CO_2})$ and the relationship between the mole fractions, $X_{CO_2}=1-X_{CO}$, equation (41) reduces further to:

$$-\vec{N}_{CO}\left(\frac{1-bX_{CO}}{D^{eff}_{CO-CO_2}}+\frac{1}{D^{eff}_{CO,k}}\right)=\frac{\mathrm{p}}{RT}\nabla X_{CO}+\frac{X_{CO}}{RT}\left(1+\frac{Bp}{\mu_m D^{eff}_{CO,k}}\right)\nabla p \qquad (42)$$

where $b=1-\sqrt(M_{CO}/M_{CO_2})$

Assuming that diffusion only take place in the x direction, approximating ∇X_{CO} by $\Delta \mathrm{X_{CO}}/\Delta x$ and rearranging leads to:

$$\Delta X_{CO}=\left(-\vec{N}_{CO}\left(\frac{1-bX_{CO}}{D^{eff}_{CO-CO_2}}+\frac{1}{D^{eff}_{CO,k}}\right)-\frac{X_{CO}}{RT}\left(1+\frac{Bp}{\mu_m D^{eff}_{CO,k}}\right)\nabla p\right)\cdot\frac{\mathrm{RT}}{\mathrm{p}}\Delta \mathrm{x} \qquad (43)$$

The pressure difference can be calculation with [9]:

$$\nabla p=\frac{-RT\sum_i^n\frac{N_i}{D^{eff}_{i,k}}}{1+\sum_i^n\frac{X_iBp}{\mu_m D^{eff}_{i,k}}}=\frac{-RT\vec{N}_{CO}\left(\frac{1}{D^{eff}_{CO,k}}+\frac{\sqrt{M_{CO}\,/\,M_{CO_2}}}{D^{eff}_{CO_2,k}}\right)}{1+\frac{X_{CO}Bp}{\mu_m D^{eff}_{CO,k}}+\frac{(1-X_{CO})Bp}{\mu_m D^{eff}_{CO_2,k}}} \qquad (44)$$

Equation (43) can thus be rewritten to

$$\Delta X_{CO}=\left(-\vec{N}_{CO}C_1-\vec{N}_{CO}X_{CO}\mathrm{C}_2\right)\cdot\Delta \mathrm{x} \qquad (45)$$

where:

$$\mathrm{C}_1=\left(\frac{1-bX_{CO}}{D^{eff}_{CO-CO_2}}+\frac{1}{D^{eff}_{CO,k}}\right)\cdot\frac{\mathrm{RT}}{\mathrm{p}} \qquad (46)$$

$$\mathrm{C}_2=\left(1+\frac{Bp}{\mu_m D^{eff}_{CO,k}}\right)\frac{-\left(\frac{1}{D^{eff}_{CO,k}}+\frac{\sqrt{M_{CO}\,/\,M_{CO_2}}}{D^{eff}_{CO_2,k}}\right)}{1+\frac{X_{CO}Bp}{\mu_m D^{eff}_{CO,k}}+\frac{(1-X_{CO})Bp}{\mu_m D^{eff}_{CO_2,k}}}\cdot\frac{\mathrm{RT}}{\mathrm{p}} \qquad (47)$$

Since b is low $(1-\sqrt(M_{CO}/M_{CO_2})=0.2)$ and $D^{eff}_{CO-CO_2}$ and $D^{eff}_{CO,k}$ are the same order of magnitude at the operation conditions, C_1 will not vary much when X_{CO} is varied. Also, since $D^{eff}_{CO,k}$ and $D^{eff}_{CO_2,k}$ are at the same order of magnitude, the denominator of C_2, and consequently C_2, will not vary much with changes in X_{CO}. Indeed, calculating and comparing the two constant at $X_{CO}=0$ and $X_{CO}=1$ showed only a difference of 6 % compared to values calculated at $X_{CO}=0.5$.
From Figure 3 it can be seen that the mole fraction decrease linear from the channel to the reaction zone. Thus, it is reasonable to fix X_{CO} as:

$$X_{CO}=\frac{X_{CO}|_c+(X_{CO}|_c+\Delta X_{CO})}{2}=\frac{X_{CO}|_c}{2}+\frac{X_{CO}|_c}{2}+\frac{\Delta X_{CO}}{2} \qquad (47)$$

Inserting into equation 45 and rearranging yields:

$$\Delta X_{CO} + \frac{\Delta X_{CO}}{2} \vec{N}_{CO} C_2 \Delta x = \left(-\vec{N}_{CO} C_1 - \vec{N}_{CO} X_{CO}|_c \mathrm{C}_2\right) \cdot \Delta \mathrm{x} \tag{48}$$

$$\Delta X_{CO} = \frac{\left(-\vec{N}_{CO} C_1 - \vec{N}_{CO} X_{CO}|_c \mathrm{C}_2\right) \cdot \Delta \mathrm{x}}{1 + 0.5 \vec{N}_{CO} C_2 \Delta x} \tag{49}$$

Since the diffusion flux, $\vec{N}_{CO}$, and distance, Δx, are rather small in this study, the term $0.5\vec{N}_{CO}C_2\Delta \mathrm{x}$ in the denominator of equation (49) will be of the order of magnitude 10^{-2}. This means that the mole fraction difference can be expresses as in equation (50) and since $\vec{N}_{CO}$ is directly proportional to the current distribution, the linear relationship observed in Figure 10 is reasonable.

$$\Delta X_{CO} \approx -\vec{N}_{CO}\left(C_1 + X_{CO}|_c \mathrm{C}_2\right) \cdot \Delta \mathrm{x} \tag{50}$$

4. Conclusion

In this work, two models for diffusion from the gas channel through the electrode layer towards the reaction interface of a solid oxide electrolysis cell have been set up and solved using COMSOL Multiphysics. The simulations showed that carbon formation may be an operational risk due to diffusion limitations that influence the reactant mole fractions in the electrode material. The risk may be severe for CO_2-electrolysis, but is also significant for co-electrolysis.

When the ε/τ ratio is less than 0.3 or the pore diameter, d_p, is less than 1 µm, the concentration gradient of CO from the channel to the interface becomes large and care must be taken in selecting an appropriately conservative (low) current density and gas conversion or a high operating temperature to avoid carbon formation. When including the effect of the rib from the interconnect, it is clear that the rib causes an increase in the CO mole fraction even at low widths. The effect of the rib on the CO concentration at the electrode-electrolyte interface can be approximated by a simple linear function of the current density and channel gas composition for CO_2-electrolysis. This function needs to be updated if the parameters relating to the cell (ε, τ, d_e, d_p, w_{pitch}, w_{rib}) are changed. However, once that is done, it allows for an easy and low computational cost inclusion to existing cell and stack models. The perfect observed linear fit was justified by examine the dusty gas model.

Simulation of two cases from the literature, where carbon formation was observed, showed that the observed carbon formation can be explained by diffusion limitations.

The results show clearly that diffusion limitations on transport of reactants and products in electrolyzer cells may lead to significant concentration gradients inside the electrode material. This in turn may create conditions favorable for the formation of carbon even under operating conditions where carbon formation would not otherwise be expected to occur based solely on the channel gas composition. Our work shows that models accounting for both reaction and diffusion inside SOEC electrodes are needed - both at the design stage and during operation - as means to avert potentially devastating carbon formation.

Acknowledgements

This project is a collaboration between the CHEC Research center at DTU Chemical Engineering and Haldor Topsoe A/S and is partially funded by the Danish Industrial Ph.D. Fellowship Programme administered by Innovation Fund Denmark.

List of Symbols

a_c	Carbon affinity
c	Fitting parameter
c_p	Heat capacity / J mol^{-1} K^{-1}
C_1	Diffusion term used in equation (45)
C_2	Pressure difference term used in equation (45)
d	Fitting parameter
d_{anode}	Depth of anode / µm
d_c	Cell depth / µm
d_e	Depth of cathode / µm
$d_{\mathrm{electrolyte}}$	Depth of electrolyte / µm
d_p	Pore diameter / µm
$D_{\mathrm{i,k}}^{\mathrm{eff}}$	Effective Knudsen diffusion coefficient of species i / m^2 s^{-1}
$D_{\mathrm{i,j}}^{\mathrm{eff}}$	Effective binary diffusion coefficient of species i and j / m^2 s^{-1}
E_{act}	Activation energy / kJ mol^{-1}
F	Faradays constant / 96485 C mol^{-1}
ΔH	Reaction enthalpy / J mol^{-1}
$\vec{\imath}$	Current density flux / A cm^2
$\vec{\imath_t}$	Applied current density at the boundary / A cm^2
K_1	Equilibrium constant / atm^{-1}
k	Thermal conductivity / W m^{-1} K^{-1}
M	Molar mass / g m^{-3}
m	Fitting parameter
$\vec{N_\iota}$	Molar flux of species i/ mol m^{-2} s^{-1}
n_e	Number of electrons
p	Pressure / atm
R	Universal gas constant / 8.31445 J mol^{-1} K^{-1}
r	Reaction rate / mol m^{-3} s^{-1}
T	Temperature / K
T_B	Equilibrium temperature for the Boudouard reaction / K
U_{cell}	Cell voltage / V
Q_{eq}	Reaction quotient / atm^{-1}
Q	Heat source / W m^{-3}
q_0	Heat convection / W m^{-2}
X_i	Mole fraction of species i
w_{pitch}	Halfwidth of the pitch / mm
w_{rib}	Halfwidth of the rib / mm
α	Charge transfer coefficient
β	Ratio of gas species at reaction interface
ε	Porosity
η	Ovenpotential / V

σ	Average collision diameter / m
σ_{el}	Electrical conductivity / $S\ \mathrm{cm}^{-1}$
σ_{io}	Ionic conductivity / $S\ \mathrm{cm}^{-1}$
γ	Pre-factor / A m^{-2}
ρ	Density / g cm^{-3}
τ	Tortuosity
μ	Viscosity / Pa s
Ω	Dimensionless collision integral
Φ	Potential / V

4 Appendix

4.1 Evaluation of validity of isothermal assumption

In order to validate the assumption of isothermal conditions, the modelling domain of the 1d model was extended to include the electrolyte and anode, and the governing energy equation was added.

The steady state governing equation for the energy is given by:

$$0 = -k_{eff}\nabla^2 \cdot T + Q \tag{51}$$

Where k_{eff} is the effective conduction, Q is the heat source. k_{eff} is calculated from the conduction of the fluid and solid in the porous media:

$$k_{eff} = \epsilon k_{fluid} + (1-\epsilon)k_{solid} \tag{52}$$

For the electrolyte, the effective conduction coefficient reduces to $k_{eff} = k_{solid}$.

The heat source Q, is calculated from the reaction heat from the electrochemical reactions (16 and 17), the water-gas shift reaction and the Joule heating:

$$Q = Q_{H_2O} + Q_{CO_2} + Q_{WGS} + Q_J \tag{53}$$

$$Q = \left(\frac{\beta}{2F}\Delta H_{H_2O} + \frac{(1-\beta)}{2F}\Delta H_{CO_2} + U_{cell}\right) \cdot \frac{\vec{\imath}}{d_i} + \Delta H_{WGS} R_{wgs} \tag{54}$$

Where ΔH_i is the reaction enthalpy for the reaction (calculated from [60]) and U_{cell} is the cell voltage calculated as:

$$U_{cell} = E + \eta_{act}^{anode} + \eta_{act}^{cathode} + \eta_{ohmic} \tag{55}$$

Where E is the equilibrium potential (including concentration overpotential) and is expressed from the Nernst's equation [51]:

$$E = E_{CO_2} = 1.46713 - 0.0004527 \cdot T + \frac{RT}{2F}\ln\left(\frac{p_{CO}(p_{O_2})^{0.5}}{p_{CO_2}}\right) \tag{56}$$

$\eta_{act}^{anode}$and $\eta_{act}^{cathode}$ are the activation potentials calculated with the Butler-Volmer equation and using a power law to calculate the exchange current densities [61]:

$$i = i_{0,anode}\left(\exp\left(\frac{\alpha_{anode}\, n_e F \eta_{act}^{anode}}{RT}\right) - \exp\left(\frac{-(1-\alpha_{anode}) n_e F \eta_{act}^{anode}}{RT}\right)\right) \tag{57}$$

$$i = i_{0,cathode} \left(\exp\left(\frac{\alpha_{cathode}\, n_e F \eta_{act}^{cathode}}{RT} \right) - \exp\left(\frac{-(1-\alpha_{cathode}) n_e F \eta_{act}^{cathode}}{RT} \right) \right) \tag{58}$$

$$i_{0,anode} = \gamma_{anode} \left(p_{O_2,anode} \right)^m \exp\left(\frac{-E_{act,anode}}{RT} \right) \tag{59}$$

$$i_{0,anode} = \gamma_{cathode} \left(p_{CO_{cathode}} \right)^c \left(p_{CO_2,cathode} \right)^d \exp\left(\frac{-E_{act,cathode}}{RT} \right) \tag{60}$$

η_{ohmic} is the ohmic loss due to resistance:

$$\eta_{ohmic} = R_{ohm} i \tag{61}$$

$$R_{ohm} = \frac{d_{anode}}{\sigma_{anode}} + \frac{d_{electrolyte}}{\sigma_{electrolyte}} + \frac{d_{cathode}}{\sigma_{cathode}} \tag{62}$$

Where d is the thickness of the layers and σ is the electrical conductivity. The electrical conductivity is given in section 2.3.

All the heat sources, except the reaction enthalpy for the water-gas shit reaction, are placed in the electrolyte [62].

As a boundary condition, the heat convection to the channels are calculated using a Nusselt number of 3.68 [62] and assuming a rectangular channel with a width of 2 mm and a height of 1 mm:

$$\frac{\partial k_{\text{eff}} T|_{x=0}}{\partial x} = \frac{Nu \cdot k_{fluid}}{D_H} \cdot \left(T - T_g \right) \tag{63}$$

$$\frac{\partial k_{\text{eff}} T|_{x=\text{d}_{\text{cell}}}}{\partial x} = \frac{Nu \cdot k_{fluid}}{D_H} \cdot \left(T - T_g \right) \tag{64}$$

At both gas channels the gas temperature, T_g, is 1023 K. In the cathode channel the properties of CO_2 is used and in the anode channel the properties air is used. Heat transfer via radiation is neglected.

Table 5 list the parameters used and table 6 shows the maximum temperature deviation between the solid part of the cell and the channel. From table 6 it can be seen that the temperature difference is within ±2 K. Since figure 5 showed that small temperature differences does not influence the diffusion, the isothermal assumption is fair to make.

Table 5. Parameter values

Parameter	Value	Unit	Source
Temperature, T	1023	K	
Pitch width, w_{pitch}	1	mm	
Rib width, w_{rib}	0.5	mm	
Cathode depth, d_e	400	µm	
Porosity, ε	0.3	-	
Tortuorosity, τ	3	-	
Pore diameter	0.5	µm	
Thickness anode, d_{anode}	15	µm	
Thickness electrolyte, $d_{electrolyte}$	15	µm	
Thermal conductivity, cathode	7.5	$W\ m^{-1}\ K^{-1}$	[63]
Thermal conductivity, electrolyte	2.3	$W\ m^{-1}\ K^{-1}$	[64]
Thermal conductivity, anode	0.8	$W\ m^{-1}\ K^{-1}$	[63]
Thermal conductivity, CO_2	0.066	$W\ m^{-1}\ K^{-1}$	[65]
Thermal conductivity, air*	0.070	$W\ m^{-1}\ K^{-1}$	[65]
Density, cathode	5.5	$g\ cm^{-3}$	[63]
Density, electrolyte	5.8	$g\ cm^{-3}$	[64]

Density, cathode	6.5	g cm^{-3}	[66]
Pre-factor anode, γ_{anode}	$1.52 \cdot 10^8 T$	A m^{-2}	[61]
Pre-factor cathode, $\gamma_{cathode}$	$4.56 \cdot 10^6 T$	A m^{-2}	[61]
Activation energy anode, $E_{act,anode}$	139.86	kJ mol^{-1}	[61]
Activation energy cathode, $E_{act,cathode}$	118.64	kJ mol^{-1}	[61]
Charge transfer coefficient anode, α_{anode}	0.65	-	[61]
Charge transfer coefficient cathode, $\alpha_{cathode}$	0.62	-	[61]
Fitting parameter, *c*	-0.058	-	[61]
Fitting parameter, *d*	0.25	-	[61]
Fitting parameter, *m*	0.22	-	[61]

*Calculated as 79 % N_2 and 21 % O_2

Table 6. Temperature difference at various current densities.

Current density, A cm^{-2}	Maximum temperature difference, K	
	CO_2-electrolysis. Channel composition: 50 % CO, 50 % CO_2	CO-electrolysis. Channel composition: 33% CO, 27% CO_2 26% H_2 and 14% H_2O
0.25	-1.7	-1.5
0.5	-1.8	-1.5
0.75	-0.8	-0.2
1	+1.2	+2.0

References

[1] Y. Tao, S. D. Ebbesen, M. B. Mogensen, *J. Electrochem. Soc.* **2014**, *161*, 3.

[2] T. L. Skafte, C. Graves, P. Blennow, J. Hjelm, *ECS Trans.* **2015**, *68*, 1.

[3] J.-W. Snoeck, G. F. Froment, M. Fowles, *Ind. Eng. Chem. Res.* **2002**, *41*, 17.

[4] H. He, J. M. Hill, *Appl. Catal. A Gen.* **2007**, *317*, 2.

[5] Y. Kim, J. H. Kim, J. Bae, C. W. Yoon, S. W. Nam, *J. Phys. Chem. C* **2012**, *116*, 24.

[6] Y. Tao, S. D. Ebbesen, M. B. Mogensen, *J. Electrochem. Soc.* **2014**, *161*, 3.

[7] J. Yuan, B. Sundén, *Int. J. Heat Mass Transf.* **2014**, *69*.

[8] Y. Vural, L. Ma, D. B. Ingham, M. Pourkashanian, *J. Power Sources* **2010**, *195*, 15.

[9] A. Bertei, C. Nicolella, *J. Power Sources* **2015**, *279*.

[10] R. Suwanwarangkul, E. Croiset, M. W. Fowler, P. L. Douglas, E. Entchev, M. A. Douglas, *J. Power Sources* **2003**, *122*, 1.

[11] S. Wang, W. M. Worek, W. J. Minkowycz, *Int. J. Heat Mass Transf.* **2012**, *55*, 15–16.

[12] S. Helveg, J. Sehested, J. R. Rostrup-Nielsen, *Catal. Today* **2011**, *178*, 1.

[13] J. R. Rostrup-Nielsen, *J. Catal.* **1972**, *27*, 3.

[14] P. K. D. Bokx, A. J. H. M. Kock, E. Bolellard, W. Klop, J. W. Geus, *J. Catal.* **1985**, *96*, 2.

[15] A. J. H. M. Kock, P. K. D. Bokx, E. Bolellard, W. Klop, J. W. Geus;, *J. Catal.* **1985**, *96*, 2.

[16] C. H. Bartholomew, *Catal. Rev.* **2007**, *24*, 1.

[17] M. C. Annesini, V. Piemonte, L. Turchetti, *Chem. Eng. Trans.* **2007**, *11*.

[18] H. Bengaard, *J. Catal.* **2002**, *209*, 2.

[19] J. P. Coad, J. C. Rivière, *Surf. Sci.* **1971**, *25*, 3.

[20] P. B. Tøttrup, *J. Catal.* **1976**, *42*.

[21] J. R. Rostrup-Nielsen, J. Sehested, in *Stud. Surf. Sci. Catal.* (Eds.: J.J. Spivey, G.W.

Roberts, B.H. Davi), Elsevier, **2001**, pp. 1–12.
[22] W. Li, Y. Shi, Y. Luo, Y. Wang, N. Cai, *J. Power Sources* **2015**, *276*.
[23] C. M. Finnerty, N. J. Coe, R. H. Cunningham, R. M. Ormerod, *Catal. Today* **1998**, *46*, 2–3.
[24] M. Ito, T. Tagawa, S. Goto, *Appl. Catal. A Gen.* **1999**, *177*, 1.
[25] V. Subotić, C. Schluckner, J. Mathe, J. Rechberger, H. Schroettner, C. Hochenauer, *J. Power Sources* **2015**, *295*.
[26] S. D. Ebbesen, M. Mogensen, *J. Power Sources* **2009**, *193*, 1.
[27] J. Aicart, F. Usseglio-Viretta, J. Laurencin, M. Petitjean, G. Delette, L. Dessemond, *Int. J. Hydrogen Energy* **2016**, *41*, 39.
[28] C. Graves, S. D. Ebbesen, M. Mogensen, *Solid State Ionics* **2011**, *192*, 1.
[29] Y. Shi, Y. Luo, N. Cai, J. Qian, S. Wang, W. Li, H. Wang, *Electrochim. Acta* **2013**, *88*.
[30] I. Alstrup, B. S. Clausen, C. Olsen, R. H. H. Smits, J. R. Rostrup-Nielsen, in *Stud. Surf. Sci. Catal.* (Ed.: A. Parmaliana et al), Elsevier Science, **1998**, pp. 5–14.
[31] P. Fan, X. Zhang, D. Hua, G. Li, *Fuel Cells* **2016**.
[32] K. Sasaki, Y. Teraoka, *J. Electrochem. Soc.* **2003**, *150*, 7.
[33] J.-W. Snoeck, G. F. Froment, M. Fowles, *Ind. Eng. Chem. Res.* **2002**, *41*, 17.
[34] S. Primdahl, M. Mogensen, *J. Electrochem. Soc.* **1997**, *144*, 10.
[35] S. B. Adler, *Solid State Ionics* **1998**, *111*, 1–2.
[36] J.-W. Kim, *J. Electrochem. Soc.* **1999**, *146*, 1.
[37] J. D. Duhn, A. D. Jensen, S. Wedel, C. Wix, *J. Power Sources* **2016**, *336*.
[38] M. Ni, *Int. J. Hydrogen Energy* **2012**, *37*, 8.
[39] V. Novaresio, M. García-Camprubí, S. Izquierdo, P. Asinari, N. Fueyo, *Comput. Phys. Commun.* **2012**, *183*, 1.
[40] E. Hern, D. Singh, P. N. Hutton, N. Patel, M. D. Mann, *J. Power Sources* **2004**, *138*.
[41] E. Resch, Numerical and Experimental Characterisation of Convective Transport in Solid Oxide Fuel Cells, Queen's University, Kingston, Ontario, Canada, **2008**.
[42] J. Laurencin, D. Kane, G. Delette, J. Deseure, F. Lefebvre-Joud, *J. Power Sources* **2011**, *196*, 4.
[43] S. . Aruna, M. Muthuraman, K. . Patil, *Solid State Ionics* **1998**, *111*, 1–2.
[44] D. Simwonis, F. Tietz, D. Stover, *Solid State Ionics* **2000**, *132*.
[45] A. Weber, E. Ivers-Tiffée, *J. Power Sources* **2004**, *127*, 1–2.
[46] C. Stoots, J. O'Brien, J. Hartvigsen, *Int. J. Hydrogen Energy* **2009**, *34*, 9.
[47] J. Aicart, M. Petitjean, J. Laurencin, L. Tallobre, L. Dessemond, *Int. J. Hydrogen Energy* **2015**, *40*, 8.
[48] V. Menon, V. M. Janardhanan, O. Deutschmann, *ECS Trans.* **2013**, *57*, 1.
[49] J. Aicart, J. Laurencin, M. Petitjean, L. Dessemond, *Fuel Cells* **2014**, *14*, 3.
[50] J. R. Rostrup-Nielsen, L. J. Christiansen, *Concepts In Syngas Manufacture*, Imperial College Press, London, **2011**.
[51] M. Ni, *J. Power Sources* **2012**, *202*.
[52] R. E. Williford, L. a. Chick, G. D. Maupin, S. P. Simner, J. W. Stevenson, *J. Electrochem. Soc.* **2003**, *150*, 8.
[53] G. Brus, K. Miyawaki, H. Iwai, M. Saito, H. Yoshida, *Solid State Ionics* **2014**, *265*.
[54] Y. Shi, C. Li, N. Cai, *J. Power Sources* **2011**, *196*, 13.
[55] W. Li, H. Wang, Y. Shi, N. Cai, *Int. J. Hydrogen Energy* **2013**, *38*.
[56] G. Hawkes, J. O'Brien, C. Stoots, B. Hawkes, *Int. J. Hydrogen Energy* **2009**, *34*, 9.
[57] G. Hawkes, J. O'Brien, C. Stoots, S. Herring, M. Shahnam, *Heat Transf. Vol. 4* **2005**.
[58] W. Li, Y. Shi, Y. Luo, N. Cai, *J. Power Sources* **2013**, *243*.
[59] Y. Elesin, M. F. Madsen, T. K. Petersen, *Proc. 11th Eur. SOFC SOEC Forum 2014* **2014**, July.

[60] M. W. Chase Jr, in *J. Phys. Chem. Ref. Data, Monogr. 9*, **1998**, pp. 1–1951.
[61] A. Leonide, S. Hansmann, E. Ivers-Tiffée, *ECS Trans.* **2010**, *28*, 11.
[62] J. Laurencin, F. Lefebvre-Joud, G. Delette, *J. Power Sources* **2008**, *177*, 2.
[63] T. Kawashima, M. Hishinuma, *Mater. Trans. Jim* **1996**, *37*, 9.
[64] K. W. Schlichting, N. P. Padture, P. G. Klemens, *J. Mater. Sci.* **2001**, *36*, 12.
[65] B. Todd, J. B. Young, *J. Power Sources* **2002**, *110*, 1.
[66] S. Paydar, M. H. Shariat, S. Javadpour, *Int. J. Hydrogen Energy* **2016**.

Bibliography

[1] L. S. Mahmud, A. Muchtar and M. R. Somalu, *Renew. Sustain. Energy Rev.*, 2017, **72**, 105–116, DOI: `10.1016/j.rser.2017.01.019`.

[2] M. Kadowaki, *ECS Trans.*, 2017, **68**, 15–22, DOI: `10.1149/06801.0015ecst`.

[3] J. B. Hansen, *Faraday Discuss.*, 2015, **182**, 9–48, DOI: `10.1039/C5FD90071A`.

[4] J. Larminie and A. Dicks, *Fuel Cell Systems Explained*, John Wiley and Sons Ltd, Sussex, 2nd edn., 2003.

[5] H.-H. Möbius, *High Temp. Solid Oxide Fuel Cells*, 2003, 23–51, DOI: `10.1016/B978-185617387-2/50019-2`.

[6] A. Stambouli and E. Traversa, *Renew. Sustain. Energy Rev.*, 2002, **6**, 433–455, DOI: `10.1016/S1364-0321(02)00014-X`.

[7] W. Donitz and E. Erdle, *Int. J. Hydrogen Energy*, 1985, **10**, 291–295, DOI: `10.1016/0360-3199(85)90181-8`.

[8] W. Donitz, G. Dietrich, E. Erdle and R. Streicher, *Int. J. Hydrog. Energy Hydrog. Energy*, 1988, **13**, 283–287, DOI: `10.1016/0360-3199(88)90052-3`.

[9] R. J. F. V. Gerwen, *High Temp. Solid Oxide Fuel Cells*, 2003, 363–392, DOI: `10.1016/B978-185617387-2/50030-1`.

[10] V. M. Janardhanan and O. Deutschmann, *ECS Trans.*, 2007, **7**, 1939–1943, DOI: `10.1149/1.2729306`.

[11] S. H. Jensen, PhD Thesis, Risø National Laboratory Information, Denmark, 2006, ISBN: 8755035698.

[12] D. J. L. Brett, A. R. Kucernak, P. Aguiar, S. C. Atkins, N. P. Brandon, R. Clague, L. F. Cohen, G. Hinds, C. Kalyvas, G. J. Offer, B. Ladewig, R. Maher, A. Marquis, P. Shearing, N. Vasileiadis and V. Vesovic, *ChemPhysChem*, 2010, **11**, 2714–31, DOI: `10.1002/cphc.201000487`.

[13] R. C. Maher, G. Offer, N. P. Brandon and L. F. Cohen, *MRS Proceedings*, 2012, **1385**, DOI: `10.1557/opl.2012.852`.

[14] S. C. Singhal, *Solid Oxide Fuels Cells: Facts and Figures*, editor J. T. Irvine and P. Connor, Springer London, London, 2013, volume 55, Pages 1–23, ISBN: 978-1-4471-4455-7, DOI: `10.1007/978-1-4471-4456-4`.

[15] D. J. L. Brett, A. Atkinson, N. P. Brandon and S. J. Skinner, *Chem. Soc. Rev.*, 2008, **37**, 1568–78, DOI: `10.1039/b612060c`.

[16] N. Laosiripojana, W. Wiyaratn, W. Kiatkittipong, A. Arpornwichanop, A. Soottitantawat and S. Assabumrungrat, *Eng. J.*, 2009, **13**, 65–84, DOI: `10.4186/ej.2009.13.1.65`.

[17] A. Aarva, S. J. McPhail and A. Moreno, ECS Trans. ECS, 2009, volume 25, Pages 313–322, DOI: `10.1149/1.3205539`.

[18] R. Bove and S. Ubertini, *J. Power Sources*, 2006, **159**, 543–559.

[19] G. L. Hawkes, J. E. O. Brien, C. M. Baca and R. P. Travis, *Proc. FUELCELL2008 6th Int. Conf. Fuel Cell Sci. Eng. Technol.*, 2008, 1–9.

[20] V. Novaresio, M. García-Camprubí, S. Izquierdo, P. Asinari and N. Fueyo, *Comput. Phys. Commun.*, 2012, **183**, 125–146, DOI: `10.1016/j.cpc.2011.08.003`.

[21] M. Andersson, J. Yuan and B. Sundén, Adv. Comput. Methods Heat Transf. X, WIT Press, Southampton, UK, 2008, volume I, Pages 69–79, DOI: `10.2495/HT080071`.

[22] U. K. Chakraborty, *Energy*, 2011, **36**, 801–802.

[23] V. M. Janardhanan and O. Deutschmann, *Zeitschrift für Phys. Chemie*, 2007, **221**, 443–478, DOI: `10.1524/zpch.2007.221.4.443`.

[24] S. Kakac, A. Pramuanjaroenkij and X. Zhou, *Int. J. Hydrogen Energy*, 2007, **32**, 761–786, DOI: `10.1016/j.ijhydene.2006.11.028`.

[25] S. A. Hajimolana, M. A. Hussain, W. A. W. Daud, M. Soroush and a. Shamiri, *Renew. Sustain. Energy Rev.*, 2011, **15**, 1893–1917, DOI: `10.1016/j.rser.2010.12.011`.

[26] C. O. Colpan, I. Dincer and F. Hamdullahpur, *Int. J. Energy Res.*, 2008, **32**, 336–355, DOI: `10.1002/er.1363`.

[27] D. Bhattacharyya and R. Rengaswamy, *Ind. Eng. Chem. Res.*, 2009, **48**, 6068–6086, DOI: `10.1021/ie801664j`.

[28] M. Secanell, J. Wishart and P. Dobson, *J. Power Sources*, 2011, **196**, 3690–3704.

[29] K. Wang, D. Hissel, M. Péra, N. Steiner, D. Marra, M. Sorrentino, C. Pianese, M. Monteverde, P. Cardone and J. Saarinen, *Int. J. Hydrogen Energy*, 2011, **36**, 7212–7228.

[30] K. N. Grew and W. K. Chiu, *J. Power Sources*, 2012, **199**, 1–13.

[31] M. Lee, G. Park and V. Radisavljevic-Gajic, 2013 5th Int. Conf. Model. Simul. Appl. Optim. IEEE, 2013, Pages 1–6, DOI: `10.1109/ICMSAO.2013.6552683`.

[32] M. Laguna-Bercero, *J. Power Sources*, 2012, **203**, 4–16, DOI: `10.1016/j.jpowsour.2011.12.019`.

[33] M. Mogensen, S. H. Jensen, A. Hauch, I. Chorkendorff and T. Jacobsen, Ceram. Eng. Sci. Proc. 2008, volume 28, Pages 91–101.

[34] M. Ni, M. K. Leung and D. Y. Leung, *Int. J. Hydrogen Energy*, 2008, **33**, 2337–2354, DOI: `10.1016/j.ijhydene.2008.02.048`.

[35] J. Stempien, Q. Sun and S. Chan, *J. Power Technol.*, 2013, **93**, 216–246.

[36] T. Ramos, *Fuel electrodes - Part I (Teachning material for course "SOFC &Electrolysis Course" at DTU*, 2014.

[37] S. Bedogni, S. Campanari, P. Iora, L. Montelatici and P. Silva, *J. Power Sources*, 2007, **171**, 617–625, DOI: `10.1016/j.jpowsour.2007.07.014`.

[38] VDM Metals GmbH, *VDM Crofer 22 APU, Material Data Sheet No. 4046*, 2010, `http://www.vdm-metals.com/fileadmin/user_upload/Downloads/Data_Sheets/Data_Sheet_VDM_Crofer_22_APU.pdf` (visited on May 27, 2017).

[39] U.S. Department of Energy, *Hydrogen storage*, 2017, `https://energy.gov/eere/fuelcells/hydrogen-storage` (visited on May 22, 2017).

[40] X. D. Peng, *Ind. Eng. Chem. Res.*, 2012, **51**, 16385–16392, DOI: `10.1021/ie3002843`.

[41] M. Shiraki, H. Yakabe and H. Uchida, *ECS Trans.*, 2013, **57**, 3261–3267, DOI: `10.1149/05701.3261ecst`.

[42] Z. Wang, M. Mori and T. Araki, *Int. J. Hydrogen Energy*, 2010, **35**, 4451–4458, DOI: `10.1016/j.ijhydene.2010.02.058`.

[43] A. Petersson and A. Wellinger, *IEA Bioenergy*, 2009, 10–11.

[44] J. B. Hansen, F. Fock and H. H. Lindboe, *ECS Trans.*, 2013, **57**, 3089–3097, DOI: `10.1149/05701.3089ecst`.

[45] N. B. Jakobsson, C. F. Pedersen and J. B. Hansen, *Patent: WO 2014154253 A1: A process for producing CO from CO2 in a solid oxide electrolysis cell*, 2014.

[46] F. C. Pedersen, J. B. Hansen, T. Rostrup-Nielsen, J. U. Nielsen, H. Olsson and K. H. Andersen, *Apparatus for production of high purity carbon monoxide*, 2013.

[47] S. Ravn, *On-site carbon monoxide generation takes the next step*, 2016, `https://www.topsoe.com/news/2016/12/site-carbon-monoxide-generation-takes-next-step` (visited on May 22, 2017).

[48] Haldor Topsoe A/S, *eCOs – Dynamic CO generation plants*, 2014, `https://www.teesing.com/files/redirect/2014_eCOs_Press.pdf` (visited on May 22, 2017).

[49] NASA Jet Propulsion Laboratory, *MOXIE - Mars 2020 Rover*, 2017, `https://mars.nasa.gov/mars2020/mission/instruments/moxie/` (visited on May 23, 2017).

[50] NASA Jet Propulsion Laboratory, *MOXIE Functional Block Diagram*, 2015, `https://mars.nasa.gov/multimedia/images/?ImageID=7391` (visited on May 24, 2017).

[51] Q. Fu, C. Mabilat, M. Zahid, A. Brisse and L. Gautier, *Energy Environ. Sci.*, 2010, **3**, 1382, DOI: `10.1039/c0ee00092b`.

[52] D. Y. C. Leung, G. Caramanna and M. M. Maroto-valer, *Renew. Sustain. Energy Rev.*, 2014, **39**, 426–443, DOI: `10.1016/j.rser.2014.07.093`.

[53] S. D. Ebbesen and M. Mogensen, *J. Power Sources*, 2009, **193**, 349–358, DOI: `10.1016/j.jpowsour.2009.02.093`.

[54] A. L. Dipu, Y. Ujisawa, J. Ryu and Y. Kato, *Ann. Nucl. Energy*, 2015, **81**, 257–262, DOI: `10.1016/j.anucene.2015.02.046`.

[55] S. H. Jensen, X. Sun, S. D. Ebbesen, R. Knibbe and M. Mogensen, *Int. J. Hydrogen Energy*, 2010, **35**, 9544–9549, DOI: `10.1016/j.ijhydene.2010.06.065`.

[56] E. Lay-Grindler, J. Laurencin, J. Villanova, P. Cloetens, P. Bleuet, A. Mansuy, J. Mougin and G. Delette, *J. Power Sources*, 2014, **269**, 927–936, DOI: `10.1016/j.jpowsour.2014.07.066`.

[57] Y. Zheng, Q. Li, W. Guan, C. Xu, W. Wu and W. G. Wang, *Ceram. Int.*, 2014, **40**, 5801–5809, DOI: `10.1016/j.ceramint.2013.11.020`.

[58] W. Li, Y. Shi, Y. Luo and N. Cai, *J. Power Sources*, 2013, **243**, 118–130, DOI: `10.1016/j.jpowsour.2013.05.119`.

[59] W. Li, H. Wang, Y. Shi and N. Cai, *Int. J. Hydrogen Energy*, 2013, **38**, 11104–11109, DOI: `10.1016/j.ijhydene.2013.01.008`.

[60] C. Graves, S. D. Ebbesen and M. Mogensen, *Solid State Ionics*, 2011, **192**, 398–403, DOI: `10.1016/j.ssi.2010.06.014`.

[61] M. Ni, *J. Power Sources*, 2012, **202**, 209–216, DOI: `10.1016/j.jpowsour.2011.11.080`.

[62] M. Ni, *Int. J. Hydrogen Energy*, 2012, **37**, 6389–6399, DOI: `10.1016/j.ijhydene.2012.01.072`.

[63] J. Aicart, F. Usseglio-Viretta, J. Laurencin, M. Petitjean, G. Delette and L. Dessemond, *Int. J. Hydrogen Energy*, 2016, **41**, 17233–17246, DOI: `10.1016/j.ijhydene.2016.07.269`.

[64] C. Stoots, J. O'Brien and J. Hartvigsen, *Int. J. Hydrogen Energy*, 2009, **34**, 4208–4215, DOI: `10.1016/j.ijhydene.2008.08.029`.

[65] P. Kofstad and R. Bredesen, *Solid State Ionics*, 1992, **52**, 69–75, DOI: `10.1016/0167-2738(92)90092-4`.

[66] S. Fontana, R. Amendola, S. Chevalier, P. Piccardo, G. Caboche, M. Viviani, R. Molins and M. Sennour, *J. Power Sources*, 2007, **171**, 652–662, DOI: `10.1016/j.jpowsour.2007.06.255`.

[67] S. N. Rashkeev and M. V. Glazoff, *Int. J. Hydrogen Energy*, 2011, **37**, 1280–1291, DOI: `10.1016/j.ijhydene.2011.09.117`.

[68] T. L. Skafte, *Lifetime limiting effects in pre-commercial solid cell devices*, 2017.

[69] M. Keane, *Materials Interactions and Degradation Processes in Solid Oxide Electrolysis Cells*, University of Connecticut, 2014.

[70] M. Ni, *Int. J. Hydrogen Energy*, 2012, **37**, 1731–1745, DOI: `10.1016/j.ijhydene.2011.10.042`.

[71] M. Ni, M. Leung and D. Leung, *Int. J. Hydrogen Energy*, 2007, **32**, 2305–2313, DOI: `10.1016/j.ijhydene.2007.03.001`.

[72] A. Weber and E. Ivers-Tiffée, *J. Power Sources*, 2004, **127**, 273–283, DOI: `10.1016/j.jpowsour.2003.09.024`.

[73] G. Hawkes, J. O'Brien, C. Stoots, S. Herring and M. Shahnam, *Heat Transf. Vol. 4*, 2005, 27–36, DOI: `10.1115/HT2005-72565`.

[74] G. Hawkes, J. O'Brien, C. Stoots and B. Hawkes, *Int. J. Hydrogen Energy*, 2009, **34**, 4189–4197, DOI: `10.1016/j.ijhydene.2008.11.068`.

[75] M. Peksen, A. Al-Masri, L. Blum and D. Stolten, *Int. J. Hydrogen Energy*, 2013, **38**, 4099–4107, DOI: `10.1016/j.ijhydene.2013.01.072`.

[76] Y. Elesin, M. F. Madsen and T. K. Petersen, *Proc. 11th Eur. SOFC SOEC Forum 2014*, 2014, B11.15–B11.23.

[77] Y. Tao, S. D. Ebbesen and M. B. Mogensen, *J. Electrochem. Soc.*, 2014, **161**, F337–F343, DOI: `10.1149/2.079403jes`.

[78] S. Helveg, J. Sehested and J. Rostrup-Nielsen, *Catal. Today*, 2011, **178**, 42–46, DOI: `10.1016/j.cattod.2011.06.023`.

[79] J. R. Rostrup-Nielsen, *J. Catal.*, 1972, **27**, 343–356, DOI: `10.1016/0021-9517(72)90170-4`.

[80] J.-W. Snoeck, G. F. Froment and M. Fowles, *Ind. Eng. Chem. Res.*, 2002, **41**, 4252–4265, DOI: `10.1021/ie010666h`.

[81] P. K. D. Bokx, A. Kock, E. Bolellard, W. Klop and J. W. Geus, *J. Catal.*, 1985, **96**, 454–467, DOI: `10.1016/0021-9517(85)90314-8`.

[82] A. Kock, P. K. D. Bokx, E. Bolellard, W. Klop and J. W. Geus; *J. Catal.*, 1985, **96**, 468–480.

[83] C. H. Bartholomew, *Catal. Rev.*, 2007, **24**, 67–112, DOI: `10.1080/03602458208079650`.

[84] M. C. Annesini, V. Piemonte and L. Turchetti, *Chem. Eng. Trans.*, 2007, **11**, 21–26.

[85] H. Bengaard, *J. Catal.*, 2002, **209**, 365–384, DOI: `10.1006/jcat.2002.3579`.

[86] J. Coad and J. Rivière, *Surf. Sci.*, 1971, **25**, 609–624, DOI: `10.1016/0039-6028(71)90148-8`.

[87] P. B. Tøttrup, *J. Catal.*, 1976, **42**, 29–36.

[88] J. R. Rostrup-Nielsen and J. Sehested, Whisker Carbon Revisited, in *Stud. Surf. Sci. Catal.* Editor J. Spivey, G. Roberts and B. Davi, Elsevier, 2001, volume 139, Pages 1–12, DOI: `10.1016/S0167-2991(01)80174-9`.

[89] W. Li, Y. Shi, Y. Luo, Y. Wang and N. Cai, *J. Power Sources*, 2015, **276**, 26–31, DOI: `10.1016/j.jpowsour.2014.11.106`.

[90] C. M. Finnerty, N. J. Coe, R. H. Cunningham and R. Ormerod, *Catal. Today*, 1998, **46**, 137–145, DOI: `10.1016/S0920-5861(98)00335-6`.

[91] H. Kiehne, *Battery Technology Handbook*, Expert Verlag GmbH, Renningen-Malsheim, 2nd edn., 2003.

[92] J. Rostrup-Nielsen and D. L. Trimm; *J. Catal.*, 1977, **48**, 155–165.

[93] J. Sehested, P. L. Hansen, S. Helveg, C. Lo, B. S. Clausen, J. R. Rostrup-nielsen and F. Abild-pedersen, *Nature*, 2004, **427**, 426–429, DOI: `10.1038/nature02308.1.`.

[94] Y. Tao, S. D. Ebbesen, W. Zhang and M. B. Mogensen, *ChemCatChem*, 2014, **6**, 1220–1224, DOI: `10.1002/cctc.201300941`.

[95] J. R. Rostrup-Nielsen, Catalytic Steam Reforming, in *Catal. Sci. Technol.* Editor J. Anderson and M. Boudart, Springer Verlag, Berlin, 5th edn., 1984, ch. 1.

[96] J. Rostrup-Nielsen and L. J. Christiansen, *Concepts In Syngas Manufacture*, Imperial College Press, London, 2011, ISBN: 978-1848165670.

[97] W. Y. Lee, J. Hanna and A. F. Ghoniem, *J. Electrochem. Soc.*, 2013, **160**, F94–F105, DOI: `10.1149/2.051302jes`.

[98] C. M. Grgicak, R. G. Green and J. B. Giorgi, *J. Mater. Chem.*, 2006, **16**, 885–897, DOI: `10.1039/b515016g`.

[99] H. Tagawa, D. Simwonis, F. Tietz and D. Stover, *Solid State Ionics*, 2000, **132**, 241–251.

[100] S. Gao, J. Li and Z. Lin, *J. Power Sources*, 2014, **255**, 144–150, DOI: `10.1016/j.jpowsour.2014.01.033`.

[101] A. Hauch, K. Brodersen, M. Chen and M. B. Mogensen, *Solid State Ionics*, 2016, **293**, 27–36, DOI: `10.1016/j.ssi.2016.06.003`.

[102] D. Simwonis, F. Tietz and D. Stover, *Solid State Ionics*, 2000, **132**, 241–251, DOI: `10.1016/S0167-2738(00)00650-0`.

[103] P. Boldrin, E. Ruiz-trejo, J. Mermelstein, J. Miguel and N. P. Brandon, *Chem. Rev.*, 2016, **116**, 13633–13684, DOI: `10.1021/acs.chemrev.6b00284`.

[104] J. B. Hansen, *J. Catal.*, 2015, **328**, 280–296, DOI: `10.1016/j.jcat.2015.04.014`.

[105] *NIST Chemistry WebBook, NIST Standard Reference Database Number 69*, editor P. Linstrom and W. Mallard, National Institute of Standards and Technology, Gaithersburg MD, 20899, 2014.

[106] B. J. McBride, M. J. Zehe and S. Gordon, *Tech. Rep. NASA*, 2002, **211556**, 291.

[107] C. L. Yaws, *Yaws' Handbook of Thermodynamic Properties for Hydrocarbons and Chemicals*, Knovel, 2009, ISBN: 978-1-60119-797-9.

[108] N. Christiansen, S. Primdahl, M. Wandel, S. Ramousse and A. Hagene, *E C S Trans.*, 2013, **57**, 43–52, DOI: `10.1149/05701.0043ecst`.

[109] M. Chen, X. Sun, A. Hauch, K. Brodersen, B. Charlas, S. Molin, K. Agersted, V. Venkatachalam, W.-r. Kiebach, Y.-l. Liu, J. Jonna, C. R. Graves, J. R. Bowen, J.-c. Njodzefon, M. B. Mogensen, P. V. Hendriksen, P. Blennow and C. F. Pedersen, *Final report Energinet.dk project no. 2013-1-12013*, technical report, Department of Energy Conversion and Storage (DTU Energy), Roskilde, 2015, Page 25.

[110] R. Knibbe, L. Traulsen, A. Hauch, S. D. Ebbesen and M. Mogensen, *J. Electrochem. Soc.*, 2010, **157**, B1209–B1217, DOI: `10.1149/1.3447752`.

[111] J. D. Duhn, A. D. Jensen, S. Wedel and C. Wix, *J. Power Sources*, 2016, **336**, 261–271, DOI: `10.1016/j.jpowsour.2016.10.060`.

[112] T. Heiredal-Clausen and C. Buchholtz Frederiksen, *Patent: WO2014177212: GAS INLET FOR SOEC UNIT*, 2014.

[113] A. Bertei and C. Nicolella, *J. Power Sources*, 2015, **279**, 133–137, DOI: `10.1016/j.jpowsour.2015.01.007`.

[114] P. D. Neufeld, A. R. Janzen and R. A. Aziz, *J. Chem. Phys.*, 1972, **57**, 1100–1102, DOI: `10.1063/1.1678363`.

[115] R.-. B. Bird, W. E. Stewart and E. N. Lightfoot, *Transport Phenomena*, John Wiley & Sons, New York, 2nd edn., 2007, ISBN: 978-0-470-11539-8.

[116] E. N. Fuller, P. D. Schettler and J. C. Giddings, *Ind. Eng. Chem.*, 1966, **16**, 551, DOI: `10.1016/0042-207X(66)90400-3`.

[117] B. Todd and J. Young, *J. Power Sources*, 2002, **110**, 186–200, DOI: `10.1016/S0378-7753(02)00277-X`.

[118] I. Amdur and L. M. Shuler, *J. Chem. Phys.*, 1963, **38**, 188–194, DOI: `10.1063/1.1733460`.

[119] H. Zhu, R. J. Kee, V. M. Janardhanan, O. Deutschmann and D. G. Goodwin, *J. Electrochem. Soc.*, 2005, **152**, A2427, DOI: `10.1149/1.2116607`.

[120] V. Menon, V. M. Janardhanan and O. Deutschmann, *Chem. Eng. Sci.*, 2013, **110**, 83–93, DOI: `10.1016/j.ces.2013.10.025`.

[121] J. Aicart, J. Laurencin, M. Petitjean and L. Dessemond, *Fuel Cells*, 2014, **14**, 430–447, DOI: `10.1002/fuce.201300214`.

[122] P. Kerkhof, *Chem.Eng.J.*, 1996, **64**, 319–343, DOI: `10.1016/S0923-0467(96)03134-X`.

[123] J. B. Young and B. Todd, *Int. J. Heat Mass Transf.*, 2005, **48**, 5338–5353, DOI: `10.1016/j.ijheatmasstransfer.2005.07.034`.

[124] Y. Vural, L. Ma, D. B. Ingham and M. Pourkashanian, *J. Power Sources*, 2010, **195**, 4893–4904, DOI: `10.1016/j.jpowsour.2010.01.033`.

[125] S. Wang, W. M. Worek and W. Minkowycz, *Int. J. Heat Mass Transf.*, 2012, **55**, 3933–3945, DOI: `10.1016/j.ijheatmasstransfer.2012.03.024`.

[126] M. F. Johnson and W. E. Stewart, *J. Catal.*, 1965, **4**, 248–252, DOI: `10.1016/0021-9517(65)90015-1`.

[127] N. Epstein, *Chem. Eng. Sci.*, 1989, **44**, 777–779, DOI: `10.1016/0009-2509(89)85053-5`.

[128] G. Brus, K. Miyawaki, H. Iwai, M. Saito and H. Yoshida, *Solid State Ionics*, 2014, **265**, 13–21, DOI: `10.1016/j.ssi.2014.07.002`.

[129] Z. Horak and P. Schneider, *Chem. Eng. J.*, 1971, **2**, 27–35, DOI: `10.1016/0300-9467(71)87004-1`.

[130] J. Haugaard and H. Livbjerg, *Chem. Eng. Sci.*, 1998, **53**, 2941–2948, DOI: `10.1016/S0009-2509(98)00108-0`.

[131] E. Mason and A. Malinauskas, *Gas transport in porous media: the dusty-gas model : Chemical engineering monographs 17.* Elsevier, Amsterdam, 1983, ISBN: 0444421904.

[132] R. Jackson, *Transport in porous catalysts*, Elsevier, Amsterdam, 1977, ISBN: 0444415939.

[133] Von E.Wicke und R. Kallenbach, *Kolloid Zeitschrift*, 1941, **97**, 135–151.

[134] K. Hou, M. Fowles and R. Hughes, *Chem. Eng. Res. Des.*, 1999, **77**, 55–61, DOI: `10.1205/026387699525873`.

[135] N. Mouchot and A. Zoulalian, *Holzforschung*, 2002, **56**, 318–326, DOI: `10.1515/HF.2002.051`.

[136] R. E. Williford, L. a. Chick, G. D. Maupin, S. P. Simner and J. W. Stevenson, *J. Electrochem. Soc.*, 2003, **150**, A1067, DOI: `10.1149/1.1586300`.

[137] S. T. Kolaczkowski, *Catal. Today*, 2003, **83**, 85–95, DOI: `10.1016/S0920-5861(03)00218-9`.

[138] F. Zhang, R. E. Hayes and S. T. Kolaczkowski, *Chem. Eng. Res. Des.*, 2004, **82**, 481–489, DOI: `10.1205/026387604323050191`.

[139] J. Valus and P. Schneider, *Appl. Catal.*, 1981, **1**, 355–366, DOI: `10.1016/0166-9834(81)80053-X`.

[140] K. Soukup, P. Schneider and O. Šolcová, *Chem. Eng. Sci.*, 2008, **63**, 1003–1011, DOI: `10.1016/j.ces.2007.10.032`.

[141] K. Soukup, P. Schneider and O. Šolcová, *Chem. Eng. Sci.*, 2008, **63**, 4490–4493, DOI: `10.1016/j.ces.2008.06.020`.

[142] Y. A. Cengel, R. H. Turner and J. M. Cimbala, *Fundamentals of Thermal-Fluid Sciences*, McGraw-Hill, New York, 3rd edn., 2008, Pages 782–783, 914, ISBN: 978-007-126631-4.

[143] O. Zienkiewicz, R. Taylor and P. Nithiarasu, Convection-Dominated Problems: Finite Element Approximations to the Convection-Diffusion-Reaction Equation, in *Finite Elem. Method Fluid Dyn.* Elsevier, Oxford, 2014, ch. Chapter 2, Pages 31–85, DOI: `10.1016/B978-1-85617-635-4.00002-9`.

[144] COMSOL AB., *COMSOL Multiphysics - Reference Manual*, 2015, Pages 183–189.

[145] F. Usseglio-Viretta, J. Laurencin, G. Delette, J. Villanova, P. Cloetens and D. Leguillon, *J. Power Sources*, 2014, **256**, 394–403, DOI: `10.1016/j.jpowsour.2014.01.094`.

[146] D. H. Jeon, J. H. Nam and C.-J. Kim, *J. Electrochem. Soc.*, 2006, **153**, A406, DOI: `10.1149/1.2139954`.

[147] G. Sin, K. V. Gernaey and A. E. Lantz, *Biotechnol. Prog.*, 2009, **25**, 1043–1053, DOI: `10.1021/bp.166`.

[148] M. D. Mckay, R. J. Beckman and W. J. Conover, *Technometrics*, 1979, **21**, 239–245, DOI: `10.1080/00401706.1979.10489755`.

[149] H. Iwai, N. Shikazono, T. Matsui, H. Teshima, M. Kishimoto, R. Kishida, D. Hayashi, K. Matsuzaki, D. Kanno, M. Saito, H. Muroyama, K. Eguchi, N. Kasagi and H. Yoshida, *J. Power Sources*, 2010, **195**, 955–961, DOI: `10.1016/j.jpowsour.2009.09.005`.

[150] M. Kishimoto, K. Miyawaki, H. Iwai, M. Saito and H. Yoshida, *Fuel Cells*, 2013, **13**, 476–486, DOI: `10.1002/fuce.201200174`.

[151] J. R. Wilson, J. S. Cronin and S. A. Barnett, *Scr. Mater.*, 2011, **65**, 67–72, DOI: `10.1016/j.scriptamat.2010.09.025`.

[152] D. A. G. Bruggeman, *Ann. Phys.*, 1937, **421**, 160–178, DOI: `10.1002/andp.19374210205`.

[153] A. Berson, H. W. Choi and J. G. Pharoah, *Phys. Rev. E - Stat. Nonlinear, Soft Matter Phys.*, 2011, **83**, 1–12, DOI: `10.1103/PhysRevE.83.026310`.

[154] W. Kong, Q. Zhang, X. Xu and D. Chen, *Energies*, 2015, **8**, 13953–13959, DOI: `10.3390/en81212406`.

[155] D. Lee, J. Lee, J. Kim, H. Lee and H. Song, *Solid State Ionics*, 2004, **166**, 13–17.

[156] A. Jena and K. Gupta., *Ceram. Eng. Sci. Proc.*, 2005, **26**, 169.

[157] E. Resch, MSc. Thesis, Queen's University, Kingston, Ontario, Canada, 2008.

[158] D. Simwonis, H. Thülen, F. Dias, A. Naoumidis and D. Stöver, *J. Mater. Process. Technol.*, 1999, **92-93**, 107–111.

[159] K.-R. Lee, S. Choi, J. Kim, H.-W. Lee and J.-H. Lee., *J. Power Sources*, 2005, **140**, 226–234.

[160] Y. Wang, F. Yoshiba, T. Watanabe and S. Weng, *J. Power Sources*, 2007, **170**, 101–110.

[161] J. Yuan and B. Sundén, *J. Heat Transfer*, 2005, **127**, 1380.

[162] J. Hwang, C. Chen and D. Lai, *J. Power Sources*, 2005, **140**, 235, 242.

[163] U. Pasaoguillari and C. Wang, Proc. Electrochem. Soc. (Solid Oxide Fuels Cells VIII, Paris), 2003, Page 1403.

[164] T. Nishino, H. Iwai and K. Suzuki, *J. Fuel Cell Sci. Technol.*, 2006, **3**, 33–44.

[165] H. Zhu and R. Kee, *J. Power Sources*, 2003, **117**, 61–74.

[166] M. Ni, M. K. Leung and D. Y. Leung, *J. Power Sources*, 2006, **163**, 460–466, DOI: `10.1016/j.jpowsour.2006.09.024`.

[167] V. M. Janardhanan and O. Deutschmann, *J. Power Sources*, 2006, **162**, 1192–1202.

[168] R. Suwanwarangkul, E. Croiset, M. Pritzker, M. Fowler, P. Douglas and E. Entchev, *J. Power Sources*, 2006, **154**, 74–85.

[169] M. Politis, E. Kikkinides, M. Kainourgiakis and A. Stubos, *Microporous Mesoporous Mater.*, 2008, **110**, 92–99.

[170] T. Aloui and K. Halouani, *Appl. Therm. Eng.*, 2007, **171**, 696–705.

[171] I. Perdana, B. W. Tyoso, I. M. Bendiyasa, Rochmadi, S. K. Wirawan and D. Creaser, *Chem. Eng. Res. Des.*, 2009, **87**, 1438–1447, DOI: `10.1016/j.cherd.2009.03.004`.

[172] P. Hjalmarsson, X. Sun, Y. L. Liu and M. Chen, *J. Power Sources*, 2013, **223**, 349–357, DOI: `10.1016/j.jpowsour.2012.08.063`.

[173] W. Li, Y. Shi, Y. Luo and N. Cai, *Int. J. Hydrogen Energy*, 2014, **39**, 13738–13750, DOI: `10.1016/j.ijhydene.2014.03.014`.

[174] J. Yu, Y. Wang and S. Weng, *J. Fuel Cell Sci. Technol.*, 2012, **9**, 021011, DOI: `10.1115/1.4005625`.

[175] J. Kirtley, A. Singh, D. Halat, T. Oswell, J. M. Hill and R. A. Walker, *J. Phys. Chem. C*, 2013, **117**, 25908–25916, DOI: `10.1021/jp408192e`.

[176] J. Kuhn and O. Kesler, *J. Power Sources*, 2014, **246**, 430–437, DOI: `10.1016/j.jpowsour.2013.07.106`.

[177] V. Subotić, C. Schluckner, J. Mathe, J. Rechberger, H. Schroettner and C. Hochenauer, *J. Power Sources*, 2015, **295**, 55–66, DOI: `10.1016/j.jpowsour.2015.06.133`.

[178] V. Subotić, C. Schluckner, H. Schroettner and C. Hochenauer, *J. Power Sources*, 2016, **302**, 378–386, DOI: `10.1016/j.jpowsour.2015.10.071`.

[179] T. Klemensø, PhD thesis, Technical University of Denmark, 2005.

[180] C. Schluckner, V. Subotić, V. Lawlor and C. Hochenauer, *Int. J. Hydrogen Energy*, 2017, **42**, 4434–4448, DOI: `10.1016/j.ijhydene.2016.11.162`.

[181] M. Ito, T. Tagawa and S. Goto, *Appl. Catal. A Gen.*, 1999, **177**, 15–23, DOI: `10.1016/S0926-860X(98)00251-8`.

[182] D. Chen, R. Lødeng and A. Holmen, *Self-stabilization of Ni catalysts during carbon dioxide reforming of methane*, Elsevier, 2004, volume 147, Pages 181–186, ISBN: 9780444515995, DOI: `10.1016/S0167-2991(04)80048-X`.

[183] Y. Tao, S. D. Ebbesen and M. B. Mogensen, *J. Electrochem. Soc.*, 2014, **161**, F337–F343, DOI: `10.1149/2.079403jes`.

[184] T. L. Skafte, C. Graves, P. Blennow and J. Hjelm, *ECS Trans.*, 2015, **68**, 3429–3437, DOI: `10.1149/06801.3429ecst`.

[185] J. Rechberger, A. Kaupert, J. Hagerskans and L. Blum, *Transp. Res. Procedia*, 2016, **14**, 3676–3685, DOI: `10.1016/j.trpro.2016.05.442`.

[186] V. A. C. Haanappel, P. Batfalsky, S. M. Gross, L. G. J. de Haart, J. Malzbender, N. H. Menzler, V. Shemet, R. W. Steinbrech and I. C. Vinke, *J. Fuel Cell Sci. Technol.*, 2007, **4**, 11–18, DOI: `10.1115/1.2393301`.

[187] R. L. Iman and W. Conover, *Commun. Stat. - Simul. Comput.*, 1982, **11**, 311–334, DOI: `10.1080/03610918208812265`.

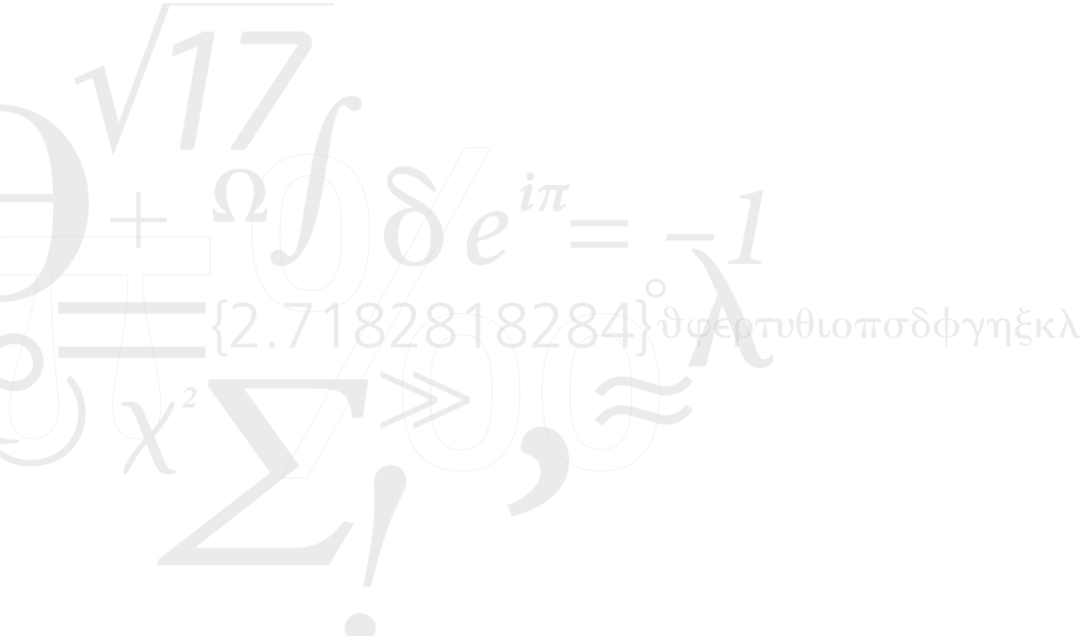
$\sqrt{17}$
$e^{i\pi} = -1$
{2.7182818284}
ϑφερτυθιοπσδφγηξκλ
χ^2